Universiteit Antwerpen

Faculteit Wetenschappen
Departement Fysica

Plasmonics in graphene and related materials

Plasmonica in grafeen en gerelateerde materialen

Proefschrift voorgelegd tot het behalen van de graad van doctor in de wetenschappen aan de Universiteit Antwerpen te verdedigen door

Ben Van Duppen

Promotoren
Prof. Dr. François Peeters
Prof. Dr. Marco Polini

Mei 2016

Members of the Jury:

Chairman
Prof. Dr. Nick Van Remortel, Universiteit Antwerpen, Belgium

Supervisors
Prof. Dr. François Peeters, Universiteit Antwerpen, Belgium
Prof. Dr. Marco Polini, Istituto Italiano di Tecnologia, Genova, Italy

Members
Prof. Dr. Sandra Van Aert, Universiteit Antwerpen, Belgium
Prof. Dr. Jacques Tempère, Universiteit Antwerpen, Belgium
Prof. Dr. David Neilson, University of Camerino, Italy
Prof. Dr. Alexander Grigorenko, University of Manchester, UK

This work was supported by the Flemish Science Foundation.

Contact Information

Ben Van Duppen
G.U. 212
Groenenborgerlaan 171
2020 Antwerpen
Belgium
ben.vanduppen@uantwerpen.be

Acknowledgements

In this thesis, I present several projects on plasmonics in which I was involved as a researcher. Before diving into the physics, I want to thank the members of the jury and my collaborators on these projects, without whom this work never could have been done.

I would especially like to express my gratitude to all the members of the research team in Pisa. Thanks to them, and the endless blackboard discussions, I regained my passion for physics which gave me the motivation I needed to write this thesis. Thanks to Marco for having his endless patience and, even more, for him endlessly challenging me to solve new problems in the simplest ways possible. I hope that we can continue working together in the same way.

I would like to thank all members of the CMT group in Antwerp and especially François for the vast amount of corrections and comments he provided me with during the writing of this thesis and for all the opportunities I had during my PhD to explore both the scientific and the real world.

The last nine years, I had the honour of studying physics and persuing my PhD in the company of an extraordinary group of friends. I really enjoyed the loud and open lunch-time discussions that sharpened my world view, thanks!

Finally, I would like to thank my friends and family for the immense support I've had during the writing of this thesis and especially my boyfriend, Ward, who was there for me every time I needed advice, food or simply a hug.

I hope you will enjoy the work.

Ben Van Duppen — Antwerp, May 2016

Voor Oma, mijn allergrootste fan

Samenvatting

Deze thesis stelt onderzoek voor naar de plasmon eigenschappen van grafeen en gerelateerde materialen. Plasmonen zijn collectieve dichtheidsoscillaties van de elektronvloeistof dat aanwezig is in deze twee-dimensionele materialen. Binnen de zogenaamde "Willekeurige Fase Benadering" ("Random Phase Approximation") worden vijf verschillende platformen onderzocht op hun plasmon eigenschappen: sterk gedoteerd grafeen, een grafeen-hexagonaal boor-nitride heterostructuur met ongebalanceerde valleien, siliceen in de nabijheid van externe velden, grafeen onder de invloed van een sterke elektrische stroom, en een rooster van grafeen nanostrips.

Voor het sterk gedoteerd grafeen is er gevonden dat hoewel de energie dispersie van de afzonderlijke elektronen driehoekig vervormd is, de plasmonen nog steeds isotroop zijn. Dit is het gevolg van de hexagonale symmetrie van het grafeen kristal.

Het grafeen neergelegd op hexagonaal boor-nitride toont onder bepaalde omstandigheden twee nieuwe soorten plasmon modi. Één van hen is een akoestische mode die ladingsneutraal is in de lange golflengte limiet, maar die licht gedempt is. De andere is een ongedempte mode die voor korte golflengten bestaat en deels ladingsneutraal is.

Ook in siliceen kunnen plasmonen voorkomen als golven in het elektron fluïdum. Bovendien is aangetoond dat deze plasmonen beïnvloed kunnen worden door externe elektrische- en uitwisselingsvelden door hun levensduur te veranderen met het in- en uitschakelen van mogelijke enkele-deeltjes excitaties van een bepaald spin- en vallei type.

Wanneer men een sterke elektrische stroom doorheen grafeen laat vloeien, veranderen ook de optische eigenschappen van het kristal. De optische absorptie wordt dubbelbrekend als een functie van de hoek tussen de richting van de stroom en de polarisatie richting van het licht. Verder worden de plasmonen in grafeen gecollimeerd in de richting van de

stroom en krijgen ze een niet-reciproke energie dispersie.

De excitatie van plasmonen in grafeen nanostrips is tot slot beschreven met een semiklassieke theorie. Aangezien de plasmonen lokaal de dichtheid en snelheid van de elektronen in de elektronvloeistof beïnvloeden, veranderen ze ook de optische absorptie die bij gevolg oscilleert met de dubbele frequentie van de geëxciteerde plasmonen. Deze opstelling bewijst dat het mogelijk is om met grafeen een plasmon-gestimuleerde optische modulator te creëren.

Deze thesis presenteert nieuwe inzichten in het veld van plasmonica in grafeen en gerelateerde materialen. De resultaten kunnen helpen het ultieme doel van plasmonica te bereiken, namelijk het gebruik ervan in de fotonica.

Abstract

This thesis presents an inquiry into the plasmonic properties of graphene and related two-dimensional materials. Plasmons, or high frequency collective density oscillations of the electron liquid, are treated in a linear response framework within the “Random Phase Approximation”. In this thesis, the plasmonic response of five distinct platforms is scrutinised: strongly doped graphene, a graphene-hexagonal boron nitride heterostructure with valley imbalance, silicene in the presence of external fields, graphene with a strong electric current, and an array of graphene nanostripes.

For the strongly doped graphene sheet, it is found that even though the single-particle energy dispersion is trigonally warped, the plasmon dispersion remains isotropic. This is attributed to the hexagonal symmetry of the graphene crystal.

In the case of a graphene sheet deposited on hexagonal boron nitride, it is shown that under specific circumstances, valley polarisation induces two new kinds of plasmon modes. One of them is an acoustic mode that is charge neutral in the long-wavelength limit and is slightly damped. The other one is an undamped mode that exists for short wavelengths and is partly charge neutral.

It is shown that silicene also hosts plasmons in its electron liquid. In the case of silicene, it is, furthermore, shown that external electric and exchange fields can be used to change the plasmon damping by switching single-particle excitations of a specific spin and valley type on and off.

When graphene is subjected to a strong electric current, its optical properties are affected. The optical absorption acquires a birefringent character with respect to the direction of the current flow and the plasmon modes are shown to become collimated in the downstream direction. It is demonstrated that the plasmon modes acquire a non-reciprocal

dispersion as well.

The excitation of plasmons in graphene nanostripes is finally considered in a semiclassical framework. The plasmons change the local density and velocity of the electron liquid. As a result, it is shown that the absorption of the nanoribbons oscillate with twice the frequency of the excited plasmons. This is used as a proof of concept for a high-frequency plasmon-assisted optical modulator.

This thesis provides new insights into the field of plasmonics of graphene and related materials. The results could help to achieve the main goal of plasmonics in 2D materials, i.e. the use of their plasmons in photonic applications.

List of publications

During the course of my PhD project, I had the chance to work on several topics with many different collaborators. Here, I list the works I worked on that are so far submitted or published. I chose to focus this thesis on a selected number of these topics that are related to plasmonics. Some of the topics discussed in the thesis will be added to the list as soon as the respective manuscript is finished.

1. Y. M. Xiao, **B. Van Duppen**, W. Xu, and F. M. Peeters: *Infrared to terahertz optical conductivity of n-type and p-type monolayer* MoS_2 *in the presence of Rashba effect*, (manuscript in preparation).
2. A. Chaves, **B. Van Duppen**, M. Z. Mayers, J. Kunstman, F. M. Peeters, and D. R. Reichman: *Theory of indirect excitons and trions in van der Waals heterostructures*, (manuscript in preparation).
3. M. Van der Donck, C. De Beule, B. Partoens, F. M. Peeters, and **B. Van Duppen**: *Piezoelectricity in asymmetrically strained bilayer graphene*, 2D Materials (2016) (submitted).
4. M. Van der Donck, F. M. Peeters, and **B. Van Duppen**: *Comment on "Creating in-plane pseudomagnetic fields in excess of 1000 T by misoriented stacking in a graphene bilayer"*, Physical Review B (2016) (submitted).
5. N. Missault, P. Vasilopoulos, F.M. Peeters, and **B. Van Duppen**: *Spin- and valley-dependent miniband structure and transport in silicene superlattices.* Physical Review B **93**, 125425 (2016).

6. M. Van der Donck, F. M. Peeters, and **B. Van Duppen**: *Transport properties of bilayer graphene in a strong in-plane magnetic field*, Physical Review B **93**, 115423 (2016).
7. **B. Van Duppen**, A. Tomadin, A.N. Grigorenko, and M. Polini: *Current-induced birefringent absorption and non-reciprocal plasmons in graphene.* 2D Materials **3**, 015011 (2016) (Open access).
8. H.M. Abdullah, M. Zarenia, H. Bahlouli, F.M. Peeters, and **B. Van Duppen**: *Gate tunable layer selectivity of transport in bilayer graphene nanostructures.*, Europhysics Letters **113**, 17006 (2016).
9. N. Missault, P. Vasilopoulos, V. Vargiamidis, F.M. Peeters, and **B. Van Duppen**: *Spin- and valley-dependent transport through arrays of ferromagnetic silicene junctions.* Physical Review B **92**, 195423 (2015).
10. **B. Van Duppen**, P. Vasilopoulos, and F. M. Peeters: *Spin and valley polarization of plasmons in silicene due to external fields*. Physical Review B **90**, 035142 (2014).
11. **B. Van Duppen** and F. M. Peeters: *Thermodynamic properties of the electron gas in multilayer graphene in the presence of a perpendicular magnetic field.* Physical Review B **88**, 245429 (2013).
12. P. M. Krstajić, **B. Van Duppen**, and F. M. Peeters: *Plasmons and their interactions with electrons in trilayer graphene*. Physical Review B **88**, 195423 (2013).
13. **B. Van Duppen** and F. M. Peeters: *Four-band tunneling in bilayer graphene*. Physical Review B **87**, 205427 (2013).
14. **B. Van Duppen**, S. H. R. Sena, and F. M. Peeters: *Multiband tunneling in trilayer graphene*. Physical Review B **87**, 195439 (2013).
15. **B. Van Duppen** and F. M. Peeters: *Klein paradox for a pn junction in multilayer graphene*. Europhysics Letters **102**, 27001 (2013).
16. **B. Van Duppen** and F. M. Peeters: *Comment on Chiral tunneling in trilayer graphene [Appl. Phys. Lett. 100, 163102 (2012)].* Applied Physics Letters **101**, 226101 (2012).
17. J. Tempère, E. Vermeylen, and **B. Van Duppen**: *Skyrmion rows, vortex rows, and phase slip lines in sheared multi-component condensates*. Physica C: Superconductivity **479**, 61, (2012).

Contents

List of Abbreviations

2D	Two-dimensional
2DEG	Two-dimensional electron gas
3D	Three-dimensional
AFM	Atomic force microscope
ARPES	Angle resolved photoemession spectroscopy
(s)BZ	(superlattice) Brillouin zone
C	Carbon
CaF_2	Calcium difloride
CVD	Chemical vapour deposition
DOS	Density of states
EELS	Electron energy-loss spectroscopy
EM	Electro-magnetic
Eu	Europium
e-e	Electron-electron
FD(D)	Fermi-Dirac (distribution)
GaAs	Gallium arsenide
g/hBN	Graphene/hbN
hBN	Hexagonal boron nitride
IR	Infrared
Ir	Iridium
LRF	Linear response function
LRT	Linear response theory
MDF	Massless Dirac Fermions
MIR	Mid-infrared
MoS_2	Molybdenum disulfide
(N)NN	(Next) Nearest-neighbour
PHES	Particle-hole excitation spectrum
QED	Quantum electrodynamics
RPA	Random phase approximation
SiC	Silicon carbide
SiO_2	Silicon dioxide
SOC	Spin-orbit coupling
SP(P)	Surface plasmon (polariton)
s-SNOM	Scattering-type scanning near-field optical microscope
TB	Tight-binding
TLG	Trilayer graphene
ZrB_2	Zirconium diboride

CHAPTER 1

Introduction

1.1 Plasmons in graphene

1.1.1 A history of plasmons

The history of plasmonics starts very early with creative craftsmen from ancient times that made beautiful colourful glass goblets by mixing metallic (gold and silver) particles with glass, creating stained-glass. A very famous, still remaining, artefact, the Lycurgus cup, is shown in Fig. 1.1. This cup has a greenish colour when light reflects on its surface. However, when a white light source is placed inside the cup, it turns red. The physical reason being that the electronic liquid in the metallic particles in the glass absorb and scatter light for short wavelengths in the visible part of the electro-magnetic (EM) spectrum (blue and green). Therefore, when observing the cup in reflected light, it looks greenish. In he same way these colours are filtered from the light passing through it which makes the cup look red [1]. The microscopic phenomenon that causes the metallic particles to absorb and scatter light in a specific frequency range is the excitation of a *plasmon*, a collective oscillation of the electron liquid.

Scientific research on plasmons started at the beginning of last century when Wood reported the results of an uneven distribution of light in a diffraction grating spectrum [2]. Lord Rayleigh tried to explain Wood's experimental results, but failed in his attempt [3]. After about 40 years, Fano [4] theoretically explained the so-called Wood's anomalies by using Sommerfeld's theory. This theory was developed in 1899 in the context of

Figure 1.1: Picture of the Lycurgus cup, an fourth-century Roman cup. Left: If light shines on the outside of the cup, it looks green. Right: If a white light source is put inside the cup, it looks red. This is due to the gold and silver nanoparticles in the glass that feature plasmon resonances in the blue-green spectral range. Image courtesy of the British Museum.

radio waves propagating along the surface of a conductor of finite conductivity [5]. Fano managed to extend it to the visible range of the EM spectrum in order to explain the observations made by Woods. An important result of this study was that the EM waves could propagate tangential to the surface of a conductor, but are very strongly damped in the transversal direction. Therefore, these modes are bound to the surface of the conductive material.

In parallel with the search for the explication of Wood's anomalies, also the research on the fourth fundamental state of matter, started by Crookes in 1879 [6], was important for the field of plasmonics. Langmuir and Tonks studied the behaviour of ionized gasses, called plasmas, and showed that plasmas can sustain ion and electron oscillations that are formed as waves in the electron density, so-called *plasma waves* [7, 8]. These waves are the same as the ones found by Fano, but in Fano's case they can be quantized and are, therefore, called plasmons.

Later on, Bohm and Pines found that electrons passing through foils experience energy losses. They attributed these to the excitation of plasmons in the bulk of the material and identified it as a collective phenomenon of the electron liquid [9–11]. However, this could not account for all losses that were observed in experiments and Ritchie [12], Powell and Swan [13] suggested that this was related to a phenomenon occurring at the interface of the material with the environment. The study of Stern and Ferrell [14] on the plasma oscillations of a degenerate electron gas at a material's surface explained the phenomenon theoretically and they called it a *surface plasmon* (SP).

When exciting SPs with light, the EM radiation couples to the electron density oscillation and forms a hybrid mixture of electrons and light, a so-called *surface plasmon polariton* (SPP) [15]. The wavelength of this SPP is much shorter than that of the free-space photon that excited the SPP. In that way, the SPP in noble metals have been shown to compress the incident light over ten times, leading to a very high energy density [16].

Since the first observations by Wood in the beginning of last century, the scientific understanding of plasmons has improved drastically and researchers began to understand that they could use these waves in the electron liquid to their advantage. At the end of last century, this understanding led to the birth of a new subfield, called *plasmonics*.

1.1.2 Plasmonics

Plasmonics [17] aims to exploit the peculiar properties of plasmons in a various range of applications. Over the last decade, the field has been very successful in integrating plasmons in applications as diverse as nano-biosensing, where researchers were able to detect a single hemoglobin molecule [18], and the enhancement of photovoltaic devices [19]. Furthermore, it was integrated in nanophotonic systems [20], it was used to make metamaterials that can optically cloak objects [21], to make single photon transistors for quantum computations [22, 23] and to enhance Raman spectroscopy [24, 25]. Notice that all these applications are active in the visible range of the EM spectrum.

As explained in the previous section, SPPs can be considered as light waves that are confined to the interface between a conductor and a dielectric because of their interaction with the electrons of the conductor [26]. Because they are trapped at the surface of the conductor, the SPPs can be used to concentrate and channel light in any direction by engineering the surface using subwavelength structures. Doing so, one could make optical circuits, rather than electronical circuits, to process light by logic elements before being converted back into free-space light [26]. In order to achieve this, one needs to have plasmons that are long lived and strongly confined. However, this is often a contradiction since the stronger the light is confined, the more it interacts with the metallic substrate and the shorter its life time will be [27].

Another issue that needs to be overcome is the lack of tunability plasmonic systems. Because of the momentum mismatch between free-space photons and plasmons, one needs to engineer special subwavelength structures for plasmons to be excited. Several mechanisms have been developed to ensure that light couples to the electron liquid, e.g. using prism coupling [28, 29], scattering from topological defects [30] or putting a periodic corrugation of the conductor's surface [31]. It has been noticed that for all of these it is hard to change the frequency of the plasmon within the same set-up.

In order to overcome the limitations of SPPs at the surface of metals, a new candidate has risen to the attention of plasmonic researchers since 2004. The name of this material is *graphene*.

1.1.3 The advent of graphene

Graphene, a single layer of graphite, was the first truly two-dimensional (2D) material ever synthesised [32–34]. Since its separation from a bulk graphite crystal with the famous scotch-tape method in 2004, it is arguably the most intensively studied material ever. Together with the intense scientific effort, also the understanding of the material's properties surges at a tremendous pace.

One of the reasons that graphene research progresses so fast is that graphene is living up to the theoretical expectations of its extraordinary properties [35]. Some of the well known successes are: a very high room-temperature electron mobility [36] that matched theoretical expectations [37], an exceptionally large thermal conductivity [38], an optical absorption that is exactly 2.3% over a wide spectral range [39] and only depends on fundamental physical constants, and the ability to sustain extremely high electric current densities (10^6 times larger than copper) [40]. The main reason for the exceptionally good match between theory and experiment is the availability of high-quality graphene samples [35]. These are still made mainly by mechanical exfoliation [32] although different techniques for creating graphene, like chemical vapour deposition, are being perfectionised at a rapid pace [35].

In the wake of ongoing graphene research, also other 2D materials were synthesised. These materials can be made up from graphene, like graphene multilayers [41, 42] or chemically functionalised graphene [43] or have completely different constituents like the transition metal dichalcogenides (such as MoS_2 [44]), hexagonal boron nitride [45] or silicene [46]. The physical properties of these 2D materials all differ from each other and are interesting in their own respect. Furthermore, because there is now an entire portfolio of different building blocks available, it is possible to device so-called *van der Waals heterostructures* that consist of different materials stacked on top of each other allowing to tailor the physical properties of the structure at will [47].

Graphene and a lot of its related 2D materials are electrically conductive. The electrons in these materials form an electron liquid that is also two-dimensional since the material itself is two-dimensional. In the same way as the 2D electronic liquid at the surface of a conductor is capable of supporting plasmon modes, the electrons in graphene can be excited in a collective fashion. This forms the basis of *graphene plasmonics*.

1.1.4 Introducing: graphene plasmonics

Soon after graphene was synthesised, plasmons in the 2D electron liquid were observed by means of electron energy-loss spectroscopy (EELS) [48, 49]. These experiments proved the existence of plasmons in graphene and the first proof of one of the major advantages of graphene plasmons over plasmonic excitations in other materials, i.e. their easy tunability over a wide frequency range. Indeed, the frequency of plasmons in graphene scales with the electron concentration $n_{\rm c}$ as $\omega_{\rm pl} \propto n_{\rm c}^{1/4}$ [50]. Because the carrier concentration in graphene is known to be easily tunable from a hole-doped system to an electron-doped system by the use of electrostatic gating [34, 51], this allows one to adjust the plasmon frequency continuously.

In the EELS experiments, the necessary momentum for the excitation of plasmons was delivered by the electrons. However, the use of light as a means to excite plasmons and make SPPs was hindered by the fact that the usual plasmonic excitation methods, like prisms and corrugation, cannot be applied to graphene [52]. Therefore, researchers have developed a wide range of different techniques to overcome the momentum mismatch by using for example sub-wavelength nanoribbon structures or disk arrays [53, 54]. This created localised plasmons of which the frequency depends on the size of the nanostructure. The experiments showed the existence of plasmons in the terahertz to infra-red (IR) range of the EM spectrum. This introduced a new advantage of graphene plasmons, namely the fact that they can reside outside the visible part of the spectrum. Therefore, graphene plasmons are very promising for applications that use this part of the spectrum [54–56].

Another way to overcome the momentum mismatch is to use the tip of an atomic force microscope (AFM) to couple light to the electron liquid [57, 58]. This allowed researchers to measure propagating plasmons in graphene. It has been found that graphene plasmons are confined much stronger than plasmons in metallic structures and that plasmon wavelengths can be over 150 times shorter than the corresponding free-space photon wavelength. Furthermore, these plasmons can have very long lifetimes of up to $500~{\rm fs}$ [59]. The fact that graphene plasmons feature such a large confinement of EM radiation also make them an ideal platform for strong light-matter interaction and nonlinear optics [60, 61].

The field of plasmonics in graphene and related materials is evolving rapidly with a plethora of experiments and theoretical proposals appearing in literature every week. In this thesis, more details about experimental progress that is related to the studied topics will be provided. Further background on graphene plasmonics can be found in the reviews Refs. [50, 52, 62–67].

1.2 Goal and structure of the thesis

The goal of the thesis is to investigate the plasmonic properties of graphene and related materials and how plasmons respond to changes in the environment or in the electronic properties of the crystal. In particular, it is investigated how one can engineer set-ups that host plasmons with longer lifetimes and whether plasmons can be used for the basis of light modulation set-ups.

The thesis is structured as follows:

In chapter 2 the electronic properties of graphene are briefly reviewed. In this chapter the necessary mathematical concepts that will be used throughout the thesis are introduced, the peculiar electronic properties of graphene are refreshed and some comments on experimentally achievable parameter ranges are made. As an example of an electronic graphene peculiarity, the chiral tunnelling characteristics of a graphene multilayer are elaborated upon.

In chapter 3 the optical response of graphene is scrutinised. This forms the basis of the linear response scheme used in the thesis to model how light couples to the electrons in a two-dimensional material. The chapter also presents an examination of the experimental challenges that need to be overcome in order to observe plasmons in graphene. The chapter ends with a discussion on plasmarons in monolayer, bilayer and trilayer graphene as an example of how plasmons affect the electronic properties of 2D materials.

In chapter 4 the framework developed in the previous chapters is applied to the case of a strongly doped graphene flake. In the chapter the following question is answered: **How are graphene plasmons affected by the hexagonal symmetry of the lattice?**

In chapter 5 a graphene sample that is encapsulated by hexagonal boron nitride is considered. After revisiting the effect of the hBN crystal on the graphene plasmons, the graphene system is valley polarised and the effect of the polarisation is investigated. In the chapter the following question is answered: **How can one excite charge neutral plasmons by valley polarising a graphene flake?**

In chapter 6 the focus is shifted to a new kind of 2D material, called *silicene*. This material has the same structure as graphene, but here the carbon atoms are replaced by silicon atoms. In contrast to graphene, the system has a band gap that can be tuned by applying external fields. In the chapter the following question is answered: **How do external fields**

influence the lifetime of plasmons in silicene?

In chapter 7 a graphene system is, again, considered, but now the fact that it can support very large current densities is exploited. This chapter investigates how the optical and plasmonic properties of graphene change when a large current flows through the sample. In the chapter the following question is answered: **How does an electric current influence the optical properties of graphene and can it be used to enhance the lifetime of plasmons in graphene?**

In chapter 8 the results obtained in the previous chapter are used to model the effect of plasmons in graphene nanostripes on the optical properties of the nanostripe itself. In the chapter the following question is answered: **Can plasmons excited by a mid-infrared laser be used to modulate the amplitude of a telecom laser?**

1.3 Collaborations and publications

The research presented in this thesis is the fruit of several collaborations. The thesis is inspired by many discussions, research notes and joint publications.

The research was supervised by Prof. Dr. François Peeters from the University of Antwerp and co-supervised by Prof. Dr. Marco Polini from Istituto Italiano di Tecnologia, Genova. For the particular chapters the research was performed in collaboration with:

- Chapter 3: for the part about plasmarons in trilayer graphene: Dr. Predrag Krstajić (University of Belgrade, Serbia).
- Chapter 4: Dr. Francesco Pellegrino (Scuola Normale Superiore, Pisa, Italy).
- Chapter 5: Dr. Andrea Tomadin (Istituto Italiano di Tecnologia, Genova, Italy).
- Chapter 6: Prof. Dr. Panagiotis Vasilopoulos (Concordia University, Canada).
- Chapter 7: Dr. Andrea Tomadin (Istituto Italiano di Tecnologia, Genova, Italy) and Prof. Dr. Alexander Grigorenko (University of Manchester, UK).
- Chapter 8: Iacopo Torre (Scuola Normale Superiore, Pisa, Italy), Dr. Andrea Tomadin (Istituto Italiano di Tecnologia, Genova, Italy) and Prof. Dr. Alexander Grigorenko (University of Manchester, UK).

The work presented in this thesis has been published in scientific journals or is currently being prepared as a manuscript. This concerns the following chapters:

- Chapter 2: A manuscript about chiral tunnelling in graphene multilayers was published in Europhysics Letters [68].
- Chapter 3: The part about plasmarons in trilayer graphene was published in Physical Review B [69].
- Chapter 4: A manuscript is in preparation.
- Chapter 5: This research is a part of a manuscript about plasmons in graphene superlattices that is in preparation.
- Chapter 6: A manuscript about plasmons in silicene was published in Physical Review B [70].
- Chapter 7: A manuscript about the effect of a finite current on graphene optics and plasmonics was published in 2D Materials [71].
- Chapter 8: A theoretical and an experimental manuscript are being prepared.

All works published during the course of the PhD research period can be found in the CV attached at the end of the thesis.

CHAPTER 2

Electronic properties of graphene

In this chapter the single-particle electronic properties of graphene are reviewed. First the energy band spectrum of the charge carriers in graphene is derived from its hexagonal atomic structure. It is shown that the conduction and valence bands have peculiar band crossings in two points in the Brillouin zone. Around these points all the interesting physics happens since there the electrons have a linear dispersion and, therefore, acquire a chiral character as will be explained below. To elucidate the effect of chirality of charge carriers, tunnelling through potential barriers is briefly discussed and it is shown that for graphene multilayers the chirality of the charge carriers strongly determines the tunnelling characteristics.

This chapter briefly reviews the theoretical concepts that are common to graphene electronics and is mainly meant to introduce the readers that are unfamiliar with graphene physics. Secondly, it also determines the notation for the succeeding chapters. The chapter ends with an analysis of the range of experimentally achievable doping and their relation to the graphene Fermi level and chemical potential. The latter allows to make an estimate of which phenomena are experimentally accessible.

The study of the relation between the chirality of the charge carriers and the tunnelling characteristics of multilayer graphene was published in Europhysics Letters [68].

2.1 Electrons in a carbon chicken wire

2.1.1 Formation of the chicken wire

Carbon atoms posses six electrons that form a ground state in the configuration $1s^2 2s^2 2p^2$. This means that two electrons fill the lowest energy $1s$-orbital, two electrons fill the next $2s$-orbital and the remaining two live in the $2p$-orbitals. As the $2s$-orbital has an energy that is about 4 eV smaller than the $2p$-orbital [72], it is energetically more favourable to put two electrons in the $2s$-state. In the presence of other atoms, however, the four electrons are redistributed equally among the $2s$- and three $2p$-orbitals by exciting one electron from the $2s$-state into a $2p$-orbital. This allows the carbon atom to form covalent bonds with up to four partners and is the basis of carbon chemistry.

Upon formation of the crystal, the number of bonds formed with the carbon's neighbours depends on the hybridisation of the s- and p-orbitals. The concept of hybridisation is necessary since in the excited state, the four electrons occupy the four quantum mechanically equivalent states $|2s\rangle$, $|2p_x\rangle$, $|2p_y\rangle$ and $|2p_z\rangle$. Because they are equivalent, they cannot be distinguished anymore and the electron will occupy a superposition of these states. The superposition of one s-orbital with n p-orbitals is called an sp^n hybridised orbital. The uniqueness of carbon lies in the fact that it can form different hybridisations and, as a consequence, feature different crystallographic configurations. If the carbon is sp^3 hybridised, it can form four covalent bonds. This leads to the formation of diamond with an C-C bond length of 1.54 [73]. If the carbon is sp^2 hybridised, it forms layers of carbon organized in hexagons that are stacked on top of each other in a material known as graphite. The in-plane bond length is 1.42 and makes the sp^2 bond, therefore, stronger than that of diamond. However, the inter-plane bond is a weak van der Waals bond and the inter-plane distance is about 3.35 . An sp^1 hybridised carbon atom cannot form a carbon allotrope, but can be found in hydrocarbons like acetylene [74].

In this work, the sp^2 hybridised carbon atoms are the main interest. As shown in Figs. 2.1 and 2.2, this means that each carbon atom can form a covalent bond with three other atoms and that the angle in between the bonds measures $120°$. The first organic molecule that has these sp^2 hybridised bonds, benzene, was found by Kekulé in 1865 [76]. It consists six carbon atoms forming a hexagon. Each carbon atom has a covalent bond (called a σ-bond) with two other carbon atoms and with a hydrogen atom as shown in Fig. 2.2. Because the s- and two of the p-orbitals are involved in the sp^2 hybridised orbital, there is one occupied p-orbital left for each carbon atom. These orbitals form a so-called π-bond with one of the neighbouring atoms as shown in Fig. 2.2. Symmetry considerations require all bonds in benzene to be equivalent. Indeed if one rotates the hexagon over an angle of $60°$, the system is mapped on itself, but the π-bonds have switched partners.

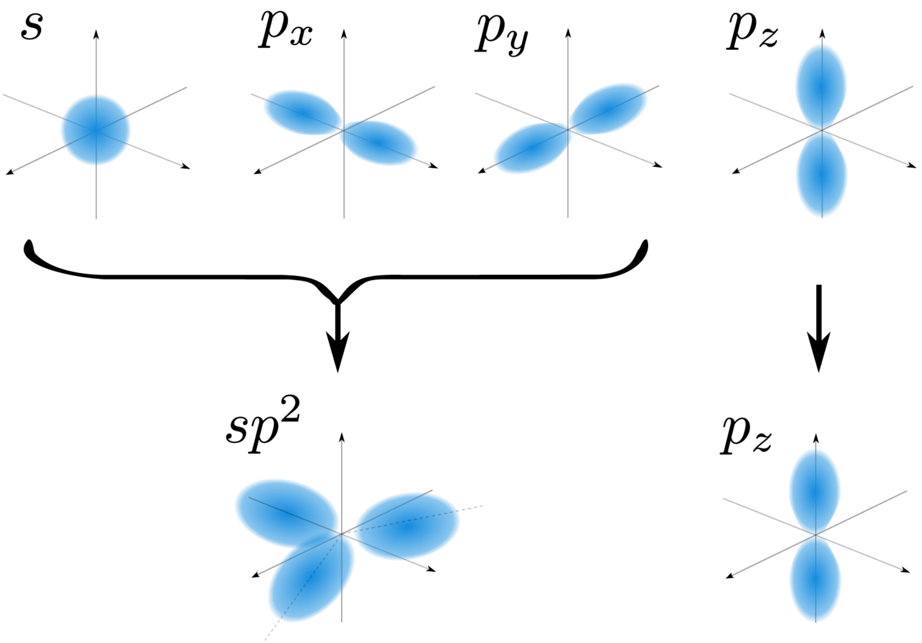

Figure 2.1: Electronic orbital hybridisation to form an sp^2 hybridised state. The s-, p_x- and p_y-orbitals merge into the hybridised state while the p_z-orbital remains unaffected. The three different lobs of the sp^2 hybridised state are positioned under an angle of 120° with respect to each other. Figure taken from Ref. [75].

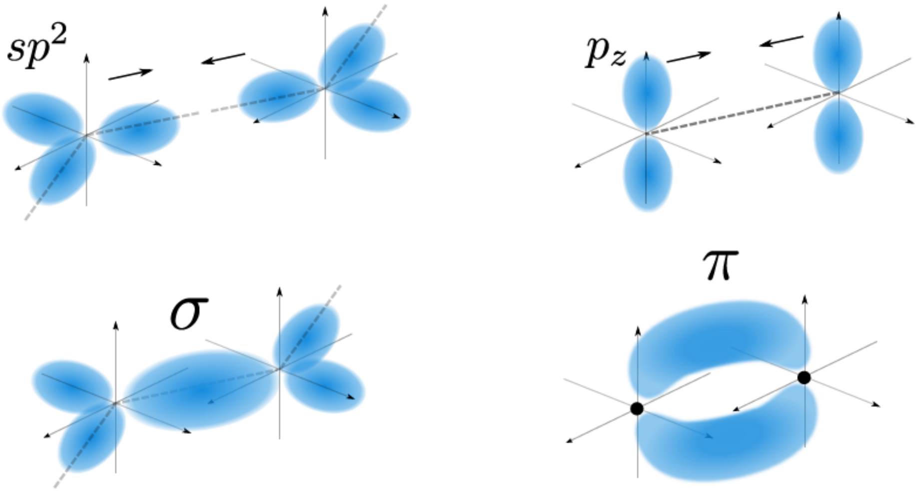

Figure 2.2: Formation of the σ and π bands by combining two sp^2 hybridised orbitals. Figure taken from Ref. [75].

This observation led Linus Pauling [77] in 1931 to conclude that the quantum mechanical ground state of the benzene molecule is a superposition of the two forms presented in Fig.2.3(a). This means that the π-bond is smeared out above the entire benzene ring.

Graphene can be considered as a tiling of benzene rings next to each other filling a 2D plane and forming a honeycomb lattice as shown in Fig. 2.3(b). Each carbon atom is sp^2 hybridised and forms σ-bonds with three of its neighbours. The π-bond formed by the remaining p-orbital is delocalized over the entire plane. It are the electrons in the π-bond that are of interest since their delocalization over the entire graphene crystal allows them to move freely around and form the electron liquid that is of interest for the study of this thesis.

2.1.2 Crystallographic structure

The honeycomb lattice formed by the carbon atoms is not a Bravais lattice since two neighbouring atoms are crystallographically inequivalent. Indeed, it is not possible to form a honeycomb lattice with only one atom in the crystalographic unit cell [78]. Therefore, one can consider the hexagonal lattice as the combination of two trigonal sublattices that are usually labeled as A and B sublattices [79] as shown in Fig. 2.3(b).

The distance between the carbon atoms of different sublattices is $a_0 = 0.142$ nm [79]. Three vectors, denoted by $\boldsymbol{\delta}_i$, connect each site on the A sublattice with one on the B lattice. Following the notation by Goerbig [72], these vectors are in the basis $\boldsymbol{e}_i$ with $i = x, y$:

$$\begin{aligned}
\boldsymbol{\delta}_1 &= \frac{a_0}{2}\left(\sqrt{3}\boldsymbol{e}_x + \boldsymbol{e}_y\right), \\
\boldsymbol{\delta}_2 &= \frac{a_0}{2}\left(-\sqrt{3}\boldsymbol{e}_x + \boldsymbol{e}_y\right), \\
\boldsymbol{\delta}_3 &= -a_0\boldsymbol{e}_y.
\end{aligned} \tag{2.1}$$

The triangular Bravais lattice is then generated by the basis vectors

$$\begin{aligned}
\boldsymbol{a}_1 &= \sqrt{3}a_0\boldsymbol{e}_x, \\
\boldsymbol{a}_2 &= \frac{\sqrt{3}a_0}{2}\left(\boldsymbol{e}_x + \sqrt{3}\boldsymbol{e}_y\right).
\end{aligned} \tag{2.2}$$

Correspondingly, the reciprocal lattice is spanned by the reciprocal basis vectors

$$\begin{aligned}
\boldsymbol{b}_1 &= \frac{2\pi}{\sqrt{3}a_0}\left(\boldsymbol{e}_x - \frac{\boldsymbol{e}_y}{\sqrt{3}}\right), \\
\boldsymbol{b}_2 &= \frac{4\pi}{3a_0}\boldsymbol{e}_y.
\end{aligned} \tag{2.3}$$

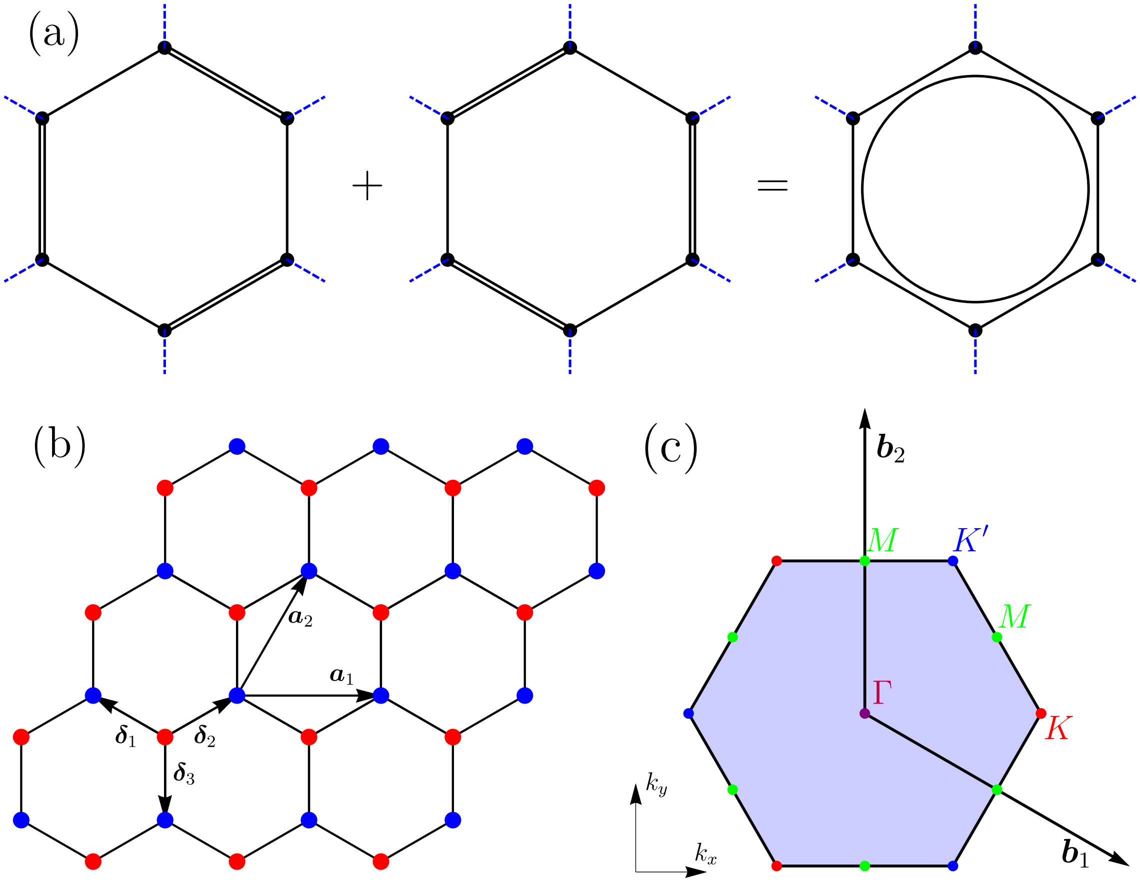

Figure 2.3: (a) Delocalisation of the π-bond in a benzene molecule. The blue dashes lines correspond to coupling to hydrogen atoms. (b) A graphene flake can be considered as a tiling of benzene rings where the bonds with hydrogen atoms are replaced by carbon atoms. The π-bond is delocalised over the entire graphene plane. The blue atoms correspond to the A sublattice while the red atoms denote the B trigonal sublattice. The vectors $\boldsymbol{a}_1$ and $\boldsymbol{a}_2$ are the basis vectors of the crystal, while the vectors $\boldsymbol{\delta}_i$ are defined in Eq. (2.1). (c) First Brillouin zone of graphene. The vectors $\boldsymbol{b}_i$ are the respective reciprocal basis vectors. The first Brillouin zone is indicated as a shaded hexagon. On top of the hexagon, the high symmetry points Γ, M, K and K' are indicated.

The first Brioullin zone (BZ) of the corresponding reciprocal lattice also has a hexagonal form as shown in Fig. 2.3(c). The center of the hexagon is usually referred to as the Γ point. Long wave-length excitations are situated near the Γ point. The corners of the BZ are other crystallographic high symmetry points and are called the K and K' points. Notice that the six corners of the BZ represent only two inequivalent points since the other are connected by the reciprocal basis vectors from Eq. (2.3). The K and K' points are situated at

$$\boldsymbol{K}^{(\prime)} = \pm \frac{4\pi}{3\sqrt{3}a_0} \boldsymbol{e}_x. \tag{2.4}$$

In this equation, the $+(-)$ refers to the K (K') point.

Finally there are high symmetry point on the middle of the edge connecting the K points. These points are called the M points. There are three distinct M points in a hexagonal lattice [80]. As will be shown in the next section, the crystallographic high symmetry points are of prime importance to the electronic properties of graphene.

Eq. (2.2) allows to calculate the concentration of carbon atoms in a graphene flake [72]. The surface area of the unit cell spanned by the basis vectors in Eq. (2.2) is $A_{\text{UC}} = 3\sqrt{3}a_0^2/2 = 0.052$ nm^2. This means that the carbon atom concentration is $n_C = 2/A_{\text{UC}} = 3.8 \times 10^{15}$ cm^{-2}. This concentration also equals the number of electrons in the π-bond of undoped graphene. It is interesting to compare the here quoted concentrations to the carrier concentrations induced by doping as discussed in the following chapters.

2.2 Electronic band structure

Already in the fourties, Wallace [81] derived the electronic band structure of π electrons for a honeycomb lattice within the tight-binding (TB) approximation. Wallace was mainly interested in the description of electrons in graphite, but, along the way, also described the electronic properties of a single graphite sheet. Here the formalism will be briefly refreshed to set the notation and to be served as future reference [72].

In the tight-binding formalism, the total wave function is written as a superposition of atomic orbital wave functions. Because there are two atoms per unit cell, the electron wave function will have the form

$$\psi_{\boldsymbol{k}}\left(\boldsymbol{r}\right) = a_{\boldsymbol{k}}\psi_{\boldsymbol{k}}^{(A)}\left(\boldsymbol{r}\right) + b_{\boldsymbol{k}}\psi_{\boldsymbol{k}}^{(B)}\left(\boldsymbol{r}\right). \tag{2.5}$$

Here, $\psi_{\boldsymbol{k}}^{(A,B)}\left(\boldsymbol{r}\right)$ are the Bloch wave functions of the appropriate sublattice and $a_{\boldsymbol{k}}$ and $b_{\boldsymbol{k}}$ are the respective weights. Invoking lattice periodicity, these Bloch wave functions can be written as

$$\psi_{\boldsymbol{k}}^{(j)}\left(\boldsymbol{r}\right) = \sum_{\boldsymbol{R}_j} e^{i\boldsymbol{k}.\boldsymbol{R}_j}\phi^{(j)}\left(\boldsymbol{r} + \boldsymbol{\delta}_j - \boldsymbol{R}_j\right). \tag{2.6}$$

In Eq. (2.6), the $\phi^{(j)}(\boldsymbol{r})$ denote the atomic orbitals of the atom of sublattice $j = A, B$ at position $\boldsymbol{r}$.

With the help of Eq. (2.5), now the Schrödinger equation, $H|\psi_{\boldsymbol{k}}\rangle = \varepsilon_{\boldsymbol{k}}|\psi_{\boldsymbol{k}}\rangle$, can be solved as a matrix equation by projecting on $\langle\psi_{\boldsymbol{k}}|$ such that one finds the matrix relations

$$(a^*_{\boldsymbol{k}}, b^*_{\boldsymbol{k}})\, H_{\boldsymbol{k}} \begin{pmatrix} a_{\boldsymbol{k}} \\ b_{\boldsymbol{k}} \end{pmatrix} = \varepsilon_{\boldsymbol{k}}\, (a^*_{\boldsymbol{k}}, b^*_{\boldsymbol{k}})\, S_{\boldsymbol{k}} \begin{pmatrix} a_{\boldsymbol{k}} \\ b_{\boldsymbol{k}} \end{pmatrix}. \tag{2.7}$$

Here the Hamiltonian matrix $H_{\boldsymbol{k}}$ and the overlap matrix $S_{\boldsymbol{k}}$ are hermitian and defined as

$$H_{\boldsymbol{k}} = \begin{pmatrix} \left\langle \psi^{(A)}_{\boldsymbol{k}} | H | \psi^{(A)}_{\boldsymbol{k}} \right\rangle & \left\langle \psi^{(A)}_{\boldsymbol{k}} | H | \psi^{(B)}_{\boldsymbol{k}} \right\rangle \\ \left\langle \psi^{(B)}_{\boldsymbol{k}} | H | \psi^{(A)}_{\boldsymbol{k}} \right\rangle & \left\langle \psi^{(B)}_{\boldsymbol{k}} | H | \psi^{(B)}_{\boldsymbol{k}} \right\rangle \end{pmatrix}, \tag{2.8}$$

$$S_{\boldsymbol{k}} = \begin{pmatrix} \left\langle \psi^{(A)}_{\boldsymbol{k}} | \psi^{(A)}_{\boldsymbol{k}} \right\rangle & \left\langle \psi^{(A)}_{\boldsymbol{k}} | \psi^{(B)}_{\boldsymbol{k}} \right\rangle \\ \left\langle \psi^{(B)}_{\boldsymbol{k}} | \psi^{(A)}_{\boldsymbol{k}} \right\rangle & \left\langle \psi^{(B)}_{\boldsymbol{k}} | \psi^{(B)}_{\boldsymbol{k}} \right\rangle \end{pmatrix}. \tag{2.9}$$

If one assumes that the atomic orbitals are orthonormal, i.e. $S_{\boldsymbol{k}} = I_2$, the 2×2 unit matix, the electronic energy bands $\varepsilon_{\lambda\boldsymbol{k}}$ are obtained from the eigenvalues of Eq. (2.8).

Since the A and B sublattices are chemically equivalent, their on-site energy is the same and equal to the energy of the π orbital. This will only cause a shift of the energy bands, which is physically irrelevant and will be omitted [82]. Assuming only nearest-neighbour (NN) atomic orbital overlap, the TB Hamiltonian from Eq.(2.8) has a vanishing diagonal. The off-diagonal elements can be cast into the form

$$\left\langle \psi^{(j)}_{\boldsymbol{k}} | H | \psi^{(j')}_{\boldsymbol{k}} \right\rangle = \int d\boldsymbol{r}\, \phi^{*,(j)}(\boldsymbol{r})\, H \phi^{(j')}(\boldsymbol{r} + \boldsymbol{\delta}_1) \sum_{\boldsymbol{R}_l \in \mathcal{V}^{(j)}_{\text{NN}}} e^{i\boldsymbol{k}.\boldsymbol{R}_l} = (-t)\, f^{jj'}_{\boldsymbol{k}}. \tag{2.10}$$

In this equation, $\mathcal{V}^{(j)}_{\text{NN}}$ is the set of vectors connecting sublattice j with its NN and $-t$ represents the integral in the second part of the equation and is the called the *hopping amplitude*. The function $f^{AB}_{\boldsymbol{k}}$ sums over all atoms of the sublattice B around sublattice A. As seen in Fig. 2.3(b) this corresponds to a sum over the vectors $\boldsymbol{\delta}_l$ and gives

$$f^{AB}_{\boldsymbol{k}} = \sum_{l=1}^{3} e^{-i\boldsymbol{k}.\boldsymbol{\delta}_l} = \left(f^{BA}_{\boldsymbol{k}}\right)^*. \tag{2.11}$$

Eq. (2.11) finally yields the well known TB graphene Hamiltonian

$$H_{\boldsymbol{k}} = -t \begin{pmatrix} 0 & f^{AB}_{\boldsymbol{k}} \\ \left(f^{AB}_{\boldsymbol{k}}\right)^* & 0 \end{pmatrix}. \tag{2.12}$$

The eigenstates of the Hamiltonian are

$$\Psi_{\lambda \boldsymbol{k}} = \frac{1}{\sqrt{2}} \left(\begin{array}{c} 1 \\ \lambda e^{i\varphi_{\boldsymbol{k}}} \end{array} \right) , \tag{2.13}$$

where

$$\varphi_{\boldsymbol{k}} = \arg \left(f_{\boldsymbol{k}}^{AB} \right) \ , \tag{2.14}$$

denotes the relative phase between the two sublattice componentes and $\lambda = \pm 1$ indicates the conduction (valence) band. Eq. (2.13) shows that both spinor components are occupied with the same probability. This reflects the fact that the two sublattices are equivalent from a physical point of view; they are both carbon atoms with the same on-site potential (that is taken to be zero in this case). The eigenstate in Eq. (2.13) is shown in the sublattice representation. The position representation will add an additional plane wave phase factor. The physical interpretation of the function $\varphi_{\boldsymbol{k}}$ is given in the following section. The corresponding eigenvalues are

$$\varepsilon_{\lambda \boldsymbol{k}} = \lambda t \left| f_{\boldsymbol{k}}^{AB} \right| = \lambda t \sqrt{1 + 4 \cos \left(\frac{\sqrt{3}}{2} k_x a_0 \right)^2 + 4 \cos \left(\frac{\sqrt{3}}{2} k_x a_0 \right) \cos \left(\frac{3}{2} k_y a_0 \right)} . \tag{2.15}$$

The energy scale of the bands is set by the hopping amplitude t. This is obtained by fitting Eq. (2.15) to spectroscopic measurements [82–84]. The hopping amplitude is found to be $-t = 2.8$ eV.

Fig. 2.4 shows the energy band structure from Eq. (2.15) in the reciprocal plane. The earlier defined high symmetry points play an important role. At the Γ point the energy band is extremal reaching an energy of $\pm 3t$ while at the K and K' points the energy vanishes and the conduction and valence bands touch each other. In between the K and K' points, the energy reaches a saddle point at the M point for an energy $\pm t$. As shown in Fig. 2.4(c), the energy spectrum is linear near the K and K' points. This linearity is the consequence of the hexagonal symmetry of the crystal and gives rise the the many unconventional electronic properties of the charge carriers in graphene.

The above reasoning neglects inter-atomic hoppings beyond nearest-neighbour. However, if next-nearest-neighbour (NNN) hopping is included, this will contribute as an additional term proportional to $(\varepsilon_{\lambda \boldsymbol{k}}/t)^2$ that needs to be added to the energy dispersion in Eq. (2.15) [72]. The strength of this additional term is measured as $t_{\mathrm{NNN}} \simeq 0.1t$ and is the same for the electrons and holes. Therefore, NNN hopping breaks electron-hole symmetry. This effect is shown in Fig. 2.4(c). Because the effect is negligible for low-energy excitations, the NNN hoppings will be neglected in the rest of this work and the system is always considered particle-hole symmetric.

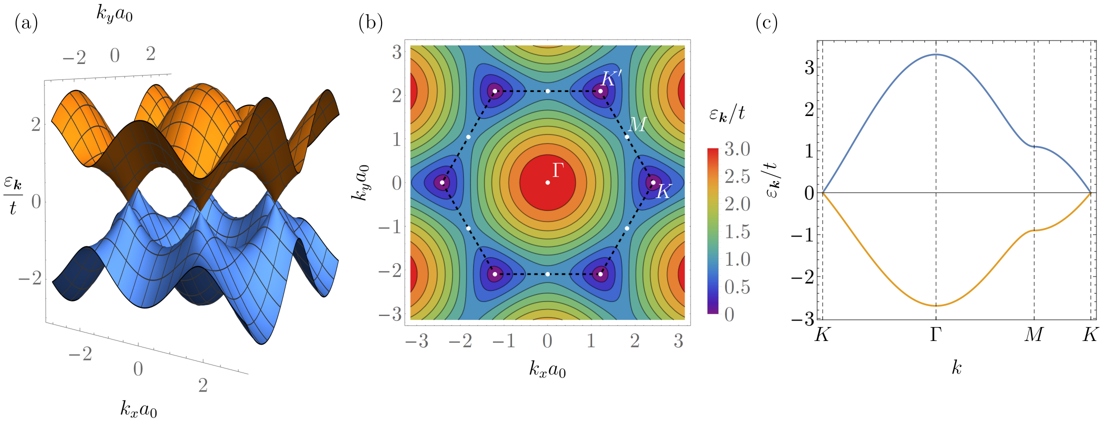

Figure 2.4: Energy bands of graphene in reciprocal space. (a) Shows the 3D valence (blue) and conduction (orange) bands. (b) Shows a contour plot of the conduction band. On top of the contour plot, the high symmetry points Γ, M, K and K' are indicated in white. The first Brillouin zone is indicated by black dashed lines. (c) Shows a slice of the energy bands along a path connecting the high symmetry points. The linear crossing at the K point is clearly visible. In (c) also the next nearest neighbour hopping has been introduced with a value of $t_{NNN} = 0.1t$ such that the electron-hole symmetry is broken.

Fig. 2.4(b) also shows that around the K and K' points the energy spectrum has a trigonal shape for energies $\varepsilon_{\boldsymbol{k}} < t$. This is the consequence of the trigonal symmetry of the lattice and is called the *trigonal warping* of the energy spectrum.

Since for undoped graphene, the valence band is completely occupied and the conduction band is empty, the Fermi level will cross the energy spectrum in exactly these points of contact. Furthermore, the corresponding Fermi surface is a set of points, rather than curves as is usual for 2D systems. If the system is doped up to a Fermi level $E_{\mathrm{F}} < t$, the Fermi surface consists of circles around the K and K' points that become trigonally warped if the Fermi level increases. Since these points are relatively far away from each other in reciprocal space, only scattering processes that are short ranged (in real space), i.e. $\Delta k \sim 1/a_0$, and high in energy (of the order of t) are able to scatter carriers over the energy barrier at the M point and in between the Fermi circles. Because these processes are not frequent away from the edges of the graphene flake, usually one can consider the charge carriers living near the K and K' points as independent from each other. This notion is expressed by the *valley degeneracy* of the charge carriers. Indeed, one can consider carriers residing near the K or K' points are being in a separate energy valley. The fact that graphene charge carriers carry an additional valley quantum number has been investigated in many studies that aim to use it for logic operations, the so-called *valleytronics* [85, 86].

2.2.1 Derivation of the Dirac-Weyl Hamiltonian

In order to describe the charge carriers near the K and K' point, the Hamiltonian in Eq. (2.12) can be expanded up to first order in the deviation $\boldsymbol{q}$ from the position of the K points defined in Eq. (2.4), i.e by $\boldsymbol{k} = \boldsymbol{K}^{(\prime)} + \boldsymbol{q}$ where $\boldsymbol{K}^{(\prime)}$ was defined in Eq. (2.4) as :

$$H_{\boldsymbol{q}}^{\xi} = \xi \hbar v_{\mathrm{F}} \left(\begin{array}{cc} 0 & q_x - i\xi q_y \\ q_x + i\xi q_y & 0 \end{array} \right). \tag{2.16}$$

In Eq. (2.16), $\xi = 1\ (-1)$ denotes that the expansion is performed around the $K\ (K')$ point and

$$\hbar v_{\mathrm{F}} = 3a_0 t/2, \tag{2.17}$$

where $v_{\mathrm{F}} \sim 10^6$ m/s is the graphene Fermi velocity. This allows to write the $\xi = +1$ Hamiltonian in its famous form

$$H_{\boldsymbol{q}}^{+1} = H_{\mathrm{D}}(\boldsymbol{q}) = \hbar v_{\mathrm{F}} \boldsymbol{\sigma} \cdot \boldsymbol{q}, \tag{2.18}$$

where $\boldsymbol{\sigma} = (\sigma_x, \sigma_y)$, is a vector of Pauli matrices.

The Hamiltonian in Eq. (2.18) is the 2D form of the famous Dirac Hamiltonian [87] that describes relativistic particles. The difference between this Hamiltonian and that of Dirac is that the mass m is set to zero and the speed of light c is replaced by the Fermi velocity $v_{\mathrm{F}} \sim c/300$. Furthermore, the two components of the spinor that describes the eigenstates of this equation refer to the sublattices A and B instead of the spin-up and spin-down states. This is called *sublattice pseudospin* [34]. The equivalence between the low energy graphene Hamiltonian and the Dirac Hamiltonian is the basis of the comparison of graphene carrier dynamics with that of relativistic particles. The use of this equivalence has resulted in e.g. the observation of Klein tunnelling in graphene [88, 89] as discussed in the following section.

The energy eigenvalue corresponding with the Hamiltonian in Eq. (2.16) can be easily inferred as

$$\varepsilon_{\lambda\boldsymbol{q}}^{\xi} = \lambda \hbar v_{\mathrm{F}} \left|\boldsymbol{q}\right|, \tag{2.19}$$

and is indeed linear in q as proposed earlier. Notice that the energy spectrum is independent from ξ as $\lambda = \pm 1$ denotes the conduction (valence) band. Finally, also the eigenstates of the Hamiltonian in Eq. (2.16) can be obtained as

$$\Psi_{\lambda\boldsymbol{q}}^{\xi} = \frac{1}{\sqrt{2}} \left(\begin{array}{c} 1 \\ \xi\lambda e^{i\varphi_{\boldsymbol{q}}} \end{array} \right). \tag{2.20}$$

Here, $\varphi_{\boldsymbol{q}} = \arctan\left(q_y/q_x\right)$ is the angle of the vector $\boldsymbol{q}$ with the k_x axis.

The expansion up to first order in $\boldsymbol{q}$ implies that $|\boldsymbol{q}| \ll |\boldsymbol{K}| \sim 1/a_0$, this is called the *continuum limit* [72]. Using the expression for the energy from Eq. (2.19), the condition for the continuum limit yields $\left|\varepsilon^{\xi}_{\lambda\boldsymbol{q}}\right| = 3a_0 t\,|\boldsymbol{q}|/2 \ll t$. This condition is equivalent to the separation of the two energy valleys. Therefore, in the continuum limit, the two valleys are disconnected and the total system can be described by the effective Hamiltonian in the basis given by the four spinor

$$\Psi^T = \left(\psi^A_K, \psi^B_K, \psi^B_{K'}, \psi^A_{K'}\right), \tag{2.21}$$

as the 4×4 matrix

$$H_{\text{eff}}(\boldsymbol{q}) = \begin{pmatrix} H_{\text{D}}(\boldsymbol{q}) & 0 \\ 0 & -H_{\text{D}}(\boldsymbol{q}) \end{pmatrix}. \tag{2.22}$$

In the basis, Eq. (2.21), the A and B components near the K' valley are exchanged in order to identify the Dirac Hamiltonian in Eq. (2.22). The effective Hamiltonian is diagonal in the two valleys and describes the graphene charge carriers as independent from the other valley. Therefore, one often only incorporates the other valley as a degeneracy factor $g_{\text{v}} = 2$.

Up to now, the real electron spin has always been disregarded. Because spin-orbit coupling in graphene is very small ($\Delta_{\text{SO}} \simeq 2.4\ \text{K} = 0.2\ \text{meV}$) [90], the spin of the electrons and holes in the system will only contribute as an additional degeneracy factor of $g_{\text{s}} = 2$. In other materials, such as silicene, both the spin and valley degeneracy is lifted and the system consists of four flavours of fermions that each have their own dispersion. This system will be considered in chapter 6.

2.2.2 Experimental verification of the energy spectrum

The simple model presented in the previous section describes with remarkable accuracy the band structure of graphene. This was experimentally verified by angle resolved photoemession spectroscopy (ARPES) [91]. In these kinds of experiments, X-rays are shot at the crystal and the electrons that are excited from the crystal are subsequently collected while keeping track of their propagation direction. The energy difference and momentum difference between the incident photon and exciting electron caries the information about the valence electrons in the system. As a consequence the band structure of the crystal can be found.

In Fig. 2.5 the results of ARPES experiments are shown [91]. The band structure of the π-bands from Eq. (2.15) completely fits the obtained results as shown in Fig. 2.4(c). The valence band is linear near the K and K' points at the corners of the first Brillouin zone as shown in Fig. 2.5(a). Fig. 2.5(b) shows that around the K and K' points the

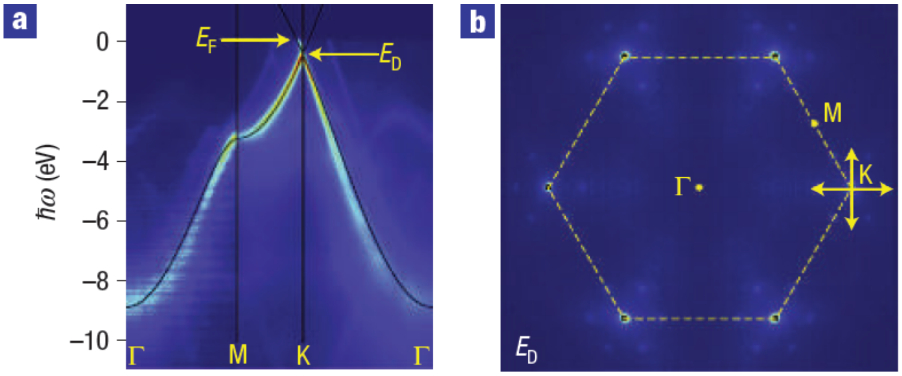

Figure 2.5: ARPES measurement of the energy dispersion of epitaxial graphene (Figure taken from Ref. [91].

energy spectrum is isotropic. This is the case for an energy up to about $1\ \mathrm{eV}$. Therefore, the conic approximation is indeed valid. Note that in the results of Fig. 2.5 the Dirac point energy, E_D, is not at exactly zero energy because of residual doping in the system.

2.3 Chirality of the charge carriers

One of the most peculiar properties of the graphene charge carriers is the fact that they are chiral particles. If one defines the helicity operator as the projection of the pseudospin on the direction of motion,

$$\eta_{\boldsymbol{q}} = \frac{\boldsymbol{\sigma} \cdot \boldsymbol{q}}{|\boldsymbol{q}|}, \tag{2.23}$$

then one can express the Hamiltonian in Eq. (2.16) as $H^{\xi}_{\boldsymbol{q}} = \xi \hbar v_\mathrm{F} \left|\boldsymbol{q}\right| \eta_{\boldsymbol{q}}$. Therefore, in the absence of inter-valley scattering, helicity is a conserved quantity, i.e. $[H^{\xi}_{\boldsymbol{q}}, \eta_{\boldsymbol{q}}] = 0$. Eq. (2.23) shows that the helicity of two oppositely propagating particles is opposite. As a consequence, back-scattering within the same valley is prohibited. Therefore, if particles are incident perpendicularly on a potential barrier, they have to tunnel with unit probability using the hole states in the barrier as shown in Fig. 2.6(a). This tunnelling effect is independent from the height or width of the barrier and is called *Klein tunnelling* as it was first predicted by Klein for relativistic electrons [92]. In graphene, this effect was experimentally observed [89].

These kinds of peculiar tunnelling properties are not only limited to graphene. Also its derivatives like multilayer graphene and silicene show a degree of chirality assisted tunnelling. Recently, it was shown that the tunnelling through pn junctions in graphene

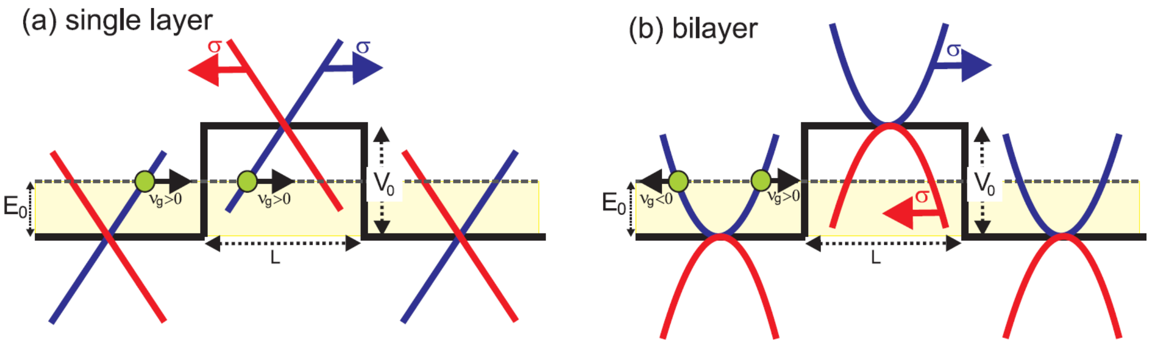

Figure 2.6: Chirally assisted tunnelling for electrons impinging perpendicularly on a potential barrier in (a) single layer graphene and (b) bilayer graphene. E_0 denotes the Fermi energy, V_0 the height of the potential, v_g the group velocity and the energy bands are coloured according to the direction of their pseudospin with blue bands having a pseudospin pointing right and red bands pointing left. Illustration taken from Ref. [93].

multilayers with an arbitrary number of layers is chirally assisted or suppressed depending on the interplay between the pseudospin and the direction of propagation [68]. In a rhombohedrally (ABC) stacked graphene multilayer the Hamiltonian of the two lowest lying energy bands can be written as

$$H_n \sim q^n(\cos(n\varphi_{\boldsymbol{q}})\sigma_x + \sin(n\varphi_{\boldsymbol{q}})\sigma_y) \,. \tag{2.24}$$

Here, n denotes the number of layers, $\varphi_{\boldsymbol{q}}$ the angle of charge carrier with the x-axis and $\sigma_{x,y}$ are the respective Pauli matrices that correspond to the sub-lattice pseudospin. Notice that in the case of a graphene multilayer the two components of the spinor are the sites at the two outer graphene layers that have no atom underneath them [68]. As can be easily infered from Eq. (2.24), the energy dispersion for low energy follows a power law $\varepsilon_{\boldsymbol{q}} \sim q^n$. It was found that there are so-called *magic angles* [94] at which chirally suppressed of assisted tunnelling occurred that follow the simple relation

$$\phi_n^m = \frac{m\pi}{2n}, \text{ for } m \in \{1-n, \ldots, 0, \ldots, n-1\} \,, \tag{2.25}$$

The tunnelling is chirally suppressed if the difference $\Delta_n^m = n - m$ is even, while it is chirally enhanced when Δ_n^m is odd [68]. While the chirally enhanced transmission is labelled Klein tunnelling, the chirally suppressed tunnelling is called *anti-Klein tunnelling*. Inserting the angles from Eq. (2.25) in the Hamiltonian from Eq. (2.24), one notices that the sublattice pseudospin operator σ_x or σ_y commute with the Hamiltonian for this particular angle. The conservation of pseudospin in the x- or y-direction at these angles is the origin of the chirally enhanced or suppressed tunnelling.

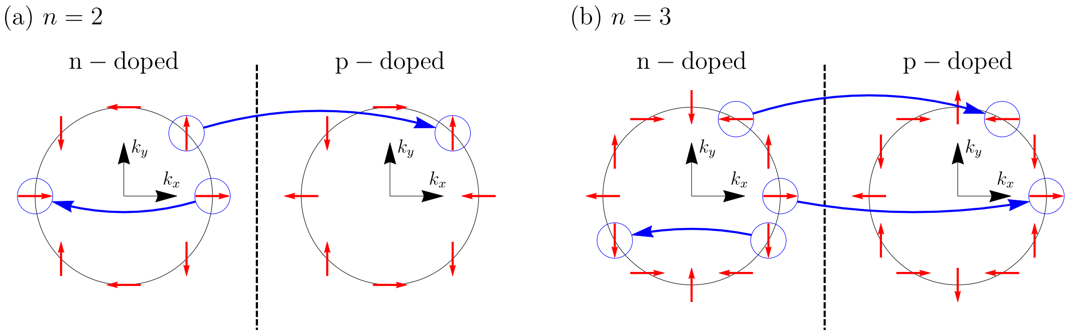

Figure 2.7: Schematic picture of the pseudospin matching for (a) bilayer graphene and (b) rhombohedral trilayer graphene at the boundary between an n-doped and a p-doped region. The small red arrows show the direction of the pseudospin at the corresponding point in reciprocal space. The blue arrows pointing to the right mark the possible angles for which tunnelling is chirally enhanced. The blue arrows pointing to the left mark the chirally supported back scattering events. Figure taken from Ref. [68].

As explained before, the chiral enhancement of tunnelling is peculiar. However, also the chiral suppression is unexpected. For example, in bilayer graphene, tunnelling at normal incidence is suppressed, indeed $\Delta_n^m = 2 - 0$. However, bilayer graphene is gapless, so there are hole states that could carry the current through the pn-junction just as for single layer graphene. The reason for this is that at normal incidence the hole states inside the potential barrier are disconnected from the electron states outside the junction because they have an opposite pseudospin. This chirally assisted disconnection of electron and hole states at the same energy can be considered as a *cloaking* of the states inside the junction from the outside world [95].

Fig. 2.7 shows, schematically, the conservation of pseudospin in multilayers at the boundary between a p- and n-doped region. This figure shows that the angles where Klein tunnelling is expected are exactly the angles where pseudospin is conserved in the boundary crossing, while for the anti-Klein tunnelling the counter propagating states have the same pseudospin. In Fig. 2.8 a numerical calculation of the transmission at a pn-junction is shown. The results confirm the existence of the magic angles.

2.4 Carrier concentration and the density of states

The carrier concentration in doped graphene is the sum of the hole concentration n_h and the electron concentration n_e which are found by integrating the Fermi-Dirac (FD) distribution

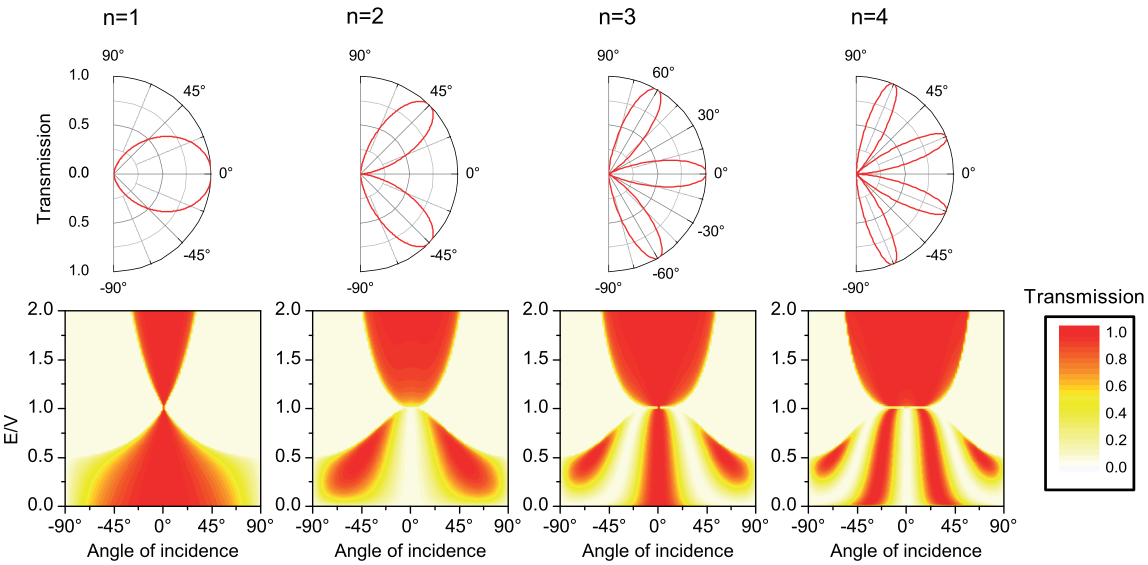

Figure 2.8: Transmission probability through a pn junction in multilayer graphene for $n = 1, \ldots, 4$ layers. The top row shows the angle-dependent transmission for electrons with $E_{\mathrm{F}} = V/2$, where V is the potential difference between the two regions. The bottom row gives countour plots of the angle and energy dependence of the transmission. Figure taken from Ref. [68].

function over reciprocal space as

$$n_e(\mu, T) = N_{\mathrm{f}} \int \frac{d\boldsymbol{k}}{(2\pi)^2} f_{\mathrm{D}}\left(\varepsilon_{+\boldsymbol{k}}, \mu, T\right) , \tag{2.26}$$

$$n_h(\mu, T) = N_{\mathrm{f}} \int \frac{d\boldsymbol{k}}{(2\pi)^2} \left(1 - f_{\mathrm{D}}\left(\varepsilon_{-\boldsymbol{k}}, \mu, T\right)\right) . \tag{2.27}$$

where $N_{\mathrm{f}} = g_{\mathrm{s}} g_{\mathrm{v}} = 4$ counts the number of fermion flavours. The total carrier concentration is the sum of these two quantities, i.e. $n_c(\mu, T) = n_e(\mu, T) + n_h(\mu, T)$. The FD distribution function is

$$f_{\mathrm{D}}\left(\varepsilon, \mu, T\right) = \frac{1}{1 + \exp\left(\frac{\varepsilon - \mu}{k_{\mathrm{B}} T}\right)} . \tag{2.28}$$

In Eq. (2.28), k_{B} is the Boltzmann constant, μ is the chemical potential and T is the (electron) temperature. If the chemical potential μ is considered to be positive, then at $T = 0$ the valence band is fully occupied and the hole concentration is zero. In that case the FD distribution reduces to a step function running up to the Fermi level defined as

$E_\mathrm{F} \equiv \mu\left(T=0\right)$ and the carrier density is

$$n_c\left(E_\mathrm{F},0\right) = \int_0^{E_\mathrm{F}} d\varepsilon D\left(\varepsilon\right) = \frac{N_\mathrm{f} E_\mathrm{F}^2}{4\pi\left(\hbar v_\mathrm{F}\right)^2}\,. \tag{2.29}$$

In the second equation of Eq. (2.29) the graphene density of states (DOS) [79] was introduced

$$D\left(\varepsilon\right) = \frac{N_\mathrm{f}\left|\varepsilon\right|}{2\pi\left(\hbar v_\mathrm{F}\right)^2}\,. \tag{2.30}$$

From Eq. (2.29) one can obtain the expression for the Fermi level as

$$E_\mathrm{F} = \hbar v_\mathrm{F}\sqrt{\frac{4\pi}{N_\mathrm{f}} n_c}\,. \tag{2.31}$$

At finite temperature, the carrier concentration n_c can be analytically calculated as well. The necessary integral is

$$\int_0^\infty dx \frac{x}{\exp(x-x_0)+1} = -\mathrm{Li}_2\left(-\exp(x_0)\right)\,, \tag{2.32}$$

where $\mathrm{Li}_2(x)$ is the dilogarithm function [96]. Therefore, the carrier concentration at finite temperature becomes

$$n_c\left(\mu,T\right) = \frac{N_\mathrm{f}(k_\mathrm{B}T)^2}{2\pi(\hbar v_\mathrm{F})^2}\left[-\mathrm{Li}_2\left(-e^{\mu/(k_\mathrm{B}T)}\right) - \mathrm{Li}_2\left(-e^{-\mu/(k_\mathrm{B}T)}\right)\right]\,. \tag{2.33}$$

Eq. (2.33) reduces in the $T=0$ limit to Eq. (2.29).

In a closed system, the total number of particles does not change. However, it is possible that due to thermal excitation, electrons from the valence band are excited to the conduction band. This affects the electron and hole concentration and increases the total carrier concentration. In a closed system, one can define the dopant concentration, $n_d(\mu,T) = n_e(\mu,T) - n_h(\mu,T)$, that does not change due to thermal excitation and, therefore, corresponds to the number of carriers in the system at zero Kelvin. The dopant concentration is given by

$$n_d\left(\mu,T\right) = \frac{N_\mathrm{f}(k_\mathrm{B}T)^2}{2\pi(\hbar v_\mathrm{F})^2}\left[-\mathrm{Li}_2\left(-e^{\mu/(k_\mathrm{B}T)}\right) + \mathrm{Li}_2\left(-e^{-\mu/(k_\mathrm{B}T)}\right)\right]\,. \tag{2.34}$$

To find the chemical potential as a function of dopant concentration and temperature, the inverse of Eq. (2.34) needs to be calculated numerically. This is shown in Fig. 2.9 in terms of the dimensionless quantities μ/E_F and $k_\mathrm{B}T/E_\mathrm{F}$. The result shows that for a

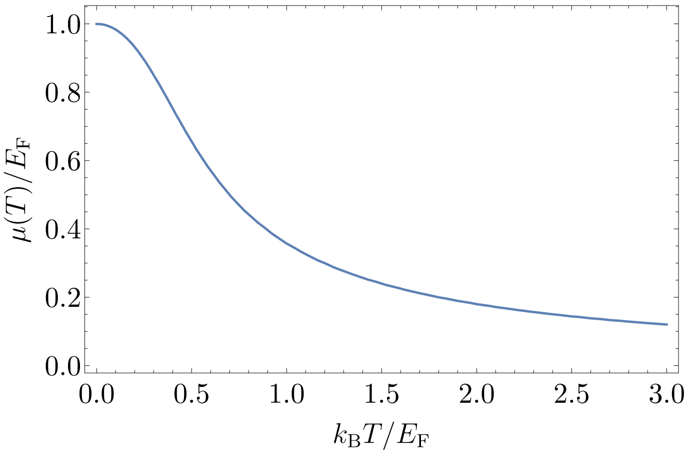

Figure 2.9: Temperature dependence of the chemical potential for a doped graphene sample with Fermi level E_{F}.

fixed dopant concentration, the chemical potential decreases with increasing temperature in order to compensate for the thermally excited carriers from the valence band.

In Fig. 2.10 the carrier concentration is shown as a function of the chemical potential μ. The possible doping levels in graphene depend on the way doping is achieved. The most common way is to use electrostatic gating. An electrostatic gate changes locally the potential above the flake such that electrons or holes are accumulated in the sample and the carrier concentration is affected. In this way the gate voltage induces a surface charge density given by $n_{\mathrm{eg}} = \epsilon_0 \epsilon V_{\mathrm{g}}/(te)$, where $\epsilon_0 \epsilon$ is the dielectric constant of the dielectric between the gate and the graphene flake, e is the elementary charge, t is the thickness of the dielectric and V_{g} is the gate voltage[32]. The biggest advantage of electrostatic doping is that it is gate-tunable. Indeed, by reversing the polarisation of the gate, the graphene flake can be continuously changed from a hole-doped to an electron-doped sample. The highest possible carrier concentration obtained by electrostatic gating is of the order of $n_{\mathrm{eg}} = 10^{13}\ \mathrm{cm}^{-2}$ [97].

Graphene flakes are, however, never perfectly clean and charged impurities positioned on the sample can modify the carrier density. Furthermore, the electron density is also locally varied and at low carrier concentration, so-called *electron-hole puddles* are formed [98]. These puddles are local regions that are electron or hole doped. The local concentration can range up to $n_{\mathrm{ehp}} \simeq 3.9 \times 10^{10}\ \mathrm{cm}^{-2}$ which corresponds to $E_{\mathrm{F}} \simeq 23\ \mathrm{meV}$ [98]. At finite temperature there is also a finite concentration of thermally excited carriers, which is for room temperature of the order of the thermal energy, i.e. $E_{\mathrm{F}} \simeq 25\ \mathrm{meV}$ at room temperature. These limit the lowest possible doping in graphene as well.

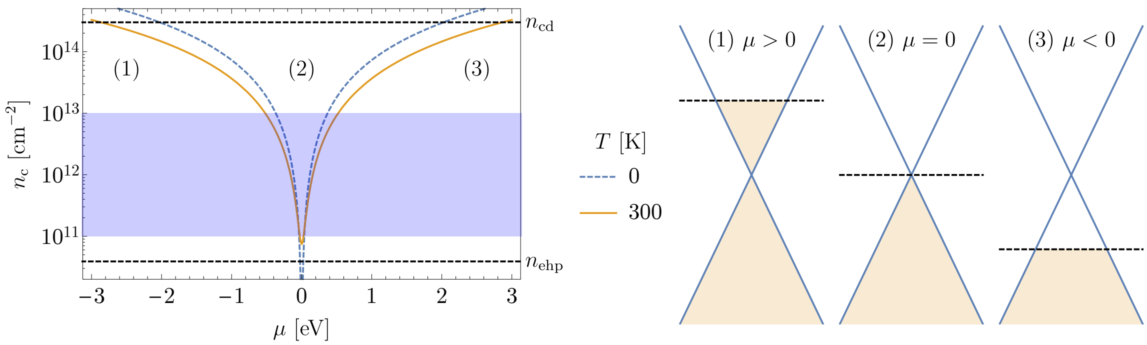

Figure 2.10: Doping levels of graphene as a function of the chemical potential μ. The left plot shows the relation between chemical potential and carrier concentration at zero (dashed blue curve) and room temperature (solid orange curve). The highest recorded chemical doping n_{cd} [100] and the typical concentration of electron-hole puddles n_{ehp} are indicated by horizontal black dashed lines. The blue shaded region is the region of interest of this thesis. The right panel shows schematically the different doping levels of the Dirac cone as indicated by the numbers (1), (2) and (3) in the left panel.

External atoms can be used to intentionally dope the graphene flake. This can be done by replacing some of the carbon atoms by for example nitrogen ($n_{\mathrm{cd}} \simeq 10^{13}\ \mathrm{cm}^{-2}$) [99]. Other researchers have found that by intercalating graphite with FeCl_3, a doping of up to $n_{\mathrm{cd}} \simeq 3 \times 10^{14}\ \mathrm{cm}^{-2}$ can be established [100]. Subsequently, a gate can be used to vary the chemical potential around the new doping level.

Accounting for the above mentioned limitations, in this thesis doping levels in the range $n_c \sim 10^{11} - 10^{13}\ \mathrm{cm}^{-2}$ will be used since they are readily achievable by gating in exfoliated graphene samples [101]. In Fig. 2.10 this region is shaded in blue.

CHAPTER 3

Optical response of a graphene flake

In this chapter the optical response of graphene is reviewed. This requires introducing all fundamental concepts from linear response theory (LRT) that are necessary for future understanding of how the chiral electron liquid in a graphene flake responds to an incident photon.

First, the general framework of LRT is introduced and then applied to graphene to calculate the response to external scalar potentials in the absence of electron-electron interactions. This will turn out to be a very accurate description of graphene photon absorption.

Secondly, electron-electron (e-e) interactions are accounted for on the level of the random phase approximation (RPA) and the crystals optical response is re-evaluated at this level. Electron-electron interactions introduce a new sort of collective mode in the system, the *plasmon*. The properties of the graphene plasmon are then briefly reviewed. Furthermore, the current state of the experimental progress concerning graphene plasmons is reviewed. This forms a strong motivation for the investigation of plasmons in 2D materials in the next chapters.

Finally, as an example of the effect of plasmons to the electronic properties of graphene plasmarons in monolayer, bilayer and trilayer graphene are considered. The existence of plasmarons in graphene was shown to be measurable with ARPES techniques and, also, proves the existence of graphene plasmons. In this section, the plasmaron dispersion for trilayer graphene is shown. The work on plasmarons in trilayer graphene was published in Physical Review B [69].

3.1 Linear response to external fields

The response of an electron liquid to an exteral perturbation can be can be calculated in the LRT framework if the external perturbation is small [102, 103]. Therefore, the measured response will contain only information of the unperturbed system and not of the system with perturbation.

In the LRT the effect of the external probe is calculated to linear order in the strength of the probing field (e.g. the amplitude of the electric field). The proportionality constant relating the measurement to the probing field only depends on the properties of the unperturbed system. In LRT this proportionality constant is called a *linear response function* (LRF). The study of the properties of these LRFs is the central goal of most of the work presented in this thesis.

In the remainder of this section the framework of the LRT and the formal definition of LRFs is presented. This presentation will be along the lines presented in the book by Giuliani and Vignale, Ref. [102].

3.1.1 Linear response functions

Consider a system described by a time-independent Hamiltonian $\hat{H}$ and a probe that acts on this system with the operator $\hat{B}$ and the time-dependent external field $F\left(t\right)$. The total Hamiltonian can then be written as

$$\hat{H}_F\left(t\right) = \hat{H} + F\left(t\right)\hat{B}. \tag{3.1}$$

The external field is applied at a certain moment in time, denoted by t_0, such that for $t < t_0$ the system is in the ground state of $\hat{H}$. This state is given by the occupation of the eigenstates of the system $\left|\psi_n\right\rangle$ where the occupation of each eigenstate is given by

$$P_n = \frac{e^{-\beta E_n}}{\mathcal{Z}}, \tag{3.2}$$

where $\beta = \left(k_{\mathrm{B}}T\right)^{-1}$ with T the temperature and k_{B} Boltzmann's constant, E_n is the energy of the n^{th} eigenstate and $\mathcal{Z} = \sum_n e^{-\beta E_n}$ is the canonical partition sum.

In order to measure the effect of the external field on the system, one needs to measure the effect on the expectation value of operator $\hat{A}$, associated to an observable of the system, at time $t > t_0$. This quantity is expressed as

$$\left\langle \hat{A} \right\rangle_F \left(t\right) = \sum_n P_n \left\langle \psi_n\left(t\right) \left| A \right| \psi_n\left(t\right) \right\rangle. \tag{3.3}$$

In Eq. (3.3) the notation $\langle \ldots \rangle_F$ denotes calculation of the expectation value with respect to the perturbed state. To find the quantity expressed in Eq. (3.3), one needs to find the time evolution of each eigenstate under the influence of the external field $F(t)$. This time evolution is determined by the Schrödinger equation

$$i\hbar \frac{\partial}{\partial t} \left| \psi_n(t) \right\rangle = \hat{H}_F(t) \left| \psi_n(t) \right\rangle, \tag{3.4}$$

where the initial condition $\left| \psi_n(t_0) \right\rangle = \left| \psi_n \right\rangle$ must be satisfied. It is well known that formally this leads to the equation [104]

$$\left| \psi_n(t) \right\rangle = \hat{U}(t, t_0) \left| \psi_n(t_0) \right\rangle, \tag{3.5}$$

where $\hat{U}(t, t_0)$ is the unitary time-evolution operator. In the absence of a perturbation this operator becomes

$$\hat{U}_0(t, t_0) \equiv \hat{U}(t, t_0) \Big|_{F=0} = e^{-i\hat{H}(t-t_0)}. \tag{3.6}$$

In order to find the time evolution presented in Eq. (3.5) in the presence of a perturbation, the problem has been reduced to the determination of the operator $\hat{U}(t, t_0)$. This determination shall be performed up to first order in F and hence will constitute the linear approximation. In the presence of the external perturbation, the total time-evolution operator can be written as

$$\hat{U}(t, t_0) = \hat{U}_0(t, t_0) \hat{U}_F(t, t_0), \tag{3.7}$$

where $\hat{U}_0(t, t_0)$ is defined in Eq. (3.6) and describes the time evolution of the ground state. The effect of the external field is now combined in the operator $\hat{U}_F(t, t_0)$. Eq. (3.7) transforms the Schrödinger equation (3.4) into

$$i\hbar \frac{\partial}{\partial t} \hat{U}_F(t, t_0) = F(t) \hat{B}(t - t_0) \hat{U}_F(t, t_0), \tag{3.8}$$

where $\hat{B}(t) \equiv \hat{U}_0^\dagger(t, t_0) \hat{B} \hat{U}_0(t, t_0)$ is the time evolution of the operator $\hat{B}$ in the Heisenberg picture [104]. Note that the initial condition for this equation is $\hat{U}_F(t_0, t_0) = 1$. Therefore, if one expands the operator $\hat{U}_F(t, t_0)$ to first order in $F(t)$, i.e. $\hat{U}_F(t, t_0) = 1 + F(t) \hat{U}_{F,1}(t, t_0)$, the Eq. (3.8) can be solved for $\hat{U}_{F,1}(t, t_0)$ as

$$\hat{U}_{F,1}(t, t_0) = -\frac{i}{\hbar} \int_{t_0}^{t} dt' \hat{B}(t' - t_0) F(t') + \mathcal{O}\left[F^2\right], \tag{3.9}$$

so the total time-evolution operator to first order in F is given by

$$\hat{U}(t, t_0) \approx \hat{U}_0(t, t_0) \left[1 - \frac{i}{\hbar} \int_{t_0}^{t} dt' \hat{B}(t' - t_0) F(t') \right]. \tag{3.10}$$

Eq. (3.10) is the crucial approximation made in LRT. Using this expression, one can calculate the expectation value from Eq. (3.3) as

$$\begin{aligned}
\left\langle\psi_n(t)\left|\hat{A}\right|\psi_n(t)\right\rangle &= \left\langle\psi_n(t_0)\left|\hat{U}_0^\dagger(t,t_0)\,\hat{A}\hat{U}_0(t,t_0)\right|\psi_n(t_0)\right\rangle \\
&\quad+\frac{i}{\hbar}\int_{t_0}^{t}dt'F^*(t')\left\langle\psi_n(t_0)\left|\hat{B}^\dagger(t'-t_0)\,\hat{A}(t-t_0)\right|\psi_n(t_0)\right\rangle \\
&\quad-\frac{i}{\hbar}\int_{t_0}^{t}dt'F(t')\left\langle\psi_n(t_0)\left|\hat{A}(t-t_0)\,\hat{B}(t'-t_0)\right|\psi_n(t_0)\right\rangle \\
\left\langle\hat{A}\right\rangle_F(t)-\left\langle\hat{A}\right\rangle_0 &= -\frac{i}{\hbar}\int_{t_0}^{t}dt'\left\langle\left[\hat{A}(t),B(t')\right]\right\rangle_0 F(t'),
\end{aligned} \tag{3.11}$$

here, $\langle\ldots\rangle_0$ denotes the ensemble average of the thermal equilibrium, i.e.

$$\left\langle\hat{A}\right\rangle_0=\sum_n P_n\left\langle\psi_n(t_0)\left|\hat{A}\right|\psi_n(t_0)\right\rangle. \tag{3.12}$$

Eq. (3.11) is the main result of this derivation. This equation expresses that the deviation of the expectation value of $\hat{A}$ from the unperturbed result, under the influence of the external field that couples to $\hat{B}$ with strength F, is determined by the commutator $\left[\hat{A},\hat{B}\right]$ integrated over the amount of time passed since the start of the perturbation at t_0. This equation expresses exactly what one wants to obtain: a measure for the deviation from the unperturbed result due to the external perturbation. Denoting this as $\left\langle\hat{A}\right\rangle_1(t)\equiv\left\langle\hat{A}\right\rangle_F(t)-\left\langle\hat{A}\right\rangle_0$, one can rewrite Eq. (3.11) as

$$\left\langle\hat{A}\right\rangle_1(t)=\int_0^\infty d\tau\chi_{AB}(\tau)\,F(t-\tau), \tag{3.13}$$

where the *retarded linear response function* $\chi_{AB}(\tau)$ is introduced. Its definition is

$$\chi_{AB}(\tau)\equiv-\frac{i}{\hbar}\Theta(\tau)\left\langle\left[\hat{A}(\tau),\hat{B}\right]\right\rangle_0. \tag{3.14}$$

Here, the assumption has been made that the perturbing field tends to zero as $t\to-\infty$ in order to replace the upper boundary of the integral in Eq. (3.13) [102].

3.1.2 Response function of a non-interacting electron liquid

In the absence of electron-electron interaction, the linear response function can be derived in a basis where only single-particle states and single particle energies are necessary. For this, the operators $\hat{A}$ and $\hat{B}$ can be written in second quantisation as [104]

$$\begin{aligned}\hat{A} &= \sum_{\alpha\beta} A_{\alpha\beta}\hat{a}^{\dagger}_{\alpha}\hat{a}_{\beta}, &(3.15)\\ \hat{B} &= \sum_{\alpha\beta} B_{\alpha\beta}\hat{a}^{\dagger}_{\alpha}\hat{a}_{\beta}. &(3.16)\end{aligned}$$

Here $\hat{a}^{\dagger}_{\alpha}$ and $\hat{a}_{\alpha}$ are the creation and annihilation operators of an electron in a state α respectively. These operators diagonalize the non-interacting Hamiltonian exactly

$$\hat{H}_0 = \sum_{\alpha} \varepsilon_{\alpha}\hat{a}^{\dagger}_{\alpha}\hat{a}_{\alpha}, \tag{3.17}$$

where ε_{α} is the energy of state α. If the perturbation is included in the Hamiltonian,

$$\hat{H}_{F0} = \hat{H}_0 + F\left(t\right)\hat{B}, \tag{3.18}$$

one can determine the response function $\chi^{(0)}_{AB}\left(\tau\right)$. The superscript (0) denotes the fact that interactions are turned off and, therefore, it is the *non-interacting response function*. Using Eq. (3.14) one finds

$$\begin{aligned}\chi^{(0)}_{AB}\left(\tau\right) &= -\frac{i}{\hbar}\Theta\left(\tau\right)\sum_{\alpha\beta\gamma\delta} A_{\alpha\beta}B_{\gamma\delta}e^{i\left(\varepsilon_{\alpha}-\varepsilon_{\beta}\right)\tau/\hbar}\left\langle\left[\hat{a}^{\dagger}_{\alpha}\hat{a}_{\beta},\hat{a}^{\dagger}_{\gamma}\hat{a}_{\delta}\right]\right\rangle_0\\ &= -\frac{i}{\hbar}\Theta\left(\tau\right)\sum_{\alpha\beta} A_{\alpha\beta}B_{\beta\alpha}e^{i\left(\varepsilon_{\alpha}-\varepsilon_{\beta}\right)\tau/\hbar}\left(n_{\alpha}-n_{\beta}\right)\ . &(3.19)\end{aligned}$$

Eq. (3.19) is obtained by noticing that the number operator is $\hat{n}_{\alpha} = \hat{a}^{\dagger}_{\alpha}\hat{a}_{\alpha}$ and that the commutator of the Fermionic creation and annihilation operators can be calculated as follows:

$$\left[\hat{a}^{\dagger}_{\alpha}\hat{a}_{\beta},\hat{a}^{\dagger}_{\gamma}\hat{a}_{\delta}\right] = \delta_{\beta\gamma}\hat{a}^{\dagger}_{\alpha}\hat{a}_{\delta} - \delta_{\alpha\delta}\hat{a}^{\dagger}_{\gamma}\hat{a}_{\beta}\ . \tag{3.20}$$

Usually if the external perturbation is periodic in time with angular frequency ω, i.e. $F\ e^{-i\omega t}$, one is interested in the time Fourier transform. This yields for Eq. (3.19)

$$\chi^{(0)}_{AB}\left(\omega\right) = \lim_{\eta\to0^+}\int_{-\infty}^{\infty} d\tau\chi^{(0)}_{AB}(\tau)e^{i(\omega+i\eta)\tau} = \lim_{\eta\to0^+}\sum_{\alpha\beta}\frac{n_{\alpha}-n_{\beta}}{\hbar\omega+\varepsilon_{\alpha}-\varepsilon_{\beta}+i\hbar\eta}A_{\alpha\beta}B_{\beta\alpha}. \tag{3.21}$$

Here, n_{α} is the occupation probability of the eigenstate α of the non-interacting Hamiltonian. Notice that in the formula above, only single-particle properties of the system are considered. The limit of η needs to be considered for positive values only which is the consequence of causality. It can be easily seen that if $\eta < 0$, the response of the system would exponentially grow in time instead of decreasing after being excited. This is not physical.

3.1.3 Density-density response function of graphene

Using the formalism explained in the previous section, a very important quantity, the *density-density response function* of graphene, can now be calculated. This quantity describes the response of the chiral electron liquid in graphene to an external scalar potential. Later it will be shown that the response to a longitudinal electric field is the same as the response to a scalar field.

The non-interacting Hamiltonian is in second quantisation given by

$$\hat{H}_0 = \sum_{\lambda \boldsymbol{k}} \varepsilon_{\lambda \boldsymbol{k}} \hat{c}^{\dagger}_{\lambda \boldsymbol{k}} \hat{c}_{\lambda \boldsymbol{k}} \,. \tag{3.22}$$

Here, $\hat{c}^{\dagger}_{\alpha}$ and $\hat{c}_{\alpha}$ are, respectively, creation and annihilation operators of a particle in state α and $\varepsilon_{\lambda \boldsymbol{k}}$ is the energy dispersion given by Eq. (2.15). In the absence of e-e interaction, all states can be labeled by $\alpha = \lambda \boldsymbol{k}$, the band index and momentum as was shown in Eq. (2.20). Note that no approximation near the Dirac points has been made yet. In order to find the density response function, the density operator in second quantisation can be written as [105]

$$\hat{n}_{\boldsymbol{q}} = \sum_{\boldsymbol{k}\lambda\lambda'} \mathcal{D}_{\lambda\lambda'} \left(\boldsymbol{k}, \boldsymbol{k}+\boldsymbol{q}\right) \hat{c}^{\dagger}_{\lambda \boldsymbol{k}} \hat{c}_{\lambda' \boldsymbol{k}+\boldsymbol{q}}. \tag{3.23}$$

In Eq. (3.23) the function $\mathcal{D}_{\lambda\lambda'}$ comes from the evaluation of the density operator in the single-particle states. This quantity is called the *density vertex* and is given by the projection of the non-interacting eigenstates Eq. (2.13) onto each other:

$$\mathcal{D}_{\lambda\lambda'} \left(\boldsymbol{k}, \boldsymbol{k}'\right) = \langle \Psi_{\lambda \boldsymbol{k}} | \Psi_{\lambda' \boldsymbol{k}'} \rangle = \frac{1 + \lambda\lambda' e^{i(\varphi_{\boldsymbol{k}'} - \varphi_{\boldsymbol{k}})}}{2} \,. \tag{3.24}$$

Notice that the angle $\varphi_{\boldsymbol{k}}$ in the low energy limit around the Dirac points reduces to the angle $\varphi_{\boldsymbol{k}}$ between the vector $\boldsymbol{k}$ and the x-axis as discussed in Sec. 2.2.1. The density vertex carries the chirality of the Dirac particles in the system and decouples oppositely propagating charge carriers of the same band. Indeed, if two particles have opposite momentum $\boldsymbol{k}' = -\boldsymbol{k}$, the angle between them is $\varphi_{-\boldsymbol{k}} - \varphi_{\boldsymbol{k}} = \pi$ and then the density vertex reduces to

$$\mathcal{D}_{\lambda\lambda'} \left(\boldsymbol{k}, -\boldsymbol{k}\right) = \frac{1}{2} \left(1 - \delta_{\lambda\lambda'}\right). \tag{3.25}$$

This means that if they belong to the same energy band, the density vertex is zero and they decouple. Furthermore, if they have the same direction, inter-band coupling is zero.

Now one can determine the density-density response function of graphene as

$$\begin{aligned}\chi_{nn}^{(0)}(\boldsymbol{q},\omega) &= \frac{1}{L^2}\chi_{n_{\boldsymbol{q}}n_{-\boldsymbol{q}}}^{(0)}(\omega) = \frac{1}{L^2}\sum_{\lambda\boldsymbol{k},\lambda'\boldsymbol{k}'}\frac{n_{\lambda\boldsymbol{k}} - n_{\lambda'\boldsymbol{k}'}}{\hbar\omega + \varepsilon_{\lambda\boldsymbol{k}} - \varepsilon_{\lambda'\boldsymbol{k}'} + i\hbar\eta}\left|(n_{\boldsymbol{q}})_{\lambda\boldsymbol{k},\lambda'\boldsymbol{k}'}\right|^2 \\ &= \frac{1}{L^2}\sum_{\lambda\lambda'\boldsymbol{k}}\left|\mathcal{D}_{\lambda\lambda'}(\boldsymbol{k},\boldsymbol{k}+\boldsymbol{q})\right|^2\frac{n_{\lambda\boldsymbol{k}} - n_{\lambda'\boldsymbol{k}+\boldsymbol{q}}}{\hbar\omega + \varepsilon_{\lambda\boldsymbol{k}} - \varepsilon_{\lambda'\boldsymbol{k}+\boldsymbol{q}} + i\hbar\eta}. \qquad (3.26)\end{aligned}$$

Because electrons and holes are considered, the occupation probability $n_{\lambda\boldsymbol{k}}$ is given by the Fermi Dirac distribution function

$$n_{\lambda\boldsymbol{k}} \equiv f_{\mathrm{D}}(\varepsilon_{\lambda\boldsymbol{k}},\mu,T) = \left(1 + \exp\left(\frac{\varepsilon_{\lambda\boldsymbol{k}} - \mu}{k_{\mathrm{B}}T}\right)\right)^{-1}. \qquad (3.27)$$

Furthermore, the chirality factor becomes

$$\left|\mathcal{D}_{\lambda\lambda'}(\boldsymbol{k},\boldsymbol{k}+\boldsymbol{q})\right|^2 = \frac{1 + \lambda\lambda'\cos(\varphi_{\boldsymbol{k}} - \varphi_{\boldsymbol{k}+\boldsymbol{q}})}{2}. \qquad (3.28)$$

If inter-valley scattering processes are disregarded, $|\boldsymbol{q}| \ll |\boldsymbol{K}|$, it suffices to only consider the system near the Dirac points. In the continuum limit around the two Dirac points, the system will obtain the same single-particle properties in both valleys and therefore the response of the valley resolved electron liquid will be formally the same as Eq. (3.26) but with an additional valley degeneracy factor $g_{\mathrm{v}} = 2$. Furthermore, up to now the spin degeneracy has been disregarded. Because there are no spin symmetry breaking processes involved, also the spin degree of freedom of the charge carriers will only contribute as a degeneracy factor $g_{\mathrm{s}} = 2$. Therefore, in the continuum limit, the density-density response function is

$$\chi_{nn}^{(0)}(\boldsymbol{q},\omega) = \frac{N_{\mathrm{f}}}{L^d}\sum_{\lambda\lambda'\boldsymbol{k}}\left|\mathcal{D}_{\lambda\lambda'}(\boldsymbol{k},\boldsymbol{k}+\boldsymbol{q})\right|^2\frac{n_{\lambda\boldsymbol{k}} - n_{\lambda'\boldsymbol{k}+\boldsymbol{q}}}{\hbar\omega + \varepsilon_{\lambda\boldsymbol{k}} - \varepsilon_{\lambda'\boldsymbol{k}+\boldsymbol{q}} + i\hbar\eta}. \qquad (3.29)$$

Now the energy $\varepsilon_{\lambda\boldsymbol{k}}$ is given by the linear Dirac cone approximation, Eq. (2.19). The next section will be devoted to a calculation of the density response of the chiral liquid in graphene at zero Kelvin. As before, $N_{\mathrm{f}} = g_{\mathrm{v}}g_{\mathrm{s}}$ corresponds to the number of Fermion species in the system.

3.1.4 Calculation of the density response function in graphene at T=0

The derivation of the calculation of the density-density response function outlined here follows the one presented by Wunsch *et al.* [106]. Without loss of generality, the chemical potential μ is considered positive, $\mu \geq 0$, such that the system is electron doped. Hole doping can be obtained by making use of the particle-hole symmetry of the system.

At $T = 0$, the Fermi-Dirac distribution function, Eq. (3.27), becomes

$$n_{\lambda \boldsymbol{k}} = \Theta\left(E_{\mathrm{F}} - \lambda \hbar v_{\mathrm{F}} k\right), \tag{3.30}$$

where the Fermi level is $E_{\mathrm{F}} \equiv \mu(T=0)$ and $\Theta(\ldots)$ is the Heaviside step function. From Eq. (3.30) it follows that intra-valence band transition are suppressed since in that case the two occupation functions appearing in the numerator of the response function, Eq. (3.29), cancel each other for all vectors $\boldsymbol{k}$. This is a consequence of the Pauli exclusion principle because the valence band is considered to be completely filled. Next, one can notice that because the chirality factor only depends on the product of λ and λ', the sum over the band indices can be used to regroup the terms according to inter-band and intra-band transitions as follows:

$$\chi^{(0)}_{nn}\left(\boldsymbol{q}, \omega\right) = -\chi^{-}_{\Lambda}\left(\boldsymbol{q}, \omega\right) + \chi^{-}_{E_{\mathrm{F}}}\left(\boldsymbol{q}, \omega\right) + \chi^{+}_{E_{\mathrm{F}}}\left(\boldsymbol{q}, \omega\right). \tag{3.31}$$

Here the function $\chi^{\pm}_{A}\left(q, \omega\right)$ is given by

$$\begin{aligned} \chi^{\pm}_{A}\left(\boldsymbol{q}, \omega\right) &= g_{\mathrm{s}} g_{\mathrm{v}} \int_{k<A} \frac{d\boldsymbol{k}}{\left(2\pi\right)^{2}} \sum_{\alpha=\pm 1} \frac{\alpha \left|\mathcal{D}_{\pm}\left(\boldsymbol{k}, \boldsymbol{k}+\boldsymbol{q}\right)\right|^{2}}{\hbar\omega + \alpha\left(\varepsilon_{\boldsymbol{k}} \mp \varepsilon_{\boldsymbol{k}+\boldsymbol{q}}\right) + i\hbar\eta} \qquad (3.32) \\ &= \frac{D\left(E_{\mathrm{F}}\right)}{2\pi} \int_{k<A} d\bar{\boldsymbol{k}} \sum_{\alpha=\pm 1} \frac{\alpha \left|\mathcal{D}_{\pm}\left(\bar{\boldsymbol{k}}, \bar{\boldsymbol{k}}+\bar{\boldsymbol{q}}\right)\right|^{2}}{\bar{\omega} + \alpha\left(\bar{k} \mp \left|\bar{\boldsymbol{k}}+\bar{\boldsymbol{q}}\right|\right) + i\bar{\eta}}\,. \qquad (3.33) \end{aligned}$$

For notational convenience, in this formula the subscript ± of $\mathcal{D}_{\pm}$ denotes the product of λ and λ', the energy is defined as $\varepsilon_{\boldsymbol{k}} \equiv \varepsilon_{+\boldsymbol{k}}$, and the wave vectors are made dimensionless as

$$\bar{\boldsymbol{k}} \equiv \boldsymbol{k}/k_{\mathrm{F}}\,,\ \bar{\boldsymbol{q}} \equiv \boldsymbol{q}/k_{\mathrm{F}}\,,\ \bar{\omega} \equiv \hbar\omega/E_{\mathrm{F}}\,. \tag{3.34}$$

Here $k_{\mathrm{F}} \equiv E_{\mathrm{F}}/\left(\hbar v_{\mathrm{F}}\right)$ is the Fermi wave vector. The procedure to make the equation dimensionless introduces the graphene density of states $D\left(E_{\mathrm{F}}\right)$ from Eq. (2.30), evaluated at the Fermi level E_{F}.

In Eq. (3.31) the response is expressed as a sum of three contributions. The first one describes inter-band processes that excite electrons from the valence band into the conduction band and is present even in the absence of electron doping. This term is non-zero due to the presence of a continuum of filled electrons in the valence band and can be thought of as excitations from the vacuum constituted by a filled valence band and empty conduction band. Therefore this term is usually called the *vacuum contribution*. The second and third terms correspond to inter- and intra-band contributions respectively. These terms are only finite if the system is doped.

In the next two paragraphs the different response function are calculated and their analytical solutions are presented.

Imaginary part

The imaginary part of the response function from Eq. (3.33) can be easily obtained if one uses the theorem by Sokhotskii - Plemelj [107]

$$\lim_{\eta\to0^+}\int_a^b dx\frac{f\left(x\right)}{x\pm i\eta}=\mp i\pi\int_a^b dx f\left(x\right)\delta\left(x\right)+\mathcal{P}\int_a^b dx\frac{f\left(x\right)}{x}, \tag{3.35}$$

where $\delta\left(x\right)$ is the delta function and $\mathcal{P}$ denotes the prime value of the integral. As a consequence, the imaginary part of the integral from Eq. (3.33) is (the barred notation is suppressed for clarity)

$$\begin{aligned}\mathrm{Im}\chi_A^{\pm}\left(\boldsymbol{q},\omega\right) = & -\frac{D\left(E_{\mathrm{F}}\right)}{2}\sum_{\alpha=\pm1}\alpha\int_0^A dkk\\ & \times\int_0^{2\pi}d\theta\left|\mathcal{D}_{\pm}\left(\boldsymbol{k},\boldsymbol{k}+\boldsymbol{q}\right)\right|^2\delta\left(\omega+\alpha\left(k\mp\left|\boldsymbol{k}+\boldsymbol{q}\right|\right)\right).\end{aligned} \tag{3.36}$$

The angular part of this integral runs over the angle θ which can be chosen to be the angle between $\boldsymbol{k}$ and $\boldsymbol{q}$. However, the vertex factor from Eq. (3.28) depends on the angle between $\boldsymbol{k}$ and $\boldsymbol{k}+\boldsymbol{q}$. This can be accounted for by rewriting the vertex factor as

$$\left|\mathcal{D}_{\pm}\left(\boldsymbol{k},\boldsymbol{k}+\boldsymbol{q}\right)\right|^2=\frac{1}{2}\left(1\pm\frac{k+q\cos\left(\theta\right)}{\left|\boldsymbol{k}+\boldsymbol{q}\right|}\right). \tag{3.37}$$

Notice that because of the isotropy of the Dirac cone, the response function does not depend on the angle of $\boldsymbol{q}$. Therefore, from now on only the dependence on its magnitude q will be considered. The angular integral can be performed. Replacing the integral over θ by one over $y=\left|\boldsymbol{k}+\boldsymbol{q}\right|=\sqrt{k^2+2kq\cos(\theta)+q^2}$, one finds

$$\begin{aligned}I_{\text{ang}}^{\alpha\beta} &= 2\int_0^{\pi}d\theta\frac{1}{2}\left(1+\beta\frac{k+q\cos\left(\theta\right)}{\left|\boldsymbol{k}+\boldsymbol{q}\right|}\right)\delta\left(\omega+\alpha\left(k-\beta\left|\boldsymbol{k}+\boldsymbol{q}\right|\right)\right)\\ &= \int_{k-q}^{k+q}\frac{dy}{k}\frac{2yk+\beta\left(y^2+k^2-q^2\right)}{\sqrt{\left(2kq\right)^2-\left(y^2-k^2-q^2\right)^2}}\delta\left(y-\beta\left(\alpha\omega+k\right)\right)\end{aligned} \tag{3.38}$$

Here, $I_{\text{ang}}^{\alpha\beta}$ is the angular integral of Eq. (3.36) and $\beta=\pm1$. This intermediate result shows that the integral only contributes if the argument of the δ function vanishes for a y in the range $[k-q,k+q]$. The result is

$$I_{\text{ang}}^{\alpha\beta}=\frac{1}{k}\sqrt{\frac{\left(2\alpha k+\omega\right)^2-q^2}{q^2-\omega^2}}F_{\text{Im}}^{\alpha\beta}\left(k,q,\omega\right), \tag{3.39}$$

where the function $F_{\mathrm{Im}}^{\alpha\beta}(k,q,\omega)$ is given by

$$\begin{aligned} F_{\mathrm{Im}}^{\alpha\beta}(k,q,\omega) &= \Theta(\beta)\,\Theta(q-\omega)\,\Theta\left(k-\frac{q-\alpha\omega}{2}\right) \\ &+ \Theta(-\beta)\,\Theta(-\alpha)\,\Theta(\omega-q)\left[\Theta\left(\frac{\omega+q}{2}-k\right)-\Theta\left(\frac{\omega-q}{2}-k\right)\right]. \end{aligned} \tag{3.40}$$

This function divides the (q,ω) plane in different parts where intra-band contributions are only possible if $q>\omega$ and inter-band contributions if $q<\omega$.

The imaginary part of the vacuum contribution is subsequently inferred as

$$\begin{aligned} \mathrm{Im}\chi_{\Lambda}^{-}(q,\omega) &= \frac{D(E_{\mathrm{F}})}{2}\frac{q\Theta(\omega-q)}{\sqrt{\omega^2-q^2}}\int_{\frac{\omega-q}{2}}^{\frac{\omega+q}{2}}dk\sqrt{1-\left(\frac{\omega-2k}{q}\right)^2} \\ &= \frac{\pi D(E_{\mathrm{F}})}{8}\frac{\Theta(\omega-q)}{\sqrt{\omega^2-q^2}}q^2. \end{aligned} \tag{3.41}$$

For the intra-band term, the integral yields

$$\begin{aligned} \mathrm{Im}\chi_{E_{\mathrm{F}}}^{+}(q,\omega) &= -\frac{D(E_{\mathrm{F}})}{2}\frac{\Theta(q-\omega)\,q^2}{\sqrt{q^2-\omega^2}}\sum_{\alpha}\alpha\int_{\frac{q-\alpha\omega}{2}}^{1}dk\sqrt{\left(\frac{2k+\alpha\omega}{q}\right)^2-1} \\ &= \frac{D(E_{\mathrm{F}})}{8}\frac{\Theta(q-\omega)\,q^2}{\sqrt{q^2-\omega^2}} \\ &\times \left[\Theta\left(1-\frac{q+\omega}{2}\right)G_{>}\left(\frac{2+\omega}{q}\right)-\Theta\left(1-\frac{q-\omega}{2}\right)G_{>}\left(\frac{2+\omega}{q}\right)\right]. \end{aligned} \tag{3.42}$$

Similarly, the imaginary part of the inter-band contribution is

$$\begin{aligned} \mathrm{Im}\chi_{E_{\mathrm{F}}}^{-}(q,\omega) &= \frac{D(E_{\mathrm{F}})}{8}\frac{\Theta(\omega-q)\,q^2}{\sqrt{\omega^2-q^2}}\Bigg[\Theta\left(1-\frac{\omega-q}{2}\right)\pi \\ &-\Theta\left(\frac{\omega+q}{2}-1\right)\Theta\left(1-\frac{\omega-q}{2}\right)G_{<}\left(\frac{-2+\omega}{q}\right)\Bigg]. \end{aligned} \tag{3.43}$$

Here, $G_{<}(x)$ is defined as

$$G_{<}(x)=x\sqrt{1-x^2}-\arccos(x). \tag{3.44}$$

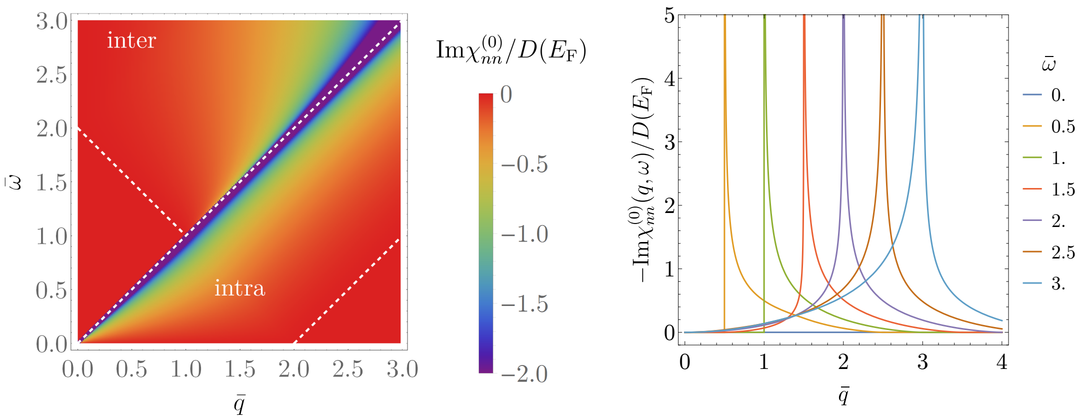

Figure 3.1: Imaginary part of the non-interacting density-density response function $\chi_{nn}^{(0)}(q,\omega)$. In the left plot the function is shown in the (q,ω) plane where the intra- and inter-band continua are shown by dashed white lines. The right figure shows a cut of the function at different values of ω as indicated. The quantities are expressed in the dimensionless units defined in Eq. (3.34).

In Fig. 3.1 the imaginary part of the non-interacting response function $\chi_{nn}^{(0)}(q,\omega)$ is calculated. Notice that the function vanishes in a triangle in the left lower corner of the $(\bar{q},\bar{\omega})$ plane and that the function diverges towards the $\bar{q}=\bar{\omega}$ line. The physical origin of this will be discussed in a following section.

Real part

The real part can now be found by making use of the Kramers-Kronig relation [102, 108, 109] that connects the real and imaginary part of the response function as:

$$\mathrm{Re}\chi_{AB}\left(\omega\right)=\mathcal{P}\int_{-\infty}^{\infty}\frac{d\nu}{\pi}\frac{\mathrm{Im}\chi_{AB}\left(\nu\right)}{\nu-\omega}\,. \tag{3.45}$$

Applying this to the expression for the vacuum response function yields

$$\mathrm{Re}\chi_{\Lambda}^{-}\left(q,\omega\right)=\frac{D\left(E_{\mathrm{F}}\right)q^{2}}{8}\mathcal{P}\int_{0}^{\infty}d\nu'\frac{1}{\nu'+q-\omega}\frac{1}{\sqrt{\nu'}\sqrt{\nu'+2q}}\,. \tag{3.46}$$

One can use the following identity [110]

$$\int_{0}^{\infty}x^{\lambda-1}f\left(x\right)dx=\frac{2\pi i}{1-e^{2\pi i\lambda}}\sum_{\text{poles of }f(x)}\mathrm{Res}\left(z^{\lambda-1}f\left(z\right)\right), \tag{3.47}$$

which can be used for $\lambda = 1/2$ such that

$$\mathrm{Re}\chi_{\Lambda}^{-}\left(q,\omega\right) = \frac{\pi D\left(E_{\mathrm{F}}\right)q^{2}}{8} i \lim_{z\rightarrow\omega-q}\frac{1}{\sqrt{z}\sqrt{z+2q}} = \frac{\pi D\left(E_{\mathrm{F}}\right)}{8}\frac{\Theta\left(q-\omega\right)q^{2}}{\sqrt{q^{2}-\omega^{2}}} \,. \tag{3.48}$$

The real part of the intra- and inter-band contributions can be calculated directly by combining them as

$$\begin{aligned}
\mathrm{Re}\chi_{E_{\mathrm{F}}}\left(q,\omega\right) &= \mathrm{Re}\chi_{E_{\mathrm{F}}}^{-}\left(q,\omega\right) + \mathrm{Re}\chi_{E_{\mathrm{F}}}^{+}\left(q,\omega\right) && (3.49)\\
&= \frac{D\left(E_{\mathrm{F}}\right)}{2\pi}\mathcal{P}\int_{k<1} d\boldsymbol{k} \sum_{\alpha,\beta=\pm1}\left|\mathcal{D}_{\beta}\left(\boldsymbol{k},\boldsymbol{k}+\boldsymbol{q}\right)\right|^{2}\frac{\alpha}{\omega+\alpha\left(k-\beta\left|\boldsymbol{k}+\boldsymbol{q}\right|\right)}\\
&= \frac{D\left(E_{\mathrm{F}}\right)}{2\pi}\sum_{\alpha=\pm1}\mathcal{P}\int_{0}^{1} dkk\int_{0}^{2\pi} d\theta\frac{2k+\alpha\omega+q\cos\left(\theta\right)}{\left(k+\alpha\omega\right)^{2}-\left|\boldsymbol{k}+\boldsymbol{q}\right|} \,. && (3.50)
\end{aligned}$$

The angular integral of Eq. (3.50) can be evaluated as

$$\mathrm{Re}\chi_{E_{\mathrm{F}}}\left(q,\omega\right) = \frac{D\left(E_{\mathrm{F}}\right)}{2}\sum_{\alpha=\pm1} -1 + \mathcal{P}\int_{0}^{1} dk\sqrt{\frac{\left(2k+\alpha\omega\right)^{2}-q^{2}}{\omega^{2}-q^{2}}}F_{\mathrm{Re}}^{\alpha}\left(k,q,\omega\right) \;, \tag{3.51}$$

where the function $F_{\mathrm{Re}}^{\alpha}\left(k,q,\omega\right)$ is

$$\begin{aligned}
F_{\mathrm{Re}}^{\alpha}\left(k,q,\omega\right) &= \Theta\left(q-\omega\right)\Theta\left(\frac{q-\alpha\omega}{2}-k\right) && (3.52)\\
&+ \Theta\left(\omega-q\right)\Big[\Theta\left(\alpha\right)\\
&\quad +\Theta\left(-\alpha\right)\left(\Theta\left(\frac{\omega-q}{2}-k\right)-\Theta\left(k-\frac{\omega+q}{2}\right)\right)\Big] \,,
\end{aligned}$$

which provides the final expression for the real part of $\chi_{E_{\mathrm{F}}}\left(q,\omega\right)$:

$$\frac{\mathrm{Re}\chi_{E_{\mathrm{F}}}\left(q,\omega\right)}{D\left(E_{\mathrm{F}}\right)} = -1 + \frac{q^{2}}{8\sqrt{\left|\omega^{2}-q^{2}\right|}}\left(\Theta\left(\omega-q\right)H_{\mathrm{inter}}(q,\omega) + \Theta\left(q-\omega\right)H_{\mathrm{intra}}(q,\omega)\right) \,. \tag{3.53}$$

In Eq. (3.53), the functions describing the inter- and intra-band response are

$$H_{\mathrm{intra}}(q,\omega) = \pi\Theta\left(1-\frac{q+\omega}{2}\right) + \sum_{\gamma=\pm1}\gamma\Theta\left(\frac{q-\gamma\omega}{2}-1\right)G_{<}\left(\frac{2\gamma+\omega}{q}\right) \;, \tag{3.54}$$

$$H_{\mathrm{inter}}(q,\omega) = G_{>}\left(\frac{2+\omega}{q}\right) - \sum_{\gamma=\pm1}\Theta\left(\gamma\left(\frac{\omega-\gamma q}{2}-1\right)\right)G_{>}\left(\gamma\frac{\omega-2}{q}\right) \,. \tag{3.55}$$

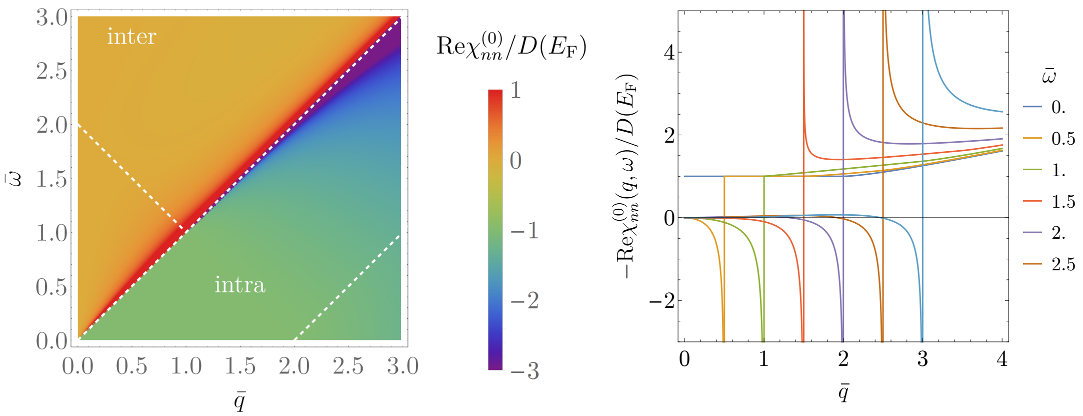

Figure 3.2: Real part of the non-interacting density-density response function $\chi_{nn}^{(0)}(q,\omega)$. In the left plot the function is shown in the (q,ω) plane where the intra- and inter-band continua are shown by dashed white lines. The right figure shows a cut of the function at different values of ω as indicated. The quantities are expressed in the dimensionless units defined in Eq. (3.34).

Here, the function $G_>(x)$ is defined as

$$G_>(x) = x\sqrt{x^2-1} - \mathrm{arcosh}(x) \ . \tag{3.56}$$

The real part of the response function is shown in the (q,ω) plane in Fig. 3.2. Also this function divergences near the $\bar{q} = \bar{\omega}$ line.

3.1.5 Finite temperature response function

In the previous sections, an analytical expression was derived for the density response function at zero Kelvin. As seen in Eq. (3.29), the temperature enters the response function through the Fermi Dirac distribution function. There is an elegant identity, proposed by Maldague [111], that relates the finite temperature response function to the zero temperature form. If the latter can be found analytically, the former is related by a simple integration. The relation comes from the integral identity [102]

$$\frac{1}{e^x+1} = \int_{-\infty}^{\infty} \frac{\Theta(y-x)}{4\cosh^2\left(\frac{y}{2}\right)} dy. \tag{3.57}$$

At $T = 0$ the Fermi Dirac distribution is given by Eq. (3.30), and, using the above expression, it can be written as

$$f_{\mathrm{D}}(\varepsilon,\mu,T) = \int_{-\infty}^{\infty} \frac{\Theta(y-\varepsilon_{\lambda\boldsymbol{k}})}{4k_{\mathrm{B}}T\cosh^2\left(\frac{y-\mu}{2k_{\mathrm{B}}T}\right)} dy \ . \tag{3.58}$$

Therefore, the distribution functions from the definition of the response function, Eq. (3.29) can be replaced by this integral identity. Because the response function is linear in the Fermi Dirac distribution functions, the order of integration can be reversed such that the finite temperature response function can be written as

$$\chi^{(0)}_{nn}\left(\boldsymbol{q},\omega;T\right)=\int_{-\infty}^{\infty}\frac{\chi^{(0)}_{nn}\left(\boldsymbol{q},\omega;0\right)\Big|_{E_{\mathrm{F}}\to y}}{4k_{\mathrm{B}}T\cosh^{2}\left(\frac{y-\mu}{2k_{\mathrm{B}}T}\right)}dy. \tag{3.59}$$

This relation shows that the finite temperature response function is a weighted average of the zero-temperature form over the chemical potential μ. In Fig. 3.3 the effect of finite temperature on the response function is shown. Notice that the divergence of the real and imaginary parts are not very much affected as shown in Figs. 3.3(a) and (c). This is because a finite temperature smears the function over a range of chemical potential values around the Fermi energy. However, on the line $v_{\mathrm{F}}q=\omega$, the response functions diverge no matter what is the value of the Fermi energy. Therefore, all contributions of the response function on this line still give a diverging contribution. Figs. 3.3(b) and (d) show the static limit of the response function, i.e. $\omega\to 0$ for a closed system. For small $\bar{q}$, the response function first drops and then increases again as a function of temperature. This is because of the renormalisation of the chemical potential $\mu(T)$ as discussed in Sec. 2.4.

3.1.6 Response function and the particle-hole excitation spectrum

The response function calculated in the previous section contains information of the chiral liquid in the absence of inter-particle interaction. More specifically it expresses how the density responds to an external potential with frequency ω and wave vector q. This function can be used to calculate the energy dissipated in the system due to the external potential [102]. If one considers a periodic perturbation that couples to the density, such that the total Hamiltonian becomes

$$\hat{H}_{F}\left(t\right)=\hat{H}+\hat{n}_{-\boldsymbol{q}}F_{\omega}e^{-i(\omega+i\eta)t}+\text{c.c.}\,, \tag{3.60}$$

where c.c. denotes the Hermitian conjugate of the previous term. The total power W delivered by the external field over the course of one period T is

$$W=\frac{1}{T}\int_{0}^{T}\frac{\partial}{\partial t}\left\langle\psi\left(t\right)\middle|\hat{H}_{F}\left(t\right)\middle|\psi\left(t\right)\right\rangle dt\,. \tag{3.61}$$

The integrand of this expression corresponds to the instantaneous power that is averaged by the integration. Using the Hellmann-Feynmann theorem [113] W can be calculated as

$$W=\frac{1}{T}\int_{0}^{T}-i\omega F_{\omega}e^{-i\omega t}\left\langle\hat{n}_{-\boldsymbol{q}}\right\rangle_{1}\left(t\right)dt+\text{c.c.}\,. \tag{3.62}$$

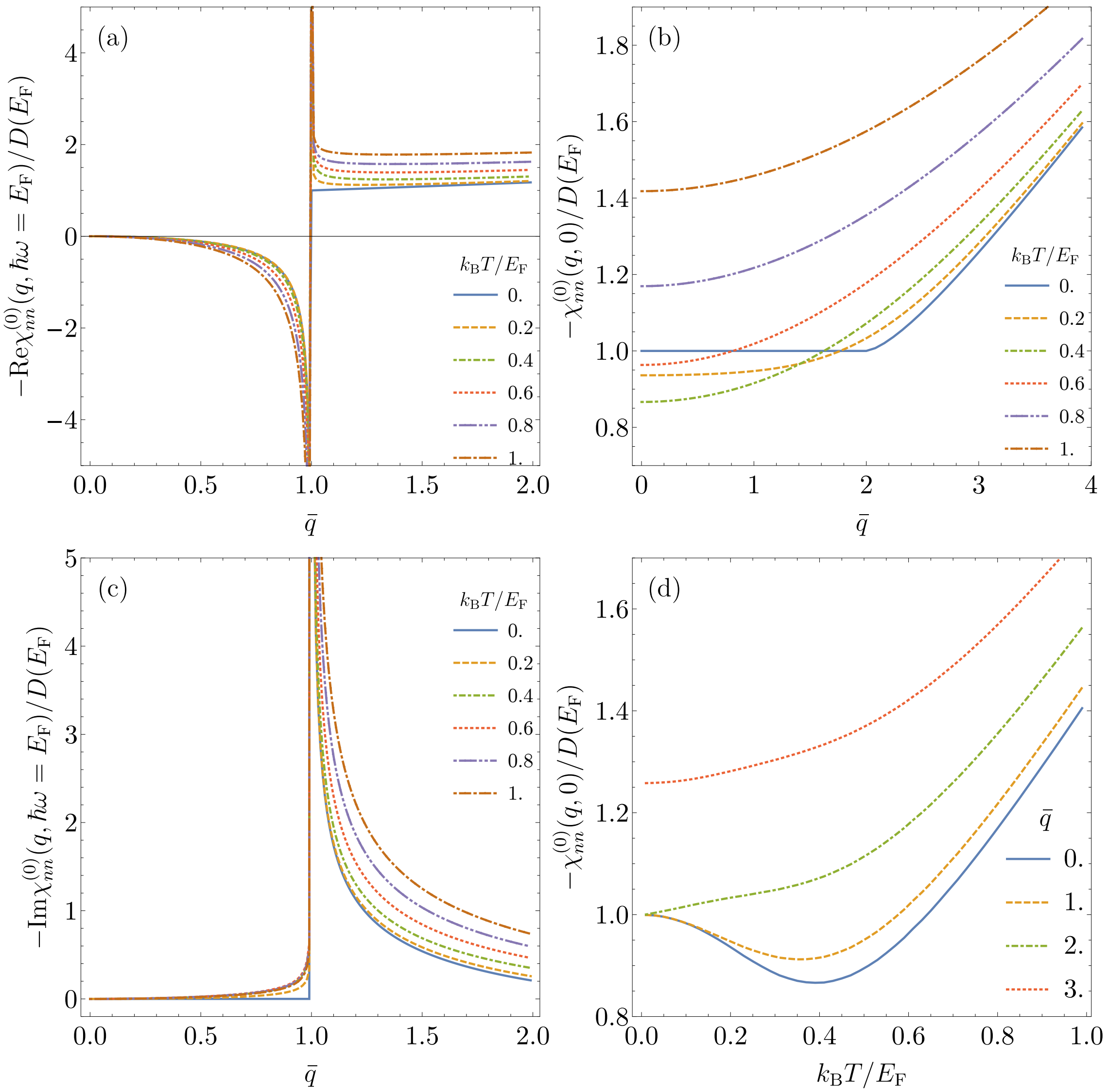

Figure 3.3: Density response function of graphene at different temperatures. Panels (a) and (c) show respectively the real and imaginary part for $\bar{\omega} = 1$ at different temperatures as indicated by the legend as a function of $\bar{q} = \hbar v_\mathrm{F} q/E_\mathrm{F}$. In these panels, the system is assumed to be in contact with the environment such that the chemical potential does not depend on the temperature. Notice that the divergence at $\bar{q} = \bar{\omega}$ is not tempered by the finite temperature. Panels (b) and (d) show the static response function as a function of $\bar{q}$ and temperature respectiveley. In these two panels, the system is considered to be isolated from the enivronment and, therefore, the chemical potential does adapt itself to temperature. This is the origin of the difference in behaviour between small and large temperature. Notice that the results are exactly the same as those obtained in Ref. [112], but using a different approach.

In Eq. (3.62) $\langle \hat{n}_{-\boldsymbol{q}} \rangle_1$ denotes the expectation value, up to linear order, of the density operator $\hat{n}_{-\boldsymbol{q}}$, that was defined in Eq. (3.13). According to LRT this quantity is determined by the density-density response function as

$$\langle \hat{n}_{\boldsymbol{q}} \rangle_1 (t) = \chi_{n_{\boldsymbol{q}} n_{-\boldsymbol{q}}} (\omega) \, F_\omega e^{-i\omega t} + \text{c.c.} \,. \tag{3.63}$$

Inserting this expression in Eq. (3.62), one finds that only terms that compensate the time dependent phase factor $\exp(-\omega t)$ survive. Therefore, the dissipated power is

$$\begin{aligned} W &= \frac{1}{T} \int_0^T -i\omega \, |F_\omega|^2 \, \chi^*_{n_{-\boldsymbol{q}} n_{\boldsymbol{q}}} (-\omega) \, dt + \text{c.c.} \,, \\ &= -2 \, |F_\omega|^2 \, \omega \text{Im} \chi_{n_{\boldsymbol{q}} n_{-\boldsymbol{q}}} (\omega) \ , \\ &= -2 \, |F_\omega|^2 \, \omega L^2 \text{Im} \chi_{nn} (\boldsymbol{q}, \omega) \ . \end{aligned} \tag{3.64}$$

In the last equation, the surface area of the sample, L^2 , shows up. This was introduced in the definition of $\chi_{nn} (\boldsymbol{q}, \omega)$ in Eq. (3.26). Eq. (3.64) shows that the power dissipated in the system is determined by the imaginary part of the response function. Therefore, if an external perturbation acts on the system with energy $\hbar\omega$ and wave vector $\boldsymbol{q}$, the amount of absorbed energy is determined by the imaginary part of the response function. Eq. (3.64) holds in general for every periodic perturbation that couples to the system. In this section the focus will be on a scalar perturbation that couples to the electron density.

In the absence of interactions, energy can be absorbed form an external perturbation by exciting single carriers in the Dirac cone. A non zero imaginary part of $\chi^{(0)}_{nn} (q, \omega)$ means that the electron liquid can absorb energy by single-particle excitations that can occur as an intra-band transition or as an inter-band transition as shown in Fig. 3.4. In graphene the band structure is linear and, therefore, the intra-band transitions are only possible outside the graphene *light-cone* which is defined as

$$\hbar\omega = \hbar v_{\text{F}} q \,. \tag{3.65}$$

On the other hand, inter-band transitions can occur solely inside the light-cone. Inspecting the imaginary part of the response function shown in Fig. 3.1 shows that the imaginary part is non-zero in two regions separated by the light-cone. In these regions, inter- and intra-band transitions, as shown in the right panel of Fig. 3.4, are possible. These regions in the (q, ω) plane are called the *particle-hole excitation spectra* (PHES).

From a simple geometrical analysis, it can be inferred that the intra-band PHES occupies the region between the light-cone Eq. (3.65) and the boundary

$$\hbar\omega = \hbar v_{\text{F}} \left(q - 2k_{\text{F}} \right) . \tag{3.66}$$

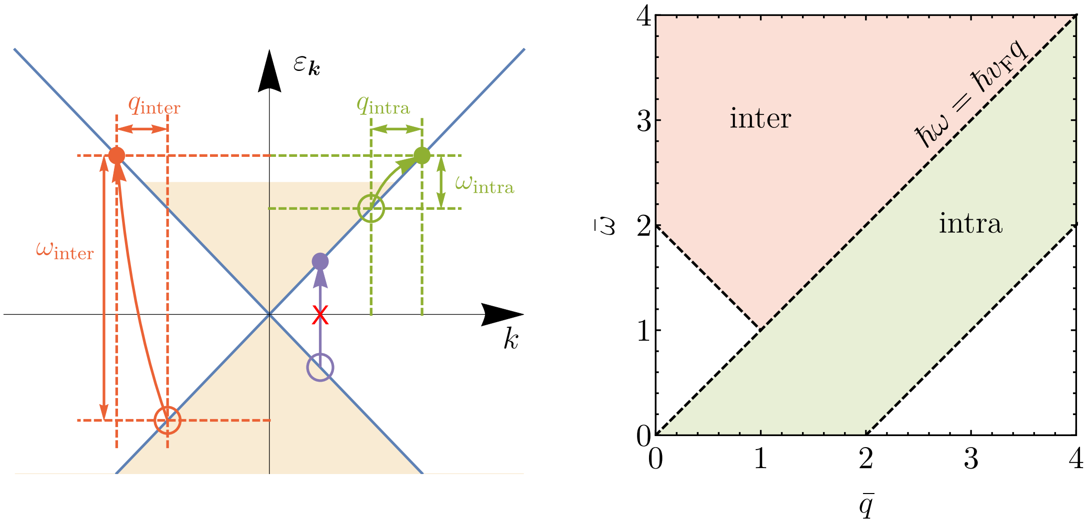

Figure 3.4: Left: Possible single-particle transitions in the Dirac cone. The shading displays the occupied states. The green arrow illustrates an intra-band transition, the orange arrow displays an inter-band transition with corresponding ω and q indicated. The purple arrow corresponds to a Pauli-blocked inter-band transition. Right: regions in the (q, ω) plane where the single-particle processes are possible. These regions are called the particle-hole excitation spectra.

This follows because intra-band transitions along the cone follow Eq. (3.65) while the intra-band transition with the largest possible wave vector follows Eq. (3.66).

The inter-band PHES occupies the region above the light-cone Eq. (3.65), but is also bound by the boundary

$$\hbar\omega = \hbar v_{\rm F}\left(2k_{\rm F} - q\right). \tag{3.67}$$

This is a consequence of *Pauli blocking* and is shown in the left panel of Fig. 3.4. For small wave vector q, the only possible inter-band transition occurs if the energy is large enough to be able to excite an electron from deep in the valence band to just above the Fermi level. For transitions that happen at $q = 0$ this condition yields that an inter-band transition is only possible if the energy is

$$\hbar\omega > 2E_{\rm F}. \tag{3.68}$$

Comparing the inter-band PHES with the imaginary part of the response function, one observes that in the region where Pauli blocking is active, the imaginary part indeed vanishes. Because single-particle processes are not present in the Pauli blocked region, it is an interesting region in the (q, ω) plane to observe collective phenomena as there will be no particle-hole excitations processes that could be responsible for damping.

3.1.7 Spectral weight distribution and sum rules

From the definition of the response function, Eq. (3.21), it follows that the following symmetry relations for the parity in ω hold:

$$\begin{aligned} \mathrm{Re}\chi_{nn}(\boldsymbol{q},\omega) &= \mathrm{Re}\chi_{nn}(\boldsymbol{q},-\omega)\ , && (3.69) \\ -\mathrm{Im}\chi_{nn}(\boldsymbol{q},\omega) &= -\mathrm{Im}\chi_{nn}(\boldsymbol{q},-\omega)\ . && (3.70) \end{aligned}$$

This allows one to write the real part as a series for large ω as

$$\mathrm{Re}\chi_{nn}(\boldsymbol{q},\omega) = -\sum_{j=0}^{\infty} \frac{\int_{-\infty}^{\infty} d\nu \nu^{2j+1} \mathrm{Im}\chi_{nn}(\boldsymbol{q},\nu)}{\pi\omega^{2j+2}}\ . \tag{3.71}$$

Here, the even parts of the expansion are zero because of the anti-symmetry of the imaginary part from Eq. (3.70). On the other hand, invoking the original definition of the response function from Eq. (3.14), it is possible to Taylor expand it around $\omega \to \infty$:

$$\chi_{AB}(\omega) = \frac{1}{\hbar}\sum_{j=0}^{\infty} \frac{i^j}{\omega^{j+1}} \left\langle [\hat{A}^{(j)}, \hat{B}] \right\rangle_0\ , \tag{3.72}$$

where $A^{(j)}$ is the j^{th} derivative with respect to the the time. This is given in the Heisenberg picture as [104]

$$A^{(j)} = \left(\frac{i}{\hbar}\right)^j \left[\hat{H}, \ldots [\hat{H}, \hat{A}] \ldots\right]\ . \tag{3.73}$$

Focussing on the $j = 1$ term, this leads for the density-density response function to the relations [102]:

$$-\frac{2}{\pi}\int_0^{\infty} d\omega\omega \mathrm{Im}\chi_{nn}(\boldsymbol{q},\omega) = \left\langle \left[\left[\hat{n}_{\boldsymbol{q}}, \hat{H}\right], \hat{n}_{-\boldsymbol{q}}\right] \right\rangle_0 . \tag{3.74}$$

This expression relates the first moment of the distribution $\mathrm{Im}\chi_{nn}$ in the ω range to a quantity that only depends on the density and is called the *f-sum rule* [102]. Using the expressions from before, this quantity can be calculated in the long wavelength limit, i.e. $q \to 0$ as [114]

$$\int_0^{\Lambda} d\omega\omega \mathrm{Im}\chi_{nn}^{(0)}(\boldsymbol{q},\omega) = -\frac{q^2 N_{\mathrm{f}} \Lambda}{16\hbar}\ . \tag{3.75}$$

In Eq. (3.75) a cut-off Λ was introduced. This cut-off is important because the occupation of the sea of valence electrons is in principle infinite. The fact that this result depends on a cut-off is peculiar since for crystals the f-sum rule should be cut-off independent [103].

However, as before, this is a consequence of the Dirac cone approximation. Indeed, since the result depends on the behaviour of the response function for large ω, it is no longer allowed to approximate the system by a Dirac cone, but the full energy spectrum, Eq. (2.15), should be used. Upon restoring the periodicity of the crystal, the f-sum divergence is removed and the sum is proportional to the total number of Fermions in the system. A similar cut-off also occurs in a three-dimensional (3D) relativistic problem where the sum corresponds to the number of Fermions contained in the vacuum, which is clearly a divergent quantity [115].

Even with the ultra-violet cut-off, it is useful to consider the f-sum rules since they only rely on the total number of particles of the system and, therefore, do not change when electron-electron interaction is switched on. This statement remains true also if the number of particles depends on the cut-off because in general the commutator of the interaction part and the density vanishes. Similarly it can be used to determine the spectral weight transfer when the system is being doped because in that case, the Hamiltonian needs to be extended with a term $\sim \mu\hat{N}$ where μ is the chemical potential and $\hat{N}$ the number operator. Also this term does not contribute to the commutator from Eq. (3.74).

In the undoped and non-interacting case, the imaginary part of the response function $\chi^{(0)}_{nn}(q,\omega)$ is given by Eq. (3.41) and one finds

$$\begin{aligned}\int_0^\Lambda d\omega\omega\mathrm{Im}\left[\chi^{\mathrm{vac}}_{nn}(q,\omega)\right] &= -\frac{q^2N_\mathrm{f}}{16\hbar}\int_0^\Lambda d\omega\omega\frac{\Theta(\omega-v_\mathrm{F}q)}{\sqrt{\omega^2-(v_\mathrm{F}q)^2}} \\ &\approx -\frac{q^2N_\mathrm{f}}{16\hbar}\int_{v_\mathrm{F}q}^\Lambda d\omega\left(1+\mathcal{O}\left[\left(\frac{v_\mathrm{F}q}{\omega}\right)^2\right]\right) \\ &= -\frac{q^2N_\mathrm{f}\Lambda}{16\hbar}+\mathcal{O}\left[q^3\right] \qquad (3.76)\end{aligned}$$

However, upon doping of the sample, the response function acquires an additional intra-band and inter-band part as defined in Eqs. (3.42) and (3.43) respectively. The intra-band part contributes as

$$\begin{aligned}\int_0^\Lambda d\omega\omega\mathrm{Im}\left[\chi^{+}_{E_\mathrm{F}}(q,\omega)\right] &= -\frac{N_\mathrm{f}E_\mathrm{F}}{2\pi(\hbar v_\mathrm{F})^2}\int_0^{v_\mathrm{F}q} d\omega\frac{\omega^2}{\sqrt{(v_\mathrm{F}q)^2-\omega^2}} \\ &= -\frac{q^2N_\mathrm{f}\Lambda_\mathrm{F}}{8\hbar}, \qquad (3.77)\end{aligned}$$

where $\Lambda_\mathrm{F} \equiv E_\mathrm{F}/\hbar$. In this case, the cut-off is chosen such that $\Lambda \ll \Lambda_\mathrm{F}$. In the first equation the upper boundary is replaced by the light cone because the inter-band part is explicitly considered. However, the total inter-band response function of the doped system also acquires an additional term. As seen before, this term leads to Pauli blocking of the vacuum response function for energies up to $2E_{\mathrm{F}}$. Therefore, the inter-band contribution of a doped system is zero up to $2E_{\mathrm{F}}$ and the sum-rule has the form

$$\int_{2E_{\mathrm{F}}}^{\Lambda} d\omega\omega \mathrm{Im}\left[\chi_{E_{\mathrm{F}}}^{-}\left(q,\omega\right)\right] = -\frac{q^2 N_{\mathrm{f}}\Lambda}{16\hbar} + \frac{q^2 N_{\mathrm{f}}\Lambda_{\mathrm{F}}}{8\hbar}. \tag{3.78}$$

This equation shows that the total weight is indeed conserved and that Pauli blocking redistributes the weight from the inter-band transitions to intra-band processes.

3.1.8 Current response in graphene

An incident electro-magnetic (EM) field can be written as an electric and magnetic field propagating perpendicular to each other and to the direction of motion of the wave. The electric field $\boldsymbol{E}\left(\boldsymbol{r},t\right)$ and magnetic field $\boldsymbol{B}\left(\boldsymbol{r},t\right)$ are related to each other via the scalar potential $\phi\left(\boldsymbol{r},t\right)$ and the vector potential $\boldsymbol{A}\left(\boldsymbol{r},t\right)$ as [116]

$$\begin{aligned} \boldsymbol{E}\left(\boldsymbol{r},t\right) &= -\boldsymbol{\nabla}\phi\left(\boldsymbol{r},t\right) - \frac{1}{c}\frac{\partial \boldsymbol{A}\left(\boldsymbol{r},t\right)}{\partial t}, & (3.79)\\ \boldsymbol{B}\left(\boldsymbol{r},t\right) &= \boldsymbol{\nabla}\times\boldsymbol{A}\left(\boldsymbol{r},t\right). & (3.80) \end{aligned}$$

Here, c denotes the speed of light. These relations are invariant under the gauge transformation[102]

$$\begin{aligned} \phi\left(\boldsymbol{r},t\right) &\to \phi\left(\boldsymbol{r},t\right) - \frac{1}{c}\frac{\partial \Lambda\left(\boldsymbol{r},t\right)}{\partial t}, & (3.81)\\ \boldsymbol{A}\left(\boldsymbol{r},t\right) &\to \boldsymbol{A}\left(\boldsymbol{r},t\right) + \boldsymbol{\nabla}\Lambda\left(\boldsymbol{r},t\right), & (3.82) \end{aligned}$$

where $\Lambda\left(\boldsymbol{r},t\right)$ is differentiable but an arbitrary function of $\boldsymbol{r}$ and t. This means that a scalar potential $V\left(\boldsymbol{r},t\right) = -e\phi\left(\boldsymbol{r},t\right)$ that couples to the density can be eliminated by a suitable gauge transformation given by

$$\Lambda\left(\boldsymbol{r},t\right) = -\frac{c}{e}\int_0^t dt' V\left(\boldsymbol{r},t'\right). \tag{3.83}$$

This on the other hand introduces a vector potential that has the form

$$\boldsymbol{A}\left(\boldsymbol{r},t\right) = -\frac{c}{e}\int_0^t dt' \boldsymbol{\nabla} V\left(\boldsymbol{r},t'\right). \tag{3.84}$$

Because of gauge invariance, the response of the system to a scalar potential $V\left(\boldsymbol{r},t\right)$ or a vector potential $\boldsymbol{A}\left(\boldsymbol{r},t\right)$ from Eq. (3.84) is the same and therefore the corresponding response functions should also be related. Notice that this only holds for a specific type of vector potentials, namely the ones that can be written as a gradient of a scalar function. These are called *longitudinal vector potentials* because their spacial Fourier transform is proportional to $\boldsymbol{q}$.

A vector potential perturbing the non-interacting electron liquid couples to the current-density $\boldsymbol{j}$. In the case of graphene however, the current-density operator $\widehat{\boldsymbol{j}}_{\boldsymbol{q}}$, which is defined as de derivative of the Hamiltonian with respect to $\boldsymbol{q}$, has the form [117]

$$\widehat{\boldsymbol{j}}_{\boldsymbol{q}} = \frac{\partial \hat{H}_0}{\partial \boldsymbol{q}} = v_{\mathrm{F}} \sum_{\alpha\beta\boldsymbol{k}} \mathcal{D}^{\sigma}_{\lambda\lambda'}\left(\boldsymbol{k}, \boldsymbol{k}+\boldsymbol{q}\right) \hat{c}^{\dagger}_{\lambda\boldsymbol{k}} \hat{c}_{\lambda'\boldsymbol{k}+\boldsymbol{q}}, \tag{3.85}$$

where the *current-density vertex* is given by

$$\mathcal{D}^{\sigma}_{\lambda\lambda'}\left(\boldsymbol{k}, \boldsymbol{k}'\right) = \left\langle \Psi_{\lambda\boldsymbol{k}} \left|\boldsymbol{\sigma}\right| \Psi_{\lambda'\boldsymbol{k}'} \right\rangle, \tag{3.86}$$

for $\boldsymbol{\sigma} = (\sigma_x, \sigma_y)$ a vector of Pauli matrices. This form of the current-density operator is enforced by the continuity equation [118]

$$i\hbar \frac{\partial \hat{n}_{\boldsymbol{q}}}{\partial t} = \left[\hat{n}_{\boldsymbol{q}}, \hat{H}_0\right] = \hbar \boldsymbol{q} \cdot \widehat{\boldsymbol{j}}_{\boldsymbol{q}}. \tag{3.87}$$

The peculiar current-density vertex from Eq. (3.86) allows to relate the current-current response function to the pseudospin-pseudospin response function as

$$\chi^{(0)}_{\boldsymbol{jj}}\left(\boldsymbol{q}, \omega\right) = v_{\mathrm{F}}^2 \chi^{(0)}_{\boldsymbol{\sigma\sigma}}\left(\boldsymbol{q}, \omega\right). \tag{3.88}$$

Because of the continuity equation (3.87), one can also relate the density-density response function to the pseudospin-pseudospin response function as [118]

$$\chi^{(0)}_{nn}\left(q, \omega\right) = \frac{v_{\mathrm{F}} q}{\omega^2} \left\langle \left[\hat{\sigma}_{\boldsymbol{q},x}, \hat{n}_{-\boldsymbol{q}}\right]\right\rangle_0 + \frac{v_{\mathrm{F}}^2 q^2}{\omega^2} \chi^{(0)}_{\sigma_x\sigma_x}\left(q\boldsymbol{e}_x, \omega\right). \tag{3.89}$$

Note that in Eq. (3.89) there appears an *anomalous commutator* as first term and that the density response is related to the longitudinal response pseudospin response, i.e. the response in the direction of the wave vector $\boldsymbol{q}$. Therefore in the pseudospin-pseudospin response function the wave vector is fixed along the x-axis[1].

The appearance of the anomalous commuator in Eq. (3.89) is a direct consequence of the fact that the graphene charge carriers are non-Galilean invariant. In a Galilean invariant system this commutator is zero and Eq. (3.89) reduces to the well-known relation between

---

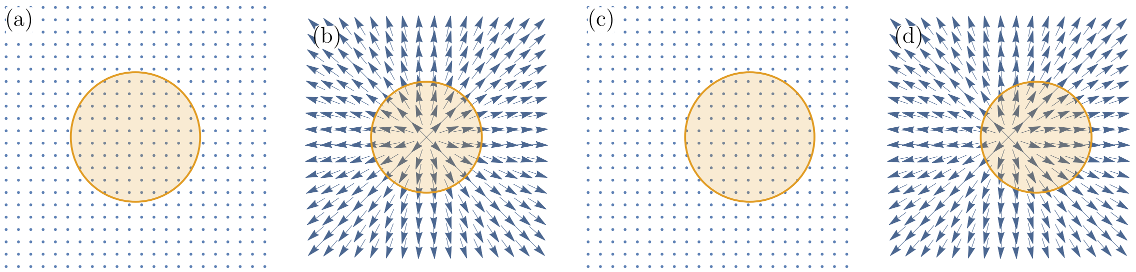

Figure 3.5: Galilean boost in a system with a pseudospin texture. (a) Displays the Fermi circle (in reciprocal space) in the absence of a pseudospin texture. Upon a boost of the Fermi circle to the right (Fig. (c)), the two situations are indistinguishable for a co-moving observer. Fig. (b) and (d) display the situation for when the carriers do have pseudospin. Now it is clear that the co-moving observer can distinguish between the two systems. The figure is inspired by Ref. [119].

the longitudinal current-current response function and the density-density response function. [102]

Because, as seen before, the charge carriers in graphene have a pseudospin degree-of-freedom that is oriented parallel to the direction of motion, a Galilean boost of the system will be visible by the relative orientation of the pseudospin of the charge carriers with respect to the center of momentum space as shown in Fig. 3.5. In the boosted system, the charge carriers behave as if they are subject to a *pseudomagnetic field* that tilts the pseudospin in the direction along the boost [119]. The appearance of the pseudomagnetic field clearly breaks Galilean invariance. If the charge carriers are only described by their momentum, then a Galilean boost will keep the system invariant[2].

In order to calculate the anomalous commutator, one needs to take care of the infinite sea of electrons occupying the valence band, therefore the commutator will depend on an ultra-violet cut off vector k_{max}. Calculating within the non-interacting limit it becomes [114]

$$\langle[\hat{\sigma}_{\boldsymbol{q},x},\hat{n}_{-\boldsymbol{q}}]\rangle_0 = \sum_{|\boldsymbol{k}|<k_{\text{max}}} \cos\left(\varphi_{\boldsymbol{k}}\right) n_{-,\boldsymbol{k}} - \cos\left(\varphi_{\boldsymbol{k}-\boldsymbol{q}}\right) n_{-,\boldsymbol{k}-\boldsymbol{q}}. \tag{3.90}$$

Here $n_{-,\boldsymbol{k}}$ are the occupation numbers of the non-interacting valence band as defined in Eq. (3.27). Eq. (3.90) makes clear that the commutator depends on the difference between

---

[1] Notice that Eq. (3.89) is only valid in the non-interacting limit. This is why the average $\langle\ldots\rangle_0$ has to be taken with respect to the non-interacting ground state. If interactions are taken into account, the continuity equation (3.87) is no longer satisfied and additional terms need to be taken into account [119].

[2] Notice that in a crystal Galilean invariance is always broken because of the absence of translational invariance. However, this is usually overcome in the continuum approximation that reduces the background formed by the crystal atoms to an effective band-mass m_b in the $\boldsymbol{k}.\boldsymbol{p}$ Hamiltonian.

the states in a circle around the origin and those around the origin shifted by the vector $\boldsymbol{q}$. This exemplifies how the lack of Galilean invariance, induces a non-zero commutator. Furthermore, only the states deep in the Dirac sea contribute to the sum. In the long wavelength limit the commutator is calculated as[114]

$$\langle [\hat{\sigma}_{\boldsymbol{q},x}, \hat{n}_{-\boldsymbol{q}}] \rangle_0 = \frac{q N_{\mathrm{f}} \varepsilon_{\mathrm{max}}}{4\pi\hbar v_{\mathrm{F}}}, \tag{3.91}$$

where $\varepsilon_{\mathrm{max}} = \hbar v_{\mathrm{F}} k_{\mathrm{max}}$.

Thanks to the relation between the current response function and the pseudospin response function Eq. (3.88), the longitudinal current response function is related to the density response through Eq. (3.89). More specifically, because the anomalous commutator discussed in the previous paragraph is real, the imaginary part of the two response functions can be related with each other as

$$\mathrm{Im}\chi^{(0)}_{nn}(q,\omega) = \frac{q^2}{\omega^2}\mathrm{Im}\chi^{J}_{L}(q,\omega), \tag{3.92}$$

where $\chi^{J}_{L}(q,\omega) \equiv \chi^{(0)}_{j_x j_x}(q\boldsymbol{e}_x,\omega)$ is the longitudinal part of the response function which describes the response of the system parallel to the wave vector $\boldsymbol{q}$.

In general, the current-current response function for homogeneous and isotropic systems can always be decomposed in components parallel and perpendicular to the wave vector $\boldsymbol{q}$ as [102]

$$\chi^{J}_{j_\alpha j_\beta}(\boldsymbol{q},\omega) = \chi^{J}_{L}(q,\omega)\frac{q_\alpha q_\beta}{q^2} + \chi^{J}_{T}(q,\omega)\left(\delta_{\alpha\beta} - \frac{q_\alpha q_\beta}{q^2}\right). \tag{3.93}$$

Here the *transverse response function* is defined as $\chi^{J}_{T}(q,\omega) \equiv \chi_{j_x j_x}(q\boldsymbol{e}_y,\omega)$. This expression makes it explicit that the response function depends on the direction of the wave vector $\boldsymbol{q}$ according to only two components. As a consequence, the longitudinal (transverse) component of the current induced by the vector potential depends only on the longitudinal (transverse) component of $\boldsymbol{A}$, i.e.

$$\boldsymbol{j}_{L(T)}(q,\omega) = \frac{e}{c}\chi^{J}_{L(T)}(q,\omega)\boldsymbol{A}_{L(T)}(q,\omega), \tag{3.94}$$

where $\boldsymbol{U}_{L(T)}$ denotes the longitudinal (transverse) component of vector $\boldsymbol{U}$.

3.1.9 Graphene conductivity and absorption

Having found an expression for the current-current response function allows to define the graphene conductivity. Indeed, the electrical conductivity tensor $\sigma_{\alpha\beta}(\omega)$ is defined through

Ohm's law as [116]

$$-ej_{\alpha}\left(0,\omega\right)=\sum_{\beta}\sigma_{\alpha\beta}\left(\omega\right)E_{\beta}\left(\omega\right). \tag{3.95}$$

Remember that the addition of $-e$ is because the current density is defined as a particle current density. Eq. (3.95) expresses the response of an electron liquid to the application of an electric field $\boldsymbol{E}\left(\omega\right)$. Because of Eq. (3.79) this is related to the vector potential as $\boldsymbol{A}\left(\omega\right)=-\frac{ic}{\omega}\boldsymbol{E}\left(\omega\right)$. The current-current response function also determines a relation between the induced current and a vector potential for $q=0$ as

$$-ej_{\alpha}\left(0,\omega\right)=\frac{e}{c}\sum_{\beta}\chi^{J}_{\alpha\beta}\left(0,\omega\right)A_{\beta}\left(\omega\right). \tag{3.96}$$

Comparing Eq. (3.95) with Eq. (3.96) yields an expression for the conductivity tensor [102]

$$\sigma_{\alpha\beta}\left(\omega\right)=\frac{ie^{2}}{\omega}\chi^{J}_{\alpha\beta}\left(0,\omega\right). \tag{3.97}$$

If an external electric field $\boldsymbol{E}_{\text{ext}}\left(\boldsymbol{r},\omega\right)$ is incident on the graphene plane, then one can find the total absorbed power as the power dissipated in the system by the induced current density $\boldsymbol{j}_{\text{ind}}\left(\boldsymbol{r},\omega\right)$. The average dissipated power over one cycle of the oscillation is given by

$$P_{\text{abs}}\left(\omega\right)=\int d\boldsymbol{r}\frac{1}{2}\text{Re}\left[\boldsymbol{E}^{*}_{\text{ext}}\left(\boldsymbol{r},\omega\right)\cdot\left(-e\right)\boldsymbol{j}_{\text{ind}}\left(\boldsymbol{r},\omega\right)\right], \tag{3.98}$$

The induced current density $\boldsymbol{j}_{\text{ind}}\left(\omega\right)$ is related to the external field by the conductivity as stated in Eq. (3.95). Therefore, the absorbed power becomes

$$P_{\text{abs}}\left(\omega\right)=\frac{1}{2}\text{Re}\left[\sigma_{L}\left(\omega\right)\right]\int d\boldsymbol{r}\left|\boldsymbol{E}_{\text{ext}}\left(\boldsymbol{r},\omega\right)\right|^{2}. \tag{3.99}$$

Because the induced current density is projected on the external electric field, only the longitudinal part of the conductivity, $\sigma_{L}\left(\omega\right)$, remains. On the other hand, the total incident power is [116]

$$P_{\text{in}}\left(\omega\right)=\frac{c}{8\pi}\int d\boldsymbol{r}\left|\boldsymbol{E}_{\text{ext}}\left(\boldsymbol{r},\omega\right)\right|^{2}, \tag{3.100}$$

which shows that the absorption is given by

$$A\left(\omega\right)=\frac{P_{\text{abs}}\left(\omega\right)}{P_{\text{in}}\left(\omega\right)}=\frac{4\pi}{c}\text{Re}\left[\sigma_{L}\left(\omega\right)\right]. \tag{3.101}$$

Inserting subsequently the relation between the current response function and the conductivity, Eq. (3.97), and between the density response and the longitudinal part of the current response function, Eq. (3.92) yields the final expression for the absorption

$$A\left(\omega\right)=-\frac{4\pi e^{2}}{c}\lim_{q\to 0}\frac{\omega\mathrm{Im}\chi_{nn}\left(q,\omega\right)}{q^{2}}\;. \tag{3.102}$$

Note that because, as seen before, the imaginary part of the density-density response function is negative, the minus sign in front of the formula will be compensated for and the absorption is positive.

Eq. (3.102) provides a new important use for the response function: the $q\to 0$ limit of its imaginary part determines the optical absorption of the electron liquid. Now one can investigate this limit for the analytical solutions presented in Sec. 3.1.4. Because $\hbar v_{\mathrm{F}}q<\hbar\omega$, only the inter-band processes are non zero

$$\mathrm{Im}\chi_{nn}^{(0)}\left(q,\omega\right)\to-\frac{D\left(E_{\mathrm{F}}\right)}{8}\frac{\left(\hbar v_{\mathrm{F}}q\right)^{2}}{E_{\mathrm{F}}\sqrt{\left(\hbar\omega\right)^{2}-\left(\hbar v_{\mathrm{F}}q\right)^{2}}}\Theta\left(\hbar\omega-2E_{\mathrm{F}}\right)\pi, \tag{3.103}$$

where the dimensions have been restored for clarity. Using this expression, the real part of the longitudinal conductivity can be calculated as

$$\mathrm{Re}\sigma_{xx}(\omega)=N_{\mathrm{f}}\sigma_{\mathrm{uni}}\Theta(\hbar\omega-E_{\mathrm{F}}). \tag{3.104}$$

In this expression the universal optical conductivity is introduced

$$\sigma_{\mathrm{uni}}=\frac{e^{2}}{4\hbar}\;. \tag{3.105}$$

The graphene optical conductivity is therefore equal to σ_{uni} times the number of fermion flavours in the system. Inserting it into the expression for the absorption yields

$$A\left(\omega\right)=\pi\alpha_{\mathrm{QED}}\frac{N_{\mathrm{f}}}{4}\Theta\left(\hbar\omega-2E_{\mathrm{F}}\right). \tag{3.106}$$

In Eq. (3.106), $\alpha_{\mathrm{QED}}=e^{2}/\left(\hbar c\right)\approx 1/137$ is the quantum electrodynamics (QED) fine-structure constant [120]. Because the number of fermions in the system, $N_{\mathrm{f}}=4$, the absorption is maximum $\pi\alpha_{\mathrm{QED}}=2.3\%$.

This result is very remarkable. To begin with, notice that apart from the Θ-function, the absorption is independent from any material parameter, just as the optical conductivity. The absorption reaches a universal value of $\pi\alpha_{\mathrm{QED}}$ that only depends on fundamental constants. Furthermore, the Θ-function is zero if $\hbar\omega<2E_{\mathrm{F}}$. This is a consequence of

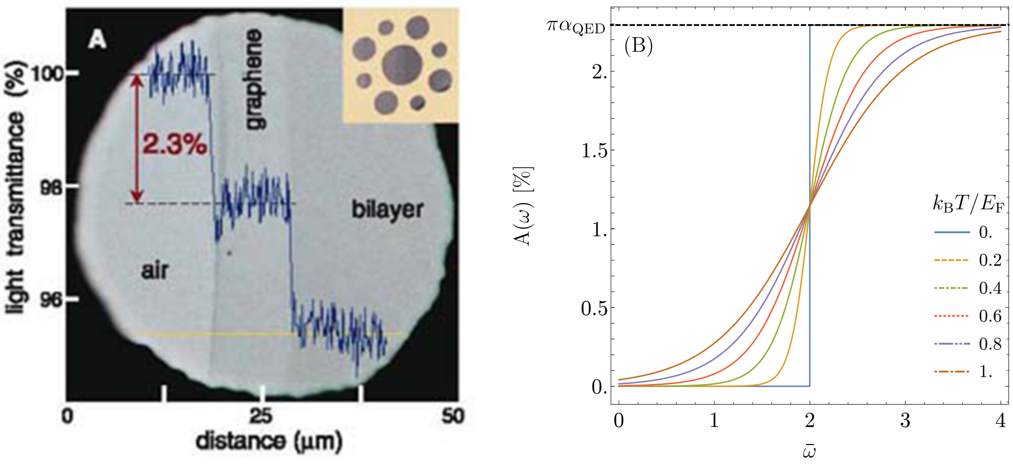

Figure 3.6: (a) Picture of an optical microscope that identifies a single layer and a bilayer of graphene by its light transmittance. Figure taken from [39]. (b) Light absorption of graphene as a function of the incident photon energy for different values of the temperature.

Pauli blocking since it is necessary for the incident photons to have an energy that is large enough to bridge the gap set by the Fermi level. Finally the value of 2.3% absorption is also remarkably large bearing in mind that this is the absorption by only a single layer of atoms. As a comparison, note that a GaAs heterostructure has an absorption that is about 50 times smaller for the same thickness [39, 121, 122]. The peculiar absorption properties of graphene were noticed early on and were used to identify the number of layers of a graphite sample by optical microscopy [39, 121] as shown in Fig. 3.6.

Finally, one can also find the finite temperature absorption by considering the finite temperature response function as defined in Eq. 3.59 :

$$\begin{aligned} A\left(\omega, T\right) &= \pi\alpha_{\mathrm{QED}}\frac{N_{\mathrm{f}}}{4}\int_{-\infty}^{\infty}\frac{\Theta\left(\hbar\omega-2y\right)}{4k_{\mathrm{B}}T\cosh^{2}\left(\frac{y-\mu(T)}{2k_{\mathrm{B}}T}\right)}dy \\ &= \pi\alpha_{\mathrm{QED}}\frac{N_{\mathrm{f}}}{8}\left(1-\tanh\left(\frac{2\mu\left(T\right)-\hbar\omega}{k_{\mathrm{B}}T}\right)\right) \end{aligned} \tag{3.107}$$

In Fig. 3.6(b) the finite temperature absorption is shown for different temperatures and different graphene doping.

3.1.10 Graphene fine structure constant

In the previous section, it was shown that the absorption of graphene is determined solely by fundamental quantities, more specifically the QED fine structure constant:

$$\alpha_{\text{QED}} = \frac{e^2}{\hbar c} \approx \frac{1}{137}. \tag{3.108}$$

This constant characterises the strength of the electromagnetic interaction between elementary charge particles in vacuum [120]. For charge carriers in graphene however, one can define an analogous quantity that characterises the strength of the inter-particle interaction. This quantity can be inferred by considering the continuum Hamiltonian for the Dirac 2D electron gas:

$$\hat{H} = v_{\text{F}} \sum_i \boldsymbol{\sigma} \cdot \hat{\boldsymbol{p}}_i + \frac{1}{2} \sum_{i \neq j} \frac{e^2}{\epsilon \left| \hat{\boldsymbol{r}}_i - \hat{\boldsymbol{r}}_j \right|}. \tag{3.109}$$

Here the first part measures the total kinetic energy of all the particles in the electron gas while the second term measures the Coulomb interaction energy of the system. In Eq. (3.109) , $-e$ is the electron's charge and ϵ is the environmental dielectric constant that screens the inter-particle interaction. The importance of the electron-electron interactions is determined by the ratio of the contribution of the second term with respect to the first term of Eq. (3.109). For a doped graphene sheet, the typical distance between the electrons is determined by the inverse Fermi wave vector k_{F}^{-1}. Therefore, the energetic contribution of the interaction term is $E_{\text{Coulomb}} = e^2 k_{\text{F}}/\epsilon$. Furthermore, the first term contributes as the kinetic energy of the particles, i.e. $E_{\text{kin}} = \hbar v_{\text{F}} k_{\text{F}}$. Therefore, the ratio of the two is

$$\alpha_{\text{ee}} \equiv \frac{E_{\text{Coulomb}}}{E_{\text{Kin}}} = \frac{e^2}{\epsilon \hbar v_{\text{F}}} \approx \frac{2.2}{\epsilon}. \tag{3.110}$$

Eq. (3.110) shows that the importance of the Coulomb interaction is determined by the dimensionless parameter α_{ee}. Notice that α_{ee} has the same structure as the QED fine structure constant α_{QED}, but where the speed of light c is replaced by the Fermi velocity $v_{\text{F}} \simeq c/300$ and where the screening due to the dielectric environment of the graphene flake is accounted for through ϵ. Because of the similarity, α_{ee} is commonly known as the *graphene fine structure constant* [50]. When discussing electron-electron interactions in graphene, this parameter can be used to "turn on" and "turn off" interactions and its strength quantifies the importance of interactions.

3.2 Plasmons in graphene

Plasmons are collective density oscillations that arise due to the electron-electron interaction [50]. As explained in the introduction, they exist in many metals and semiconductors. Here, however, the focus will be on plasmons in graphene and other two-dimensional materials. Plasmons can be described using the LRT framework set up in the previous section. However, one needs to take one step further and consider interaction between the electrons. This will be done on the level of the *random phase approximation* (RPA).

From a classical point of view, one can think of plasmons as the response of an interacting electron liquid to an external electric field that causes a disturbance in the density distribution. Suppose that an electric field impinges on a graphene sample, then the electron liquid will redistribute itself in order to screen the electric field. This can be written as a time and space dependent density profile

$$n\left(\boldsymbol{r},t\right)=n_0+n_1\left(\boldsymbol{r},t\right), \tag{3.111}$$

where n_0 is the equilibrium electron concentration and $n_1\left(\boldsymbol{r},t\right)$ the density disturbance. In trying to screen the electric field, the electron liquid will, however, overshoot and there will be a finite restoring force acting on the electron liquid that aims at reinstating the equilibrium distribution. The subsequent restoring of the electric field induced by the density redistribution corresponds to a density oscillation, a plasma wave. If the wave is quantised, it is called a *plasmon*.

In the long-wavelength limit, i.e. $q \ll k_{\mathrm{F}}$, the plasmon can be found on the grounds of hydrodynamics. According to hydrodynamic theory, the electron liquid is described by two variables, namely the density disturbance $n_1\left(\boldsymbol{r},t\right)$ and the associated induced current density $\boldsymbol{j}_1\left(\boldsymbol{r},t\right)$. If $\left|n_1/n_0\right| \ll 1$, these relations can be linearised. The linearised quantities are related to each other through the continuity equation

$$\frac{\partial}{\partial t}\left[n_1\left(\boldsymbol{r},t\right)\right]+\boldsymbol{\nabla}\cdot\boldsymbol{j}_1\left(\boldsymbol{r},t\right)=0, \tag{3.112}$$

and the Euler equation of motion

$$\frac{\partial}{\partial t}\left[\boldsymbol{j}_1\left(\boldsymbol{r},t\right)\right]=-\frac{\mathcal{D}}{\pi e^2}\boldsymbol{\nabla}\left[\int d\boldsymbol{r}'\frac{e^2}{\epsilon\left|\boldsymbol{r}-\boldsymbol{r}'\right|}n_1\left(\boldsymbol{r}',t\right)\right]. \tag{3.113}$$

In Eq. (3.113), the Drude weight $\mathcal{D}$ determines the relation between the induced current density and the restoring force, ϵ describes the dielectric response of the environment, and $-e$ is the electron charge. The term in square brackets in Eq. (3.113) is the total potential energy at position $\boldsymbol{r}$ due to the interaction with electrons distributed according to the density distribution $n_1(\boldsymbol{r}', t)$. In order to solve the set of coupled differential equations, one can easily write them in their Fourier transformed form:

$$\begin{aligned} \omega n_1(\boldsymbol{q},\omega) &= \boldsymbol{q}\cdot\boldsymbol{j}_1(\boldsymbol{q},\omega), & (3.114)\\ \omega\boldsymbol{j}_1(\boldsymbol{q},\omega) &= \frac{\mathcal{D}}{\pi e^2}\boldsymbol{q}v_{\boldsymbol{q}}n_1(\boldsymbol{q},\omega). & (3.115) \end{aligned}$$

Here, $v_{\boldsymbol{q}} = 2\pi e^2/(\epsilon q)$ is the 2D Fourier transform of the bare Coulomb interaction that is screened by the environmental dielectric constant ϵ [102]. These two equations finally can be combined into

$$\left(\omega^2 - \frac{\mathcal{D}}{\pi e^2}v_{\boldsymbol{q}}q^2\right)n_1(\boldsymbol{q},\omega) = 0. \tag{3.116}$$

Eq. (3.116) shows that it is possible to excite a density wave with dispersion

$$\omega_{\text{pl}}(q) = \sqrt{\frac{2\mathcal{D}}{\epsilon}q}. \tag{3.117}$$

This density wave represents the sought-after plasmon. The plasmon appearing in graphene is often called a *Dirac plasmon* [50], referring to the nature of the electrons in the system. Notice that in contrast to 3D systems, the graphene plasmon has an energy dispersion $\omega_{\text{pl}}(q) \propto \sqrt{q}$, this is a property directly related to the 2D nature of the electron system [102, 123]. As a consequence, the long-wavelength limit also implies small plasmon frequency and for $q \to 0$ the plasmon eventually vanishes.

3.2.1 The random phase approximation

In order to find plasmons in a quantum mechanical framework, one needs to include electron-electron interactions. If one calculates the density-density response function including interactions, plasmons will appear as its poles. A simple framework to include electron-electron interactions is called the random phase approximation (RPA) [102] that was originally introduced by Gell-Mann and Brückner [124] and Bohm and Pines [10] in two seemingly different ways.

If the interacting electron liquid is perturbed by an external potential $V_{\text{ext}}(\boldsymbol{r},\omega)$, then, due to the electron redistribution, this potential is screened as

$$V_{\text{sc}}(\boldsymbol{r},\omega) = V_{\text{ext}}(\boldsymbol{r},\omega) + V_{\text{ind}}(\boldsymbol{r},\omega), \tag{3.118}$$

where

$$V_{\text{ind}}(\boldsymbol{r},\omega) = \int d\boldsymbol{r}'\frac{e^2}{\epsilon|\boldsymbol{r}-\boldsymbol{r}'|}n_1(\boldsymbol{r}',\omega). \tag{3.119}$$

Note that the induced potential $V_{\text{ind}}\left(\boldsymbol{r},t\right)$ is exactly the potential that appeared in the square brackets of Eq. (3.113) that determined the restoring force in the classical picture. The RPA states that the electron liquid responds to the screened potential $V_{\text{sc}}\left(\boldsymbol{r},\omega\right)$ as if it was a non-interacting liquid, i.e.

$$n_1\left(\boldsymbol{r},\omega\right)=\int d\boldsymbol{r}'\chi_{nn}^{(0)}\left(\boldsymbol{r},\boldsymbol{r}',\omega\right)V_{\text{sc}}\left(\boldsymbol{r}',\omega\right). \tag{3.120}$$

On the other hand, the density perturbation that created the induced potential in the first place responds to the external potential as $V_{\text{ext}}\left(\boldsymbol{r},\omega\right)$

$$n_1\left(\boldsymbol{r},\omega\right)=\int d\boldsymbol{r}'\chi_{nn}^{\text{RPA}}\left(\boldsymbol{r},\boldsymbol{r}',\omega\right)V_{\text{ext}}\left(\boldsymbol{r}',\omega\right). \tag{3.121}$$

Upon spatial Fourier transforming these two equations, one can relate the response functions, in the homogeneous, case as

$$\chi_{nn}^{(0)}\left(q,\omega\right)\left[1+v_{\boldsymbol{q}}\chi_{nn}^{\text{RPA}}\left(\boldsymbol{q},\omega\right)\right]=\chi_{nn}^{\text{RPA}}\left(\boldsymbol{q},\omega\right). \tag{3.122}$$

Therefore, the *RPA density-density response function* can be calculated as

$$\chi_{nn}^{\text{RPA}}\left(\boldsymbol{q},\omega\right)=\frac{\chi_{nn}^{(0)}\left(q,\omega\right)}{1-v_{\boldsymbol{q}}\chi_{nn}^{(0)}\left(q,\omega\right)}. \tag{3.123}$$

Notice that this response function can be calculated once the non-interacting response function $\chi_{nn}^{(0)}\left(q,\omega\right)$ is known.

The density response function in the RPA shares the analytical structure with the non-interacting response function with the addition that the denominator in Eq. (3.123) can also contribute to poles of the response function. These poles are identified as the collective modes of the system [102] and are defined as the zeroes of the so-called RPA dielectric function $\varepsilon^{\text{RPA}}\left(q,\omega\right)$:

$$\varepsilon^{\text{RPA}}\left(q,\omega\right)=1-v_{\boldsymbol{q}}\chi_{nn}^{(0)}\left(q,\omega\right). \tag{3.124}$$

In general, the collective mode will appear as a pole of the density response function at the complex frequency $\omega=\text{Re}\,\omega+i\text{Im}\,\omega$ with $\text{Im}\,\omega<0$. They signal a collective mode with energy $\hbar\text{Re}\,\omega$ that decays in time with the decay rate Im ω. Intuitively, this description is justified since a pole in the response function signals an infinitely strong response at a finite external field perturbing the system. The poles of the RPA density-density response function are the (RPA) plasmons [102].

3.2.2 Electron energy loss and the dielectric function

Previously, the imaginary part of the response function was shown to determine the amount of energy absorbed by a graphene flake when an electro-magnetic wave is incident on the sample. Also the imaginary part of the dielectric function determines the response of the system to an external field, but now the one created by an incident electron. This is the central idea of electron energy-loss spectroscopy (EELS). In these experiments, one launches a particle with charge e and velocity $\boldsymbol{v}$ on the crystal. Consequently, the electric displacement field is given as [80]

$$\boldsymbol{D}\left(\boldsymbol{r},t\right) = -\boldsymbol{\nabla}\left[\frac{e}{|\boldsymbol{r}-\boldsymbol{v}t|}\right]. \tag{3.125}$$

If the system is isotropic, such that the dielectric function is a scalar rather than a tensor, then the electric field is related to the displacement field as

$$\boldsymbol{D}\left(\boldsymbol{q},\omega\right) = \varepsilon\left(\boldsymbol{q},\omega\right)\boldsymbol{E}\left(\boldsymbol{q},\omega\right). \tag{3.126}$$

Here the equation is readily Fourier transformed in time and space. The total power dissipated in the system due to the electron associated with this Fourier component then is given by [116]

$$\begin{aligned} P\left(\boldsymbol{q},\omega\right) &= \frac{1}{4\pi}\boldsymbol{E}\left(\boldsymbol{q},\omega\right)\cdot\frac{\partial\boldsymbol{D}\left(\boldsymbol{q},\omega\right)}{\partial t} \\ &= -\frac{1}{4\pi T}\left(D\left(\boldsymbol{q},\omega\right)\right)^2 \\ &\quad\times\int_0^T dt\left(\text{Re}\left[\varepsilon^{-1}\left(\boldsymbol{q},\omega\right)\right]\cos\omega t+\text{Im}\left[\varepsilon^{-1}\left(\boldsymbol{q},\omega\right)\right]\sin\omega t\right)\omega\sin\omega t \\ &= -\frac{1}{8\pi}\left(D\left(\boldsymbol{q},\omega\right)\right)^2\omega\text{Im}\left[\varepsilon^{-1}\left(\boldsymbol{q},\omega\right)\right] \\ &= \frac{1}{8\pi}\left(D\left(\boldsymbol{q},\omega\right)\right)^2\omega L\left(\boldsymbol{q},\omega\right), \end{aligned} \tag{3.127}$$

in the last line the so-called *loss function* $L\left(\boldsymbol{q},\omega\right)$ is defined. This function measures the amount of energy dissipated in the system at a given frequency ω and wave vector q due to a fast electron interacting with the electron liquid in the material. Therefore, the loss function can be directly measured in experiments.

EELS was the one of the first techniques to be applied to graphene for the investigation of the dielectric function. The use of this technique revealed Dirac plasmons in free-standing graphene [48] and graphene on SiO_2 [49]. It also revealed that a SiC substrate couples to the graphene plasmons and hybridises them with the SiC surface optical phonons [125]. The following section will be devoted to the study of Dirac plasmons in the RPA.

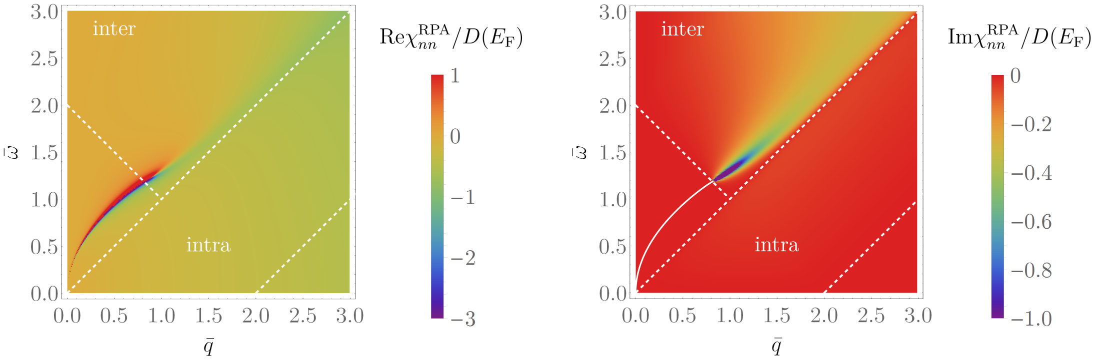

Figure 3.7: RPA density-density response function in the (q, ω) plane. The left panel shows the real part, the right panel the imaginary part. The inter- and intra-band PHES are indicated by white dashed lines. The plasmon dispersion is indicated in the plot of the imaginary part as a solid white curve. Along this line, the imaginary part is a delta function. The dielectric constant in this plot is $\epsilon = (1 + \epsilon_{\mathrm{SiO}_2})/2 = 2.45$ which corresponds to graphene on a SiO_2 substrate.

3.2.3 Dirac plasmons in the RPA

In Fig. 3.7 the real and imaginary part of the RPA density-density response function are shown in the (q, ω) plane. Compared with the non-interacting response function shown in Figs. 3.1 and 3.2, the real part now has a divergent feature for small ω and $v_{\mathrm{F}}q < \omega$. In this region the imaginary parts of both the non-interacting and RPA response functions are zero. Therefore, as a pole of the response function, this feature describes a collective mode of the system.

The dispersion $\omega_{\mathrm{pl}}(q)$ of this collective mode can be obtained by finding the roots of the RPA dielectric function from Eq. (3.124). In Fig. 3.7 the dispersion is shown in the (q, ω) plane as a numerical solution in the panel of the dielectric function. In the following sections it will be demonstrated how the dispersion can be inferred analytically in the limit $\hbar v_{\mathrm{F}} q < \hbar\omega \ll E_{\mathrm{F}}$ up to lowest order to make the connection with the plasmon introduced on hydrodynamic grounds. Next will be a discussion about the leading order correction due to inter-band processes. In the light of this discussion, a misconception in the literature will be pointed out. Finally the total, numerical, solution of the dispersion will be discussed and the lifetime and strength of the plasmon will be derived.

Analytical approximation: leading order

Using the analytical result derived in Sec. 3.1.4 in the limit $\hbar v_{\mathrm{F}} q < \hbar\omega \ll E_{\mathrm{F}}$, the dispersion $\omega_{\mathrm{pl}}(q)$ of the collective plasmon can be found analytically. First notice that the density-density response function has the same dimension as the density of states Eq. (2.30). Therefore, one can rewrite the product as

$$\begin{aligned} v_{\boldsymbol{q}} D\left(E_{\mathrm{F}}\right) &= \frac{2\pi e^2}{q\epsilon}\frac{N_{\mathrm{f}} E_{\mathrm{F}}}{2\pi\left(\hbar v_{\mathrm{F}}\right)^2} \\ &= \frac{\alpha_{\mathrm{ee}} N_{\mathrm{f}}}{\bar{q}}. \end{aligned} \tag{3.128}$$

Here the graphene fine structure constant α_{ee} from Eq. (3.110) has been identified. In the region of interest, the analytical solution of the response function reduces to

$$\chi_{nn}^{(0)}\left(q,\omega\right) = D\left(E_{\mathrm{F}}\right)\left[-1+\frac{1}{8}\frac{\bar{q}^2}{\sqrt{\bar{\omega}^2-\bar{q}^2}}\left(G_{>}\left(\frac{2+\bar{\omega}}{\bar{q}}\right)-G_{>}\left(\frac{2-\bar{\omega}}{\bar{q}}\right)\right)\right]. \tag{3.129}$$

Because the interest lies in the small $\bar{q}$ limit, the analytical function $G_{>}\left(x\right)$ defined in Eq. (3.56) needs to be expanded around $x=\infty$. Up to order x^{-4} the two functions become

$$x\sqrt{x^2-1} \approx x^2-\frac{1}{2}-\frac{1}{8x^2}-\frac{1}{16x^4}+\mathcal{O}\left[x^{-6}\right], \tag{3.130}$$

$$\operatorname{arcosh}\left(x\right) \approx \log\left(2\right)+\log\left(x\right)-\frac{1}{4x^2}-\frac{3}{32x^4}+\mathcal{O}\left[x^{-6}\right]. \tag{3.131}$$

Therefore, the term in brackets in Eq. (3.129) reduces to

$$\begin{aligned} & G_{>}\left(\frac{2+\bar{\omega}}{\bar{q}}\right)-G_{>}\left(\frac{2-\bar{\omega}}{\bar{q}}\right) \\ = & \frac{8\bar{\omega}}{\bar{q}^2}+\log\left(\frac{2-\bar{\omega}}{2+\bar{\omega}}\right)-\frac{8\bar{\omega}}{\left(4-\bar{\omega}^2\right)^2}\frac{\bar{q}^2}{8}-\frac{4\bar{\omega}+\bar{\omega}^2}{\left(4-\bar{\omega}^2\right)^2}\frac{\bar{q}^4}{2}+\mathcal{O}\left[\bar{q}^6\right]. \end{aligned} \tag{3.132}$$

In Eq. (3.132) the leading order in $\bar{q}$ comes from the intra-band contribution to the response function while the inter-band contribution only appears as a zeroth order correction with the log-term. Up to the leading order in $\bar{q}$, the response function becomes

$$\begin{aligned} \frac{\chi_{nn}^{(0)}\left(q,\omega\right)}{D\left(E_{\mathrm{F}}\right)} &= -1+\frac{1}{8}\frac{\bar{q}^2}{\bar{\omega}}\left(1+\frac{\bar{q}^2}{2\bar{\omega}^2}\right)\left(\frac{8\bar{\omega}}{\bar{q}^2}+\log\left(\frac{2-\bar{\omega}}{2+\bar{\omega}}\right)\right) \\ &= \frac{1}{2}\frac{\bar{q}^2}{\bar{\omega}^2}+\frac{1}{8}\frac{\bar{q}^2}{\bar{\omega}}\log\left(\frac{2-\bar{\omega}}{2+\bar{\omega}}\right)+\mathcal{O}\left[\bar{q}^4\right]. \end{aligned} \tag{3.133}$$

The plasmon appears in the small $\bar{\omega}$ limit. If one assures that $\bar{q}<\bar{\omega}$ also the second term needs to be dropped. Indeed, for small $\bar{\omega}$, the term with the log function reduces to

$$\frac{1}{8}\frac{\bar{q}^2}{\bar{\omega}}\log\left(\frac{2-\bar{\omega}}{2+\bar{\omega}}\right)\approx-\frac{1}{8}\bar{q}^2. \tag{3.134}$$

In this approximate limit, the plasmon dispersion equation becomes

$$\begin{aligned} 1 &= v_{\boldsymbol{q}}\chi_{nn}^{(0)}\left(q,\omega_{\text{pl}}\left(q\right)\right) \\ &= \left(\frac{1}{2}\frac{1}{\bar{\omega}_{\text{pl}}^{2}}-\frac{1}{8}\right)\alpha_{\text{ee}}N_{\text{f}}\bar{q} \end{aligned} \tag{3.135}$$

Therefore, the plasmon dispersion can be found as

$$\bar{\omega}_{\text{pl}}^{2}(\bar{q})=\frac{\alpha_{\text{ee}}N_{\text{f}}\bar{q}/2}{1+\alpha_{\text{ee}}N_{\text{f}}\bar{q}/8}\,. \tag{3.136}$$

The denominator of this expression, however, introduces terms of the same order in $\bar{q}$ as were dropped before and, therefore they also need to be suppressed. The solution for the plasmon dispersion finally is

$$\omega_{\text{pl}}^{(0)}\left(q\right)=\sqrt{\frac{\alpha_{\text{ee}}N_{\text{f}}v_{\text{F}}E_{\text{F}}}{2\hbar}q}. \tag{3.137}$$

Notice that in this result the contribution of the inter-band transitions, corresponding to the $\log$-terms in Eq. (3.133), was suppressed because it only affects the dispersion at higher order $\bar{q}$.

Apart from the $\sqrt{q}$-dependence of the plasmon frequency, Eq. (3.137) also shows that it depends on the Fermi level as $\omega_{\text{pl}}\sim\sqrt{E_{\text{F}}}$. Because the Fermi level depends on the carrier concentration as given in Eq. (2.29), i.e. $E_{\text{F}}\sim\sqrt{n_{\text{c}}}$, the plasmon frequency scales with the carrier concentration as

$$\omega_{\text{pl}}\sim n_{\text{c}}^{1/4}. \tag{3.138}$$

This result is peculiar for graphene since in a normal 2D electron gas (2DEG) the relation between the plasmon frequency and the carrier density is $\omega_{\text{pl}}\sim n_{\text{c}}^{1/2}$ [126].

The result from Eq. (3.137) coincides with the Dirac plasmon observed before using the hydrodynamic approach, Eq. (3.117), but where the Drude weight $\mathcal{D}$ is given as[50]

$$\mathcal{D}_{\text{MDF}}=N_{\text{f}}\frac{E_{\text{F}}}{\hbar}\sigma_{\text{uni}}. \tag{3.139}$$

Here, the Drude weight is labelled $\mathcal{D}_{\text{MDF}}$, referring to the character of the charge carriers, namely *massless Dirac Fermions* (MDF). The Drude weight is defined in terms of the universal optical conductivity σ_{uni} that was shown before to be the graphene optical conductivity. In Fig. 3.8 the long wavelength limit, Eq. (3.137), is plotted and shown that the result indeed matches the plasmon branch in the long wavelength limit. However, as the frequency increases, the solution fails to account for inter-band transitions and diverges from the numerical root of $\varepsilon^{\text{RPA}}\left(q,\omega\right)$. In order to account for inter-band contributions, the first sub-leading term needs to be considered as well. This will be done in the following section.

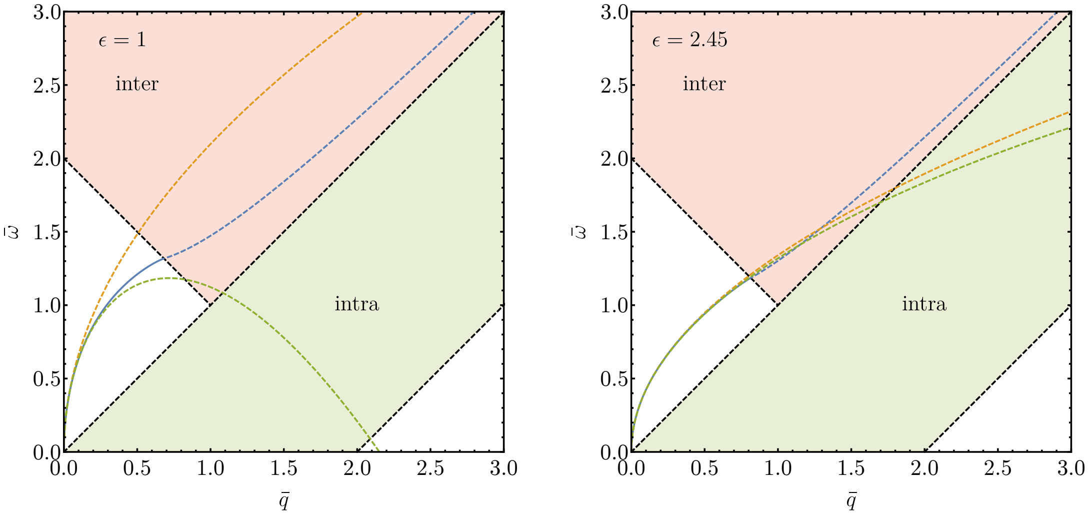

Figure 3.8: Plasmon dispersion in the (q, ω) plane for free-standing graphene (left) and graphene on SiO$_2$. The solid curve is the plasmon dispersion corresponding to the zeroes of the dielectric function. The dashed blue curve is the solution for the zero of the real part of $\varepsilon^{\mathrm{RPA}}(q\omega)$. The yellow dashed curve is $\omega_{\mathrm{pl}}^{(0)}(q)$ and the green dashed curve is the dispersion with the first sub-leading term, $\omega_{\mathrm{pl}}^{(1)}(q)$. The inter- and intra-band continua are indicated by red and green shading respectively.

Analytical approximation: first sub-leading term

Following the analysis from the previous section, it is possible to account for the first sub-leading term in the plasmon dispersion if Eq. (3.132) is kept up to second order in $\bar{q}$ [118]. One then gets

$$\begin{aligned}\frac{\chi_{nn}^{(0)}(q,\omega)}{D(E_{\mathrm{F}})} &= -1+\frac{1}{8}\frac{\bar{q}^2}{\bar{\omega}}\left(1+\frac{\bar{q}^2}{2\bar{\omega}^2}+\frac{3\bar{q}^4}{8\bar{\omega}^4}\right)\left(\frac{8\bar{\omega}}{\bar{q}^2}+\log\left(\frac{2-\bar{\omega}}{2+\bar{\omega}}\right)\right)\\ &= \frac{1}{8}\frac{\bar{q}^2}{\bar{\omega}}\log\left(\frac{2-\bar{\omega}}{2+\bar{\omega}}\right)+\frac{\bar{q}^2}{2\bar{\omega}^2}+\frac{1}{8}\frac{\bar{q}^4}{2\bar{\omega}^3}\log\left(\frac{2-\bar{\omega}}{2+\bar{\omega}}\right)+\frac{3\bar{q}^4}{8\bar{\omega}^4}+\mathcal{O}\left[\bar{q}^6\right]\ .\end{aligned} \tag{3.140}$$

Approximating the log functions for small $\bar{\omega}$, one gets with Eq. (3.134):

$$\frac{\chi_{nn}^{(0)}(q,\omega)}{D(E_{\mathrm{F}})}=\frac{\bar{q}^2}{2\bar{\omega}^2}-\frac{\bar{q}^2}{8}-\frac{1}{8}\frac{\bar{q}^4}{2\bar{\omega}^2}+\frac{3\bar{q}^4}{8\bar{\omega}^4}+\mathcal{O}\left[\bar{q}^6\right]. \tag{3.141}$$

Therefore, the plasmon equation becomes up to second order in $\bar{q}$

$$1 = \frac{\alpha_{\mathrm{ee}} N_{\mathrm{f}}}{2} \bar{q} \left[\frac{1}{\bar{\omega}_{\mathrm{pl}}^2} - \frac{1}{4} + \frac{3\bar{q}^2}{4\bar{\omega}_{\mathrm{pl}}^4} - \frac{1}{8} \frac{\bar{q}^2}{\bar{\omega}_{\mathrm{pl}}^2} \right] . \tag{3.142}$$

This equation is equivalent to the quartic equation

$$\bar{\omega}_{\mathrm{pl}}^4 = \frac{\alpha_{\mathrm{ee}} N_{\mathrm{f}}}{2} \bar{q} \left[\bar{\omega}_{\mathrm{pl}}^2 - \frac{\bar{\omega}_{\mathrm{pl}}^4}{4} - \frac{1}{8} \bar{q}^2 \bar{\omega}_{\mathrm{pl}}^2 + \frac{3\bar{q}^2}{4} \right] , \tag{3.143}$$

which can be subsequently solved with keeping the terms up to $q^{3/2}$ resulting in

$$\omega_{\mathrm{pl}}^{(1)}(q) = \omega_{\mathrm{pl}}^{(0)}(q) \left[1 + \frac{12 - (\alpha_{\mathrm{ee}} N_{\mathrm{f}})^2}{16} \frac{q}{k_{\mathrm{TF}}} \right] , \tag{3.144}$$

here $\omega_{\mathrm{pl}}^{(0)}(q)$ is the regular square root plasmon dispersion from Eq. (3.137) and k_{TF} is the Thomas-Fermi screening wave vector $k_{\mathrm{TF}} = \alpha_{\mathrm{ee}} N_{\mathrm{f}} k_{\mathrm{F}}$ [102]. The inverse of this wave vector is a measure for the length over which a point charge is screened. This result was derived in Ref. [118] and there it was noted that the sub-leading term can change sign depending on the dielectric environment which enters the problem through α_{ee}. Note however that there was a typographical error in the denominator in Eq. (3.144) in Ref. [118].

In Fig. 3.8 the green dashed curves show the plasmon dispersion with the first sub-leading term taken into account. For free-standing graphene the result matches the complete solution up to higher frequencies as expected. However, for increasing wave vector the dispersion deviates again from the full numerical result. For graphene on $\mathrm{SiO_2}$ the three dispersions match much better. In that case the factor accompanying the sub-leading term is parametrically small since now $\alpha_{\mathrm{ee}} = 2.2/2.45 = 0.897$, such that $12 - (\alpha_{\mathrm{ee}} N_{\mathrm{f}})^2 \approx 0$.

3.2.4 Lifetime of the plasmon

The Dirac plasmons in the RPA are up to now considered as exact solutions of the RPA dielectric function Eq. (3.124) with real frequency. This means that they can only exist if the imaginary part of the dielectric function vanishes and, therefore, when the imaginary part of the non-interacting density-density response function $\chi_{nn}^{(0)}(q, \omega)$ is zero. However, if one allows for modes that have a finite but long lifetime, i.e. a complex angular frequency,

$$\omega_{\mathrm{pl}}(q) \equiv \Omega_{\mathrm{pl}}(q) - i\gamma_{\mathrm{pl}}(q) , \tag{3.145}$$

then it is possible to find collective modes in the particle-hole continuum. Furthermore, the lifetime of the mode is then related to the decay rate $\gamma_{\text{pl}}(q)$. If the decay rate is considerably smaller than the plasmon frequency $\Omega_{\text{pl}}(q)$, the dielectric function can be expanded in a Taylor series [127] such that

$$\varepsilon^{\text{RPA}}\left(q,\Omega_{\text{pl}}(q)-i\gamma_{\text{pl}}(q)\right)\approx\varepsilon^{\text{RPA}}\left(q,\Omega_{\text{pl}}(q)\right)-i\gamma_{\text{pl}}(q)\left.\frac{\partial\varepsilon^{\text{RPA}}(q,\omega)}{\partial\omega}\right|_{\omega=\Omega_{\text{pl}}(q)}. \quad (3.146)$$

This expression allows to find an expression for the decay rate via the imaginary equation as

$$\gamma_{\text{pl}}(q)=\frac{\text{Im}\left[\varepsilon^{\text{RPA}}\left(q,\Omega_{\text{pl}}(q)\right)\right]}{\left.\frac{\partial\text{Re}\left[\varepsilon^{\text{RPA}}(q,\omega)\right]}{\partial\omega}\right|_{\omega=\Omega_{\text{pl}}(q)}}, \quad (3.147)$$

while the real part of the complex frequency is found via

$$\text{Re}\left[\varepsilon^{\text{RPA}}\left(q,\Omega_{\text{pl}}(q)\right)\right]=0. \quad (3.148)$$

Following this method, the plasmon dispersion can be found by finding the roots of the real part of the dielectric function. The corresponding decay rate then is determined by the imaginary part of the dielectric function. Notice that because the imaginary part of $\varepsilon^{\text{RPA}}(q,\omega)$ is always positive, the sign of the decay rate Eq. (3.147) is determined by the sign of the frequency derivative of the real part at the plasmon frequency. If this derivative is negative, the mode would grow rather than be damped in time and would represent an unphysical solution. Therefore, this solution needs to be handled with care.

Finally, note that the physical observability of a damped collective mode in practice depends on the sharpness of its resonant peak. This sharpness is captured by the so-called *quality factor* Q which is defined as

$$Q(q)\equiv\frac{\Omega_{\text{pl}}(q)}{\gamma_{\text{pl}}(q)}. \quad (3.149)$$

In Fig. 3.9 the corresponding inverse quality factor is shown as a function of the wave vector $\bar{q}$ and frequency $\bar{\omega}$. The results show that a dielectric environment that screens the electron liquid less (i.e. free-standing graphene), allows for a stable plasmon up to higher frequency. However, when the plasmon is damped, the damping increases much stronger when the inter-band PHES is entered with respect to the situation of graphene on SiO_2.

3.2.5 Spectral weight and oscillator strength

In order to understand the effect of the plasmon on the rest of the system, it is useful to consider the way in which spectral weight is redistributed due to electron-electron interactions. For this one can employ a similar technique as used before to investigate the

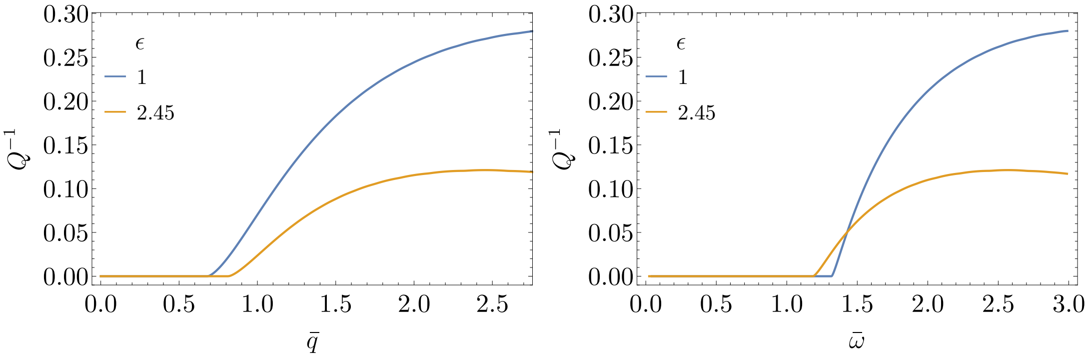

Figure 3.9: Inverse value of the quality factor for the plasmons shown in Fig. 3.8 as a function of the wave vector $\bar{q}$ (left) and frequency $\bar{\omega}$ (right).

redistribution due to the Pauli blocking of inter-band transitions. As obtained before, in general one has for graphene [114]

$$\int_0^{\Lambda} d\omega\omega \mathrm{Im}\left[\chi_{nn}\left(\boldsymbol{q},\omega\right)\right] = -\frac{q^2 N_{\mathrm{f}}\Lambda}{16\hbar}. \tag{3.150}$$

As discussed before, this equation also holds when interactions are taken into account. Then, one can evaluate this for the RPA response functions. Note that in the RPA the imaginary part of the density-density response function changes according to Eq. (3.123) such that it can be written as [102]

$$\mathrm{Im}\chi_{nn}^{\mathrm{RPA}}\left(q,\omega\right) = \frac{\mathrm{Im}\chi_{nn}^{(0)}\left(q,\omega\right)}{\left(1 - v_{\boldsymbol{q}}\mathrm{Re}\chi_{nn}^{(0)}\left(q,\omega\right)\right)^2 + \left(\mathrm{Im}\chi_{nn}^{(0)}\left(q,\omega\right)\right)^2}. \tag{3.151}$$

This means that in the long-wavelength limit $q \to 0$, the imaginary part is zero except where the denominator vanishes, i.e. at the plasmon branch. This is because the plasmon pole is, in the absence of damping, located just below the axis of Re ω at $\omega = \omega_{\mathrm{pl}}\left(q\right) - i\eta$, where η is a positive infinitesimal. Near the plasmon branch, the denominator of the response function can be approximated as

$$\varepsilon^{\mathrm{RPA}}\left(q,\omega\right) \approx \varepsilon^{\mathrm{RPA}}\left(q,\omega_{\mathrm{pl}}\left(q\right)\right) + \left.\frac{\partial\varepsilon^{\mathrm{RPA}}\left(q,\omega\right)}{\partial\omega}\right|_{\omega=\omega_{\mathrm{pl}}(q)}\left(\omega - \omega_{\mathrm{pl}}\left(q\right) + i\eta\right). \tag{3.152}$$

The first term of this expression vanishes, so the RPA response function near the plasmon pole is

$$\chi_{nn}^{\mathrm{RPA}}(q,\omega)=\frac{\chi_{nn}^{(0)}(q,\omega_{\mathrm{pl}}(q))}{\left.\frac{\partial\varepsilon^{\mathrm{RPA}}(q,\omega)}{\partial\omega}\right|_{\omega=\omega_{\mathrm{pl}}(q)}(\omega-\omega_{\mathrm{pl}}(q)+i\eta)}. \tag{3.153}$$

This means that in the limit of $\eta\to 0$ the imaginary part becomes

$$\mathrm{Im}\chi_{nn}^{\mathrm{RPA}}(q,\omega)=-\pi\frac{\mathrm{Re}\chi_{nn}^{(0)}(q,\omega)}{\left.\frac{\partial\mathrm{Re}[\varepsilon^{\mathrm{RPA}}(q,\omega)]}{\partial\omega}\right|_{\omega=\omega_{\mathrm{pl}}(q)}}\delta(\omega-\omega_{\mathrm{pl}}(q)). \tag{3.154}$$

This expression shows that the plasmon pole appears as a delta function in the (q,ω) plane. The strength of the delta peak is called the plasmon *oscillator stength* $O_{\mathrm{pl}}(q,\omega)$ [102] and is given by

$$O_{\mathrm{pl}}(q,\omega)=-\frac{\pi D(E_{\mathrm{F}})}{4}\frac{\bar{q}^{5/2}}{\bar{\omega}^2}\sqrt{\frac{\alpha_{\mathrm{ee}}N_{\mathrm{f}}}{2}} \tag{3.155}$$

If one now calculates the f-sum rule, one finds

$$\begin{aligned}\int_{v_{\mathrm{F}}q}^{2\Lambda_{\mathrm{F}}}d\omega\omega\mathrm{Im}\left[\chi_{nn}^{\mathrm{RPA}}(q,\omega)\right] &= -\left(\frac{E_{\mathrm{F}}}{\hbar}\right)^2\int_{\bar{q}}^{2}d\bar{\omega}\bar{\omega}\frac{\pi D(E_{\mathrm{F}})}{4}\frac{\bar{q}^{5/2}}{\bar{\omega}^2}\sqrt{\frac{\alpha_{\mathrm{ee}}N_{\mathrm{f}}}{2}}\delta(\bar{\omega}-\bar{\omega}_{\mathrm{pl}}(q))\\ &= -\frac{q^2N_{\mathrm{f}}\Lambda_{\mathrm{F}}}{8\hbar}.\end{aligned} \tag{3.156}$$

This is exactly the same quantity as the contribution of the intra-band part as shown in Eq. (3.77) . The RPA intra-band term in the long wavelength limit is calculated from Eq. (3.151) as

$$\mathrm{Im}\chi_{nn}^{\mathrm{RPA}}(q,\omega)=-D(E_{\mathrm{F}})\frac{4\bar{\omega}}{(\alpha_{\mathrm{ee}}N_{\mathrm{f}})^2}\sqrt{\bar{q}^2-\bar{\omega}^2} \tag{3.157}$$

such that one finds

$$\begin{aligned}\int_{0}^{v_{\mathrm{F}}q}d\omega\omega\mathrm{Im}\left[\chi_{nn}^{\mathrm{RPA}}(q,\omega)\right] &= -\left(\frac{E_{\mathrm{F}}}{\hbar}\right)^2\frac{4D(E_{\mathrm{F}})}{(\alpha_{\mathrm{ee}}N_{\mathrm{f}})^2}\int_0^{\bar{q}}d\bar{\omega}\bar{\omega}^2\sqrt{\bar{q}^2-\bar{\omega}^2}\\ &= -\frac{v_{\mathrm{F}}^2q^4}{8E_{\mathrm{F}}(\alpha_{\mathrm{ee}}N_{\mathrm{f}})^2},\end{aligned} \tag{3.158}$$

this term contributes as fourth order in q, so it is much weaker than the plasmon weight. This means that in the RPA the plasmon mode absorbs all the spectral weight up to second order in q. This mechanism can be seen by comparing the imaginary parts of the response

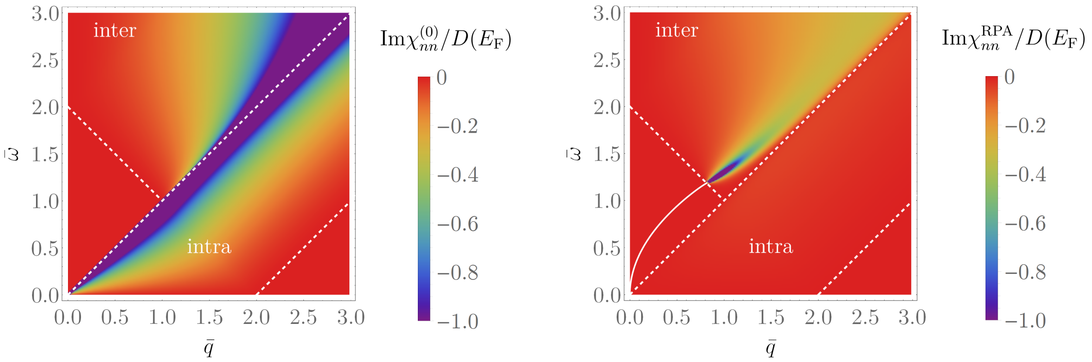

Figure 3.10: Comparison of the imaginary parts of the RPA and non-interacting density-density response functions. Both figures have the same colourscale.

function in the (q, ω) plane that are put next to each other in Fig. 3.10. For small wave vector q, it is clear that the intra-band spectral weight in the RPA response function is strongly diminished where the plasmon branch is present. Notice that this only holds in the long-wavelength limit.

3.2.6 Theoretical works in graphene plasmonics

The response function of a 2D electron gas that follows the Dirac equation was considered early on in the calculation of the polarisation tensor of massless 2D quantum electrodynamics [128–130]. This relation arises because the polarisation function, usually denoted by $\Pi^{(0)}(\boldsymbol{q}, \omega)$, that one obtains from the calculation of the bubble diagram has the same role as the non-interacting density-density response function $\chi_{nn}^{(0)}(\boldsymbol{q}, \omega)$ [102, 131]. Furthermore, Shung extended this in the framework of stage-1 intercalated graphite to also account for systems with a finite chemical potential [132]. From this, the dielectric function and the $\sqrt{q}$ - dependence of the plasmons in the RPA were calculated. In the context of graphene, the polarisation function was derived for a finite chemical potential by Ando [133], Hwang and Das Sarma [123] and Wunsch *et al.* [106].

After the prediction of Dirac plasmons, many others followed by considering similar systems like graphene double layers [134], bilayer graphene [135–139], strained graphene [140], graphene affected by superlattices [141–144], or graphene magnetoplasmons in a strong magnetic field [145–151]. Consequently, also the lifetime and damping effects on Dirac plasmons was investigated by considering the impact of disorder [152], e-e interaction [105], electron-phonon coupling [153] or substrate screening [154].

The research for Dirac plasmons is a very active research field and the list mentioned

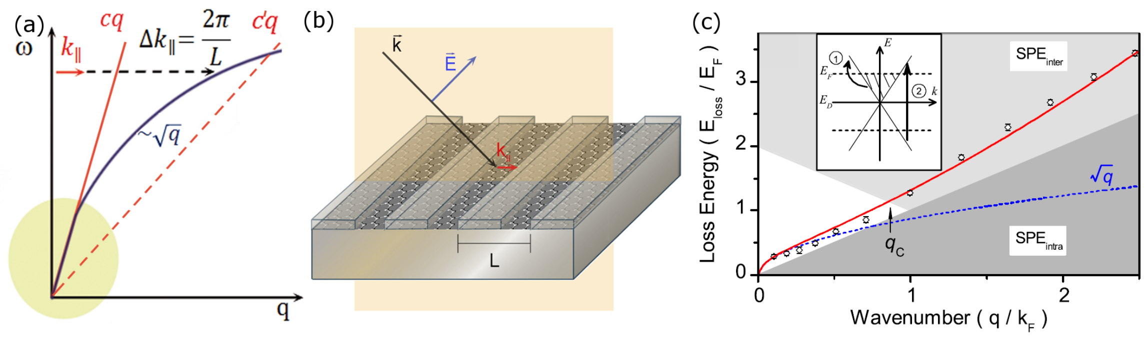

Figure 3.11: (a) Comparison of the energy spectrum of free-space photons (red curve) and plasmons (blue curve). The red dashed curve correspond to the tilted light cone due to the lower speed of light c' in an optically dense environment. The shaded circle shows the region where plasmon polariton hybridisation occurs. The arrows show how an additional periodicity can add momentum to the photon. (b) Schematic example of a grated graphene flake. The angle of the incident photon with the graphene plane determines the magnitude of the in-plane momentum $k_\parallel$ and, therefore, also determines at which frequency a plasmon can be excited. Panels (a) and (b) are adapted from Ref. [52]. (c) Measured electron energy loss due to plasmons in graphene on SiC as a function of the wavenumber (open circles). The shaded regions show the intra- and inter-band PHES. The red curve shows the RPA plasmon dispersion. The blue dashed curve shows the $\sqrt{q}$ approximation. The inset of (c) shows the different possible inter- and intra-band transitions. Panel (c) is taken from Ref. [49].

in the two previous paragraphs is far from complete. In the next section the experimental advances that thrive this activity are explained.

3.3 Experimental excitation of graphene plasmons

As mentioned in the introductory chapter, graphene plasmons have been measured by using several techniques. In this section the main methods that are being used to excite and detect plasmons are explained. This provides the necessary understanding of what is experimentally possible.

3.3.1 Momentum matching and retardation effects

If one wants to excite plasmons, it is necessary to match momentum and energy of the incident particle, usually an electron, photon or phonon. For electrons, that are used in, for example, an EELS set-up, this can be done with relative ease [48]. However, if one wants to use external photons, there is a problem because the momentum of the free-space photon is much smaller than that of the plasmon at the same energy. In Fig. 3.11(a) the plasmon momentum and photon momentum are shown together. The curve shows that for small momenta the photon and plasmon dispersion merge. Indeed, the plasmon group velocity cannot be larger than the speed of light. Therefore, it is clear that the $\sqrt{q}$ solution that was found in Eq. (3.137) cannot pertain up to very small values of q and has to merge with the light cone [52, 62]. This solution was not present in the derivation performed in the previous section because it was assumed that the Coulomb interaction is instantaneous, i.e. that the speed of light c equals infinity. This approximation is called the *non-retarded limit*. However, as explained in appendix A upon performing the calculations in the retarded limit, the dispersion of the plasmon merges with the light cone for energies satisfying $\hbar\omega < \alpha_{\mathrm{QED}} E_{\mathrm{F}}$. In this region, the free-space photon couples to the plasmon and forms a *plasmon-polariton*. The region where plasmon-polariton hybridisation occurs is indicated by the shaded circle in Fig. 3.11(a).

In the light of plasmonics, this type of plasmon-polariton is however not what one wants since the wavelength will be exactly the same as the free-space wavelength. Therefore, one needs to find a way to give the photon additional momentum. In the context of noble metal plasmonics, Otto [29] and Kretschmann [28] proposed configurations where the velocity of the incoming light is effectively reduced by a factor 2-10 by an optically dense medium. The dispersion is shown in Fig. 3.11(a) as a dashed curve. Now the plasmon can be excited at different frequency depending on the angle of the incident light that can tune the in-plane momentum of the photon to match the momentum of the plasmon. A different method is based on the engineering of sub-wavelength structures as shown in Fig. 3.11(b). Here, the breaking of translational symmetry can provide the photon with an additional momentum component stemming from the periodicity of the structure. This is schematically shown in Fig. 3.11(a). For graphene, one needs to use the latter mechanism to excite plasmons [52].

In the following section, some of the most successful methods used to excite Dirac plasmons in graphene are discussed.

3.3.2 Experimental observation of Dirac plasmons

Dirac plasmons were first observed in graphene by EELS on free-standing [48], epitaxial graphene on SiO_2 [49] and SiC [125]. In Fig. 3.11(c) the obtained plasmon dispersion is shown. The results shows that the RPA result obtained in Fig. 3.8 show a faithful description of the plasmon dispersion.

In order to use photons to excite plasmons, one has considered arrays of graphene nanoribbons where it has been shown that plasmons are excited when the incident light

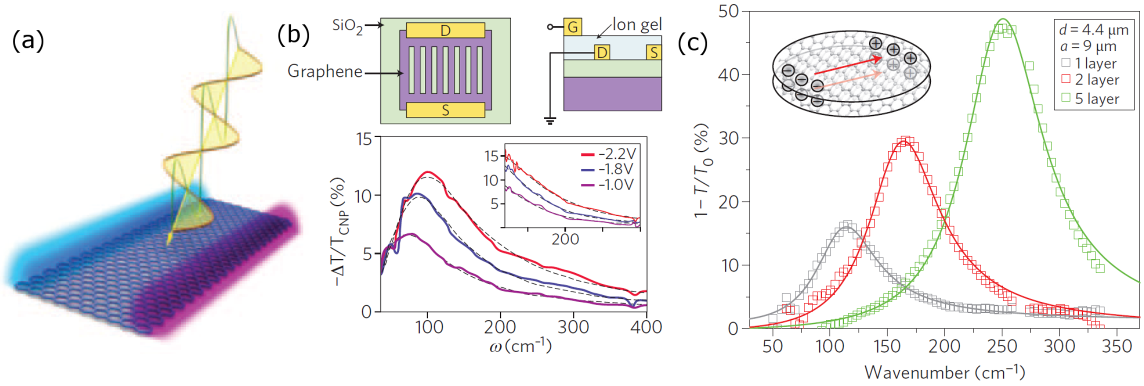

Figure 3.12: (a) Schematic picture of a plasmon excitation in a graphene ribbon. (b) Nanoribbon array set-up for the excitation of plasmons. The graph below shows the absorption spectrum for a light beam polarized perpendicular to the length of the graphene ribbon. The bump in the curve respresents the absorption due to plasmon excitation. The inset of this figure shows the absorption when the polarisation is along the length of the ribbon. The absence of a bump shows that no plasmons are excited. Figure taken from Refs. [50, 53]. (c) Absorption spectrum of stacked graphene disks for a different number of layers. Figure taken from Ref. [54].

polarisation is perpendicular to the ribbon's axis as shown in Figs. 3.12(a)-(b) [53, 155]. It was found that the plasmon frequency scales with the width of the nanoribbon as $W^{-1/2}$, confirming the $\sqrt{q}$-dependence, and with $n^{1/4}$ in agreement with Eq. (3.138). Furthermore, also patterns of graphene stacked nanodisks were investigated [54, 156, 157]. As shown in Fig. 3.12(c) the plasmonic response was greatly amplified thanks to the multiple layers. In these structures, the plasmonic response was measured in the infrared. Also here the finite size of the nanostructures made sure that the momentum mismatch was overcome. The plasmons that are obtained in these nanostructures are confined and can be considered as standing waves rather than propagating.

Another way to overcome the momentum mismatch was recently proposed by Fei *et al.* [57] and Chen *et al.* [58]. They used the tip of an atomic force microscope (AFM) to couple free-space photons to the Dirac electron liquid in graphene. As schematically shown in Fig. 3.13, this excites Dirac plasmons in the graphene flake that propagate outward and are reflected at the edges of graphene. The back-scattered radiation can be subsequently used to yield resolved infrared near-field images of the plasmon. These near-field images harbour the information about the plasmon wavelength and how it propagates in the graphene flake. This experimental set-up is called a scattering-type scanning near-field optical microscope (s-SNOM). The experiments revealed that the plasmon wavelength $\lambda_{\rm pl}$ is much smaller than the free-space wavelength λ_0 of the photon used to excite the plasmon. It was found that the ratio is $\lambda_0/\lambda_{\rm pl} \sim 40$ [58], which means that Dirac plasmons correspond

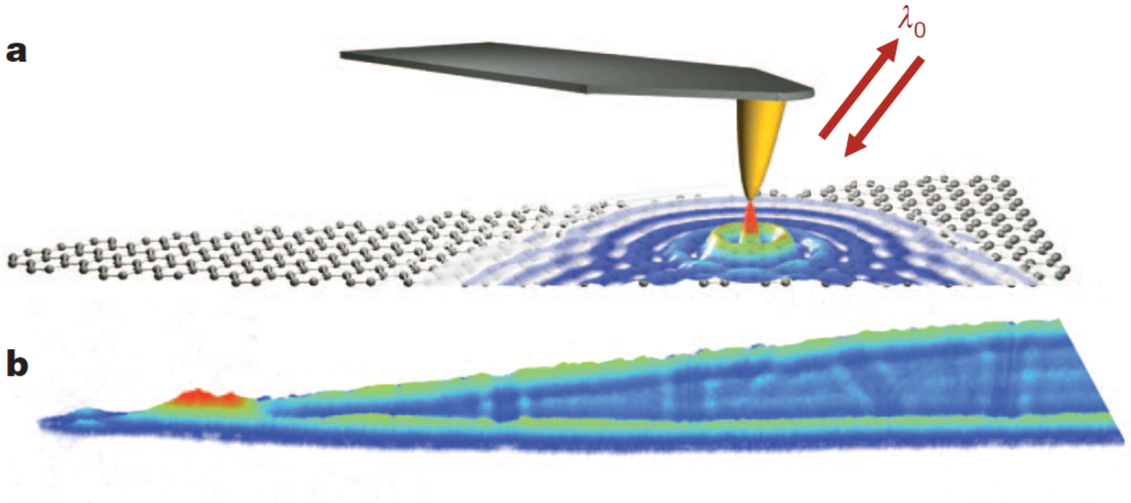

Figure 3.13: (a) Schematic working principle of a scattering type SNOM set-up to excite plasmons. (b) Real space image formed from the backscattered radiation showing the interference fringes of the plasmon. Figure taken from Ref. [58].

to very strong light confinement. As a consequence, it has been shown that plasmons in graphene can be used for very strong light-matter interaction [60]. This strong confinement of graphene plasmons made it also possible to use a single-molecule as an atomic antenna for the generation of Dirac plasmons [158].

The first experiments exciting graphene plasmons with a SNOM set-up were performed on graphene on SiO_2. However, later it was also used to investigate plasmons in graphene encapsulated by hexagonal boron nitride [59]. This platform was shown to be exceptional, featuring a confinement ratio of $\lambda_0/\lambda_{\mathrm{pl}} \sim 150$ and plasmon lifetimes of $\tau \sim 500$ fs, the longest Dirac plasmon lifetimes measured up to now.

Recently, another way of exciting Dirac plasmons was proposed. This method used gold nanorods deposited on the graphene flake as antennas that couple to the incident light [159]. The light, that is polarized along the length of the nanorod, induces a dipole, whos radiation is leaked to a graphene flake as Dirac plasmon wavefronts as shown in Fig. 3.14. Subsequently, the plasmons were imaged by a SNOM tip.

The fact that Dirac plasmons have such long lifetimes encouraged many proposals to use them as a basis for plasmonic waveguiding [160]. Therefore, graphene can play a leading role as a new platform for plasmonics [64, 66].

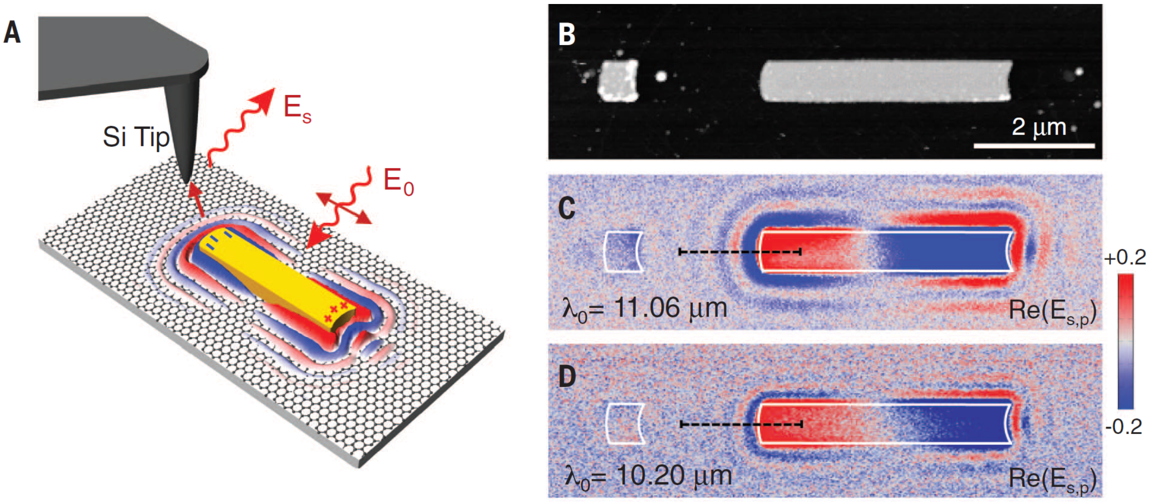

Figure 3.14: Plasmon excitation making use of metal antennas. (a) Schematic set-up showing the excitation of Dirac plasmons by an induced dipole in a gold nanorod and the subsequent imaging of the wave fronts by a SNOM tip. (b) Real space image of the nanorods used to generate the plasmon wavefronts imaged in (c) and (d) at the wavelengths as indicated. Image taken from [159].

3.4 Plasmarons in trilayer graphene

The chapter is ended with a short discussion about another way in which Dirac plasmons in graphene have been observed, be it indirectly. Indeed, it was found that the conic energy dispersion of graphene is accompanied by a second cone that is displaced in energy as depicted in Fig. 3.15 [161]. The second cone is attributed to the existence of *plasmarons* [162], a composite particle consisting of a charge carrier coupled to a plasmon. The reason for the energy shift of the second cone is the additional binding energy that is required to form the plasmon-particle composite.

As plasmons are collective excitations of the electron liquid and electrons are, naturally, a part of this liquid, the interaction between plasmons and single electrons can lead to strong effects on the self-energy of the particles [102, 161, 163]. Therefore, plasmarons correspond to poles in the self-energy. In order to evaluate the effect of plasmons on the single-particle energy dispersion, without the need of calculating the self-energy, Overhauser derived a simplified theory to account for the interaction of a (remote) electron with plasmons in the electron liquid [164].

Using the Overhauser model, it has been shown that the plasmaron dispersion in graphene can be calculated within second order perturbation theory [165]. In this analysis, the electron-plasmon interaction was derived by making use of the f-sum rule introduced in

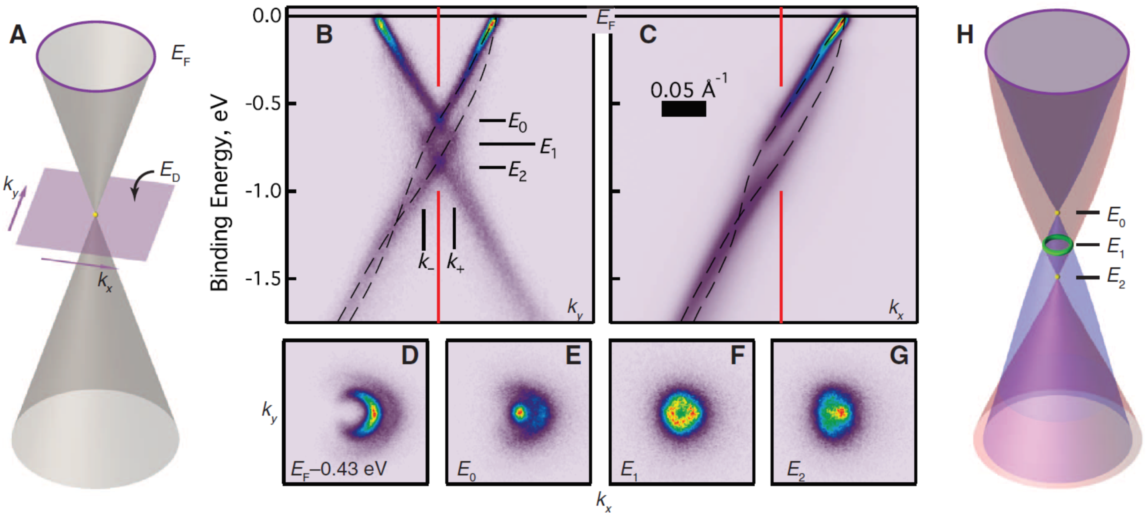

Figure 3.15: Plasmarons in monolayer graphene. (a) Normal unpertubed graphene energy spectrum. (b) and (c) Experimental ARPES spectra of doped graphene along the Γ - K direction. (d) - (g) Cuts of the ARPES spectrum at constant energy as indicated. (h) Schematic representation of the Dirac spectrum that is affected by plasmon-particle interaction. Image taken from Ref. [161].

Sec. 3.1.7 and describing the electron liquid as consisting of plasmons, rather than single-particles [166]. It was shown that this method estimates the energy shift ΔE between the plasmaron and the single-particle spectrum to be of the order of $\Delta E \sim 50 - 150\ \mathrm{meV}$. This is in agreement with experiments [161, 163].

As discussed in Sec. 2.3, it is possible to stack multiple layers of graphene to form a graphene multilayer. For bilayer graphene (BLG), stacked in a Bernal configuration [167], the low-energy properties of the electrons turn from linear to parabolic. For this system, it was possible to use the Overhauser model to estimate the energy shift between the single-particle spectrum and the plasmaron energy spectrum to be about 100 meV [168]. Following the same method, also for trilayer graphene (TLG) the plasmaron spectrum was evaluated [69]. As mentioned in Sec. 2.3, a rhombohedrally stacked graphene trilayer has a cubic single-particle energy dispersion, $\varepsilon_{\boldsymbol{k}} \sim k^3$. Therefore, also the plasmaron dispersion is cubic. In Fig. 3.16(a) the effect of electron-plasmon on the trilayer graphene dispersion is shown. Its spectrum is shifted by $\Delta E \sim 150 - 200\ \mathrm{meV}$ [69].

Rhombohedrally stacked TLG make up about 15% of CVD [169] and exfoliated TLG samples [170, 171]. The remainder has a Bernal stacking, which in the case of TLG means that the top and bottom layer are exactly above each other and the middle layer is shited over one inter-atomic distance [167]. The band structure of Bernal TLG does not have a cubic dispersion, but consists of a linear and a hyperbolic band at low energy and two

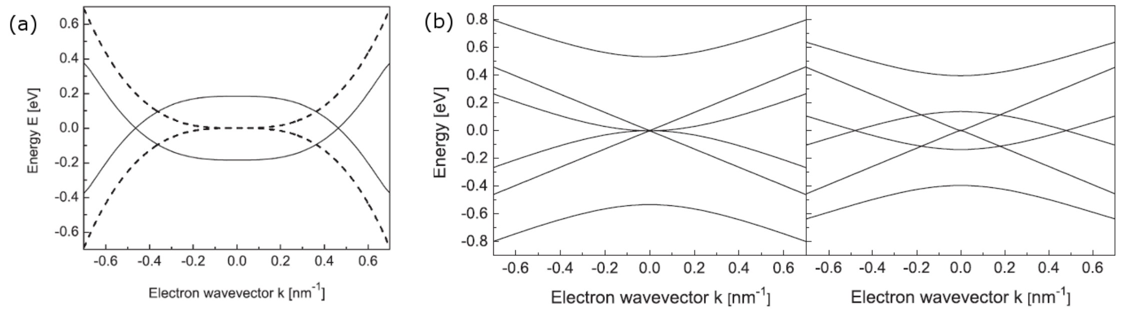

Figure 3.16: (a) Energy spectrum of rhombohedral TLG in the absence (dashed curve) and presence (solid curve) of plasmon-particle interaction. (b) Energy spectrum of Bernal TLG in the absence (left) and presence (right) of plasmon-particle interaction. Both panels are calculated for a total electron density $n_\mathrm{e} = 10^{13}\ \mathrm{cm}^{-2}$ and substrate permittivity $\epsilon_\mathrm{s} = 3.8$.

additional hyperbolic bands at larger energy [82, 172]. In Fig. 3.16(b) the band structure is shown. Also for Bernal TLG the Overhauser method has been used to calculate the effect of electron-plasmon interaction. The result is shown in Fig. 3.16(b). The hyperbolic band is shifted by $\Delta E \sim 30 - 150\ \mathrm{meV}$, while the linear band is only affected by $\Delta E \sim 1 - 5\ \mathrm{meV}$ [69]. The reason for this difference is that the shift depends on the value of the Fermi level, which is determined by the electron concentration. In TLG the electron concentration is distributed over more bands, which results in a lower Fermi level and, consequently, a smaller effect on the energy bands.

CHAPTER 4

Plasmons at large carrier doping

How are graphene plasmons affected by the hexagonal symmetry of the lattice?

In the previous chapter, the properties of the Dirac plasmon were investigated in detail. The presented analysis, however, relied on the Dirac cone approximation. This means that the doping should remain small enough to be able to disregard the trigonal symmetry of the graphene dispersion that becomes clear at larger values of the Fermi energy as shown in the energy dispersion presented in Fig. 2.4. This chapter is devoted to the plasmonic response of highly doped graphene samples and is an example of the robustness of the Dirac plasmon.

Note that because large doping implies that $E_{\mathrm{F}} \simeq t$, the energy spectrum is strongly trigonally warped. In this chapter the focus will be on the plasmonic limit, i.e. the limit for small q and small ω. This means that although the Fermi level E_{F} is large, the characteristic energy scale of the transitions taken into account is small. In the last part of this chapter the robustness is shown to be sustainable up to larger values of q and ω.

The chapter is structured as follows: In Sec. 4.1 the density-density response function for an arbitrary energy dispersion is derived in the long-wavelength limit. In Sec. 4.2 the response function is calculated for the graphene energy spectrum using general symmetry considerations and in Sec. 4.3 it is evaluated within a simplified model of a trigonally warped cone. Finally in Sec. 4.4 the corresponding plasmons are calculated analytically and in Sec. 4.5 a numerical calculation that confirms the findings is presented.

About the work presented in this chapter a small paper is being written.

4.1 Response function

Outside the Dirac cone approximation, the density-density response function defined in Eq. (3.26) needs to be adapted. If the total energy spectrum as defined in Eq. (2.15) is accounted for, the sum in Eq. (3.26) runs over the entire first Brillouin zone and the overlap function $\mathcal{D}_{\lambda\lambda'}\left(\boldsymbol{k},\boldsymbol{k}+\boldsymbol{q}\right)$ is changed as [173]

$$\left|\mathcal{D}^{f}_{\lambda\lambda'}\left(\boldsymbol{k},\boldsymbol{k}+\boldsymbol{q}\right)\right|^2=\frac{1}{2}\left(1+\lambda\lambda'\mathrm{Re}\left[\frac{f^{AB}_{\boldsymbol{k}}}{\left|f^{AB}_{\boldsymbol{k}}\right|}\frac{f^{AB}_{\boldsymbol{k}+\boldsymbol{q}}}{\left|f^{AB}_{\boldsymbol{k}+\boldsymbol{q}}\right|}\right]\right). \tag{4.1}$$

The function $f^{AB}_{\boldsymbol{k}}$ is defined in Eq. (2.11). In this way the non-interacting response function can be calculated as

$$\chi^{(0)}_{nn}\left(\boldsymbol{q},\omega\right)=\frac{1}{L^2}\sum_{\lambda\lambda'}\sum_{\boldsymbol{k}\in\mathrm{BZ}}\left|\mathcal{D}^{f}_{\lambda\lambda'}\left(\boldsymbol{k},\boldsymbol{k}+\boldsymbol{q}\right)\right|^2\frac{n_{\lambda\boldsymbol{k}}-n_{\lambda'\boldsymbol{k}+\boldsymbol{q}}}{\hbar\omega+\varepsilon_{\lambda\boldsymbol{k}}-\varepsilon_{\lambda'\boldsymbol{k}+\boldsymbol{q}}+i\hbar\eta}. \tag{4.2}$$

In Eq. (4.2), the sum runs over all wave vectors $\boldsymbol{k}$ in the first Brillouin zone.

The response function can be analytically calculated at $T=0$ in the limit

$$q\ll\frac{1}{a}\text{ and }\hbar v_{\mathrm{F}}q<\hbar\omega\ll E_{\mathrm{F}}. \tag{4.3}$$

In this limit, the overlap function becomes

$$\begin{aligned}\left|\mathcal{D}^{f}_{\lambda\lambda'}\left(\boldsymbol{k},\boldsymbol{k}+\boldsymbol{q}\right)\right|^2 &= \frac{1}{2}\left(1+\lambda\lambda'\cos\left[\arg\left(f^{AB}_{\boldsymbol{k}}\right)-\arg\left(f^{AB}_{\boldsymbol{k}+\boldsymbol{q}}\right)\right]\right),\\ &\approx \frac{1}{2}\left(1+\lambda\lambda'\right)=\delta_{\lambda,\lambda'}.\end{aligned} \tag{4.4}$$

Therefore, only intra-band transitions are taken into account. Because the valence band is completely filled, the Pauli exclusion principle prohibits intra-valence-band transitions and therefore, only intra-band transitions in the conduction band contribute to the response function. Next, because

$$\varepsilon_{\lambda\boldsymbol{k}}-\varepsilon_{\lambda\boldsymbol{k}+\boldsymbol{q}}\ll\hbar\omega, \tag{4.5}$$

the denominator of the integrand from Eq. (4.2) can be expanded as

$$\frac{1}{\hbar\omega+\varepsilon_{\lambda\boldsymbol{k}}-\varepsilon_{\lambda\boldsymbol{k}+\boldsymbol{q}}+i\hbar\eta}\approx\frac{1}{\hbar\omega}\left(1-\frac{\varepsilon_{\lambda\boldsymbol{k}}-\varepsilon_{\lambda\boldsymbol{k}+\boldsymbol{q}}}{\hbar\omega}+\mathcal{O}\left[\left(\frac{\varepsilon_{\lambda\boldsymbol{k}}-\varepsilon_{\lambda\boldsymbol{k}+\boldsymbol{q}}}{\hbar\omega}\right)^2\right]\right). \tag{4.6}$$

Notice that Eq. (4.5) ensures that $v_{\mathrm{F}}\left|\boldsymbol{q}\right| < \omega$, which is, as seen previously, necessary to obtain plasmons. Further, because of the smallness of q and the smoothness of $\varepsilon_{\lambda\boldsymbol{k}}$, the difference between the energy levels of the $\boldsymbol{k}$ and the $\boldsymbol{k}+\boldsymbol{q}$ state can be approximated as

$$\varepsilon_{\lambda\boldsymbol{k}} - \varepsilon_{\lambda\boldsymbol{k}+\boldsymbol{q}} = \sum_{i} q_i \frac{\varepsilon_{\lambda\boldsymbol{k}} - \varepsilon_{\lambda\boldsymbol{k}+\boldsymbol{q}}}{q_i} \approx -\boldsymbol{q}\cdot\boldsymbol{\nabla}_{\boldsymbol{k}}\varepsilon_{\lambda\boldsymbol{k}}. \tag{4.7}$$

Finally, a similar procedure can be used to express the difference between the occupation probability at $T=0$ as

$$n_{\lambda\boldsymbol{k}} - n_{\lambda\boldsymbol{k}+\boldsymbol{q}} = \sum_{i} q_i \frac{n_{\lambda\boldsymbol{k}} - n_{\lambda\boldsymbol{k}+\boldsymbol{q}}}{q_i} \approx \delta\left(\varepsilon_{\lambda\boldsymbol{k}} - E_{\mathrm{F}}\right)\boldsymbol{q}\cdot\boldsymbol{\nabla}_{\boldsymbol{k}}\varepsilon_{\lambda\boldsymbol{k}}. \tag{4.8}$$

This yields an approximate expression for the response function

$$\chi^{(0)}_{nn}\left(\boldsymbol{q},\omega\right) = \frac{g_{\mathrm{s}}}{L^2}\sum_{\boldsymbol{k}\in\mathrm{BZ}}\delta\left(\varepsilon_{\boldsymbol{k}} - E_{\mathrm{F}}\right)\frac{\boldsymbol{q}\cdot\boldsymbol{\nabla}_{\boldsymbol{k}}\varepsilon_{\boldsymbol{k}}}{\hbar\omega}\left(1+\frac{\boldsymbol{q}\cdot\boldsymbol{\nabla}_{\boldsymbol{k}}\varepsilon_{\boldsymbol{k}\cdot}}{\hbar\omega}\right). \tag{4.9}$$

In Eq. (4.9) the summation over the band variable λ and λ' has been performed and dropped from the notation, i.e. $\varepsilon_{\boldsymbol{k}} \equiv \varepsilon_{+1\boldsymbol{k}}$. Further the spin degeneracy has been accounted for through $g_{\mathrm{s}} = 2$.

4.2 Calculation in the valley basis

In the derivation presented in the previous section, apart from the smoothness, there has been no assumption on the specific form of $\varepsilon_{\lambda\boldsymbol{k}}$. Eq. (4.9) shows that the response function depends on the sum over the (trigonally warped) Fermi circle of the projection of the wave vector $\boldsymbol{q}$ on the gradient of the energy spectrum. Up to second order in q, Eq. (4.9) can be written as

$$\chi^{(0)}_{nn}\left(\boldsymbol{q},\omega\right) = \chi^{(0),1}_{nn}\left(\boldsymbol{q},\omega\right) + \chi^{(0),2}_{nn}\left(\boldsymbol{q},\omega\right), \tag{4.10}$$

where

$$\chi^{(0),j}_{nn}\left(\boldsymbol{q},\omega\right) = \frac{g_{\mathrm{s}}}{L^2}\sum_{\boldsymbol{k}\in\mathrm{BZ}}\delta\left(\varepsilon_{\boldsymbol{k}} - E_{\mathrm{F}}\right)\left(\frac{\boldsymbol{q}\cdot\boldsymbol{\nabla}_{\boldsymbol{k}}\varepsilon_{\boldsymbol{k}}}{\hbar\omega}\right)^j. \tag{4.11}$$

For graphene, if $E_{\mathrm{F}} < t$, the Fermi circle consists of two closed curves centred around the two Dirac points $\boldsymbol{K}$ and $\boldsymbol{K}'$ that determine the energy valleys as shown in Fig. 4.1. Notice that the two disjunct curves can be mapped onto each other by the transformation $\theta \to \theta+\pi$, where θ is the angle with the k_x-axis. This means that the summation over both curves will return the same quantity and, therefore, can be included as a valley degeneracy

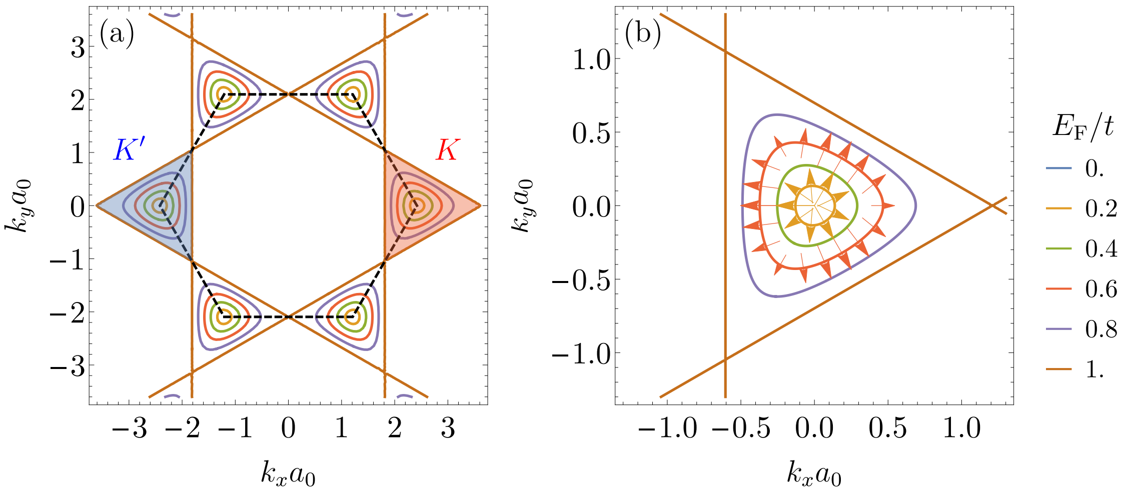

Figure 4.1: Fermi circles in graphene in reciprocal space for Fermi energies up to t. (a) The black dashed hexagon denotes the first Brillouin zone. The shaded triangles indicate the two energy valleys. Note that parts of the shaded energy valleys are outside the first Brillouin zone. They however represent the neighbourhood near the other two equivalent Dirac points and can be connected with a reciprocal lattice vector. (b) Zoom around the K-point with the arrows indicating $\boldsymbol{\nabla}\varepsilon_{\boldsymbol{k}}$ on the energy contour.

factor $g_{\mathrm{v}} = 2$. Further, because the graphene lattice has a hexagonal structure, the system is invariant under a rotation of an integer times $\phi_3 = 2\pi/3$. This symmetry is readily reflected in the energy spectrum shown in Fig. 4.1.

Upon explicitly calculating the first expression for the response function Eq. (4.11), one obtains

$$\begin{aligned}\chi^{(0),1}_{nn}(\boldsymbol{q},\omega) &= N_{\mathrm{f}} \int_0^{2\pi} \frac{d\theta}{2\pi} \int_0^{\infty} \frac{dk}{2\pi} k \delta\left(\varepsilon_{\boldsymbol{k}} - E_{\mathrm{F}}\right) \frac{\boldsymbol{q}\cdot\boldsymbol{\nabla}_{\boldsymbol{k}}\varepsilon_{\boldsymbol{k}}}{\hbar\omega}, \\ &= \frac{N_{\mathrm{f}} q}{(2\pi)^2 \hbar\omega} \int_0^{2\pi} d\theta k_{\mathrm{F}}(\theta) \frac{\left|\boldsymbol{\nabla}_{\boldsymbol{k}}\varepsilon_{\boldsymbol{k}}\right|_{k_{\mathrm{F}}(\theta)}}{\left|\partial_k \varepsilon_{\boldsymbol{k}}\right|_{k_{\mathrm{F}}(\theta)}} \cos\left(\theta_{\boldsymbol{q},\boldsymbol{\nabla}}\right). \end{aligned} \tag{4.12}$$

Here, $N_{\mathrm{f}} = g_{\mathrm{s}} g_{\mathrm{v}}$ as before, $k_{\mathrm{F}}(\theta)$ is the Fermi vector describing the Fermi circle as shown such that $\varepsilon_{k_{\mathrm{F}}(\theta)} = E_{\mathrm{F}}$, ∂_k denotes the partial derivative with respect to the magnitude of the vector $\boldsymbol{k}$, the notation $|\ldots|_{k_{\mathrm{F}}(\theta)}$ denotes evaluation at $k = k_{\mathrm{F}}(\theta)$ and $\theta_{\boldsymbol{q},\boldsymbol{\nabla}}$ is the angle between the wave vector $\boldsymbol{q}$ and the gradient of the energy.

Now one can use the symmetry of the system to rewrite the angular integration as

$$\int_0^{2\pi/3} d\theta k_{\mathrm{F}}\left(\theta\right) \frac{\left|\boldsymbol{\nabla}_{\boldsymbol{k}}\varepsilon_{\boldsymbol{k}}\right|_{k_{\mathrm{F}}(\theta)}}{\left|\partial_k\varepsilon_{\boldsymbol{k}}\right|_{k_{\mathrm{F}}(\theta)}} \left[\cos\left(\theta_{\boldsymbol{q},\boldsymbol{\nabla}}\right) + \cos\left(\theta_{\boldsymbol{q},\boldsymbol{\nabla}} + \phi_3\right) + \cos\left(\theta_{\boldsymbol{q},\boldsymbol{\nabla}} + 2\phi_3\right)\right] = 0. \tag{4.13}$$

Because of the symmetry under a rotation over a multiple of ϕ_3, the integrand is also invariant except for the angle $\theta_{\boldsymbol{q},\boldsymbol{\nabla}}$. As a consequence, the sum of the three $\cos$ terms appearing between the brackets vanishes for every angle $\theta_{\boldsymbol{q},\boldsymbol{\nabla}}$ and the first order contribution is zero. This is shown in Fig. 4.1(b) where the direction of the gradient of the energy spectrum is shown on different energy contours. It is clear that one can combine the different vectors in groups of three that all cancel each other.

The second order contribution is

$$\chi_{nn}^{(0),2}\left(\boldsymbol{q},\omega\right) = \frac{N_{\mathrm{f}} q^2}{\left(2\pi\right)^2 \left(\hbar\omega\right)^2} \int_0^{2\pi} d\theta k_{\mathrm{F}}\left(\theta\right) \frac{\left|\boldsymbol{\nabla}_{\boldsymbol{k}}\varepsilon_{\boldsymbol{k}}\right|^2_{k_{\mathrm{F}}(\theta)}}{\left|\partial_k\varepsilon_{\boldsymbol{k}}\right|_{k_{\mathrm{F}}(\theta)}} \cos^2\left(\theta_{\boldsymbol{q},\boldsymbol{\nabla}}\right). \tag{4.14}$$

The $\cos^2$ term can be rewritten as $\cos^2\left(\theta_{\boldsymbol{q},\boldsymbol{\nabla}}\right) = \frac{1}{2}\left(1 + \cos\left(2\theta_{\boldsymbol{q},\boldsymbol{\nabla}}\right)\right)$. Subsequently, the contributions of the cosine terms cancel due to trigonal symmetry and, therefore, up to second order in q, the density-density response function is

$$\chi_{nn}^{(0)}\left(q,\omega\right) \equiv \chi_{nn}^{(0)}\left(\boldsymbol{q},\omega\right) = \frac{D\left(E_{\mathrm{F}}\right)}{2\pi} \frac{\bar{q}^2}{2\bar{\omega}^2} \frac{1}{\hbar v_{\mathrm{F}}} \int_0^{2\pi} d\theta \bar{k}_{\mathrm{F}}\left(\theta\right) \frac{\left|\boldsymbol{\nabla}_{\boldsymbol{k}}\varepsilon_{\boldsymbol{k}}\right|^2_{k_{\mathrm{F}}(\theta)}}{\left|\partial_k\varepsilon_{\boldsymbol{k}}\right|_{k_{\mathrm{F}}(\theta)}}. \tag{4.15}$$

Here $\bar{q}$ and $\bar{\omega}$ are the usual dimensionless wave vector and frequency and the angular Fermi wave vector is $\bar{k}_{\mathrm{F}}\left(\theta\right) \equiv \hbar v_{\mathrm{F}} k_{\mathrm{F}}\left(\theta\right)/E_{\mathrm{F}}$. Furthermore, it was made explicit that the result does not depend on the angle of $\boldsymbol{q}$ in the system. Note that this is solely due to the trigonal symmetry of the crystal.

4.3 Response function of a warped conic spectrum

In the previous section it has been shown on general grounds that the trigonal lattice symmetry exactly cancels all angular contributions of the wave vector $\boldsymbol{q}$ to the response function. However, it is clear that the trigonal warping at large Fermi levels still affects the magnitude of the response function. The effect is quantified in this section for a simple trigonally warped spectrum.

To second order in k, the energy spectrum around the K point is [72]

$$\varepsilon_{\boldsymbol{k}} = \hbar v_{\mathrm{F}} k \left(1 - \frac{k a_0}{4} \cos\left(3\theta\right)\right). \tag{4.16}$$

In Eq. (4.16), θ is the angle with the k_x-axis. In this expression, a_0 can be used as a knob to turn on and off the trigonal warping at constant $\hbar v_\mathrm{F}$. Notice that although next-nearest-neighbour hopping also affects the energy spectrum up to second order in k by introducing an electron-hole symmetry breaking term [72], this has been neglected in the presented model because it does not qualitatively change the physical picture. Fig. 4.2 compares the full energy spectrum from Eq. (2.15) with the trigonally warped approximation from Eq. (4.16). The approximation holds for energy values up to $E_\mathrm{F} \simeq 0.8t$.

Corresponding to the energy spectrum, one can determine a Fermi wave vector $k_\mathrm{F}\left(\theta\right)$ that depends on the angle θ with the k_x axis. Form Eq. (4.16) this becomes

$$k_\mathrm{F}\left(\theta\right) = 2\frac{1-\sqrt{1-E_\mathrm{F}'\cos\left(3\theta\right)}}{a_0\cos\left(3\theta\right)}, \tag{4.17}$$

where $E_\mathrm{F}' \equiv E_\mathrm{F}a_0/\left(\hbar v_\mathrm{F}\right) = 2E_\mathrm{F}/(3t)$ is the dimensionless parameter controlling the strength of the trigonal warping. Notice that in the limit $a_0 \to 0$ the unwarped definition for the Fermi wave vector is reobtained.

The integrand of Eq. (4.15) can be calculated as

$$k_\mathrm{F}\left(\theta\right)\frac{\left|\boldsymbol{\nabla}_{\boldsymbol{k}}\varepsilon_{\boldsymbol{k}}\right|^2_{k_\mathrm{F}(\theta)}}{\left|\partial_k\varepsilon_{\boldsymbol{k}}\right|_{k_\mathrm{F}(\theta)}} = k_\mathrm{F}\left(\theta\right)\left(\left|\partial_k\varepsilon_{\boldsymbol{k}}\right|_{k_\mathrm{F}(\theta)} + \frac{\left|k^{-1}\partial_\theta\varepsilon_{\boldsymbol{k}}\right|^2_{k_\mathrm{F}(\theta)}}{\left|\partial_k\varepsilon_{\boldsymbol{k}}\right|_{k_\mathrm{F}(\theta)}}\right), \tag{4.18}$$

where ∂_θ denotes the partial derivative with respect to the angle θ. The two terms in brackets are

$$\left|\partial_k\varepsilon_{\boldsymbol{k}}\right|_{k_\mathrm{F}(\theta)} = \hbar v_\mathrm{F}\sqrt{1-E_\mathrm{F}'\cos\left(3\theta\right)}, \tag{4.19}$$

$$\frac{\left|k^{-1}\partial_\theta\varepsilon_{\boldsymbol{k}}\right|^2_{k_\mathrm{F}(\theta)}}{\left|\partial_k\varepsilon_{\boldsymbol{k}}\right|_{k_\mathrm{F}(\theta)}} = \frac{9}{4}\hbar v_\mathrm{F}\left(\sqrt{1-E_\mathrm{F}'\cos\left(3\theta\right)} + \frac{1}{\sqrt{1-E_\mathrm{F}'\cos\left(3\theta\right)}} - 2\right)\tan^2\left(3\theta\right). \tag{4.20}$$

In Fig. 4.2 the numerical evaluation of the angular integral in Eq. (4.15) is shown and compared with the unwarped spectrum. It is clear that only at Fermi levels approaching the hopping parameters t, the contribution of the trigonal warping terms become important.

4.4 Plasmons in a trigonally warped spectrum

From Eq. (4.15), it is immediately clear that the plasmon dispersion does not obtain an angular dependence due to trigonal warping. The plasmon dispersion can be calculated as

$$\omega_\mathrm{pl}\left(q\right) = \sqrt{\frac{2\mathcal{D}\left(E_\mathrm{F}'\right)}{\epsilon}q}\,, \tag{4.21}$$

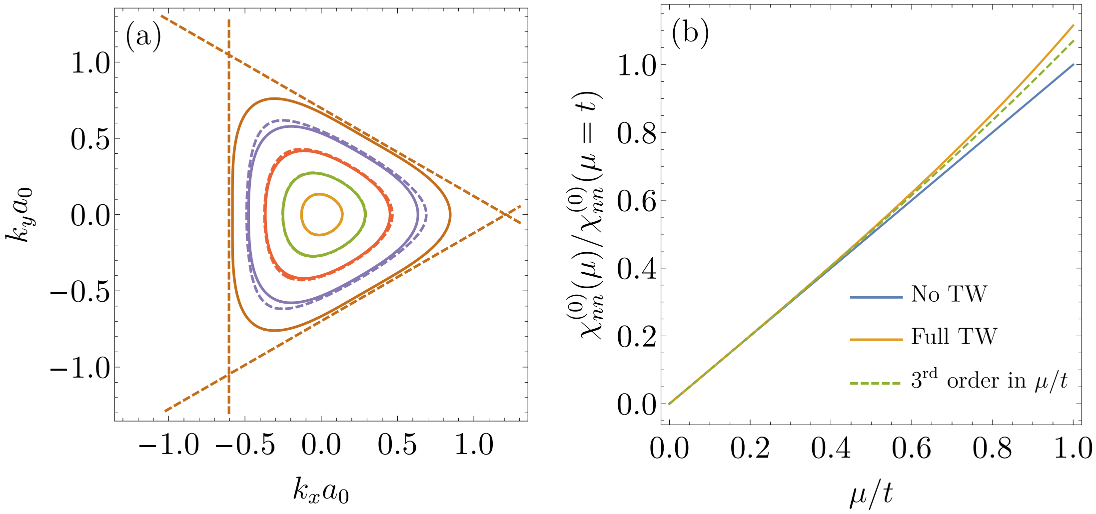

Figure 4.2: (a) Energy contours of the full dispersion (dashed curves) and the approximate dispersion from Eq. (4.16). (b) Ratio of the response function with trigonal warping with respect to the unwarped response function as indicated in the legend.

where $\mathcal{D}\left(E'_{\mathrm{F}}\right)$ is the graphene Drude weight as defined in Eq. (3.139) but renormalised due to trigonal warping. This equation makes clear that trigonal warping affects the plasmons by renormalizing the Drude weight. In Fig. 4.3 the plasmon dispersion is shown for different values of the Fermi level. Only for large chemical potential there is a discernable effect of the trigonal warping.

The integral can be determined analytically by expanding the integrand in powers of the dimensionless parameter E'_{F}. Up to second order one obtains

$$\bar{k}_{\mathrm{F}} = 1+\frac{1}{4}E'_{\mathrm{F}}\cos\left(3\theta\right)+\frac{1}{8}E'^{2}_{\mathrm{F}}\cos^{2}\left(3\theta\right), \tag{4.22}$$

$$\left|\partial_k\varepsilon_{\boldsymbol{k}}\right|_{k_{\mathrm{F}}(\theta)} = \hbar v_{\mathrm{F}}\left(1-\frac{1}{2}E'_{\mathrm{F}}\cos\left(3\theta\right)-\frac{1}{8}E'^{2}_{\mathrm{F}}\cos^{2}\left(3\theta\right)\right)+\mathcal{O}\left[E'^{3}_{\mathrm{F}}\right], \tag{4.23}$$

$$\frac{\left|k^{-1}\partial_\theta\varepsilon_{\boldsymbol{k}}\right|^2_{k_{\mathrm{F}}(\theta)}}{\left|\partial_k\varepsilon_{\boldsymbol{k}}\right|_{k_{\mathrm{F}}(\theta)}} = \frac{9}{16}\hbar v_{\mathrm{F}}E'^{2}_{\mathrm{F}}\sin^{2}\left(3\theta\right)+\mathcal{O}\left[E'^{3}_{\mathrm{F}}\right]. \tag{4.24}$$

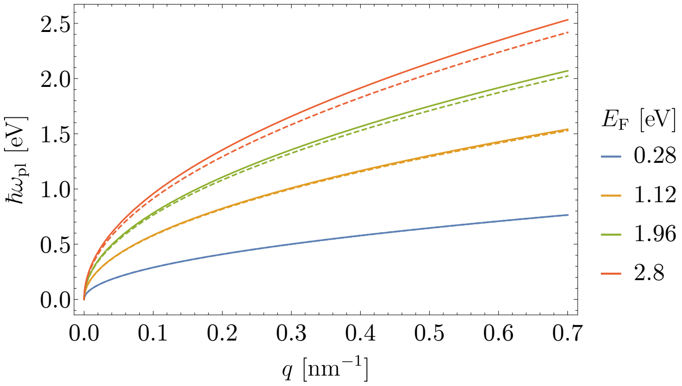

Figure 4.3: Plasmon dispersion in a trigonaly warped spectrum. The solid curves are the unwarped results, the dashed curves correspond tot the result with warping taken into account up to third order.

Therefore the integral becomes

$$\begin{aligned}\chi^{(0)}_{nn}(q,\omega) &= \frac{D(E_{\rm F})}{2\pi}\frac{\bar{q}^2}{2\bar{\omega}^2}\int_0^{2\pi}d\theta\left[1+\frac{9}{16}E_{\rm F}'^2-\frac{1}{4}E_{\rm F}'\cos(3\theta)-\frac{13}{16}E_{\rm F}'^2\cos^2(3\theta)\right]\\ &= D(E_{\rm F})\frac{\bar{q}^2}{2\bar{\omega}^2}\left[1+\frac{5}{32}E_{\rm F}'^2+\mathcal{O}\left[E_{\rm F}'^4\right]\right]. \qquad (4.25)\end{aligned}$$

Notice that any odd power in $E_{\rm F}'$ will be accompanied by an odd power of a $\cos(3\theta)$ or $\sin(3\theta)$ and will therefore not contribute due after angular integration. Subsequently, the response function is up to third order in $E_{\rm F}/t$

$$\chi^{(0)}_{nn}(q,\omega) = D(E_{\rm F})\frac{\bar{q}^2}{2\bar{\omega}^2}\left[1+\frac{5}{72}\left(\frac{E_{\rm F}}{t}\right)^2+\mathcal{O}\left[\left(\frac{E_{\rm F}}{t}\right)^4\right]\right]. \qquad (4.26)$$

In Fig. 4.2 the response function from Eq. (4.26) is compared with the full numerical solution that was obtained by performing the integration from Eq. (4.15). It is clear that this approximation describes the full solution very well.

Using Eq. (4.26), one can now calculate the renormalisation of the Drude weight due to trigonal warping. The result is:

$$\mathcal{D}\left(\frac{E_{\rm F}}{t}\right) = \mathcal{D}_{\rm MDF}\left[1+\frac{5}{72}\left(\frac{E_{\rm F}}{t}\right)^2+\mathcal{O}\left[\left(\frac{E_{\rm F}}{t}\right)^4\right]\right]. \qquad (4.27)$$

4.5 Numerical analysis outside the small q and ω limit

Up to now, the analysis of the response function and the corresponding plasmons was performed in the plasmonic limit, i.e. $\hbar v_{\mathrm{F}} q < \hbar\omega \ll E_{\mathrm{F}}$. In order to show that the invariance of the plasmon dispersion under rotation with respect to the crystal is not an artefact of the approximation, the full integral from Eq. (4.2) was performed numerically over the entire graphene Brillouin zone for an electron doping of $E_{\mathrm{F}} = 2$ eV. This corresponds to a carrier concentration $n \simeq 3 \times 10^{14}\ \mathrm{cm}^{-2}$, which corresponds to the current upper boundary for chemical doping [100].

In Fig. 4.4 the plasmon dispersion is shown for several angles between for the entire range of q and ω up to the intersection of the plasmon with the inter-band particle-hole continuum. It is clear that also for large momentum and frequency the plasmon dispersion remains unaffected by trigonal warping.

Recently, the plasmon dispersion has been calculated for a graphene flake under strain [140]. There it was noted that the dispersion does change with the direction of the wave vector $\boldsymbol{q}$. This shows that it is the trigonal symmetry of the lattice that protects the plasmon dispersion from being affected by warping. If the symmetry is broken, then the dispersion does acquire an angular dependence. Vice versa, this effect could be used to measure the strain in a graphene flake by examining the plasmon dispersion in different directions.

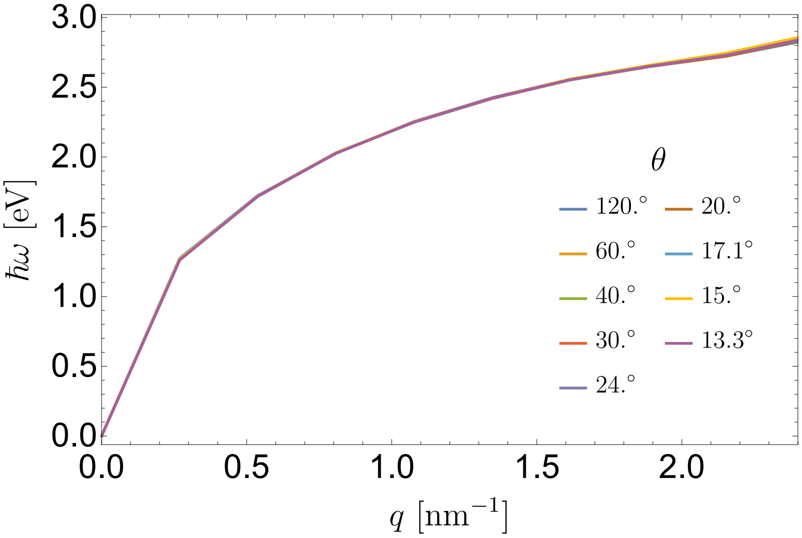

Figure 4.4: Numerically obtained plasmon dispersion for arbitrary angles with respect to the k_x-axis as indicated. The numerical calculation shows that the dispersion does not depend on the angle of $\boldsymbol{q}$ in the plane. The calculation was performed with the numerical code that previously determined the effect of strain on the density response function [140].

CHAPTER 5

Plasmons in topological graphene superlattices

How can one excite charge neutral plasmons by valley polarising a graphene flake?

This chapter is devoted to the discussion of plasmons in a graphene flake that is deposited on, or encapsulated by, slabs of hexagonal boron nitride (hBN). Research on graphene/hBN (g/hBN) heterostructures has recently been surging at a tremendous pace after the discovery that in this way one can make ultra-clean samples with exceptionally high carrier mobilities. However, the hBN environment also affects the electronic properties of the graphene flake. Being a hyperbolic metamaterial, it has an unusual optical response that couples to the graphene plasmons in certain frequency ranges. Finally, the substrate also affects the crystallographic properties of graphene and changes the topological character of the energy bands by introducing a hexagonal superlattice.

It is clear that the g/hBN system is very rich in its physical processes and therefore very interesting as an application of the LRT framework developed in the previous chapter. In this chapter, first a small review about the current research on g/hBN is given in Sec. 5.1 and then the origin of the peculiar structural properties that endow the graphene flake with a hexagonal superlattice is discussed in Sec. 5.2. The electronic properties of a valley imbalanced graphene system are outlined in Sec. 5.4 and the RPA theory for such a system is derived in Sec. 5.5. To describe the effect of the hBN environment on the e-e interaction in the graphene flake, the dielectric properties of hBN are discussed in Sec. 5.6 and finally the nature of plasmons in topological graphene superlattices is exemplified by numerical calculations in Sec. 5.7.

The research presented in this chapter will be published together with a study on edge plasmons in graphene superlattices as a joint publication.

5.1 Graphene and hBN, an ideal match

The peculiar electronic properties of graphene, as discussed in the previous chapter, were calculated for ideal hexagonal systems free from impurities, disorder, lattice deformations, special environmental conditions and much more. In an experimental set-up, however, one needs to be able to position and gate the graphene flake in the correct way in order to measure the proposed physics. In the early days, graphene was deposited on SiO_2 for mobility measurements. However, the SiO_2 substrate strongly affects the ideal graphene lattice by introducing structural deformations due to the rough surface of SiO_2 [174] or electron-phonon scattering [175]. Also charged impurities [176] and adsorbates [177] strongly limit the carrier's mobility. Mobilities in graphene on SiO_2 are typically of the order of $\mu \sim 10^4 \ \mathrm{cm}^2 \ \mathrm{V}^{-1}\mathrm{s}^{-1}$ [34], which is an order of magnitude below the theoretical limit of $\mu \sim 2 \times 10^5 \ \mathrm{cm}^2 \ \mathrm{V}^{-1}\mathrm{s}^{-1}$ for graphene at room temperature where the mobility is limited due to intrinsic electron-phonon interaction[36]. It is possible to boost this number by suspending a graphene flake such that the substrate does not interfere with the electronic properties. It was shown that suspended samples that are annealed by a strong current feature a mobility of the order of $\mu \sim 1.2 \times 10^5 \ \mathrm{cm}^2 \ \mathrm{V}^{-1}\mathrm{s}^{-1}$ at room temperature [178]. However, these suspended structures are often very fragile and, therefore, not very useful in experiments and applications.

In the search for better experimental set-ups to probe and use graphene's charge carriers, recently it was shown that exfoliated graphene deposited on hexagonal boron nitride gives very good results. This is due to the fact that the hBN surface can be made atomically smooth and is chemically inert [45]. It was shown that g/hBN can exhibit transport mobilities of the order of $\mu \sim 1.4 \times 10^5 \ \mathrm{cm}^2 \ \mathrm{V}^{-1}\mathrm{s}^{-1}$ [45]. This results in charge carriers that behave essentially ballistic over distances of the order of a micrometer [179] at room temperature.

Apart from featuring very high transport mobilities, the cleanness of the g/hBN structure also makes it a very good platform for the study of Dirac plasmons. Recently, a study of plasmons in graphene on hBN confirmed this by measuring record Dirac plasmons lifetimes in graphene encapsulated by hBN and that the plasmons feature an extraordinary strong electric field confinement [59, 153]. Another study showed that the peculiar bandstructure of g/hBN induces additional plasmon features in the infra-red [180]. The study of the plasmonic response of g/hBN structures is therefore very promising [143]. This chapter investigates Dirac plasmons in g/hBN structures within the RPA framework. The results of the study can be verified in existing optical set-ups.

5.2 Crystal and electronic structure of graphene on hBN

5.2.1 Commensurate and incommensurate stacking

If one positions a graphene flake on top of an hBN substrate, the two crystals interact with each other through van der Waals interaction between the surface atoms of hBN and the atoms in graphene, forming a so-called *van der Waals heterostructure* [47]. Both graphene and hBN have a hexagonal crystal structure, therefore, one can align the crystals in three possible commensurate configurations when stacking the two layers on top of each other. The first one consists of stacking carbon atoms on top of the boron atoms while the other carbon and nitrogen atoms are in the middle of the hexagon of the two crystals. This will be called BA-stacking and is energetically the most stable configuration [181]. However, one can also reverse it and stack a carbon atom on nitrogen, AB-stacking, or the two carbon atoms on top of both boron and nitrogen atoms, AA-stacking. The latter two are less stable than the former and, therefore, one expects the former to appear naturally.

However, the inter-atomic distance in the two crystals is slightly different. The ratio between the two lattice constants is $a_0^{\mathrm{hBN}}/a_0^{\mathrm{g}} - 1 \approx 1.8\%$ [182]. Therefore, it is clear that BA-stacking cannot persist over the entire system. Furthermore, the exact stacking of the layers also depends on the positioning of the two hexagonal lattices with respect to each other. One can combine the two materials such that the crystallographic axes of the graphene flake makes an angle of θ_{s} with those of the hBN. This provides a parameter that can be tuned to adjust the crystallographic alignment and it will turn out to be detrimental for the electronic properties of the system.

The first experiments of graphene on hBN showed that the graphene flake behaves electronically decoupled from the hBN crystal [45]. In the low energy sector, the graphene charge carriers still have a linear and gapless dispersion. However, later on it was shown that for larger electron energies, the spectrum does change and new so-called *satellite Dirac points* appeared at large energy [183, 184]. These satellite Dirac points were subsequently shown to stem from the superperiodic potential imposed on the graphene flake by the hBN [185].

The superperiodic potential arises due to the small lattice mismatch between the graphene and the hBN. As shown in Fig. 5.1(a) and (b), the stacking of two perfect crystals with slight difference in lattice constant on top of each other leads to the formation of so-called *Moiré patterns* [183, 186]. The size of these patterns depends on the angle θ_{s}. The ad-

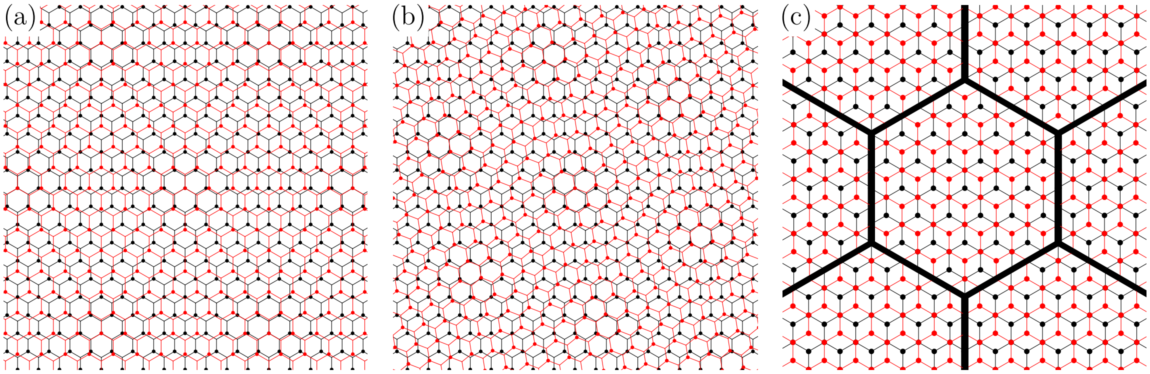

Figure 5.1: Schematic picture of the different possible stackings of graphene (black lattice) on hBN (red lattice). (a) Exact band alignment without structural relaxation of graphene. (b) A system where the two crystals are rotated with respect to each other. (c) A system of BA-stacking regions with stacking boundaries.

ditional periodicity imposed by the Moiré patterns changes the electronic spectrum by folding the bands above the graphene Brillouin zone back into the superlattice Brillouin zone (sBZ) [80]. Because the Moiré pattern is hexagonal, the sBZ also acquires a hexagonal shape with a similar system of high symmetry points as mentioned in Sec. 2.1.2. This is schematically shown in Fig. 5.2(a). In the corners of the sBZ the band energy bands touch each other again in a linear fashion, producing the satellite Dirac points as shown in Fig. 5.2(b). The generation of the satellite Dirac points was shown to hold for every hexagonal superperiodic potential applied to graphene [185].

Depending on the angle between the crystallographic axes of the two materials, the size of the Moiré pattern changes. Furthermore, for a fixed angle θ_s, the pattern can be seen as a system with local patches of AB-, BA- and AA-stacking and a continuous transition between these regions defined by the Moiré pattern. If the angle θ_s decreases to zero, however, a new type of crystal structure appears. As mentioned before, the energetically most favourable configuration is BA-stacking. Due to the difference in lattice constant between the graphene and hBN, also at $\theta_\mathrm{s} = 0$ some kind of Moiré pattern is formed where there is a continuous transition between the three different stacking possibilities as shown in Figs. 5.1 (a) and (b). However, as the AA- and AB-stacking is energetically unfavourable, it is possible that locally the bond lengths of the graphene flake adapt to the length of the hBN crystal. This change in graphene crystal structure builds up a local strain that is relaxed at lattice domain walls [181, 182]. This situation is shown in Fig. 5.1 (c). The transition between the configuration with a Moiré pattern (labelled an *incommensurate state*) and the configuration with hexagonal regions of BA-stacking separated by domain

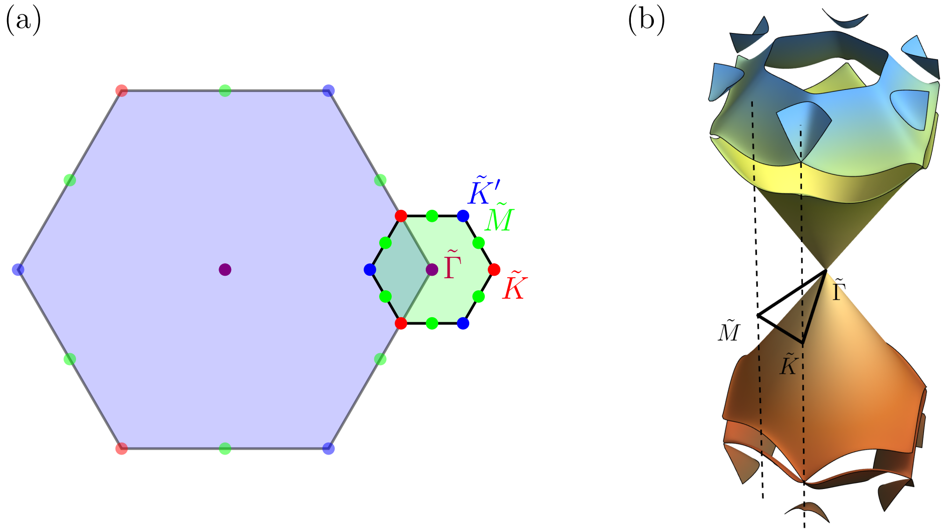

Figure 5.2: (a) Superlattice Brillouin zone (green) in reciprocal space around one of the K points of the normal graphene Brillouin zone (blue). The new high symmetry points are indicated. (b) Energy dispersion of graphene on hBN in the sBZ. At the superlattice K-points, the bands touch each other. This figure was adapted from Ref. [142].

walls (labelled a *commensurate state*) was found to occur at angles of the order of $\theta_{\mathrm{s}} \simeq 1^{\circ}$ [182]. Notice that both configurations can be modelled by applying a periodic potential to a graphene flake and therefore in both situations satellite Dirac points will occur. However, in the commensurate state this is accompanied by a global band gap because the different boron and nitrogen atoms affect the two graphene sublattices differently and therefore break the sublattice symmetry in all parts of the graphene flake in the same way [187].

Recently, it was shown that systems with commensurate stacking feature long-range topological currents that flow transversely to the applied electric field even in the absence of a magnetic field [187]. By very accurately aligning the edges of the graphene and hBN samples into a commensurate stacking, Gorbachev *et al.* measured a non-local voltage in the absence of a magnetic field when the Fermi level was tuned in the global band gap of the material. This signals a charge neutral valley current. The charge neutral valley current is a direct consequence of the topological properties of the Bloch bands as explained in the next section [188].

In this chapter, a g/hBN heterostructure with a commensurate stacking is considered. This kind of stacking is also called topological stacking since it bestows the energy bands with a topological character. The next section explains the origin of the topological structure and the appearance of a finite Hall conductivity that explains the valley currents observed in Ref. [187].

5.2.2 Topology of a gapped graphene system

The effect of a different potential to the two sublattices in graphene can be included in the continuum Hamiltonian Eq. (2.16) as a term proportional to σ_z:

$$H_{\boldsymbol{k}}^{\xi} = \hbar v_{\mathrm{F}} \left(\xi \sigma_x k_x + \sigma_y k_y\right) + \Delta \sigma_z \, . \tag{5.1}$$

In this Hamiltonian $\xi = \pm 1$ denotes the two energy valleys. In this case the system has a gap of 2Δ and an energy spectrum

$$\varepsilon_{\lambda \boldsymbol{k}} \equiv \lambda \varepsilon_{\boldsymbol{k}} = \lambda \sqrt{(\hbar v_{\mathrm{F}} k)^2 + \Delta^2} \, . \tag{5.2}$$

Here, $\lambda = \pm 1$ denotes the conduction (valence) band. The corresponding eigenstates are in the sublattice basis

$$\Psi_{\lambda \boldsymbol{k}}^{\xi} = \frac{1}{\sqrt{2\varepsilon_{\boldsymbol{k}} \left(\varepsilon_{\boldsymbol{k}} + \lambda \Delta\right)}} \begin{pmatrix} \Delta + \lambda \varepsilon_{\boldsymbol{k}} \\ \hbar v_{\mathrm{F}} \left(\xi k_x + i k_y\right) \end{pmatrix} . \tag{5.3}$$

For this system the Hall conductivity σ_{xy} will be calculated. The valley resolved Hall conductivity is related to the Berry curvature of the Bloch bands $\Omega_{k_x k_y}$ as [189, 190]

$$\sigma_{xy}^{\xi} = \frac{g_{\mathrm{s}} e^2}{\hbar} \sum_{\lambda = \pm 1} \int \frac{d\boldsymbol{k}}{(2\pi)^2} \Omega_{k_x k_y}^{\lambda, \xi} f_{\mathrm{D}}(\varepsilon_{\lambda \boldsymbol{k}}, \mu, T), \tag{5.4}$$

where e is the elementary charge and $g_{\mathrm{s}} = 2$ accounts for the spin degeneracy. The Berry curvature can be calculated as

$$\Omega_{k_x k_y}^{\lambda, \xi} = \partial_{k_x} A_y^{\lambda} - \partial_{k_y} A_x^{\lambda}, \tag{5.5}$$

where ∂_{k_j} is the derivative with respect to k_j and $\boldsymbol{A}^{\lambda}$ is the so-called Berry connection defined as

$$A_j^{\lambda} = i \left\langle \psi_{\lambda \boldsymbol{k}} \left| \partial_{k_j} \right| \psi_{\lambda \boldsymbol{k}} \right\rangle . \tag{5.6}$$

This allows to calculate the Berry connection for the gapped Dirac system under consideration as

$$A_x^{\lambda} = \frac{\hbar v_{\mathrm{F}} k_y}{2\varepsilon_{\boldsymbol{k}} \left(\varepsilon_{\boldsymbol{k}} + \lambda \Delta\right)} \text{ and } A_y^{\lambda} = \frac{-\hbar v_{\mathrm{F}} \xi k_x}{2\varepsilon_{\boldsymbol{k}} \left(\varepsilon_{\boldsymbol{k}} + \lambda \Delta\right)} . \tag{5.7}$$

Finally, the Berry curvature is obtained

$$\Omega^{\lambda,\xi}_{k_x k_y} = \frac{\xi\lambda\left(\hbar v_{\mathrm{F}}\right)^2\Delta}{2\varepsilon^3_{\boldsymbol{k}}}. \tag{5.8}$$

Using Eqs. (5.4) and (5.8), the valley resolved conductivity can be calculated. If the system is undoped, such that the Fermi level lies in the gap, the Hall conductivity becomes at $T = 0$

$$\sigma^{\xi,\mathrm{u}}_{xy} = \xi g_{\mathrm{s}}\frac{e^2}{2h}\frac{\Delta}{|\Delta|} = \xi g_{\mathrm{s}}\frac{e^2}{2h}\mathrm{sgn}\left(\Delta\right). \tag{5.9}$$

This result shows that the Hall conductivity is non-zero if the Fermi level is in the gap. However, the total Hall conductivity does vanish since the contributions of the two valleys, $\xi = \pm 1$ compensate each other. If the Fermi level is larger than the gap, i.e. $E_{\mathrm{F}} > \Delta$, then the conduction band is occupied and the Hall conductivity becomes

$$\begin{aligned}\sigma^{\xi,E_{\mathrm{F}}}_{xy} &= \sigma^{\xi,\mathrm{u}}_{xy} + \frac{g_{\mathrm{s}}e^2}{h}\xi\Delta\int_0^\infty dk\frac{\left(\hbar v_{\mathrm{F}}\right)^2 k}{2\varepsilon^3_{\boldsymbol{k}}}\Theta\left[E_{\mathrm{F}} - \varepsilon_{\boldsymbol{k}}\right] \\ &= \sigma^{\xi,\mathrm{u}}_{xy} + g_{\mathrm{s}}\frac{e^2}{2h}\xi\Delta\left[\frac{1}{E_{\mathrm{F}}} - \frac{1}{|\Delta|}\right] \\ &= \xi g_{\mathrm{s}}\frac{e^2}{2h}\frac{\Delta}{E_{\mathrm{F}}}. \end{aligned} \tag{5.10}$$

As a result, one sees that the Hall conductivity decreases inversely proportional to the Fermi level. Therefore, the effect is strongest when the Fermi level is close to the edge of the gap.

The Hall conductivity is related to the transverse current-current response function as defined in Sec. 3.1.8 in the same way as the longitudinal current-current response function is related to the optical conductivity σ_{xx}. The Hall conductivity describes the response of the electron liquid to an external electric field in the direction perpendicular to that electric field, i.e. $J_x = \sigma_{xy}E_y$. The preceding calculations, however, showed that the Hall conductivity is opposite in both valleys and, therefore, the response to an applied electric field will also be opposite in the K and K' valleys. Now one can define the so-called *valley current* J^{v} as

$$J^{\mathrm{v}}_x = J^K_x - J^{K'}_x = \sigma^{\mathrm{v}}_{xy}E_y. \tag{5.11}$$

This current is charge neutral since the same amount of charge propagates in opposite direction. However, its response can be measured by a non-local resistance measurement as shown in the left panel of Fig. 5.3. The quantity σ^{v}_{xy} is twice the single valley Hall conductivity. The energy dependence of the Hall conductivity is shown in the right panel of Fig. 5.3.

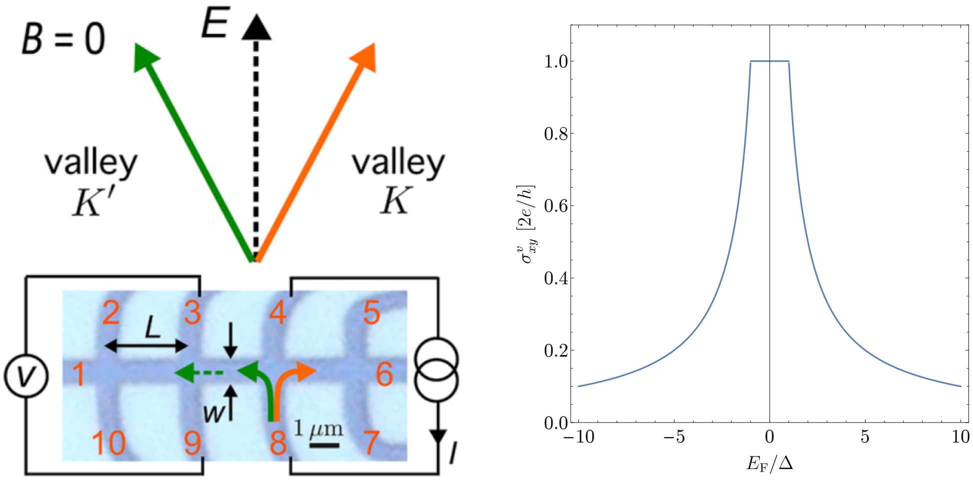

Figure 5.3: Left: Set-up to measure the non-local resistance due to the valley current. The orange arrows depict the flow in the K valley while the green arrows correspond to the K' valley. The resistance is measured over contacts 3 and 9, while the current flows from contact 8 to 4. The perpendicular current component is generated due to a non-zero Hall conductivity and flows oppositely in both valleys. This figure is adapted from Ref. [187]. Right: Fermi level dependence of the valley Hall conductivity σ_{xy}^{v}.

Notice that the valley current is generated solely by the band topology. However, in contrast with the commonly known topological states that live at the edge of a topological insulator, this valley current is a bulk current. Therefore, it only occurs when the Fermi level is tuned in the conduction or valence band and, in contrast with topological states, the corresponding Hall conductivity is not quantized as shown in Eq. (5.10). Therefore this material is sometimes dubbed a *topological conductor* and the currents are called *topological currents* [187].

As shown in Eq. (5.4), the conductivity is defined as an integration of the Berry curvature over reciprocal space. In the example at hand, the Hamiltonian is an effective model and was integrated over the entire 2D plane. In the case of g/hBN, however, one needs to perform the integration over the sBZ. Recently, it was noted that the way in which the Berry curvature is distributed over the sBZ depends on whether the stacking is commensurate or incommensurate. As shown in Fig. 5.4, if the stacking is commensurate, the contribution of the Berry curvature of the same band has the same sign throughout the band, while for an incommensurate system the contribution near the original Dirac point compensates that of the satellite Dirac points. Therefore, the total so-called *Chern*

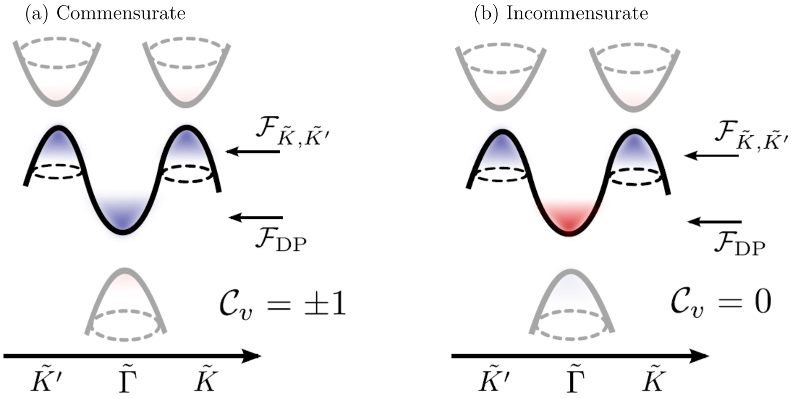

Figure 5.4: Schematical picture of the distribution of the Berry curvature over the energy bands of graphene on hBN for commensurate stacking (left) and incommensurate stacking (right). The Berry curvature is shown as a shading which is blue for a positive contribution and red for a negative contribution. It is clear that the Berry curvature is the largest near the edge of the Bloch bands. These regions are called the Berry curvature hot spots. Figure adapted from Ref. [188].

invariant C_{v}, defined as

$$C_{\mathrm{v}} = \int_{\mathrm{sBZ}} \frac{d\boldsymbol{k}}{2\pi} \Omega^{\lambda,\xi}_{k_x k_y}, \tag{5.12}$$

vanishes in the incommensurate case while it equals ± 1 in the commensurate case. Bands with a non vanishing Chern invariant are called *topological bands* and are of interest because they feature measurable topologically induced effects that are not compensated for opposite Berry curvature in an other part of the band. The topological currents detected in Ref. [187] were shown to be present in g/hBN in a commensurate stacking while not detectable in an incommensurate stacking.

5.2.3 Valley selective optical pumping

Having a different Hall conductivity in the two valleys allows to optically pump the two valleys separately by using circularly polarised light. Indeed, it was shown that for gapped graphene, the transition amplitude for inter-band processes near the Dirac point reduces to [191]

$$\left|\mathcal{P}_{\pm}(\boldsymbol{k})\right|^2 \sim \left(1 \mp \xi \frac{\Delta}{\varepsilon_{\boldsymbol{k}}}\right)^2, \tag{5.13}$$

where $\mathcal{P}_{\pm}(\boldsymbol{k}) = \left\langle \psi_{1\boldsymbol{k}} \middle| \hat{k}_x \pm i\hat{k}_y \middle| \psi_{-1\boldsymbol{k}} \right\rangle$ denotes the transition by a right-handed (left-handed) polarised light source. The response of the system is different because of the finite

Berry curvature [191]. Eq. (5.13) shows that the response is valley selective. If the Fermi level is tuned just above the gap, $\Delta/\varepsilon_{\boldsymbol{k}} \approx 1$, and then the K valley can be pumped by left-handed polarised light only while the K' valley is affected by right-handed polarised light.

The interplay of the Berry curvature and the circular polarisation of light therefore leads to valley selective interaction and if the frequency of the light is larger than the band gap 2Δ, it is possible to valley selectively pump carriers from the valence band in the conduction band. Valley selective pumping was shown before to be possible in a similar gapped system with two valleys, namely $\mathrm{MoS_2}$ [192, 193]. It is expected that the same is also possible in graphene on hBN with topological bands.

In the remainder of this chapter, the plasmonic response of a valley imbalanced system is discussed. This system can be created by valley selective pumping as discussed above or by populating the two valleys in a different way by e.g. valley selective transport [194, 195].

5.3 Model of the energy bands

The charge carriers in g/hBN are modelled as moving in a superlattice formed by stacking boundaries which can be described by an effective Hamiltonian as [188]

$$H = \hbar v_{\mathrm{F}} \boldsymbol{\sigma} \cdot \boldsymbol{k} + \Delta(\boldsymbol{r}) \sigma_z \ , \tag{5.14}$$

where $v_{\mathrm{F}} \simeq 10^6\ \mathrm{m/s}$ is the graphene Fermi velocity, $\boldsymbol{k}$ is the carrier's 2D wave vector, σ_i are the Pauli matrices and $\Delta(\boldsymbol{r})$ describes the hBN coupling to graphene as a periodic scalar potential

$$\Delta(\boldsymbol{r}) = \Delta_{\mathrm{g}} + m_3 \sum_{j=1}^{3} \cos(\boldsymbol{b}_j \cdot \boldsymbol{r}) \ . \tag{5.15}$$

In Eq. (5.15), Δ_{g} is the global band gap in the system and m_3 describes the Bragg scattering that introduces the avoided crossings at the edge of the superlattice Brillouin zone (sBZ) with $\boldsymbol{b}_j$ the reciprocal lattice vectors of the superlattice. For a commensurate stacking the signs of Δ_{g} and m_3 are equal, which was shown to be the origin of the finite Chern invariant of the topological Bloch bands [188]. Furthermore, the value of the global band gap has been measured [187] to be about $2\Delta_{\mathrm{g}} \simeq 30\ \mathrm{meV}$. This value will be used in the calculations presented in this chapter.

Due to the superlattice potential the energy spectrum is folded into a smaller Brillouin zone, the sBZ, around the K and K' points in reciprocal space. This hexagonal sBZ has new points of high symmetry that we denote by $\tilde{\Gamma}$, $\tilde{K}^{(\prime)}$ and $\tilde{M}$ as shown in Fig. 5.2. The $\tilde{\Gamma}$ point coincides with the old $K^{(\prime)}$ point.

In Fig. 5.5 the energy bands $\varepsilon_{\boldsymbol{k}}$ are shown along the high symmetry points of the sBZ for both valleys in the case of commensurate stacking. At large energy, one notices that the spectrum features mini Dirac points that are gapped due to the finite value of m_3. At the $\widetilde{\Gamma}$ point the spectrum is also gapped by the global gap $\Delta_{\rm g}$. On top of the numerically calculated energy bands, the results of an approximative model are shown as a dashed green curve. This model neglects the superlattice potential from Eq. (5.14) and only retains the global gap $\Delta_{\rm g}$ such that the Hamiltonian reduces to the one shown in Eq. (5.1). It is clear that this approximative model describes very well the energy spectrum up to $\varepsilon_{\boldsymbol{k}} \simeq \pm 300$ meV. Furthermore, the advantage of the use of this model is that the energy spectrum can be expressed analytically as

$$\varepsilon_{\lambda,\boldsymbol{k}} = \lambda\sqrt{(\hbar v_{\rm F} k)^2 + \Delta^2}\ . \tag{5.16}$$

In Eq. (5.16), Δ is the energy gap in the system and $\lambda = 1\ (-1)$ denotes the conduction (valence) band. Note that this Δ is not necessarily equal to the global gap $\Delta_{\rm g}$ defined in Eq. (5.15).

The presence of mini-cones at the superlattice Dirac points have previously been shown to induce a peculiar plasmonic response with the plasmons morphing from a hole-like plasmon for Fermi level just below the crossing to an electron-like just above it [142]. Furthermore, it was shown that new plasmon modes in the IR appear due to transitions related to these mini-cones [196]. In this chapter, the focus will be on samples with a Fermi level that is low enough not to be affected by the mini-cones.

5.4 Electronic properties in a valley imbalanced system

Without loss of generality, an electron doped system is considered. The hole response can be easily found by using particle-hole symmetry. If the conduction band has a carrier concentration of $n_{\rm tot}$, then the corresponding Fermi level $E_{\rm F}$ at $T = 0$ is given by

$$E_{\rm F} = \hbar v_{\rm F}\sqrt{4\pi\frac{n_{\rm tot}}{N_{\rm f}}} + \Delta\ . \tag{5.17}$$

In Eq. (5.17), $N_{\rm f}$ is the number of Fermion flavours. In an unpolarised system, both spin components and both valleys are degenerate, so then $N_{\rm f} = g_{\rm s} g_{\rm v} = 4$ where $g_{\rm s(v)}$ are respectively the spin and valley degeneracy factors. However, when only one valley is considered, the valley resolved Fermi level $E_{\rm F}^{\xi}$ is easily inferred as

$$E_{\rm F}^{\xi} = \hbar v_{\rm F}\sqrt{4\pi\frac{n_{\xi}}{g_{\rm s}}} + \Delta\ . \tag{5.18}$$

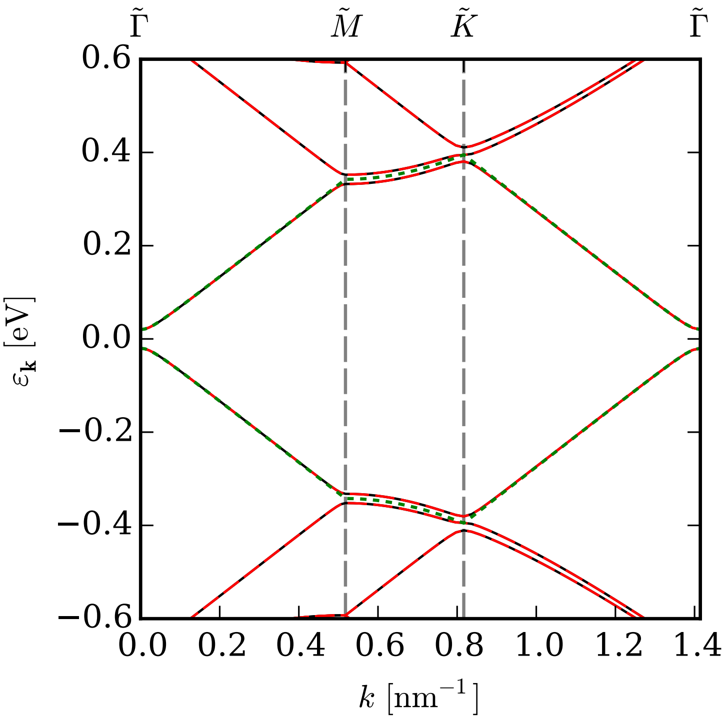

Figure 5.5: Energy spectrum along the high symmetry points of the sBZ. The black-red curves show the spectrum with the minicones at large energy. The green dashed curve shows the approximate dispersion given by Eq. (5.16). In this plot, the parameters $2\Delta_{\mathrm{g}} = 30\ \mathrm{meV}$ and $m_3 = 0$ were used.

In Eq. (5.18), $\xi = K\ (K')$ denotes the valleys as usual and n_ξ is the valley resolved carrier concentration such that $n_{\mathrm{tot}} = n_K + n_{K'}$.

If circularly polarised light impinges on the sample, it is possible to promote additional carriers from the valence band to the conduction band in only one valley as shown in Fig. 5.6. Then there exists an additional occupation of the conduction band in that valley while the valence band is partly depleted. Subsequently, the thermally excited carriers cool down and can reoccupy the holes in the valence band. However, due to the interaction with the hBN phonons, it is also possible that conduction band carriers from the other valley fill the valence band (green arrow). The end result will be a valley imbalanced system where there is a difference in carrier concentration between the two valleys denoted by

$\delta n = n_K - n_{K'}$. This results in a valley polarisation P:

$$P = \frac{\delta n}{n_{\text{tot}}} \,. \tag{5.19}$$

The polarisation P runs from -1 to $+1$ denoting that the K' to K valley is completely polarised, respectively. If the total number of charge carriers is kept constant, one can determine the valley resolved Fermi level as

$$E_{\text{F}}^{\xi}(P) = \sqrt{(\hbar v_{\text{F}} k_{\text{F}}^{\xi}(P))^2 + \Delta^2} \,, \tag{5.20}$$

where $k_{\text{F}}^{\xi}(P) = k_{\text{F}}^{0}\sqrt{1+\xi P}$ is the Fermi wave vector with $k_{\text{F}}^{0} \equiv \sqrt{\pi n_{\text{tot}}}$ the Fermi wave vector of the unpolarised system.

The mechanism described in this section is only one of many possible ways to achieve valley polarisation. Many other different mechanism have been proposed in literature that are capable of creating a valley imbalanced system [194, 195]. In the remainder of this chapter, it is assumed that the system is valley polarised, irrespective of the origin of the polarisation.

5.5 RPA theory of valley plasmons

5.5.1 Response functions and eigenmodes

The RPA density response function for an electron fluid with only one fermion flavour was previously defined in Eq. (3.120). This equation can be rewritten as

$$\left(\chi_{nn}^{\text{RPA}}\left(q,\omega\right)\right)^{-1} = \left(\chi_{nn}^{(0)}\left(q,\omega\right)\right)^{-1} - v_{\boldsymbol{q}}. \tag{5.21}$$

If different constituents of the electron fluid respond differently to external scalar potentials, then this can be accounted for in a matrix version of this equation by defining valley resolved density-density response functions. In the present case, there is a different non-interacting response function for each valley which are labelled $\chi_{K\Delta}^{(0)}$ and $\chi_{K'\Delta}^{(0)}$ for the respective valleys. Even though the particles cannot scatter into the other valley, they still interact via e-e interactions which should be accounted for on the RPA level. Therefore, there will be two RPA response functions accounting for intra-valley e-e interactions, labelled χ_{KK} and $\chi_{K'K'}$, respectively, and two that account for inter-valley interaction and which are labelled $\chi_{KK'}$ and $\chi_{K'K}$. Because Coulomb interaction is blind for the differences in valleys, the e-e interaction is the same between all species. Based on these considerations, the RPA valley resolved density-density response functions $\chi_{\xi\xi'}$ are connected

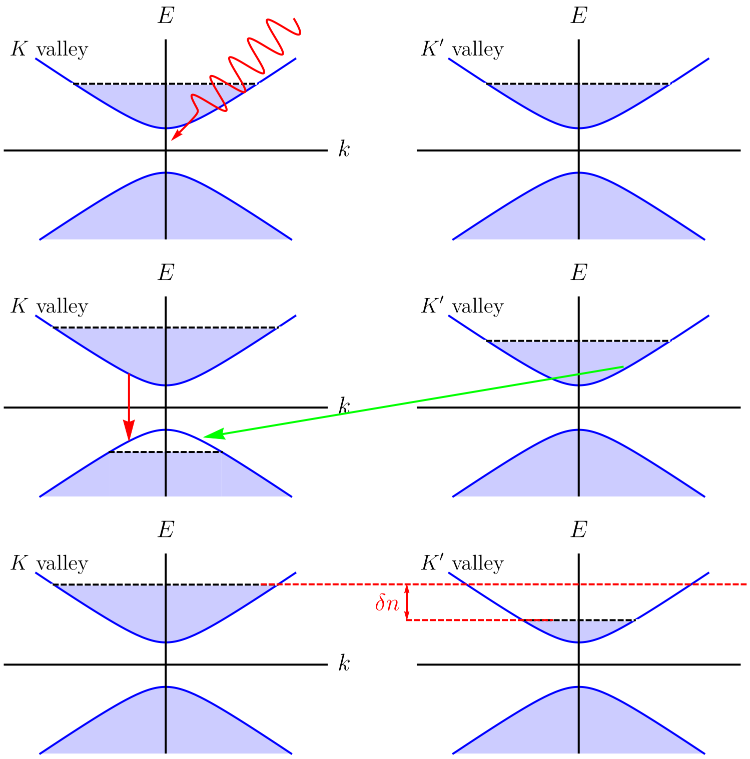

Figure 5.6: Schematic presentation of valley selective optical pumping and carrier relaxation. The top row shows the excitation of carriers in one valley resulting in the excited state depicted on the second row. Subsequently, the created hole in the valence band can be filled by carriers from the conduction band from the same valley (red arrow) or by carriers from the other valley via interaction with hBN phonons (green arrow). This results in a valley polarised system with concentration difference δn as shown in the third row.

by the matrix equation [102]

$$\begin{bmatrix} \chi_{KK} & \chi_{KK'} \\ \chi_{K'K} & \chi_{K'K'} \end{bmatrix}^{-1} = \begin{bmatrix} \chi^{(0)}_{K\Delta} & 0 \\ 0 & \chi^{(0)}_{K'\Delta} \end{bmatrix}^{-1} - V_{q,\omega} \begin{bmatrix} 1 & 1 \\ 1 & 1 \end{bmatrix} . \tag{5.22}$$

In Eq. (5.22), $V_{q,\omega}$ is the 2D Coulomb interaction in the graphene sheet that accounts for the dielectric environment and is defined as $V_{q,\omega} = v_q/\varepsilon_{\mathrm{hBN}}(q,\omega)$. Notice that hBN has a peculiar dielectric function $\epsilon_{\mathrm{s}}(q,\omega)$ that depends on both the wave vector q as the frequency ω [197]. This will be commented on in a next section.

Calculating the inverse matrix on the left-hand side of Eq. (5.22), one finds

$$\left[\begin{array}{cc}\chi_{KK} & \chi_{KK'}\\ \chi_{K'K} & \chi_{K'K'}\end{array}\right]=\frac{1}{\varepsilon_{\Delta}^{\mathrm{RPA}}\left(q,\omega\right)}\left[\begin{array}{cc}\chi^{(0)}_{K\Delta}\left(1-V_{q,\omega}\chi^{(0)}_{K'\Delta}\right) & V_{q,\omega}\chi^{(0)}_{K\Delta}\chi^{(0)}_{K'\Delta}\\ V_{q,\omega}\chi^{(0)}_{K\Delta}\chi^{(0)}_{K'\Delta} & \chi^{(0)}_{K'\Delta}\left(1-V_{q,\omega}\chi^{(0)}_{K\Delta}\right)\end{array}\right]. \tag{5.23}$$

Here, the RPA dielectric function is defined as

$$\varepsilon_{\Delta}^{\mathrm{RPA}}\left(q,\omega\right)=1-V_{q,\omega}\left(\chi^{(0)}_{K\Delta}(q,\omega)+\chi^{(0)}_{K'\Delta}(q,\omega)\right). \tag{5.24}$$

The role of the function $\chi_{\xi\xi'}$ is clear, it describes the response of the density in valley ξ to an external potential that affects the density in valley ξ'. If an external potential affects the system in a valley independent way, one is more interested in the function

$$\chi_{nn}^{\mathrm{RPA}}=\sum_{\xi\xi'}\chi_{\xi\xi'}=\frac{\chi^{(0)}_{K\Delta}+\chi^{(0)}_{K'\Delta}}{1-V_{q,\omega}\left(\chi^{(0)}_{K\Delta}+\chi^{(0)}_{K'\Delta}\right)}. \tag{5.25}$$

With this notion, the relation with the previous valley degenerate description is clear. Indeed, if the response functions in both valleys are the same, the valley degeneracy is only manifested as a factor $g_{\mathrm{v}}=2$. The equivalence is a consequence of the fact that the inter-particle interaction is the same regardless of the valley index of the two partners. If this would not be the case, like for a double layer system where the inter-layer interaction is smaller than the intra-layer interaction, the structure would be substantially different [134].

In order to probe the plasmonic response of the system, one is interested in the zeroes of the dielectric function presented in Eq. (5.24). For this, one needs the non-interacting response function of a 2D massive Dirac liquid. The full analytical solution of this response function is discussed in the next section. However, in the absence of inter-band processes, for an arbitrary energy dispersion the density-density response function can be calculated as before for the trigonal warped case. Now, the system is invariant under rotation and therefore the response function becomes according to Eq. (4.15):

$$\chi^{(0)}_{\xi\Delta}(q,\omega)=\frac{g_{\mathrm{s}}}{4\pi}\frac{q^2}{(\hbar\omega)^2}k_{\mathrm{F}}^{\xi}\left.\frac{\partial\varepsilon_{+,k}}{\partial k}\right|_{k=k_{\mathrm{F}}^{\xi}}. \tag{5.26}$$

In Eq. (5.26), the Fermi wave vector k_{F}^{ξ} differs in both valleys due to the valley polarisation.

Using Eq. (5.26), the long wavelength plasmon dispersion can be found analytically as

$$\omega_{\mathrm{pl}}^2(q)=\frac{\mathcal{D}_0 q}{\epsilon_{\mathrm{s}}}\sum_{\xi=K,K'}\frac{E_{\mathrm{F}}^{\xi}}{E_{\mathrm{F}}}\left(1-\left(\frac{\Delta}{E_{\mathrm{F}}^{\xi}}\right)^2\right). \tag{5.27}$$

In Eq. (7.84), the wave vector and frequency dependence of the dielectric constant ϵ_s was neglected.

In order to understand the physical interpretation of the plasmons, one can calculate the eigenmodes of Eq. (5.22):

$$\begin{bmatrix} \mathrm{Re}\left[\chi^{(0)}_{K\Delta}\right]^{-1} - V_{q,\omega} & -V_{q,\omega} \\ -V_{q,\omega} & \mathrm{Re}\left[\chi^{(0)}_{K'\Delta}\right]^{-1} - V_{q,\omega} \end{bmatrix} \begin{bmatrix} A_K(q) \\ A_{K'}(q) \end{bmatrix} = 0\,. \tag{5.28}$$

In Eq. (5.28), A_ξ is the amplitude of the density oscillation in valley ξ. This can be solved for the ratio of the amplitudes in both valleys,

$$\frac{A_{K'}(q)}{A_K(q)} = \frac{1}{\mathrm{Re}\left[V_{q,\omega}\chi^{(0)}_{K'\Delta}(q,\omega)\right]^{-1} - 1}. \tag{5.29}$$

The density oscillation $n_1(q,\omega)$ due to the plasmon is given by

$$n_1(q,\omega) = A_K(q)\left[n_{1,K}(q,\omega) + \frac{A_{K'}(q)}{A_K(q)} n_{1,K'}(q,\omega)\right]\,, \tag{5.30}$$

Therefore, the ratio given in Eq. (5.29) indicates the relative oscillation of the plasmon modes in both valleys. If this quantity is positive the plasmons oscillate in-phase, while if it is negative, the oscillation is in anti-phase. The magnitude of the ratio indicates relative importance of the oscillations in both valleys. The $q \to 0$ limit is given by

$$\lim_{q\to 0}\frac{A_{K'}(q)}{A_K(q)} = \frac{E_\mathrm{F}^{K'}}{E_\mathrm{F}^{K}}\frac{1-\left(\Delta/E_\mathrm{F}^{K'}\right)^2}{1-\left(\Delta/E_\mathrm{F}^{K}\right)^2}\,, \tag{5.31}$$

This is a positive quantity and is only zero if $P = 1$. Therefore, in order to find valley plasmons, i.e. plasmons where the two components oscillate in anti-phase, one needs to consider finite wave vector q.

5.5.2 Density-density response function of a gapped Dirac system

Arbitrary gap and q, ω

To find the density-density response of a gapped Dirac system at arbitrary q and ω, a similar method as outlined in Sec. 3.1.3 can be applied. However, in this case the density vertex $\mathcal{D}_{\lambda\lambda'}$ changes such that

$$\left|\mathcal{D}_{\lambda\lambda'}(\boldsymbol{k},\boldsymbol{k}')\right|^2 = \frac{1}{2}\left(1 + \lambda\lambda'\frac{(\hbar v_\mathrm{F})^2\,\boldsymbol{k}\boldsymbol{k}' + \Delta^2}{\varepsilon_{\boldsymbol{k}'}\varepsilon_{\boldsymbol{k}}}\right). \tag{5.32}$$

This equation shows that oppositely propagating modes are no longer completely decoupled. This is the consequence of the breaking of conservation of helicity. Indeed, due to the term accompanied by σ_z in the Hamiltonian in Eq. (5.1), the helicity $\eta_{\boldsymbol{q}} = \frac{\boldsymbol{\sigma}\cdot\boldsymbol{q}}{|\boldsymbol{q}|}$ does not commute any more with the Hamiltonian.

The calculation of the non-interacting response function $\chi^{(0)}_{nn}(q,\omega)$ is a lengthy calculation, but is performed in a similar way to the ungapped case as discussed in Sec. 3.1.3 [198]. It is possible to find an analytical solution that describes the real and imaginary parts in different regions of the (q,ω) plane. This solution is reported in appendix B.3 .

In Fig. 5.7 the real and imaginary parts of $\chi^{(0)}_{nn}(q,\omega)$ are plotted for a gap of size $\Delta = 0.5E_{\mathrm{F}}$. A remarkable feature of the response function for a gapped system is that the particle-hole excitation spectrum is drastically changed. Because the energy bands are hyperbolic rather than linear as in the ungapped case, the finite q boundary of the inter-band continuum is moved to larger values of the frequency. Meanwhile, the boundary of the intra-band continuum also slightly decreases because of the hyperbolicity of the energy spectrum. Because the two boundaries move away from the graphene light cone, in between the two there is a small region where no single-particle excitations are possible. In this region, the ungapped graphene response function showed divergences due to the chirality of the particles as previously discussed. In the gapped case, however, these divergences are abruptly suppressed for the imaginary part, while for the real part of the response function, the positive and negative divergences are pushed away from each other. The fact that a gap introduces a larger region free from single-particle contributions will benefit the appearance of long lived plasmon modes at large q as will be discussed in a next section.

Large gap

Fig. 5.8 shows the real and imaginary parts in the case of a relatively large gap, $\Delta = 0.9E_{\mathrm{F}}$. In this case, the low q and ω sector reduces to the well known response function of a single band 2D electron gas (2DEG) with a parabolic band as shown in Appendix B.1. This limit can be inferred analytically if one considers that the gap is comparable to the Fermi level, i.e. $\Delta \lesssim E_{\mathrm{F}}$ and that only small deviations from the bottom of the hyperbolic band are considered such that it can be approximated by

$$\varepsilon_{\lambda\boldsymbol{k}} \approx \lambda\Delta\left(1+\frac{1}{2}\left(\frac{\hbar v_{\mathrm{F}}k}{\Delta}\right)^2\right) = \lambda\Delta + \lambda\varepsilon'_{\boldsymbol{k}}\ . \tag{5.33}$$

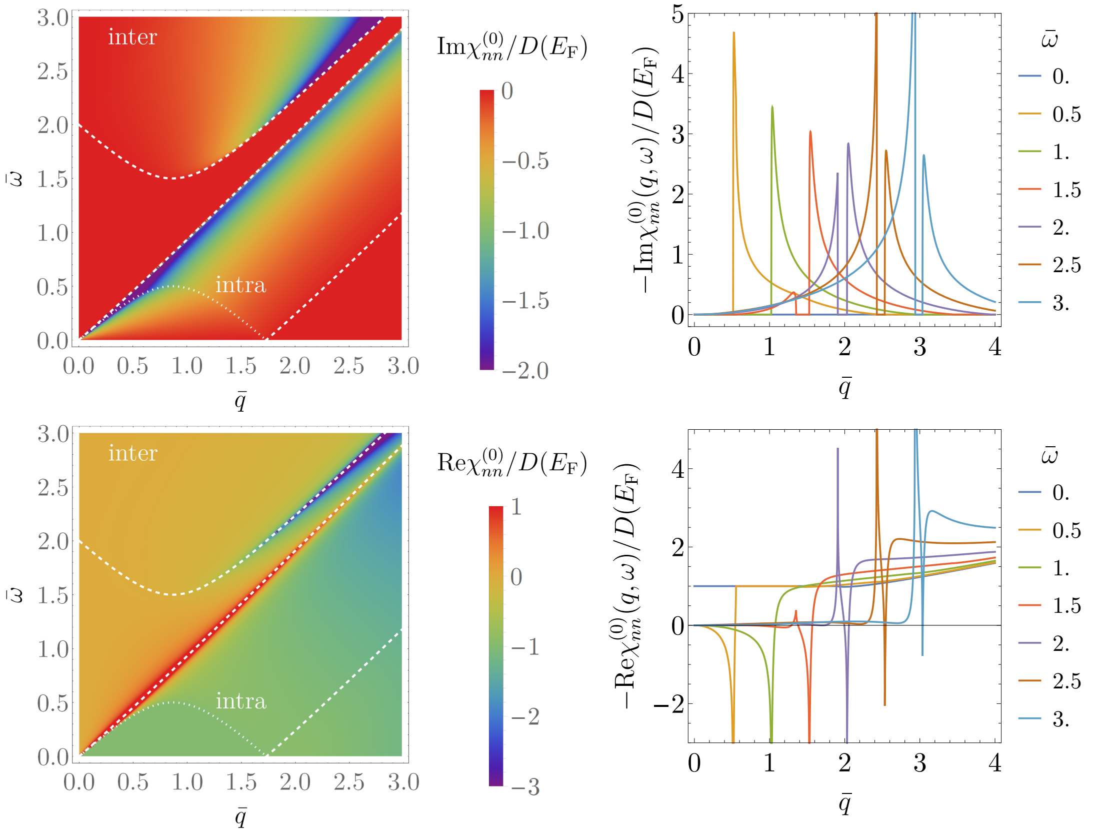

Figure 5.7: Imaginary (top row) and real (bottom row) part of the single valley response function of a gapped graphene system with gap $\Delta = 0.5E_{\mathrm{F}}$. The left column displays the response function in the (q, ω) plane. The dashed white curves in the left panels indicate the boundaries of the inter- and intra-band continua. The dotted white curve at the bottom of the figures denotes the region where the real part of the response function is -1. This region is reminiscent of the response of a 2DEG.

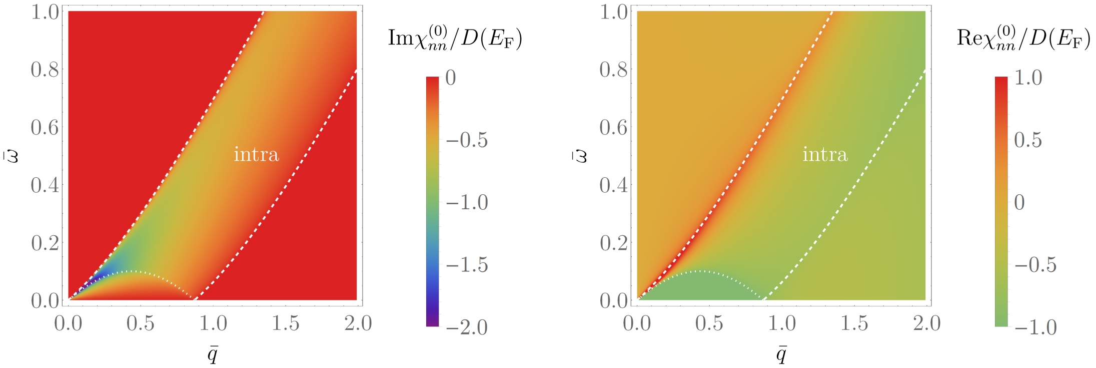

Figure 5.8: Imaginary and real part of the single valley response function of a gapped graphene system with gap $\Delta = 0.9E_\mathrm{F}$. The dashed white curves indicate the boundaries of the intra-band continuum. The dotted white curve at the bottom of the figures denotes the region where the real part of the response function is -1. This region is reminiscent of the response of a normal 2DEG.

Here, $\varepsilon'_{\boldsymbol{k}} = (\hbar k)^2/(2\Delta/v_\mathrm{F}^2)$, which corresponds to a parabolic energy band with a band mass $m_\mathrm{b} = \Delta/v_\mathrm{F}^2$. Similarly, also the density vertex can be approximated as

$$|\mathcal{D}_{\lambda\lambda'}(\boldsymbol{k},\boldsymbol{k}')|^2 = \frac{1}{2}(1+\lambda\lambda') \ , \tag{5.34}$$

which means that only intra-band transitions are possible. Because of the total occupation of the valence band, this means that only intra-conduction band contributions are relevant. Therefore, the response function reduces to

$$\chi_{nn}^{(0)}(\boldsymbol{q},\omega) = \frac{N_\mathrm{f}}{L^2}\sum_{\boldsymbol{k}} \frac{n'_{\boldsymbol{k}} - n'_{\boldsymbol{k}+\boldsymbol{q}}}{\hbar\omega + \varepsilon'_{\boldsymbol{k}} - \varepsilon'_{\boldsymbol{k}+\boldsymbol{q}} + i\hbar\eta} \ . \tag{5.35}$$

Here, the FDD is given by

$$n'_{\boldsymbol{k}} = \left(1 + \exp\left(\frac{\varepsilon'_{\boldsymbol{k}} - (\mu-\Delta)}{k_\mathrm{B}T}\right)\right)^{-1} . \tag{5.36}$$

These equations reduce to the definition of the density-density response function of a 2DEG [102] with a new Fermi level measured from Δ, i.e. $\mu' = \mu - \Delta$, and a band mass determined by the size of the gap.

5.6 Dielectric function of hBN encapsulation

5.6.1 Hyperbolic metamaterials

As incorporated in the RPA theory, the dielectric properties of hBN are rather non-trivial. This is because hBN is a so-called *hyperbolic metamaterial* [199]. This means that the dielectric properties of hBN are not isotropic, rather they are described by a dielectric tensor $\tilde{\epsilon}$:

$$\tilde{\epsilon} = \begin{bmatrix} \epsilon_x & 0 & 0 \\ 0 & \epsilon_y & 0 \\ 0 & 0 & \epsilon_z \end{bmatrix}. \tag{5.37}$$

In Eq. (5.37) the diagonal elements are defined with respect to the main crystallographic axes and are not the same. For hBN however, the crystallographic structure dictates that the components perpendicular to the anisotropy axis are the same, so $\epsilon_x = \epsilon_y = \epsilon_\perp$ and the z-direction is taken along the anisotropy axis, i.e. $\epsilon_z = \epsilon_{\|}$. If one assumes that the magnetic permeability is isotropic, then the dispersion relation for electromagnetic waves in the hBN is given by [199, 200]

$$\frac{k_x^2 + k_y^2}{\epsilon_{\|}} + \frac{k_z^2}{\epsilon_\perp} = \left(\frac{\omega}{c}\right)^2. \tag{5.38}$$

For a given ω, this dispersion relation defines a 2D surface in the 3D reciprocal space. The shape of the 2D surface depends on the dielectric quantities. As shown in Fig. 5.9, if both ϵ's are positive, the iso-energy surface is a spheroid. However, if $\epsilon_{\|} < 0$ and $\epsilon_\perp > 0$, the surface becomes a hyperbola. Further, if $\epsilon_{\|} > 0$ and $\epsilon_\perp < 0$, the hyperbola is gapped. The fact that the dispersion forms a hyperbola and that some of the principal components of the dielectric tensor are negative, gives the material the name a hyperbolic metamaterial.

A major consequence of this structure is that the hyperbolic iso-energy surface limits the possible angles for which light propagation is allowed. Indeed, as the Poynting vector, that defines the direction of energy flow of an electromagnetic wave, always points perpendicular to the iso-energy surface [201], the angle that the Poynting vector can make with the anisotropy axis is limited by the hyperbolicity of the dispersion relation. Recently, hBN was used as a hyperbolic metamaterial to provide sub-diffractional imaging [196, 202]. This imaging method uses the fact that near-field evanescent radiation of an object can couple to propagating modes in the hBN crystal if it is close enough. Then, the radiation propagates outward under the angle defined by the hyperbolic dispersion and enhances the image such that it is visible by an optical microscope. This is shown in Fig. 5.10 .

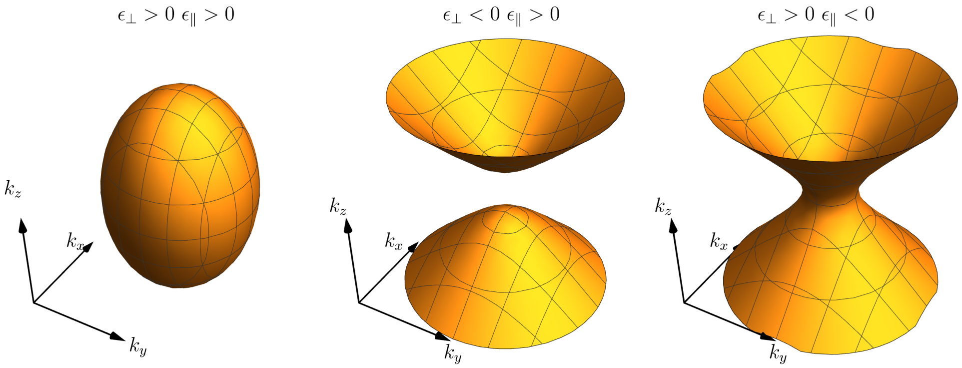

Figure 5.9: Iso-energy surfaces in 3D reciprocal space for a non-isotropic dielectric material with principal components as indicated. The right two dispersions correspond to hBN in the reststrahlen bands.

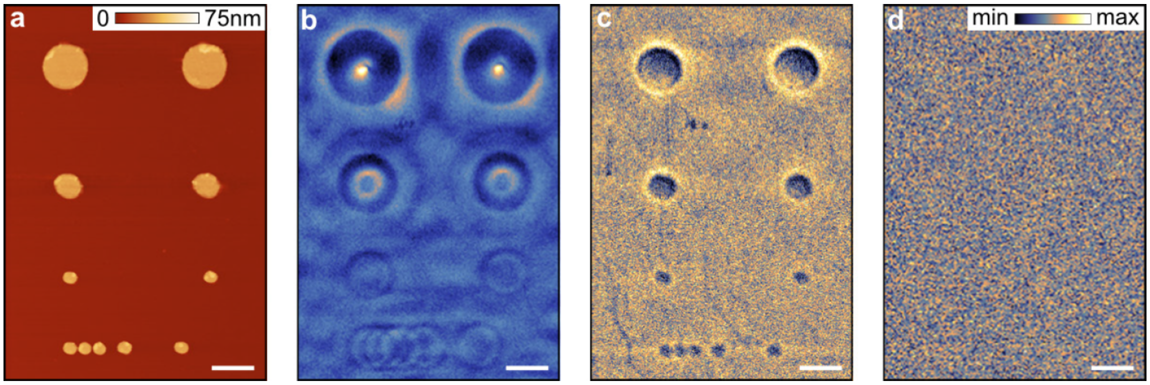

Figure 5.10: Experimental results of near-field imaging using the hyperbolicity of hBN. (a) AFM image of gold disks on a substrate. (b) and (c) are near-field images on top of hBN showing an enlarged image of the disks at two different frequencies in the reststrahlen bands. (d) Result of the same measurement but for a frequency outside the reststahlen bands. Images taken from Ref. [202].

	$\ell = x$	$\ell = z$
$\epsilon_{\ell,0}$	6.41	3.0
$\epsilon_{\ell,\infty}$	4.54	2.5
$\hbar\gamma_\ell$ [meV]	0.82	0.23
$\hbar\omega_\ell^{\mathrm{T}}$ [meV]	168	94.2
$\hbar\omega_\ell^{\mathrm{L}}$ [meV]	199.6	103.2

Table 5.1: Table summarizing the parameters for the effective model of the hBN dielectric constant given by Eq. (5.39). The parameters where determined in Ref. [201].

5.6.2 hBN as a hyperbolic metamaterial

The principal components of the dielectric tensor of hBN depend on the frequency at which the material is probed because of the presence of phonons in the system. A simple model to describe this is by a Lorentzian form [197, 203, 204]

$$\epsilon_\ell\left(\omega\right) = \epsilon_{\ell,\infty} + \frac{\epsilon_{\ell,0} - \epsilon_{\ell,\infty}}{1 - \left(\omega/\omega_\ell^T\right)^2 - i\gamma_\ell\omega/\left(\omega_\ell^T\right)^2}, \tag{5.39}$$

where ℓ denotes the principal component, $\epsilon_{\ell,\infty}$ is the limiting value for large ω, $\epsilon_{\ell,0}$ corresponds to the value at $\omega = 0$. ω_ℓ^T is the frequency of the longitudinal phonon in the direction ℓ and γ_ℓ is the damping coefficient. The values of these parameters were recently measured [201] and are tabulated in Table 5.1.

Fig. 5.11 shows the real part of $\epsilon_\perp$ and $\epsilon_\parallel$ as a function of the photon frequency. It is clear that the there are two energy regions where one of the two components becomes negative. In these regions the hBN crystal is a hyperbolic metamaterial. The boundaries of the regions are the longitudinal and transverse phonon frequencies. The longitudinal phonon frequency is related to the transverse frequency tabulated in Table 5.1 as $\omega_\ell^L = \sqrt{\epsilon_{\ell,0}/\epsilon_{\ell,\infty}}$ [205]. The regions where one of the components is negative are called the *reststrahlen bands* and are shaded in Fig. 5.11.

5.6.3 Coulomb interaction in encapsulated samples

The g/hBN samples under consideration usually consist of a SiO_2 substrate on which an hBN slab with thickness d is deposited. On top of that the graphene flake is positioned such that the edges of both samples are aligned and topological bands are formed. Finally, this structure is covered with another hBN slab with thickness d' that is not aligned with the graphene flake. A picture of such an encapsulated heterostructure is shown in Fig. 5.12(b). The thickness of the hBN slabs is typically of the order of several tens of nanometers.

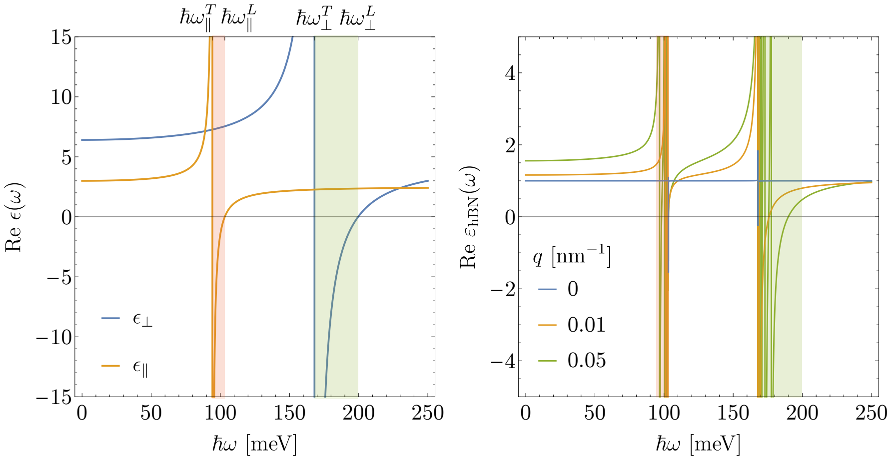

Figure 5.11: Left: frequency dependence of the principal components of the hBN dielectric tensor using the model from Eq. (5.39). Right: frequency dependence of the dielectric function of hBN as defined in Eq. (5.41) for a system consisting of a top slab of $d' = 10$ nm and $d = 50$ nm for different wave vectors q as indicated. In both figures the reststrahlen bands are indicated by shading.

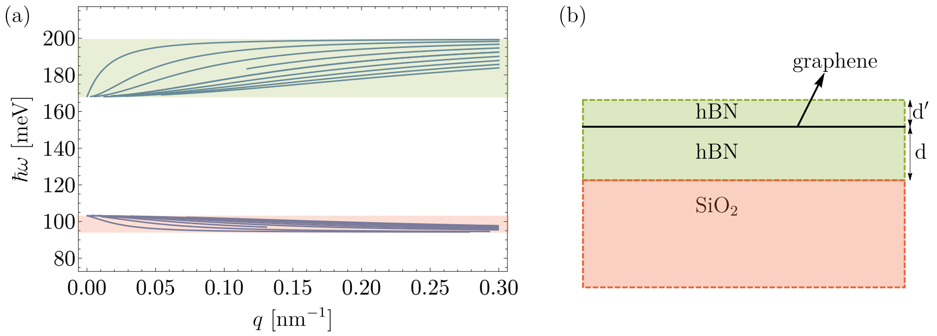

Figure 5.12: (a) Zeroes of the hBN dielectric function as defined in Eq. (5.41) showing the dispersion of the phonon-polariton modes for a system consisting of two hBN slabs with thickness $d' = 10$ nm and $d = 50$ nm. (b) hBN encapsulated graphene setup on a SiO$_2$ substrate.

The e-e interaction between the graphene charge carriers is affected by the dielectric properties of the hBN environment. As mentioned before, this is encoded in the potential $V_{\boldsymbol{q},\omega}$ introduced in Sec. 5.5.1. In order to find the screened e-e interaction in the graphene flake, one needs to solve Poisson's equation for the encapsulated sample. The derivation of this is outlined in appendix C.2 and results in a potential screened by a dielectric function determined by the hBN encapsulation as

$$V_{\boldsymbol{q},\omega} = \frac{v_{\boldsymbol{q}}}{\varepsilon_{\text{hBN}}\left(q,\omega\right)}, \tag{5.40}$$

where

$$\varepsilon_{\text{hBN}}\left(q,\omega\right) = \frac{\left(\epsilon_{\parallel}\kappa\right)^2 \cosh\left(\kappa\left(d+d'\right)\right) + \epsilon_{\parallel}\kappa\left(q^2\epsilon_a\epsilon_b + \epsilon_{\parallel}^2\kappa^2\right)\sinh\left(\kappa\left(d+d'\right)\right)/\bar{\epsilon}}{q\left[\epsilon_{\parallel}\kappa\cosh\left(\kappa d'\right) + q\epsilon_a\sinh\left(\kappa d'\right)\right]\left[\epsilon_{\parallel}\kappa\cosh\left(\kappa d\right) + q\epsilon_b\sinh\left(\kappa d\right)\right]}. \tag{5.41}$$

In Eq. (5.41) the SiO_2 dielectric environment is encoded in the variable $\epsilon_b = \epsilon_{\text{SiO}_2}$ while $\epsilon_a = 1$ denotes the vacuum above the sample. The screened wave vector $\kappa = \sqrt{\epsilon_{\perp}/\epsilon_{\parallel}}q$ determines the dependence on the thickness of the hBN slabs and finally $v_{\boldsymbol{q}}$ is the usual 2D Coulomb potential screened by the usual dielectric constant $\bar{\epsilon} = \left(\epsilon_a + \epsilon_b\right)/2$.

The encapsulation dielectric function $\varepsilon_{\text{hBN}}\left(q,\omega\right)$ depends on the frequency ω through $\epsilon_{\parallel}\left(\omega\right)$ and $\epsilon_{\perp}\left(\omega\right)$. In Fig. 5.11 this dielectric function is shown for different values of the wave vector q. The figure shows that near the boundaries of the reststrahlen bands the dielectric function diverges and that for increasing q or slab thickness the system converges to the response of an infinitely thick hBN slab, i.e. $\varepsilon_{\text{hBN}}\left(\omega\right) = \sqrt{\epsilon_{\perp}\epsilon_{\parallel}}$.

Inside the reststrahlen bands, the dielectric function shows a series of divergences that cross zero. Similar to the case of Dirac plasmons that are defined as the zeroes of the RPA dielectric function, the zeroes of the hBN dielectric function correspond to collective modes. In this case these are phonon-polariton modes. These modes are trapped in the hBN slab and, therefore, their energy dispersion discretizes as is the case for Fabry-Pérot modes. The dispersion is shown in Fig. 5.12 (a). Notice that as the numerator of Eq. (5.41) only depends on the thickness of the slabs as a sum of the two, the phonon-polariton modes are formed in the total structure as if the graphene sheet is absent.

5.7 Plasmons in graphene on hBN

5.7.1 Plasmons-phonon-polariton hybridisation

Using the RPA theory described in Sec. 5.5, the Dirac plasmons can be found from the zeroes of the real part of the dielectric function Eq. (5.24). In Fig. 5.13(a) the plasmon branch is shown in the (q, ω) plane for a valley degenerate system with a gap of $\Delta = 15\ \mathrm{meV}$ and a small Fermi level $E_{\mathrm{F}} = 30\ \mathrm{meV}$. The results show that at small wave vector q and frequency ω, the plasmon dispersion follows the approximate $\sqrt{q}$ relation derived in Eq. (7.84). However, as the frequency increases, the plasmon dispersion approaches the intra-band continuum and comes asymptotically close to it. Due to the finite band gap, the inter-band and intra-band continua move away from each other as discussed before. The region in between these two continua now allows the Dirac plasmon to remain undamped up to larger momenta q and frequency ω. In Fig. 5.13(a) also the approximate plasmon branch is shown as a dashed curve. It is clear that this approximation overestimates the frequency for a given momentum. This is due to the lack of contributions of the inter-band transitions as discussed in Sec. 3.2.3.

In Fig. 5.13(b), the RPA plasmon is calculated for the same system but with a larger doping, namely a Fermi level of $E_{\mathrm{F}} = 120\ \mathrm{meV}$. As a consequence, the band gap is now relatively smaller than before ($\Delta/E_{\mathrm{F}} = 0.25$), and, therefore, the gap between the inter- and intra-band PHES is also smaller. Because the plasmon branch now extends to larger photon energies, it also interferes with the reststrahlen bands of the hBN crystal. As shown in Fig. 5.13(b), the restrahlen bands divide the plasmon branch in three parts: one with frequency smaller than $\omega_{\parallel}^{T}$, one with frequency in between $\omega_{\parallel}^{L}$ and $\omega_{\perp}^{L}$, and one with frequency above $\omega_{\perp}^{L}$. In the first part, the plasmon branch is pushed down by the reststrahlen band until it hits the intra-band continuum. Also in the second part the plasmon adapts itself to the reststrahlen bands and is curved upward for small momenta q. For larger momenta, the plasmon branch in the second part encounters the inter-band PHES but exits it again at a little bit larger momenta. In the the third part the plasmon branch is not only pushed up by the restrahlen band, but also enters it as a hybridised form of a plasmon and a phonon-polariton. Indeed, the dashed curves show the phonon-polaritons in the restrahlen bands as discussed in Fig. 5.12(a). The upper plasmon branch starts from within the reststrahlen band and then continues as a plasmon. Inside the reststrahlen band it is therefore a *plasmon-phonon-polariton mode* [197].

Finally, notice that in the large (q, ω) sector, there is a new mode appearing in the gap between the intra- and inter-band continua (shown in red in Fig. 5.13 (b) and in the zoom in Fig. 5.14). This mode lies outside the continua and is therefore not damped by single-particle processes. This in contrast to the normal plasmon mode at the same frequency, which lies firmly inside the inter-band continuum. In this calculation, the mode starts already just below the second reststrahlen band. Inside the restrahlen band, this mode is heavily hybridised with all the Fabry-Pérot-like phonon-polariton modes of the hBN crystal.

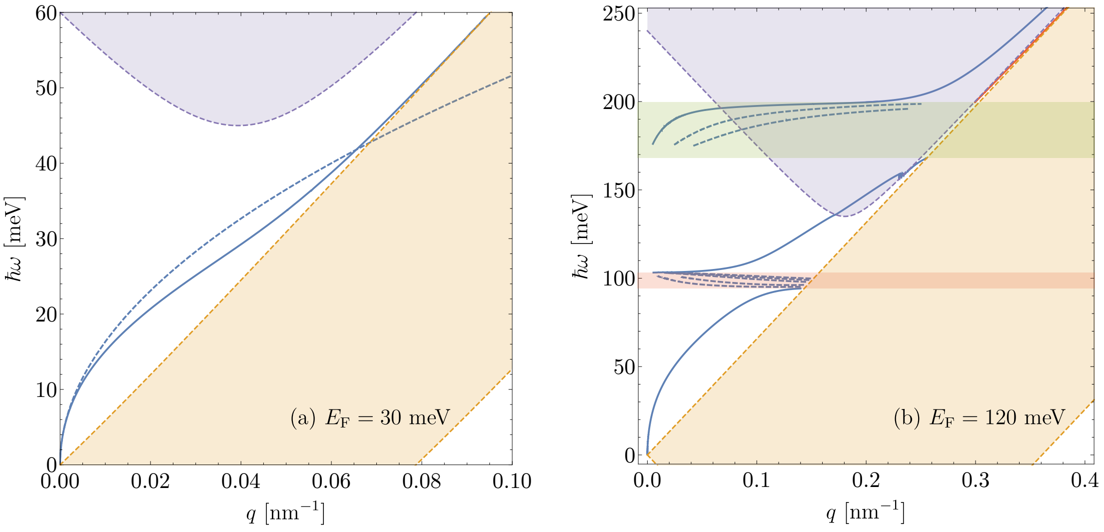

Figure 5.13: Plasmon branches for graphene encapsulated by hBN with $d' = 10$ nm, $d' = 50$ nm and $\Delta = 15$ meV. The Fermi level is $E_\mathrm{F} = 30$ meV for (a) and $E_\mathrm{F} = 120$ meV for (b). The plasmon branches are shown as solid curves. The PHES is shown as shaded regions with orange indicating the intra-band and blue indicating the inter-band PHES. The dashed curve in (a) is the low-energy approximation. In (b) the green and red shaded rectangles denote the reststrahlen bands with inside some of the phonon-polariton modes shown as dashed curves. The red mode in the upper right corner of (b) is the newly found undamped mode.

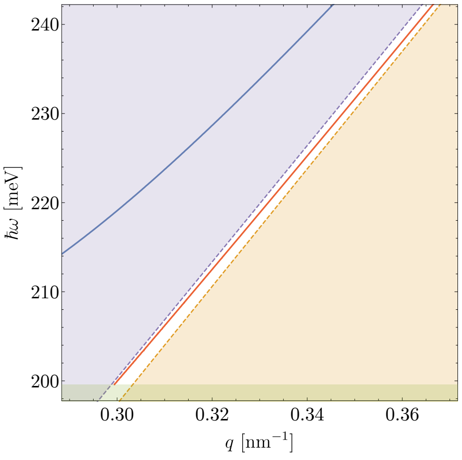

Figure 5.14: Zoom on the new plasmon mode that appears in the gap between the inter- and intra-band continua. The mode is shown by the red line.

5.7.2 Plasmons in a valley imbalanced system

If the two energy valleys are populated differently, the plasmonic response of the system is affected. In Fig. 5.15(a) the plasmon dispersion is shown for a lightly doped sample ($E_{\mathrm{F}} = 30\ \mathrm{meV}$) and different values of the polarisation P as indicated. The result shows that the stronger the valley polarisation, the closer the plasmon branch is pushed towards the intra-band continuum. However, the numerical results show that this effect is rather small.

In Fig. 5.15(b), the ratio $A_{K'}/A_K$ is shown as a function of the photon energy for the plasmons displayed in (a). This result shows that although the plasmon dispersion is not much affected by the change in valley polarisation, the same cannot be said about the relative contributions of both valleys to the plasmon. Indeed, in the absence of polarisation, $P = 0$, both valleys contribute equally to the plasmonic oscillation. However, as the polarisation increases, the K' valley is depleted and contributes less to the plasmons. As the frequency of the plasmonic oscillation increases, this contribution is further suppressed until it reaches a point where its amplitude vanishes. At this point, only the density of the K valley shows an oscillating behaviour and, consequenctly, the plasmon is *valley-polarised*. As the photon frequency increases further, this tipping point is crossed and the ratio $A_{K'}/A_K$ changes sign. This means that the plasmon in the K' valley starts oscillating in anti-phase with the K valley. This anti-phased oscillation is a similar concept as the current that was found oriented oppositely in graphene with topological bands [187]. Therefore, this kind of plasmon can be called a *valley plasmon*. Note however that in this case the minimum value of the ratio of both amplitudes is larger than -1. Therefore, the valley plasmon is not perfectly charge neutral.

In Fig. 5.16 the plasmon dispersion is shown for a sample that has a larger doping ($E_{\mathrm{F}} = 120\ \mathrm{meV}$) and us polarised with $P = 0.5$. As before, the reststrahlen bands split the plasmon dispersion in three parts. As with the lightly doped case, the polarisation does not influence the plasmon dispersion a lot as can be seen by comparing the dispersion of the polarised system (solid curve) to that of the unpolarised system (dashed curve) in Fig. 5.16 (a). However, due to the polarisation, the PHES of both valleys is strongly affected. In Fig. 5.16 (a), the PHES of the two valleys is shown as shaded regions bordered by a dashed curve (K valley) or a solid curve (K' valley). The plasmon dispersion enters the PHES of the K' valley in between the two reststrahlen bands. As shown in Fig. 5.16(b), this introduces a finite damping to the plasmon that was absent in the case of an unpolarised system. Above the second reststrahlen band, the plasmon lies firmly in the PHES of both valleys and is, therefore, strongly damped.

The quality factor plotted in Fig. 5.16(b) shows an abrupt jump when the plasmon mode enters the PHES of the K' valley. As discussed before, this frequency depends on

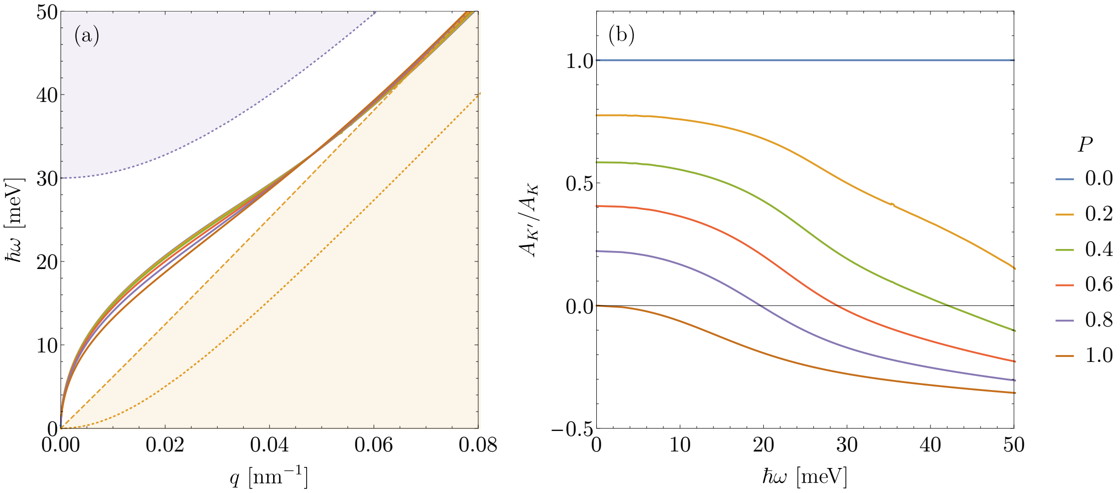

Figure 5.15: Plasmon dispersion for different valley polarisations as indicated. The PHES shown in (a) corresponds to the case of a fully polarised system, where the dashed lines indicate the boundaries of the PHES in the K valley and the dotted lines that of the K' valley. As the K' valley is depleted, the intra-band continuum also vanished. (b) The ratio of the plasmon amplitudes in both valleys for the corresponding plasmons shown in (a) as a function of the photon frequency $\hbar\omega$. The Fermi level in this figure is $E_{\mathrm{F}} = 30\ \mathrm{meV}$.

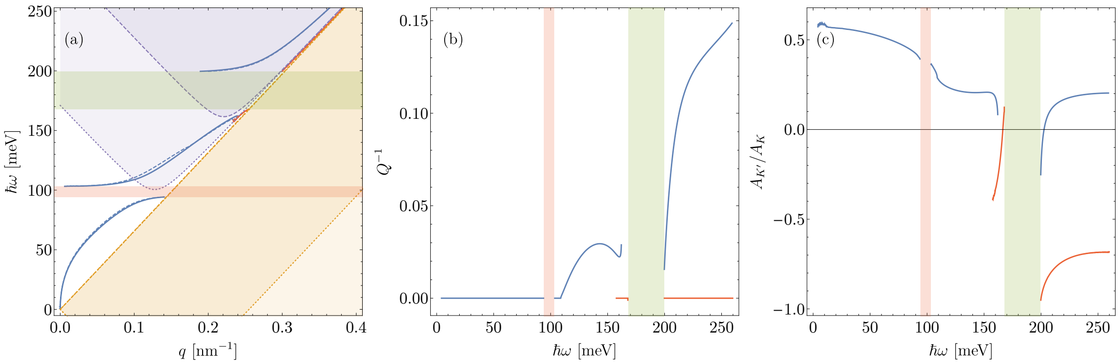

Figure 5.16: (a) Plasmon dispersion of a valley polarised system with $E_{\rm F} = 120$ meV and polarisation $P = 0.5$. The dashed curve in (a) shows the dispersion in the absence of polarisation. The blue curve shows the normal plasmon mode, the red curve shows the new plasmon mode obtained at large frequency in the gap in between the two electron-hole continua. (b) Inverse quality factor of the plasmon modes shown in (a) as a function of the photon energy. (c) Ratio of the plasmon amplitudes in both valleys as a function of the photon energy. The blue and red curves in (b) and (c) correspond to the plasmons in (a) that have the same colour.

the valley polarisation of the system. Vice versa, the frequency at which the plasmon mode is damped can be used a means to measure the valley polarisation in a valley imbalanced system. This is similar to the technique proposed to measure spin polarisation in graphene with a spin imbalance [206].

In the previous section, it was noted that due to the gap in the region between the inter- and intra-band continua a new plasmon branch appears. Also in the presence of valley polarisation, this plasmon branch is present as shown by the red curve in Fig. 5.16 (a). This plasmon branch is indeed not damped by single-particle processes as shown in the calculation of the quality factor in Fig. 5.16 (b). However, upon calculation of the ratio $A_{K'}/A_K$, it is clear that the new plasmon mode is substantially different from the normal mode. Indeed, for large ω, the mode is strongly in anti-phase and, therefore, constitutes a valley plasmon that is almost charge neutral.

5.7.3 New type of valley plasmons at very small doping

Apart from the valley plasmon mode that is found for large frequency and wave vector, the valley dependent PHES also allows for a low energy acoustic valley plasmon, similar to the spin-plasmon mode found in a spin-polarised 2DEG [207] if the system is only slightly doped. This equivalence stems from the fact that for small doping, the system reduces to an effective 2DEG as discussed before.

As seen in Fig. 5.15(a), the boundary of the intra-band PHES of the K' valley is shifted to higher values of q as the polarisation increases. This allows for a region where only the K valley can damp the plasmons by intra-band transitions. In Fig. 5.17(a) the real and imaginary parts of the dielectric function as a function of frequency ω are shown for a system with relatively large gap, i.e. $\Delta = 0.95\ E_{\mathrm{F}}$ and valley polarisation $P = 0.5$. The plots show that the imaginary part shows two peaks of large spectral weight that are shifted away from each other due to the polarisation. In between these two peaks, the real part crosses zero with a positive derivative, hence signalling the presence of a new collective mode, albeit with a finite lifetime due to the fact that the imaginary part is non-zero. Note however that because the imaginary part has a local minimum, the damping is not very strong.

In Fig. 5.17(b), the imaginary part is plotted in the small q and ω sector. In the region where it has a local minimum, dubbed the *pseudo-gap* in Ref. [207], a novel plasmon mode appears. In contrast to the normal Dirac plasmon, this mode has a linear dispersion and is therefore reminiscent of an acoustic collective mode.

Fig. 5.17(c) shows the ratio of the amplitudes in both valleys for the normal Dirac plasmon mode, ω_{D} and the linear valley plasmon mode ω_{v} as a function of the wave vector. It is clear that the acoustic mode is indeed a valley plasmon because the ratio is -1 in the long wavelength limit. This means that the acoustic mode is a charge neutral valley plasmon mode.

In Ref. [206], graphene with a spin imbalance was considered. As explained above, this is mathematically similar to a valley imbalanced graphene flake. In that work, the authors did not find a spin plasmon mode because they considered gapless graphene. The results presented in this chapter confirm their findings, but point out that if the system would be gapped, the spin plasmon mode will appear.

5.8 Conclusions of the chapter

In this chapter, a new type of plasmon is found. This plasmon mode is predicted to be present in a graphene/hBN heterostructure, a platform that is attracting a lot of attention from experimentalists due to the fact that is can be made exceptionally clean. In this chapter, the peculiar dielectric properties of the hBN crystal and the plasmonic properties of a valley imbalanced graphene sheet are combined in order to gain in depth understanding in the properties of plasmons in graphene with a topological superlattice.

The chapter reviewed the relevant processes in order to determine how valley polarisation affects its plasmonic properties. It was found that although the plasmon dispersion is

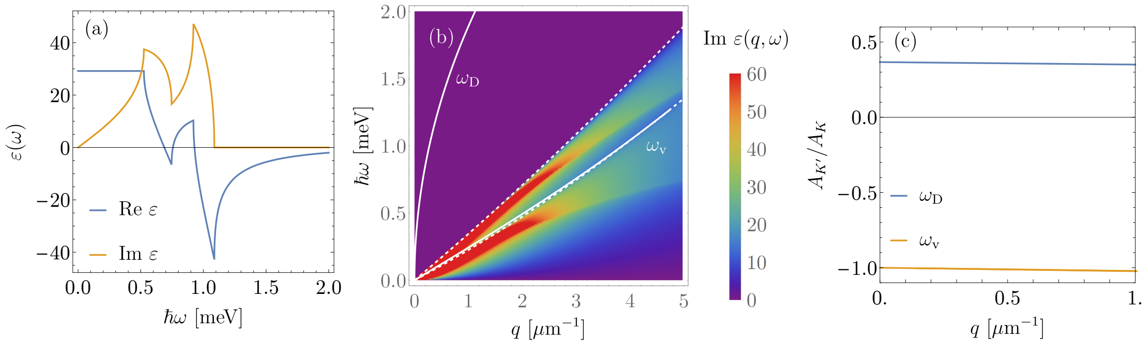

Figure 5.17: (a) Imaginary and real part of the dielectric function for a graphene/hBN heterostructure for $q = 3\ \mu\mathrm{m}^{-1}$. (b) Imaginary part of the RPA dielectric function. The Dirac plasmon ω_D and the valley plasmon ω_v are indicated as white solid curves. The white dashed curves denote the boundaries of the intra-band PHES in the two valleys. Note that there is a region of lower spectral weight in between these boundaries. This region is called the pseudo-gap. (c) Ratio of the plasmon amplitudes in both valleys for the two types of plasmons as indicated. The Fermi level is $E_\mathrm{F} = 17$ meV such that the gap is $\Delta = 0.9\ E_\mathrm{F}$.

not strongly affected by the valley polarisation, the relative phase of the plasmonic oscillations in both valleys is affected such that the plasmon consists of an oscillation in only one valley, and is, therefore, valley polarised, or that the oscillation in both valleys is in anti-phase. For larger levels of doping, it was found that the dielectric properties of the hBN substrate come into play and that the plasmon hybridises with the phonon-polaritons of the hBN crystal. Furthermore, it was shown that the valley polarisation changes the PHES of both valleys such that the plasmon becomes partly damped due to single valley electron hole excitations. Furthermore, at large wave vector, a new plasmon mode was found that is undamped because it lies in between the inter- and intra-band PHES and contains a large anti-phase plasmon component. Finally, a new valley plasmon mode was identified for very small doping in the presence of valley polarisation. The mode is acoustic and perfectly charge neutral in the long-wavelength limit.

The investigation of valley plasmons in graphene topological superlattices is highly relevant to the field. As discussed in this chapter, it is possible to pump the two energy valleys in a different way by making use of circularly polarised light. Recently, there have been proposals of new plasmon edge-modes that would be present at the edge of graphene flakes with a valley polarisation and arise solely due to the topology of the energy bands [208, 209]. The system considered in this chapter is similar, but considers the effect of a valley polarisation on the plasmon living in the bulk of graphene. Furthermore, the fact that the valley plasmons that are found in this chapter are charge neutral, make them less susceptible to to decay due to charged impurities. Indeed, because it is charge neutral, charged impurities are not able to interfere with it, in the same way as the valley current was proven to be stable as well [187]. Finally, it is important to point out that the graphene/hBN heterostructure has shown its usage in the search for long lived Dirac plasmons already before [59]. Therefore, it is expected that the proposed plasmon modes can soon be found experimentally.

CHAPTER 6

Plasmons in silicene under the influence of external fields

How do external fields influence the lifetime of plasmons in silicene?

This chapter is devoted to the investigation of plasmons in silicene, a single layer honeycomb lattice of silicon atoms, and how their properties are affected by external fields. Using a similar LRT framework as before, the plasmons are obtained from the zeroes of the RPA dielectric function. However, in this case the single-particle properties of the electrons in the crystal are substantially different from those of graphene due to a stronger spin-orbit coupling. As a result, the band structure can be tuned by external electric or magnetizing exchange fields which affect the electrons in a spin and valley dependent way. This subsequently also affects the plasmonic properties of the silicene crystal.

The structure of the chapter is as follows: in Sec. 6.1 silicene is introduced as a new two-dimensional material that features exceptional electronic properties. In Sec. 6.2 the electronic structure of the material is derived, the importance of spin-orbit coupling and the effect of external fields is discussed. In Sec. 6.3 an approximate Hamiltonian is introduced of which the response function is calculated and the PHES is derived in Sec. 6.4. In Sec. 6.5 the results of numerical calculations of plasmons in silicene are shown and discussed and finally in Sec. 6.6 the chapter is concluded.

The content of this chapter was published in Physical Review B [70].

6.1 Silicon in two dimensions

Since the realisation of graphene as a truly 2D material, researcher have been looking for ways to use it as a basis for computational devices. However, as explained in Chapter 2, the energy spectrum of graphene is gapless and, therefore, one cannot make a graphene transistor by simply gating the graphene flake [88, 94]. Because of the chemical equivalence of the two carbon atoms in the unit cell, the gapless nature of the electronic spectrum is protected. Therefore, one needs to find ways to break this equivalence. In Chapter 5 it was pointed out that depositing the graphene flake on hBN, such that the boron and nitride atoms affect the two atoms in the unit cell in a different way, exactly breaks the atomic equivalence and, therefore, a gap was opened in the energy spectrum. However, the magnitude of the gap depends sensitively on the alignment of the graphene on the hBN substrate and cannot be changed electronically.

In the quest for other ways of employing the advantage of 2D materials that feature a high mobility, another route can be taken. Instead of considering carbon atoms that form a hexagonal lattice, it is possible to use other group-IV elements like silicon, germanium or tin. This leads to the proposal of new types of 2D materials like *silicene* [210], *germanene* [211] and *stanene* [212] respectively. In this chapter, the focus will be on silicene. However, often the extension to other materials can be made relatively easy by replacing the relevant material dependent parameters.

Because the material itself is made out of silicon atoms, silicene is naturally compatible with existing silicon based nanotechnology [46]. Furthermore, in contrast to graphene, the material does have a gap in the energy spectrum. This gap is generated by spin-orbit coupling (SOC) and makes the electrons in silicene to be susceptible to external perturbations in a different way depending on the particular energy valley and their spin [213]. Together with the fact that the spin-coherence length and spin-diffusion time of silicon is much longer than that of graphene [214–216], silicene can be an excellent candidate for spintronic applications [214, 216, 217].

Creating free-standing silicene faces a huge challenge in overcoming the material's tendency for oxidation when exposed to air [46, 218, 219]. Therefore, it is necessary to encapsulate the sample with a non-reactive material [218]. To date, there have been several attempts at synthesizing silicene by epitaxial growth on metallic substrates and the likely formation on silver [210, 220, 221], ZrB_2 [222] and Ir [223] have been reported. Moreover, very recent theoretical studies predict the stability of silicene on non-metallic surfaces such as graphene [224], boron nitride or SiC [225], and in graphene-silicene-graphene structures [226]. The strong scientific activity in the field of silicene even led very recently to a silicene-based room-temperature field-effect transistor [227].

Apart from the well studied transport properties of silicene [228–232], it is interest-

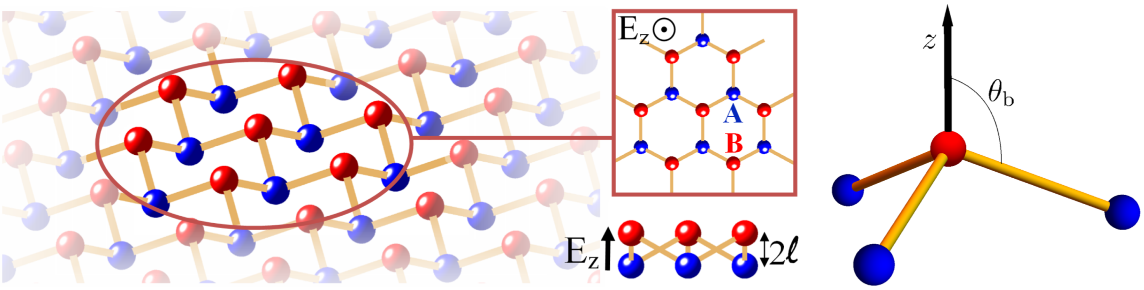

Figure 6.1: Left: Buckled hexagonal lattice structure of silicene. The blue atoms form the A sublattice, the red atoms form the B sublattice. The inset shows the top view indicating that it is a hexagonal structure. The external electric field E_z is also indicated. Right: indication of the buckling angle θ_b that measures the angle between the z-axis and the A-B bond. For illustrative purposes, the angle is exaggerated. For silicene the angle is $\theta_\text{b} = 101.7°$ [213]. The left figure is adapted from Ref. [238].

ing to investigate the plasmonic response of the 2D crystal. In this way, the spin- and valleytronic properties proposed by many to be useful in silicene, meet the field of 2D plasmonics [50].

6.2 Crystallographic and electronic structure of silicene

Silicene consists of a hexagonal lattice of silicon atoms [46, 213, 233]. Similar to graphene, the silicon atoms make up two trigonal sublattices which are called A and B sublattices. These sublattices are vertically displaced by $2\ell = 0.046$ nm [234, 235], and form the buckled structure of silicene with an angle θ_b that determines the buckling as shown in Fig. 6.1. Because silicon's ionic radius is larger than that of carbon, the interatomic distance of silicene is also larger than that of graphene, measuring $a_0 = 0.228$ nm with a lattice constant of $a = 0.386\ \text{nm}$. Because of the buckling, the conduction electrons move in a hybridisation [236] of p_z orbitals with the σ bonding orbitals and therefore the band structure features a strong spin-orbit coupling (SOC) [237]. In the following section the energy dispersion for a buckled honeycomb lattice will be calculated and the effect of the buckling on the SOC will be exemplified.

6.2.1 Low energy dispersion of a buckled hexagonal lattice

In order to find the low energy electronic properties of silicene, one needs to consider the four atomic orbitals ($3s$, $3p_x$, $3p_y$ and $3p_z$) of both atoms in the crystallographic unit cell.

This gives an eight dimensional tight-binding Hamiltonian that reads [213]

$$H_0 = \begin{bmatrix} H_\pi & H_n \\ H_n^\dagger & H_\sigma \end{bmatrix}, \tag{6.1}$$

where the basis $\left\{p_z^A, p_z^B, p_y^A, p_x^A, s^A, p_y^B, p_x^B, s^B\right\}$ has been used and H_π and H_σ denote the inter-orbital hopping following the π and σ bonds respectively. H_π is a 2×2 matrix, H_σ is a 6×6 matrix and H_n is a 2×6 matrix that connects the two bonds. This Hamiltonian corresponds to eight spin degenerate energy bands, half of which are populated by electrons as explained in appendix D. The middle two bands correspond to eigenstates that are found to be a superposition of the eight atomic orbitals as

$$\begin{aligned} \phi_1 &= u_{11} p_z^A + u_{21} s^A + \frac{u_{31}}{\sqrt{2}} \left(p_x^B + i p_y^B\right), & (6.2) \\ \phi_2 &= u_{11} p_z^B - u_{21} s^B - \frac{u_{31}}{\sqrt{2}} \left(p_x^A - i p_y^A\right). & (6.3) \end{aligned}$$

Here, the factors u_{ij} denote elements of a series of unitary transformations used to diagonalize the Hamiltonian matrix as outlined in appendix D. Because the system is hexagonal, it shares the reciprocal lattice structure with graphene and has the same high-symmetry points. Near the Dirac point K, the Hamiltonian can be projected on to the eigenstates from Eqs. (6.2) and (6.3) and gets the form [213]

$$H_K = \begin{pmatrix} \varepsilon_1 & \hbar v_{\mathrm{F}} k_- \\ \hbar v_{\mathrm{F}} k_+ & \varepsilon_1 \end{pmatrix}. \tag{6.4}$$

In Eq. (6.4) the on-site energy is denoted by ε_1 and $k_\pm = k_x \pm i k_y$, where $\boldsymbol{k} = (k_x, k_y)$ is the vector measuring the deviation from the Dirac point K. The Fermi velocity v_{F} now also depends on the mixed hoppings between different atomic orbitals and on the buckling angle θ_{b}. Eqs. (6.2) and (6.3) show that the eigenstates consist of all eight atomic orbitals. This shows the relatively strong sp^3 hybridisation of the silicene crystal.

The hybridisation depends on the buckling angle θ_{b}. If $\theta_{\mathrm{b}} = \pi/2$, i.e. for a planar structure, the hybridisation vanishes and Fermi velocity reduces to $v_{\mathrm{F}} = -\sqrt{3} V_{pp\pi} a/2$. Here, $V_{pp\pi}$ denotes the hopping amplitude between two p orbitals using a π bond. This parameter has the same function as the t considered before for graphene. Note, however, that for silicene the inter-atomic distance is larger than in the graphene case. Therefore, the hopping parameter is smaller and correspondingly also the Fermi velocity is smaller than in graphene even though the lattice constant a is larger [213]. The Fermi velocity in silicene is $v_{\mathrm{F}} \simeq 0.5 \times 10^6$ m/s, about half the value for graphene.

6.2.2 Spin-orbit coupling

The Hamiltonian in Eq. (6.4) has a linear energy spectrum that is shifted by an energy ε_1 but is gapless. Therefore, up to now, one has a similar energy band structure as graphene. However, in the above derivation no notion of spin was included. If one includes spin, also the spin-orbit coupling (SOC) should be accounted for. In contrast to graphene, the inclusion of SOC will turn out to be significant because the charge carriers move in orbitals that are strongly hybridised.

In general, the SOC contributes to the Hamiltonian as [213]

$$H_{\mathrm{so}} = \frac{\hbar}{4m_0^2c^2}\left(\boldsymbol{F}\times\boldsymbol{p}\right)\cdot\boldsymbol{\sigma}, \tag{6.5}$$

where m_0 is the bare electron mass, c is the speed of light, $\boldsymbol{\sigma}$ is the spin operator and $\boldsymbol{F}$ the force acting on the electrons due to SOC. As seen in Fig. 6.2, the force acting on an electron transitioning between neighbouring atoms should be zero because of symmetry considerations. Indeed, because the transition from sublattice A to sublattice B is equivalent to the reversed case, but the force is perpendicular to the bond connecting the two atoms, the force stemming from nearest neighbour transitions should vanish. However, for next-nearest-neighbour (NNN) transitions, there is a preferential direction because the hexagonal lattice is not symmetric with respect to the vector connecting the NNN atoms.

For silicene, due to the buckling, the force $\boldsymbol{F}$ consists of an in-plane and out-of-plane component as shown in Fig. 6.2 . The in-plane component contributes as

$$H_{\mathrm{so1}} = i\gamma_{\mathrm{so}}\left(\boldsymbol{F}_{\|}\times\boldsymbol{d}_{ij}\right)\cdot\boldsymbol{\sigma} \equiv it_{\mathrm{so}}\nu_{ij}\sigma_z. \tag{6.6}$$

In this equation, $\boldsymbol{d}_{ij}$ denotes the vector connecting the two NNN atoms, $\nu_{ij} = \boldsymbol{d}_i\times\boldsymbol{d}_j/\left|\boldsymbol{d}_i\times\boldsymbol{d}_j\right|$ with $\boldsymbol{d}_i$ the position vector of atom i and t_{so} is the hopping amplitude that will be determined later on. Notice that the quantity ν_{ij} is opposite for transitions between A sublattices and B sublattices. Because the force is oriented in the silicene plane, the σ_z component is selected by the scalar product and, therefore, this contribution will be opposite for spin-up or spin-down electrons.

The out-of-plane component of the force contributes as

$$H_{\mathrm{so2}} = i\gamma_1\left(\boldsymbol{F}_{\perp}\times\boldsymbol{d}_{ij}^0\right)\cdot\boldsymbol{\sigma} = i\gamma_{\mathrm{R}}\left(\boldsymbol{\sigma}\times\boldsymbol{d}_{ij}^0\right)\boldsymbol{F}_{\perp}^A\boldsymbol{e}_z \equiv it_{\mathrm{R}}\mu_{ij}\left(\boldsymbol{\sigma}\times\boldsymbol{d}_{ij}^0\right)_z. \tag{6.7}$$

In this equation, $\mu_{ij} = \pm 1$ for the A or B sublattices, $\boldsymbol{d}_{ij}^0 = \boldsymbol{d}_{ij}/\left|\boldsymbol{d}_{ij}\right|$ and t_{R} is the corresponding hopping amplitude.

Eqs. (6.6) and (6.7) show that the contribution of a SOC can be included in a NNN tight-binding model as [213]

$$H_{\mathrm{so}} = it_{\mathrm{so}}\sum_{\langle\langle ij\rangle\rangle_{\alpha\beta}}\nu_{ij}c_{i\alpha}^{\dagger}\sigma_{\alpha\beta}^{z}c_{j\beta} - it_{\mathrm{R}}\sum_{\langle\langle ij\rangle\rangle_{\alpha\beta}}\mu_{ij}c_{i\alpha}^{\dagger}\left(\boldsymbol{\sigma}\times\boldsymbol{d}_{ij}^0\right)_{\alpha\beta}^{z}c_{j\beta}. \tag{6.8}$$

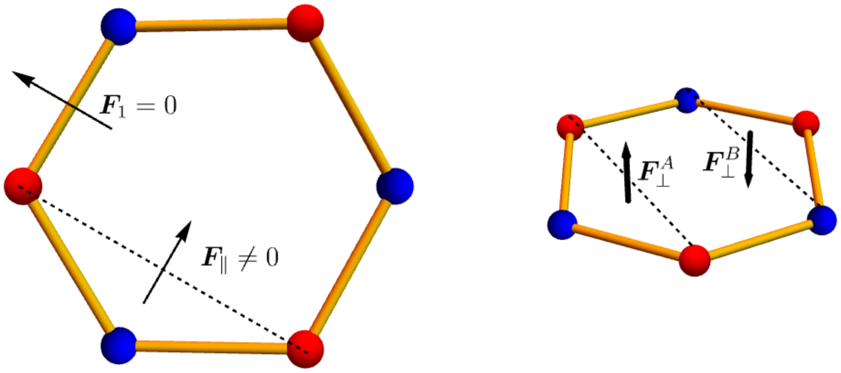

Figure 6.2: Orientation of the different forces acting due to SOC on different transitions between sublattices in silicene. The nearest-neighbour hopping $\boldsymbol{F}_1$ does not contribute because of reversal symmetry. The next-nearest-neighbour hopping does have a force contributing that can be decomposed in a portion parallel to the plane, $\boldsymbol{F}_\parallel$, and perpendicular to the plane, $\boldsymbol{F}_\perp$. Notice that these forces are opposite for both sublattices.

Here, $\langle\langle ij \rangle\rangle$ denote the NNN hopping. Together with the Hamiltonian from Eq. (6.4), neglecting the on-site energy ε_1, this becomes in the product space of sublattice and spin, i.e. $\{\psi_K^A, \psi_K^B\} \otimes \{\uparrow, \downarrow\}$, around the K point:

$$H_K = \begin{pmatrix} h_{11} & \hbar v_{\mathrm{F}} k_- \sigma_0 \\ \hbar v_{\mathrm{F}} k_+ \sigma_0 & -h_{11} \end{pmatrix}. \tag{6.9}$$

In this Hamiltonian, the element $h_{11} = -3\sqrt{3}\sigma_z t_{\mathrm{so}} - \frac{3\sqrt{3}}{2} t_{\mathrm{R}} a_0 \left(k_y \sigma_x - k_x \sigma_y\right)$ is a matrix in the spin space and σ_0 is the identity matrix in spin space. Importantly, Eq. (6.9) shows that the SOC influences both sublattices in a different way and therefore breaks sublattice symmetry. The origin of this breaking lies in the factors μ_{ij} and ν_{ij} that depend on the sublattice under consideration. Notice that the sign of h_{11} also changes under valley reversal [213].

The importance of the SOC terms is determined by the parameters t_{so} and t_{R}.These parameters can be determined using a more complete tight-binding method that relates them to the atomic orbital hopping parameters [213]. Usually, they are incorporated in corresponding energies as

$$\lambda_{\mathrm{so}} = -3\sqrt{3} t_{\mathrm{so}} = 3.9\ \mathrm{meV}, \tag{6.10}$$

$$\lambda_{\mathrm{R2}} = -\frac{3\sqrt{3}}{2} t_{\mathrm{R}} = 0.7\ \mathrm{meV}. \tag{6.11}$$

With these parameters, one can determine the energy spectrum corresponding to the Hamiltonian from Eq. (6.9) as

$$\varepsilon_{\lambda \boldsymbol{k}} = \lambda \sqrt{\left((\hbar v_{\mathrm{F}})^2 + \bar{\lambda}_{\mathrm{R2}}^2 \right) k^2 + \lambda_{\mathrm{so}}^2}. \tag{6.12}$$

This energy spectrum is shown in Fig. 6.3(a) for the different spin components. It corresponds to a doubly degenerate gapped system with gap $2\lambda_{\mathrm{so}}$. Furthermore, the $\bar{\lambda}_{\mathrm{R2}} = \lambda_{\mathrm{R2}}/a_0$ parameter affects the system by only changing the Fermi velocity and does not affect the gap.

The above described analysis explains how SOC affects the electronic properties of silicene. Although symmetry considerations cannot explain the size of the parameters quoted in Eqs. (6.10) and (6.11), they do explain how a finite value of λ_{so} breaks the sublattice symmetry and introduces a gap in the system. This is a feature of the hexagonal lattice of the material. For graphene, however, λ_{so} was determined to be parametrically small and can therefore be safely neglected [239]. The λ_{R2} parameter, on the other hand, is peculiar to silicene because it stems from the buckling of the hexagonal lattice [213]. It is related to the so-called *Rashba spin-orbit interaction* that is present in 2D systems subject to an electric field [239, 240]. However, here it surfaces even in the absence of an electric field and can, therefore, be considered as the response to an internal staggered electric field that arises due to the lattice buckling as shown in Fig. 6.2. The Rashba SOC connected to λ_{R2} is often called the *intrinsic Rashba SOC* to discriminate with the *extrinsic Rashba SOC* λ_{R1} arising due to external electric fields. The latter will be discussed in the next Section.

6.2.3 Influence of external fields on the energy spectrum

If one applies an external electric field E_z to the silicene crystal, it will affect the two trigonal sublattices in a different way. Indeed, the electric field can be incorporated as a local atomic single-particle Stark-effect term of the form [239]

$$H_{\mathrm{EF}} = eE_z \sum_i z_i, \tag{6.13}$$

where e is the elementary charge and z_i is the coordinate perpendicular to the silicene plane. Therefore, the sublattice lying at the top acquires an additional on-site energy of $E_{\mathrm{EF}} = e\ell E_z$, while for the bottom sublattice this is $E_{\mathrm{EF}} = -e\ell E_z$. This can be incorporated in the Hamiltonian Eq. (6.9) as a term $H_{\mathrm{EF}} \sim e\ell E_z \tau_z$, where τ_z is a Pauli matrix in sublattice space.

The effect of the electric field to the energy dispersion in the two valleys is shown in Fig. 6.3(b). Notice that the electric field also breaks sublattice symmetry and appears as an on-site potential. Therefore, it is in competition with the SOC parameter λ_{so}. Furthermore, the sign of λ_{so} is different for both spin types. As the electric field increases, the energy gap corresponding to spin-up electrons in the K valley is decreased while for the spin-down electrons the gap is broadened. In the K' valley the situation is reversed. As the electric field is increased, there is a critical field for which the gap completely closes and the energy spectrum becomes linear. This critical electric field is reached for $E_{\text{c}} = \lambda_{\text{so}}/e\ell = 1.7$ kV/cm.

As shown in the previous section, the Rashba SOC arises due to an internal electric field in the crystal. If an external electric field is applied, the system will respond in the same way as Eq. (6.7), but with a coupling constant that depends on the strength of the external electric field. This constant becomes [235, 239]

$$\lambda_{\text{R1}}\left(E_z\right) = \frac{eE_z z_0}{3V_{sp\sigma}} \simeq 10\ \mu\text{eV}\,\frac{E_z}{E_{\text{c}}}. \tag{6.14}$$

In this equation, z_0 is proportional to the atomic size of a slicon atom and $V_{sp\sigma}$ is a hopping parameter as defined in appendix D. The contribution of the λ_{R1} term to the Hamiltonian has the same structure as Eq. (6.7) but is not accompanied by momentum dependent factors because it does not correspond to any inter-atomic hopping. Therefore, the additional term in the Hamiltonian is

$$H_{\text{R1}}\left(E_z\right) = \lambda_{\text{R1}}\left(E_z\right)\left(\xi\tau_z\sigma_y - \tau_y\sigma_x\right)/2. \tag{6.15}$$

Here, $\xi = \pm 1$ denotes the valleys and the τ's are Pauli matrices in sublattice space.

The fact that an electric field can be used as a parameter to tune the band gap is very interesting for transport applications of the material. Furthermore, because the electric field acts oppositely to the spin components in each valley, the material can be interesting for spintronic applications [214]. However, as seen in Fig. 6.3(b), the action of the electric field is opposite between the two valleys. Therefore, an electric field alone cannot be used to select charge carriers with a specific spin since it will always be compensated by the other valley.

This can be resolved by the introduction of a magnetic exchange field that will be labeled by M. This field can be induced by ferromagnetic adatoms [241] or a ferromagentic substrate [242, 243]. This is important as this field leads to spin- and valley-polarised currents [244] and, as will be shown, brings a spin and valley texture to the particle-hole excitation spectrum (PHES). The exchange field can be introduced to the Hamiltonian as

$$H_M = M\sigma_z. \tag{6.16}$$

The value of M is predicted to be $M \approx 3$ meV for graphene deposited on a EuO substrate [242]. The exchange effect is due to the proximity of the Eu^{2+} moments and is therefore tunable by varying the distance between the substrate and the silicene layer. In this chapter a slightly larger value of M is used to make its effect more clear. In Fig. 6.3(d) the effect of different values of M on the energy spectrum is calculated. As expected, it shifts the spin-up charge carriers up and the spin-down carriers down. Furthermore, the effect is the same in both valleys.

Due to its unusual band structure and the capability of modifying it in a spin- and valley-dependent way, silicene is expected to show exotic properties such as quantum spin/valley and anomalous Hall effects [235, 237, 245], magneto-optical and electrical transport [246].

6.3 Total Hamiltonian and density of states

Combining the different Hamiltonian terms from the previous section, the behaviour of the electrons in silicene can be described using a four-band next-nearest-neighbour tight-binding model. Near the K^{ξ} point, the corresponding Hamiltonian is given by [213, 235]

$$H_{\xi} = \hbar v_F \left(\xi k_x \tau_x + k_y \tau_y\right) + \xi \tau_z h_{11} - e\ell E_z \tau_z + M\sigma_z + \lambda_{R1}\left(E_z\right)\left(\xi \tau_x \sigma_y - \tau_y \sigma_x\right)/2, \quad (6.17)$$

The Fermi velocity of the electrons is for silicene $v_F \approx 0.5 \times 10^6$ m/s [213]. One can write this Hamiltonian in the basis of atomic spin-orbital eigenfunctions of the sublattices A and B for both spin components, $\Psi = \{\psi_{A\uparrow}, \psi_{B\uparrow}, \psi_{A\downarrow}, \psi_{B\downarrow}\}^T$, near the point K as

$$H_K = \begin{bmatrix} E\left(1,1\right) & \hbar v_F k_- & ia\lambda_{\mathrm{R2}} k_- & 0 \\ \hbar v_F k_+ & E\left(1,-1\right) & i\lambda_{R1} & -ia\lambda_{\mathrm{R2}} k_- \\ -ia\lambda_{\mathrm{R2}} k_+ & -i\lambda_{R1} & E\left(-1,1\right) & \hbar v_F k_- \\ 0 & ia\lambda_{\mathrm{R2}} k_+ & \hbar v_F k_+ & E\left(-1,-1\right) \end{bmatrix}, \quad (6.18)$$

where $E\left(s_z, t_z\right) = \Delta_{s_z} t_z + M s_z$ and $\Delta_{s_z} = s_z \lambda_{\mathrm{so}} - e\ell E_z$.

In the Hamiltonian (6.17) three types of SOC are included. The λ_{so} introduces a gap in the spectrum equal for all spin components. The terms λ_{R1} and λ_{R2} mix up the spin states. However, the effect of λ_{R1} is very small as shown in Eq. (6.14). Therefore, this term shall from now on be neglected.

A unitary transformation of Eq. (6.18) allows more insight into the importance of λ_{R2}. With the combinations

$$\psi_1 = [\hbar v_F \psi_{B\uparrow} + i a_0 \lambda_{\mathrm{R2}} \psi_{A\downarrow}]/\hbar v_F', \quad (6.19)$$

$$\psi_2 = [\hbar v_F \psi_{A\downarrow} + i a_0 \lambda_{\mathrm{R2}} \psi_{B\uparrow}]/\hbar v_F', \quad (6.20)$$

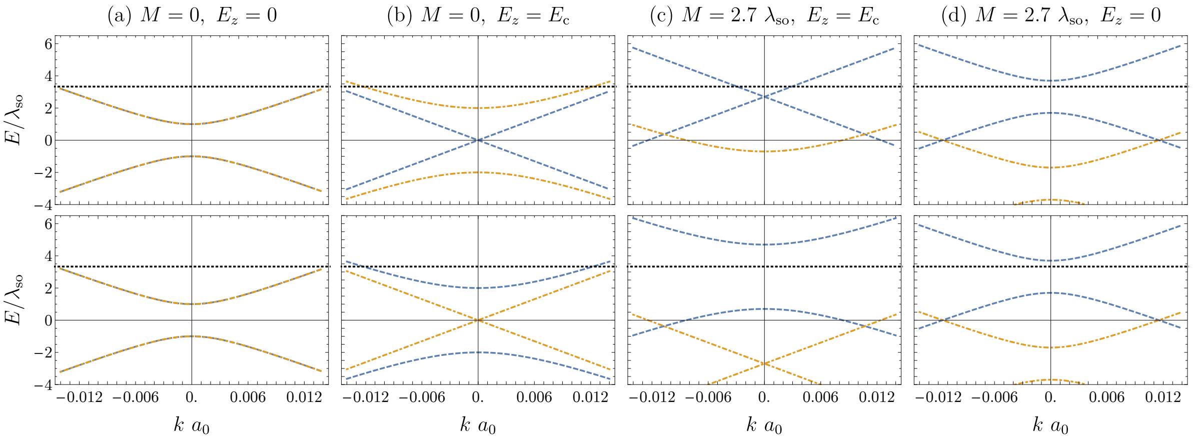

Figure 6.3: Energy spectrum of silicene versus wave vector k in the K (top row) and the K' valley (bottom row) for different values of the electric E_z and exchange M fields, as specified, and $\lambda_{\text{so}} = 3.9$ meV. The blue dashed curves pertain to $s_z = +1$ electrons and the orange dash-dotted curve to $s_z = -1$ electrons when the terms λ_{R2} are neglected. The dotted lines show the Fermi level $E_{\text{F}} = 13$ meV. This value for E_{F} will be used in the entire chapter.

where $\hbar v'_F = \hbar v_F(1+\eta^2)^{1/2}$ and $\eta = a\lambda_{\text{R2}}/\hbar v_F \approx 0.5 \times 10^{-3}$, the new basis $\Psi_{s_z} = \{\psi_{A\uparrow}, \psi_1, \psi_2, \psi_{B\downarrow}\}^T$ transforms Eq. (6.18) into the form

$$H'_+ = \begin{bmatrix} E\,(1,1) & \hbar v'_F k_- & 0 & 0 \\ \hbar v'_F k_+ & E\,(1,-1) - 2M'^2 & -2iM'c & 0 \\ 0 & 2iM'c & E\,(-1,1) + 2M'^2 & \hbar v'_F k_- \\ 0 & 0 & \hbar v'_F k_+ & E\,(-1,-1) \end{bmatrix}, \qquad (6.21)$$

where $M' = e\ell E_z + M$ and $c = \eta/(1+\eta^2)^{1/2}$.

The effect of λ_{R2} is thus threefold. To first order in η it induces a change in the Fermi velocity, $v_F \to v'_F$, and it couples the spin components by virtue of a finite electric E_z or exchange M field. Additionally, it affects the gap to second order in η by a diagonal term that is linear in E_z and M. However, these effects are very small due to the smallness of η. Therefore, λ_{R2} shall be neglected.

6.3.1 Effective Hamiltonian

The approximations referred to above decouple the two spin states. Because the valleys are independent, the charge carriers in silicene can be described as particles that have a spin- and valley-dependent gap. In the basis $\Psi_{\xi s_z} = \{\psi_{A,\xi s_z}, \psi_{B,\xi s_z}\}^T$ the Hamiltonian becomes

$$H_\xi^{s_z} = \begin{bmatrix} \Delta_{\xi s_z} + s_z M & \hbar v_F \xi k_-^\xi \\ \hbar v_F \xi k_+^\xi & -\Delta_{\xi s_z} + s_z M \end{bmatrix}, \tag{6.22}$$

where $s_z = \pm 1$ is the spin quantum number, ξ denotes the valley and $k_\pm^\xi$ equals $k_\pm$ for $\xi = +1$ and $k_\pm^*$ for $\xi = -1$. The gap is independent of M and is given by

$$2|\Delta_{\xi s_z}| = 2|\xi s_z \lambda_{\text{so}} - e\ell E_z|. \tag{6.23}$$

Equation (6.22) corresponds to a 2D Dirac Hamiltonian of particles with mass related to $\Delta_{\xi s_z}$. The energy spectrum obtained from Eq. (6.22) reads

$$\varepsilon_{\lambda \boldsymbol{k}}^{\xi, s_z} = s_z M + \lambda \sqrt{\hbar^2 v_{\text{F}}^2 k^2 + \Delta_{\xi s_z}^2}, \tag{6.24}$$

where $\lambda = 1(-1)$ denotes the electron (hole) states. For all spin and valley components the energy spectrum is shown in Fig. 6.3 for different values of ℓE_z and M. In Fig. 6.3(b) E_z attains its critical value $E_c = \lambda_{\text{so}}/e\ell$, for which the $s_z = +1$ spin component has a linear massless dispersion, while the $s_z = -1$ one has a large gap near the K point. In Fig. 6.3(c) the field M is finite; it displaces both spin components in opposite directions and results in a spectrum that is different for each spin and valley type of electron. In Fig. 6.3(d) only the M field is present and leads to spin polarisation but the valleys remain equivalent.

6.3.2 Density of states

This energy spectrum gives rise to a density of states $D(E)$ with a structure that depends sensitively on the values of the electric E_z and exchange M fields. With $\bar{E} = E - s_z M$ the full expression for $D(E)$ is [247]

$$D(E) = \sum_{\xi=\pm 1} \sum_{s_z=\pm 1} \frac{|\bar{E}|}{2\pi \hbar^2 v_F^2} \Theta\big(|\bar{E}| - |\Delta_{\xi s_z}|\big). \tag{6.25}$$

The DOS $D(E)$ is shown in Fig. 6.4 for various values of E_z and M. Notice that the DOS depends heavily on the spin and valley index of the electrons. In Fig. 6.4(c) and (d) for example, the total DOS is constant near zero energy, but it nonetheless consists of different portions of spin-up and spin-down states for each energy.

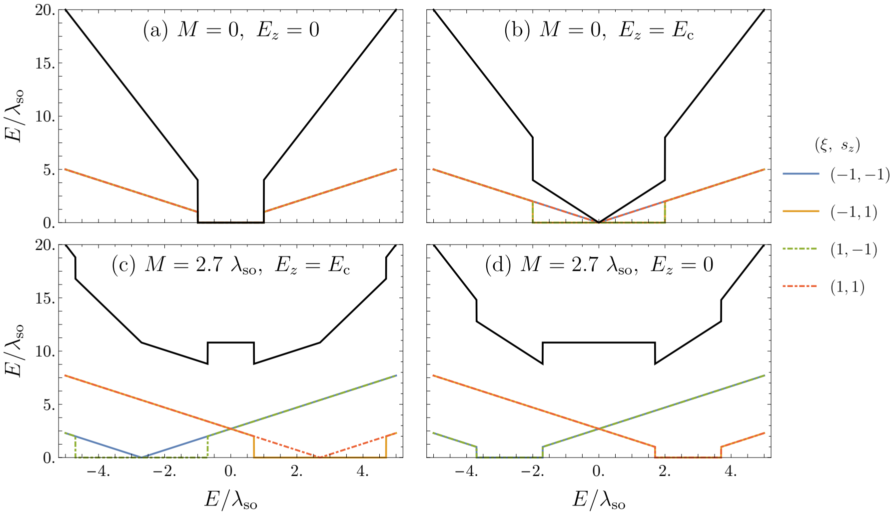

Figure 6.4: DOS in silicene for different values, specified, of the electric E_z and exchange M fields. The solid black curve is the total DOS. The other curves correspond to different valleys and spins as shown at the top of the figure. The DOS is expressed as a dimensionless quantity defined by $D'(E) = (2\pi\hbar^2 v_F^2/\lambda_{\text{so}})\, D(E)$.

6.4 Response function of silicene

To assess electron-electron interactions in the RPA, one needs to determine the corresponding RPA response function. As explained in the previous chapter, the non-interacting response function is composed of the spin and valley resolved response functions as

$$\chi_{nn}^{(0)}(q,\omega) = \sum_{\xi=\pm1} \sum_{s_z=\pm1} \chi_{\xi s_z}^{(0)}(q,\omega)\,, \tag{6.26}$$

where the summation over ξ corresponds to different valleys. For a finite-mass Dirac Hamiltonian, such as the one shown in Eq. (6.22), the spin and valley resolved non-interacting response function $\chi_{\xi s_z}^{0}$ is the same as the one considered in the previous chapter [198], but for a gap $\Delta_{\xi s_z}$ defined in Eq. (6.23) and an adapted Fermi level $E_{s_z} = E_{\text{F}} - s_z M$. Therefore, at a given Fermi level E_{F}, for each type of charge carriers, the gap will be affected differently for the different spin and valley types by the external electric and exchange fields. This is the core mechanism of spin and valley dependent optical properties in silicene.

The contributions to the response functions in Eq. (6.26) can be written as a sum of the vacuum and doped parts as in Eq. (3.31) : [106, 123]

$$\chi^{(0)}_{\xi s_z} = -\chi^{-}_{\xi s_z,\Lambda} + \chi^{+}_{\xi s_z,E_{s_z}} + \chi^{-}_{\xi s_z,E_{s_z}} \,. \tag{6.27}$$

The last two terms of Eq. (6.27) contribute only for $E_{s_z} > \Delta_{\xi s_z}$. Note that because the Fermi level E_{F} is fixed while the spectrum is displaced or deformed due to the field E_z or M, it is possible that this inequality is reversed for one valley spin state while it still holds for the others. In such a case only the vacuum part $\chi^{-}_{\xi s_z,\Lambda}$ contributes to the response of the respective state. Different possible situations are depicted in Fig. 6.3 in which the Fermi level is shown as a black dotted line. In Figs. 6.3(a) and (b) the Fermi level lies in the conduction band of all spin and valley type electrons such that intra-band transitions are possible. In Fig. 6.3(c), however, this is not the case for spin-up electrons near the K' valley. The combination of the M and E_z fields is such that the Fermi level lies in the band gap of this type of electrons and therefore intra-band transitions are excluded in this case. In Fig. 6.3(d) the two valleys are equivalent as discussed earlier, but the Fermi level lies in the gap of the spin-up electrons and excludes intra-band transitions for them. Therefore, one can write the response function as

$$\chi^{(0)}_{\xi s_z} = \Theta(E_{s_z} - \Delta_{\xi s_z})\chi^{(0)}_{\xi s_z,E_{s_z}} + \Theta(\Delta_{\xi s_z} - E_{s_z})\chi^{(0),u}_{\xi s_z} \,. \tag{6.28}$$

In this equation, $\chi^{(0),u}_{\xi s_z}$ denotes the total undoped contribution of the vacuum formed by a filled electronic valence band.

The complete expression of the dynamical response function is given in appendix B.3. In the static limit, i.e. $\omega \to 0$, it can be written as

$$\begin{aligned}
\frac{\chi^{(0)}_{\xi s_z,E_{s_z}}(q,0)}{D_0(E_{\mathrm{F}})} &= -[E_{s_z} - \frac{1}{4}\Theta\left(q - 2q_{F,s_z}\right)[\frac{2\bar{E}_{s_z} b_{\bar{q}}}{\bar{q}} - \frac{c_{\bar{q}}}{\bar{q}}\arctan\frac{b_{\bar{q}}}{2\bar{E}_{s_z}}]], \\
\frac{\chi^{(0),\mathrm{u}}_{\xi s_z}(q,0)}{D_0(E_{\mathrm{F}})} &= -\frac{1}{2}\Big[\bar{\Delta}_{\xi s_z} + \frac{c^2_{\bar{q}}}{2\bar{q}}\arcsin\frac{\bar{q}}{c_{\bar{q}}}\Big] \,.
\end{aligned} \tag{6.29}$$

In Eq. (6.29), $\bar{q} = \hbar v_{\mathrm{F}} q/E_{\mathrm{F}}$ as before, and $b_{\bar{q}} = [\bar{q}^2 - 4\bar{q}^2_{F,s_z}]^{1/2}$ and $c_{\bar{q}} = [\bar{q}^2 - 4\bar{\Delta}^2_{s_z}]^{1/2}$; the Fermi wave vector is defined as $q_{F,\xi s_z} = \hbar v_F[E^2_{s_z} - \Delta^2_{\xi s_z}]^{1/2}$. For $M = 0$ Eq. (6.29) coincides with the result of Ref. [248] and for $M = E_z = 0$ and $\lambda_{\mathrm{so}} = \Delta$ with that of Ref. [198]. Fig. 6.5 shows the static response function for various values of the fields E_z and M. This figure shows that as long as all spin and valley type electrons contribute, for low q, the static response equals the DOS at the Fermi level, $D(E_{\mathrm{F}})$, which is the case for the blue dashed and red dotted curves. However, when this is not the case, as for the other two curves, the response function decreases because in this case, for some spin and valley type electrons only inter-band contributions are allowed.

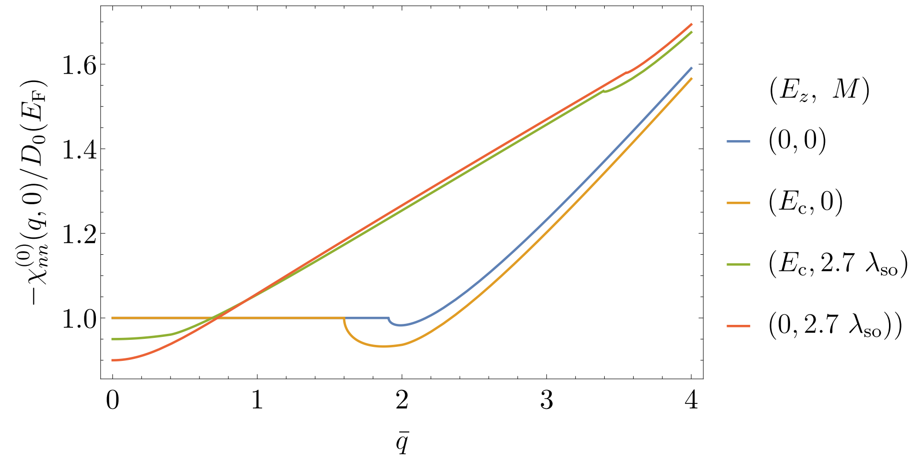

Figure 6.5: Static polarisation versus wave vector $\bar{q}$ for different values of the fields E_z and M as indicated. The Fermi level is $E_\mathrm{F} = 13$ meV and the SOC $\lambda_\mathrm{so} = 0.3E_\mathrm{F}$.

Furthermore, one can approximate the response function at small energies and momenta, $\hbar v_F q \ll \hbar\omega \ll E_\mathrm{F}$ as[198]

$$\frac{\chi^0_{\xi s_z}(q,\omega)}{D_0(E_\mathrm{F})} = \frac{\bar{q}^2 \bar{E}_{s_z}}{2\bar{\omega}^2}\left(1 - \frac{\bar{\Delta}^2_{\xi s_z}}{\bar{E}_{s_z}}\right)\Theta\left(\bar{\Delta}_{\xi s_z} - \bar{E}_{s_z}\right), \tag{6.30}$$

which is valid for all values of E_{s_z} and $\Delta_{\xi s_z}$.

6.4.1 Particle-hole excitation spectrum (PHES)

Because the fields E_z and M change the structure of the bands and the position of the Fermi level, the PHES is also subject to changes in their values. Since the valley and spin of the electrons determine how the fields affect their dispersion and Fermi level, the PHES can be different for electrons with different spin or valley index.

In Fig. 6.6 the PHES of silicene is shown for different values of E_z and M for which the energy spectra are shown in Fig. 6.3. The top row corresponds to electrons in the K valley and the bottom row to the K' valley.

Figure 6.6(a) shows that in the absence of the fields both valleys and spins are treated equally and the PHES is the same. When a finite electric field is applied, the gap is changed for each spin and the PHES of each spin near the same Dirac point is different. In the other valley, however, the effect of the electric field has the opposite effect such that the PHES is interchanged between both spin types. Figure 6.6(b) shows the PHES when the critical electric field E_c is applied. Since for this field one of the two spin states has a gapless dispersion, the PHES equals that of graphene for the spin-up state near the K valley and the spin down-state near the K' valley. The situation is reversed if E_z points in the opposite direction.

Changing the exchange field M also affects the PHES because the Fermi level of the two spin components is not the same. If the Fermi level of one component is moved inside the bandgap of the corresponding spectrum, the intra-band region completely disappears because there are no electrons left in the conduction band. This situation is depicted in Figs. 6.6(c) and (d) where a finite field M is considered. As seen in Fig. 6.3(c), for which the same fields are considered as Fig. 6.6(c), the Fermi level E_{+1} of the spin-up electrons is displaced inside the gap near the K' valley and therefore the intra-band PHES is absent in this case. The PHES of different spin and valley type electrons differs strongly, so spin and valley polarisation is expected because there are regions in the (q, ω) plane where only one spin and valley type of electrons can create an electron-hole pair.

If the field E_z is absent but the M one is finite, the spin symmetry is broken but the valleys remain equivalent. Figure 6.6(d) shows that the corresponding PHES is strongly spin dependent and spin polarisation is possible.

In the region between the intra- and inter-band PHES, it is not possible to excite a particle-hole pair. Therefore, in this region it is possible to excite stable plasmons. Inside the PHES, the plasmons do have a finite lifetime because they can decay into electron-hole pairs. Notice that the PHES has a spin and valley texture, that is, in some parts of the (q, ω) plane pair formation is allowed for only one spin and one valley component, denoted by $\{s_z, \xi\}$, but that there are also regions shared with different $\{s'_z, \xi'\}$ components. When pair formation is allowed for only one spin and valley type, it is possible to excite plasmons that contain only one specific spin or valley type of electrons and refer to them as spin- and valley-polarised plasmons.

6.4.2 Plasmons in silicene

Using the expression found in Eq. (6.26), the plasmons can be found, as usual, by investigating the zeroes of the dielectric function

$$\varepsilon^{\text{RPA}}(q, \omega) = 1 - v_q \chi^{(0)}_{nn}(q, \omega) = 1 - \frac{N_\text{f} \alpha_{ee}}{\bar{q}} \frac{\chi^{(0)}_{nn}(q, \omega)}{D_0(E_\text{F})} \tag{6.31}$$

with $v_q = 2\pi e^2/(\bar{\epsilon} q)$ the 2D Fourier transform of the Coulomb potential with an effective dielectric constant $\bar{\epsilon}$ that takes into account the medium surrounding the silicene sample. In this study free-standing silicene is considered and therefore $\bar{\epsilon} = 1$, the permittivity

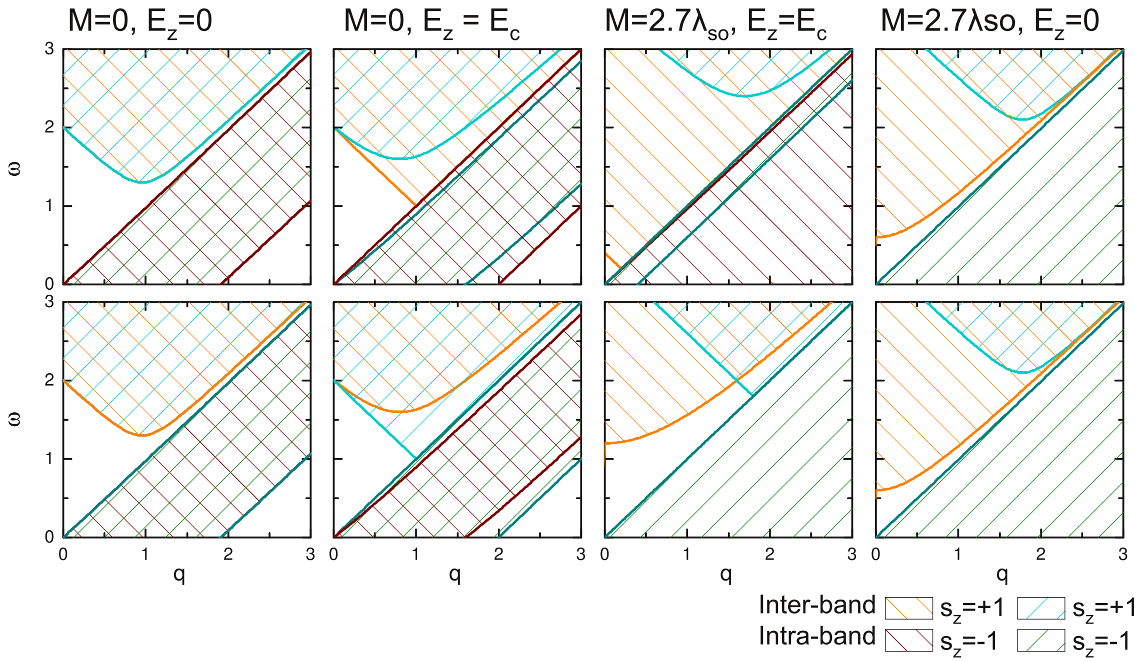

Figure 6.6: PHES of silicene for different values of the fields E_z and M as specified. The top row is for the K valley, the bottom row for the K' valley. The different hatched regions correspond to the spin type of the electrons as indicated at the top of the figure. The different colours refer to the inter- or intra-band PHES. The SOC is $\lambda_{\text{so}} = 0.3E_{\text{F}}$.

of vacuum. Recently, a new procedure to fabricate silicene, by intercalating it between two graphene layers, was proposed [226, 249]. Therefore, experimental realisation of the considered free-standing silicene system is possible. In Fig. 6.7 the real part of the RPA response function is shown in the top row.

The second equality of Eq. (6.31) features the silicene fine structure constant $\alpha_{ee} = e^2/(\bar{\epsilon}\hbar v_{\text{F}})$. This constant equals $\alpha_{ee} \approx 4$, which is twice that of graphene because the Fermi velocity in silicene is half that of graphene. Therefore, the e-e interaction in silicene is stronger.

In Fig. 6.7 the silicene loss function is shown in the bottom row. It is strong inside the inter-band PHES because here particle-hole pair formation is possible. There is, however, also a pronounced absorption curve outside the PHES. Here the response of the electron liquid is not absorbed by pair formation but by plasmon excitation.

The plasmon dispersion is found by solving the equation $\text{Re}\ \varepsilon^{\text{RPA}}\left(\mathbf{q}, \omega\right) = 0$ numer-

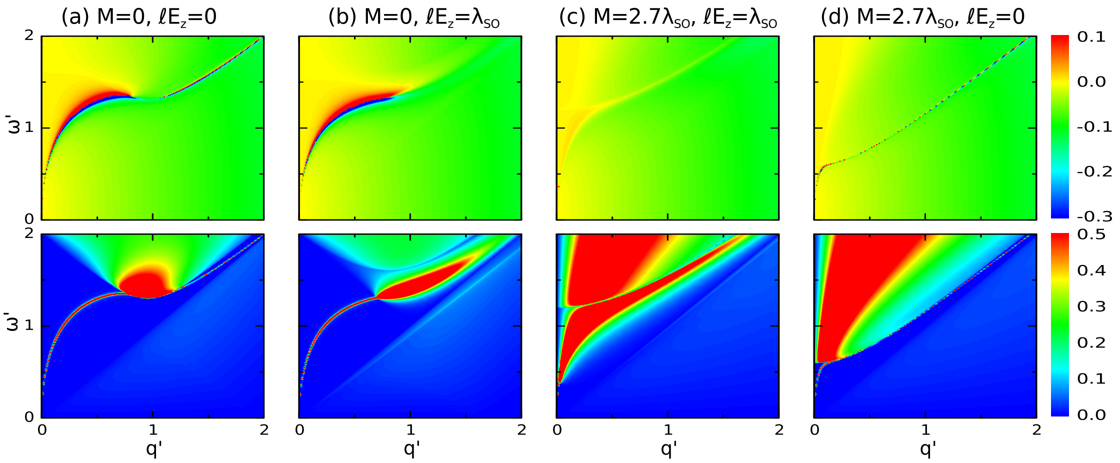

Figure 6.7: Top row: real part of the RPA response function for silicene. Bottom row: silicene electron loss function. For clarity a small imaginary part is added to ω, such that $\omega \to \omega + I\beta$ with $\beta = 10^{-4}$. The columns correspond to various values of the electric and exchange fields, as specified, that are the same as those used in the previous figures. The SOC strength is $\lambda_{\text{so}} = 0.3E_{\text{F}}$.

ically. However, for small energies and momenta one can find an approximate analytical solution upon using Eq. (6.30):

$$\bar{\omega}_{\text{pl}}^2 \approx \frac{\alpha\bar{q}}{8} \sum_{\xi,s_z=\pm1} \bar{E}_{s_z} \left(1 - \frac{\bar{\Delta}_{\xi s_z}^2}{\bar{E}_{s_z}^2}\right) \theta(\Delta_{\xi s_z} - E_{s_z}). \tag{6.32}$$

Note that again a $\sqrt{q}$ behaviour is obtained. This is typical for plasmons in 2D systems as mentioned before.

In the first row of Fig. 6.8 the plasmon branches are shown for several configurations of the electric and exchange fields. The solid curves correspond to the plasmons with zero decay rate while the dashed curves are the zeroes of the real part of ε. The plasmon dispersion given by Eq. (6.32) is shown by dash-dotted curves.

A more detailed study of the effect of the electric field on plasmons in silicene can be found in Ref. [248]; the results of this chapter reduce to those of this study for $M = 0$.

Finally, in order to asses the importance of the plasmon modes, also the oscillator strength as introduced in Sec. 3.2.5 and decay-rate are calculated in Fig. 6.8.

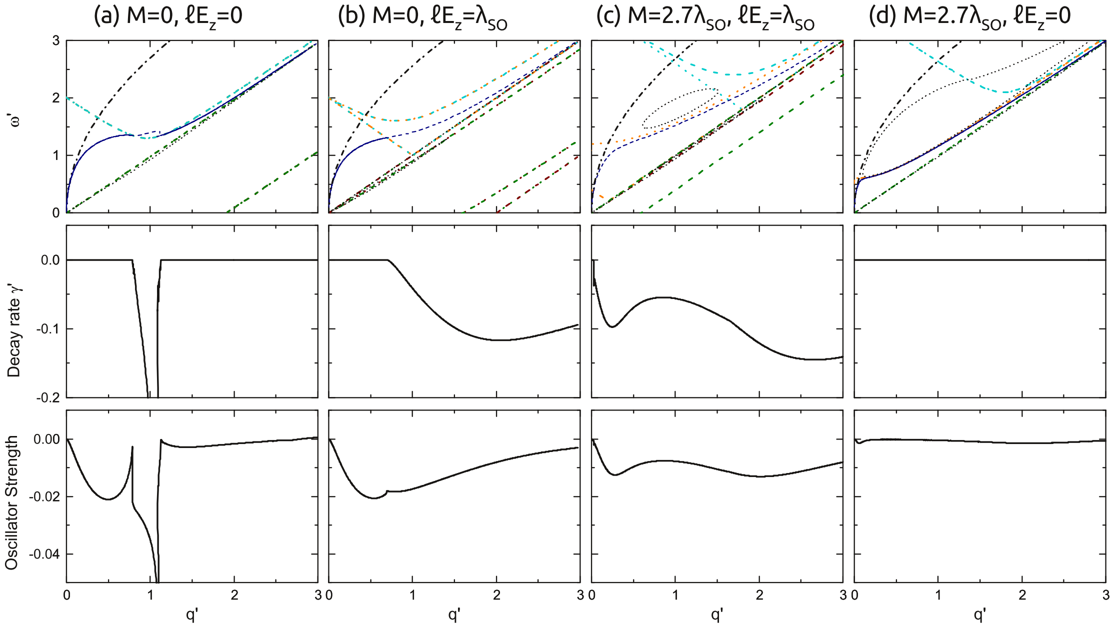

Figure 6.8: Top row: plasmon dispersion in silicene. The blue solid curve corresponds to plasmons that are not damped due to single-particle processes, the blue dashed curves are the roots of the real part of the dielectric function that are the prolonged versions of the stable branches, the blue dotted curves are the other roots of the real part of ε, the dash-dotted curve is the low-momentum approximation. The other coloured curves show the borders of the PHES of different spin and valley types as shown in Fig. 6.6 with the same colour code. The dashed curves are for the K valley and the dotted ones for the K' valley. Second and third rows: decay rate and oscillator strength, respectively, of the plasmon branches shown in blue on the first row. Each column corresponds to various values of the electric and exchange fields as specified.

6.5 Numerical results

The results shown in Figs. 6.7 and 6.8 correspond to four systems to which different electric and exchange fields are applied. These four different combinations of E_z and M correspond to the values used earlier in Figs. (6.3)-(6.6). This allows to demonstrate the different types of plasmons that can be excited in silicene.

The first column shows results for a Fermi level $E_\mathrm{F} \approx 3\lambda_\mathrm{so}$ but no external fields present. Here both spin types behave the same and a plasmon branch is obtained that is similar to that of gapped graphene as discussed before in Sec. 5.7. Note, however, that because the fine structure constant α_ee is twice that of free-standing graphene, it is interrupted by the inter-band PHES which is accompanied by a strong absorption. Inside the PHES, the decay rate increases very quickly showing the instability of the plasmon at that point. The oscillator strength of the small q plasmon branch is larger than that of the second part of the stable branch. The first part is therefore more pronounced than the second one.

In the second column E_z is the critical field, E_c, and the exchange field is zero. This particular example is especially interesting because the spectrum of the $s_z = +1$ electrons is linear and gapless while that of the $s_z = -1$ electrons has a large gap near the K valley. The corresponding plasmons have a dispersion that is similar to that of graphene, but which is interrupted by the PHES of the K spin-up electrons. The electron loss function shows that at this point the plasmon can decay into spin-up electron hole pairs near the K valley. This is supported by the increase in the decay rate, but note that this rate is much smaller than that for the first case because only one spin type per valley can induce pair formation. The oscillator strength of the plasmon outside the PHES is similar to that of the field-free case, but diminishes inside the PHES. Although the PHES and the plasmons in the two valleys depend on the spin type, they are compensated in the other valley. Therefore, in this case the plasmons are not spin polarised.

In the third column the electric and exchange fields are finite. Because of the combined effect of both fields, the PHES acquires a spin and valley texture. For very small q the plasmon branch is stable but it quickly encounters the border of the K spin-up PHES where the decay rate increases. The branch continues under the border of the K' spin-up PHES but the loss function signals its presence. The crossing of the border of the K' spin-down PHES results in a shortening of the lifetime because the plasmons can decay into two different types of electrons, the spin-up type in the K valley and the spin down one in the K' valley. Thus, in this case on obtains spin- and valley-polarised plasmons. Notice an additional feature, the oval dotted curve; this is the remnant of the plasmon branch of spin-down electrons. This oval curve, which corresponds to $\mathrm{Re}\varepsilon^{\mathrm{RPA}}(q,\omega) = 0$ contains for a given q two solutions. Only the top solution, corresponding to a positive decay rate, is a plasmon. The other solution has a negative decay rate.

The fourth column applies to the case where the electric field is absent but a very large exchange field is applied, $M \approx 2.7\lambda_\mathrm{so}$. In this situation the dispersions of both spin types are shifted with respect to each other in such a way that the Fermi level lies in the gap of the spin-up electrons while it is situated in the conduction band of the spin-down electrons. For spin-up electrons the intra-band PHES, therefore, vanishes and the inter-band PHES is shifted to lower energies. Here, there is an undamped plasmon branch that follows the border of the inter-band PHES of the spin-up electrons. Despite its stability, the oscillator strength and absorption show that it is not very pronounced. There exists, however, also a strongly damped branch that lies inside the spin-up inter-band PHES, shown by the dotted curve, which is the prolonged version of the undamped plasmon and that showing the same $\sqrt{q}$ dependence of the stable plasmon for low q. This branch indicates a spin-down plasmon but one which can decay very quickly into spin-up electron-hole pairs leading to a strong electron energy-loss in this region as shown in Fig. 6.7(d). This plasmon lies outside the PHES and is therefore neither spin- nor valley-polarised. However, the plasmon-like branch inside the spin-up PHES does resemble a spin-polarised system but with a very short lifetime.

6.6 Concluding remarks and outlook

This chapter investigated how electric (E_z) and exchange (M) fields can be used to tune the plasmonic response of the electron gas in silicene. These fields affect the PHES of electrons with opposite spin and valley indices in different ways giving the PHES a spin and valley texture and thus leading to spin- and valley-polarised plasmons. Their lifetime is, however, finite because they can easily decay into electron-hole pairs with different spin or valley indices. Further, the field M affects strongly the oscillator strength. The undamped plasmon that remains has a negligible strength and is therefore not expected to show up in experiments. If the Fermi level lies in the gap of a spin in one valley, the intra-band region of the corresponding PHES disappears. For zero E_z and finite M the spin symmetry is broken and spin polarisation is possible.

A low-momentum plasmon dispersion has been found that has the typical 2D $\sqrt{q}$ behaviour. At higher momentum, the plasmon dispersion differs from this $\sqrt{q}$ dependence. However, a strong field M can induce plasmons with finite lifetime of one spin type for which the dispersion follows closely the approximate plasmon branch.

The results reported in this work pertain to free-standing silicene since the permittivity of vacuum, ϵ_0, has been used. For silicene on a substrate the permittivity will be different and the results will be modified quantitatively. The plasmon branches will be curved downward due to the additional screening of e-e interaction by the substrate and the PHES can be avoided yielding plasmons with larger oscillator strength.

The predicted spin-and valley-polarisation of plasmons is a consequence of a mechanism similar to that responsible for directional filtering of plasmons in a 2D electron gas [250]. In this case the anisotropy of the electron dispersion renders the PHES anisotropic and damps the plasmons in one direction more than in the other. The next chapter is devoted to the investigation of the plasmonic properties of another anisotropic 2D plasmon system, namely graphene with a finite drift current.

CHAPTER 7

Current-induced birefringent absorption and non-reciprocal plasmons

How does an electric current influence the optical properties of graphene and can it be used to enhance the lifetime of plasmons in graphene?

This chapter analyses how the optical properties of a graphene sheet change when a strong current is induced in the Dirac fluid. Following Boltzmann transport theory, it is shown that this can be included by incorporating an additional term in the Fermi-Dirac distribution. Subsequently, the density-density response function is calculated with this drifted distribution. The imaginary part has an analytical solution while the real part can be obtained via the calculation of one numerical integral. It is demonstrated that an applied dc current modifies the Pauli blocking mechanism and that absorption acquires a birefringent character with respect to the angle between the in-plane light polarisation and current flow. Employing the random phase approximation at finite temperature, it is shown that graphene plasmons display a degree of non-reciprocity and collimation that can be tuned with applied current. In this chapter, the system under consideration is graphene encapsulated by hBN as considered in chapter 5. The results presented in this chapter are calculated for realistic parameters that represent empirically achievable situations. The chapter ends with some comments on how the proposed results could be measured.

The chapter is structured as follows: in Sec. 7.1 the importance of non-reciprocity in optical circuits is explained while in Sec. 7.2 the distribution function in the presence of a finite drift current is derived. In Sec. 7.3 the corresponding density-density response function is calculated at finite temperature and from this, in the $q \to 0$ limit, the absorption is derived in Sec. 7.4. In Sec. 7.5 the plasmon dispersion is calculated and its non-reciprocity is derived. Finally in Sec. 7.6 the chapter is summarised with some comments of the possibilities of measuring the proposed physics.

The content of this chapter is published in 2D Materials [71].

7.1 Non-reciprocal optical phenomena

Optical non-reciprocity arises when two oppositely propagating light rays experience a different interaction with the environment. A typical application for this is an optical isolator: a device that allows light to pass in one direction but block it in the other direction [251]. This is useful, for example, in the design of a laser where the optical isolator makes sure that the laser is protected from back reflections that could disturb the laser operation or when one wants to guide light in specific interference set-ups in for example optical communication systems [251].

Creating non-reciprocal materials can be done by breaking time-reversal symmetry. For example, magneto-optical effects were shown to feature a strong non-reciprocity [252–254]. However, the use of a magnetic field to break time-reversal symmetry is not suitable to be applied to nano-scale systems [255]. Therefore, the quest for materials or optical set-ups where non-reciprocity is generated free from magnetic fields receives a lot of attention in the photonic research world [251, 255–259].

Because plasmons represent light coupled to electrons in materials, it is of interest to look for plasmonic non-reciprocity that is also preferably free from magnetic fields. For plasmons the non-reciprocity will arise as a breaking of the symmetry of the plasmon dispersion under reversal of the direction of momentum, i.e. $\omega_{\text{pl}}(-\boldsymbol{q}) \neq \omega_{\text{pl}}(\boldsymbol{q})$. Furthermore, if one is able to show that plasmon propagation is only possible in one direction, so the plasmon is free from back-scattering, it is expected that this could enhance the plasmon lifetime in a similar way as the back-scattering-free optical modes in a topological material are protected [260–262] or as chirality reduces backscattering for electrons in graphene as discussed before in Sec. 2.3.

In graphene, non-reciprocity has recently been discussed for electron resonators where a magnetic field breaks the symmetry of counter-propagating modes [263]. Also, in the absence of a magnetic field, it has been found that at the edge of a graphene flake with a valley imbalance, there are unidirectional edge-plasmon modes that arise due to the band topology that induces an anomalous velocity that affects the boundary conditions of the system [204, 208].

In this chapter, a new way of generating non-reciprocal Dirac plasmons free from magnetic fields is presented. The main mechanism that breaks time reversal symmetry is the application of a finite drift current in the graphene flake. Graphene is very suitable for this because it has been shown that it can support ultra-high current densities without being damaged. Indeed, early on Moser *et al.* [40] proposed a simple method to suppress contamination of graphene at low temperatures inside a cryostat. Applying a source-drain bias of a few Volts across their samples, these authors induced a large current flow of up to $4\,\mathrm{mA}$, thereby removing contamination adsorbed on the surface. For a typical device width of $4\ \mu\mathrm{m}$, such current translates into an extremely large current density $J \simeq 10\ \mathrm{A/cm}$.

This chapter presents a detailed theoretical study of the optical and plasmonic properties of current-carrying graphene sheets. Previous authors [264, 265] have considered the same problem, but only reported approximate solutions that are valid for low current densities. Here, a semi-analytical approach is described, which can be applied for any current density (i.e. for drift velocities $|\boldsymbol{v}|$ as large as the graphene Fermi velocity $v_{\rm F}$) and at an arbitrary electron temperature T. The combined functionalities offered by electrical (or chemical) doping and dc currents may further enrich the graphene optoelectronic and plasmonic portfolio, possibly leading to interesting discoveries and/or potential applications. After the prepublication of the contents of this chapter, a second paper confirming the results appeared on the cond-mat repository [263].

7.2 Fermi-Dirac distribution of a drifting electron liquid

7.2.1 Boltzmann equations

Following Boltzmann transport theory, one can find the distribution function for an electron liquid in the conduction band with an applied electric field as [266, 267]

$$(\partial_t + \boldsymbol{v}_{\boldsymbol{k}} \cdot \boldsymbol{\nabla} + e\boldsymbol{E} \cdot \boldsymbol{\nabla}_{\boldsymbol{k}}) n_{\boldsymbol{k}}(\boldsymbol{r}, t) = S_{eL} + S_{ee}\ . \tag{7.1}$$

Here, $n_{\boldsymbol{k}}(\boldsymbol{r}, t)$ is the local distribution function of particles with wave vector $\boldsymbol{k}$ that needs to be obtained, $\boldsymbol{E}$ is the applied electric field, $\boldsymbol{v}_{\boldsymbol{k}}$ is the band velocity and S_{eL} and S_{ee} are the collision integrals of electrons with the lattice (e.g. with phonons) or with each other respectively.

From the Boltzmann equation, Eq. (7.1), one can derive the definitions of the conserved quantities of the system as:

$$n(\boldsymbol{r},t) = \int \frac{d^2\boldsymbol{k}}{(2\pi)^2} n_{\boldsymbol{k}}(\boldsymbol{r},t) \, , \tag{7.2}$$

$$\boldsymbol{j}(\boldsymbol{r},t) = v_{\rm F} \int \frac{d^2\boldsymbol{k}}{(2\pi)^2} \frac{\boldsymbol{k}}{k} n_{\boldsymbol{k}}(\boldsymbol{r},t) \, , \tag{7.3}$$

$$\mathcal{E}(\boldsymbol{r},t) = \int \frac{d^2\boldsymbol{k}}{(2\pi)^2} \varepsilon(\boldsymbol{k}) n_{\boldsymbol{k}}(\boldsymbol{r},t) \, . \tag{7.4}$$

Here, $n(\boldsymbol{r},t)$ is the particle density, $\boldsymbol{j}(\boldsymbol{r},t)$ the current density and $\mathcal{E}(\boldsymbol{r},t)$ the energy density.

If the graphene sample is encapsulated by hBN, as shown before, electron-lattice interaction can be neglected with respect to the e-e interaction. In this collisional regime where e-e interactions are the most important, the electron-lattice collision integral can be neglected, $S_{eL} = 0$. The e-e collision term can then be written as [267]

$$\begin{aligned} S_{ee}(\boldsymbol{k}_1) = \int \; & d\boldsymbol{k}_2 d\boldsymbol{k}_3 d\boldsymbol{k}_4 \delta(\varepsilon_{\boldsymbol{k}_1} + \varepsilon_{\boldsymbol{k}_2} - \varepsilon_{\boldsymbol{k}_3} - \varepsilon_{\boldsymbol{k}_4}) \delta^{(2)}(\boldsymbol{k}_1 + \boldsymbol{k}_2 - \boldsymbol{k}_3 - \boldsymbol{k}_4) \\ \times \; & \{[1 - n_{\boldsymbol{k}_1}][1 - n_{\boldsymbol{k}_2}] n_{\boldsymbol{k}_3} n_{\boldsymbol{k}_4} - n_{\boldsymbol{k}_1} n_{\boldsymbol{k}_2} [1 - n_{\boldsymbol{k}_3}][1 - n_{\boldsymbol{k}_4}]\} \, . \end{aligned} \tag{7.5}$$

This describes a scattering process between two particles with $\boldsymbol{k}_1$ and $\boldsymbol{k}_2$ into states with $\boldsymbol{k}_3$ and $\boldsymbol{k}_4$ where the δ functions make sure that energy and momentum are conserved in the collision. The distribution functions $n_{\boldsymbol{k}_i}$ determine the occupation probability of an electron in state $\boldsymbol{k_i}$. In equilibrium, this collision integral vanishes and, therefore, it determines a form of the distribution functions that needs to nullify the integrand of Eq. (7.5):

$$\frac{1 - n_{\boldsymbol{k}_1}}{n_{\boldsymbol{k}_1}} \frac{1 - n_{\boldsymbol{k}_2}}{n_{\boldsymbol{k}_2}} = \frac{1 - n_{\boldsymbol{k}_3}}{n_{\boldsymbol{k}_3}} \frac{1 - n_{\boldsymbol{k}_4}}{n_{\boldsymbol{k}_4}} \, . \tag{7.6}$$

This equation can be solved by taking the logarithm of both sides as:

$$\log(g_1) + \log(g_2) = \log(g_3) + \log(g_4) \, . \tag{7.7}$$

Eq. (7.7) shows that the quantity $\log(g_i) = \log(1 - n_{\boldsymbol{k}_i})/n_{\boldsymbol{k}_i}$ is conserved during the collision. This means that it should be a function of the other quantities that are conserved during the collision, i.e.

$$\log{(g_i)} = (k_{\rm B}T)^{-1}(\varepsilon_{\boldsymbol{k}_i} - \hbar\boldsymbol{V} \cdot \boldsymbol{k}_i - \mu) \, . \tag{7.8}$$

Eq. (7.8) is the most general equation that follows the requirement of energy and momentum conservation in each interaction. The quantities T, $\boldsymbol{V}$ and μ can be considered as

Lagrangian multipliers that make sure that the total conservation laws, Eqs. (7.2)-(7.4), remain valid. Solving Eq. (7.8) for the distribution functions $n_{\boldsymbol{k}_i}$, one finds

$$n_{\lambda \boldsymbol{k}_i} = \left[1 + \exp\left(\frac{\varepsilon_{\lambda \boldsymbol{k}_i} - \hbar \boldsymbol{V}(\boldsymbol{r},t)\cdot \boldsymbol{k}_i - \mu(\boldsymbol{r},t))}{k_{\rm B}T(\boldsymbol{r},t)}\right)\right]^{-1} . \tag{7.9}$$

In this equation the band index λ is restored. Note that the Lagrangian multipliers generally depend on the position $\boldsymbol{r}$ and the time t. Their physical meaning will be discussed in the next section.

7.2.2 Interpretation of the Lagrangian multipliers

Now, one can calculate the corresponding carrier concentration for graphene $n_{\rm c}(\boldsymbol{r},t)$ as before in Eq. (2.33):

$$n_{\rm c}(\boldsymbol{r},t) = n_{\rm e}(\boldsymbol{r},t) + n_{\rm h}(\boldsymbol{r},t) \;, \tag{7.10}$$

where $n_{\rm e}(\boldsymbol{r},t)$ is the electron concentration and $n_{\rm h}(\boldsymbol{r},t)$ is the hole concentration that can be calculated as

$$n_{\rm e}(\boldsymbol{r},t) = \int \frac{d^2\boldsymbol{k}}{(2\pi)^2} n_{+,\boldsymbol{k}}(\boldsymbol{r},t) \tag{7.11}$$

$$n_{\rm h}(\boldsymbol{r},t) = \int \frac{d^2\boldsymbol{k}}{(2\pi)^2} [1 - n_{-,\boldsymbol{k}}(\boldsymbol{r},t)] \;, \tag{7.12}$$

In the absence of a term proportional to $\boldsymbol{V}$, the result was calculated in Eq. (2.33). In the presence of a finite $\boldsymbol{V}$, the carrier concentration can be written as

$$n_{\rm c}(\mu,T,\beta) = N_{\rm f} \sum_{\alpha=\pm 1} \int \frac{d^2\boldsymbol{k}}{(2\pi)^2} N_\alpha(\boldsymbol{k},\mu,T,\beta) \;, \tag{7.13}$$

which depends on the position and time through the Lagrangian multipliers. This dependence will be omitted from now on. In Eq. (7.13) one has

$$N_\alpha(\boldsymbol{k},\mu,T,\beta) = \frac{1}{\exp\left\{\frac{\hbar v_{\rm F} k[1-\alpha\beta\cos(\theta)]-\alpha\mu}{k_{\rm B}T}\right\}+1} . \tag{7.14}$$

In Eq. (7.14), θ is the angle between $\boldsymbol{k}$ and $\boldsymbol{v}$ and $\beta = |\boldsymbol{V}|/v_{\rm F}$. Without loss of generality, the integral in Eq. (7.13) can be calculated by choosing $\boldsymbol{V}$ to be oriented along the $\boldsymbol{e}_x$ direction. To calculate the integral, one can replace the radial integration variable k by introducing $k' = k[1-\alpha\beta\cos(\theta)]$ such that the integral becomes

$$N_{\rm f} \int \frac{d^2\boldsymbol{k}}{(2\pi)^2} N_\alpha(\boldsymbol{k},\mu,T,\beta) = \int_0^{2\pi} \frac{d\theta}{2\pi} \frac{1}{[1-\alpha\beta\cos(\theta)]^2} \int_0^\infty \frac{k dk}{2\pi} N_\alpha(\boldsymbol{k},\mu,T,0) \;. \tag{7.15}$$

The radial integral in Eq. (7.15) reduces to the integration without $\boldsymbol{V}$, i.e. $\beta = 0$, as given in Eq. (2.33), while the angular integration can be carried out by using the residue theorem: for $0 \leq \beta < 1$ one finds

$$\int_0^{2\pi} \frac{d\theta}{2\pi} \frac{1}{[1-\alpha\beta\cos(\theta)]^2} = \frac{1}{(1-\beta^2)^{3/2}} \,. \tag{7.16}$$

Notice that this expression is independent of α that discriminated between the electrons and holes. Therefore, the radial integral from Eq. (7.15) reduces to $n_{\rm c}(\mu, T)$. The total carrier concentration at finite T, $\boldsymbol{V}$ and μ, therefore, becomes

$$n_{\rm c}(\mu, T, \beta) = \frac{n_{\rm c}(\mu, T)}{(1-\beta^2)^{3/2}} \,. \tag{7.17}$$

Similarly, one can calculate the locally averaged drift velocity of the carriers as

$$\boldsymbol{v}(\boldsymbol{r}, t) = \frac{1}{n_{\rm c}(\boldsymbol{r}, t)} \int \frac{d^2\boldsymbol{k}}{(2\pi)^2} \boldsymbol{v}_{\boldsymbol{k}} \sum_\alpha n_{\alpha\boldsymbol{k}}(\boldsymbol{r}, t) \,, \tag{7.18}$$

where $\boldsymbol{v}_{\boldsymbol{k}} = \partial_{\boldsymbol{k}} \epsilon_{\boldsymbol{k}}$ is the band velocity which becomes for graphene $\boldsymbol{v}_{\boldsymbol{k}} = v_{\rm F}\boldsymbol{k}/k$. The resulting integral is

$$\begin{aligned} \boldsymbol{v}(\boldsymbol{r}, t) &= \frac{N_{\rm f} v_{\rm F}}{n_{\rm c}(\boldsymbol{r}, t)} \int_0^\infty \frac{kdk}{2\pi} \int_0^{2\pi} \frac{d\theta}{2\pi} \cos\theta \sum_\alpha N_\alpha(\boldsymbol{k}, \mu, T, \beta), \\ &= \frac{v_{\rm F}}{n_{\rm c}(\boldsymbol{r}, t)} \int_0^{2\pi} \frac{d\theta}{2\pi} \sum_\alpha \frac{\cos\theta}{[1-\alpha\beta\cos(\theta)]^2} n_\alpha(\mu, T) = \boldsymbol{V}(\boldsymbol{r}, t) \,. \end{aligned} \tag{7.19}$$

In Eq. (7.19), it has been noticed that the angular integral can be calculated as

$$\int_0^{2\pi} \frac{d\theta}{2\pi} \frac{\cos(\theta)}{[1-\alpha\beta\cos(\theta)]^2} = \alpha \frac{\partial g_\alpha(\beta)}{\partial\beta} \tag{7.20}$$

with

$$g_\alpha(\beta) = \int_0^{2\pi} \frac{d\theta}{2\pi} \frac{1}{1-\alpha\beta\cos(\theta)} = \frac{1}{\sqrt{1-\alpha^2\beta^2}} \,. \tag{7.21}$$

Eq. (7.19) shows that the Lagrangian multiplier $\boldsymbol{V}$ that was introduced to solve Eq. (7.7) corresponds to the mean drift velocity $\boldsymbol{v}$ of the charge carriers. If the mean drift velocity is zero, the distribution function reduces to

$$n_{\lambda\boldsymbol{k}} = \left[1 + \exp\left(\frac{\varepsilon_{\lambda\boldsymbol{k}} - \mu(\boldsymbol{r}, t)}{k_{\rm B}T(\boldsymbol{r}, t)}\right)\right]^{-1} , \tag{7.22}$$

which coincides with the usual Fermi Dirac distribution with chemical potential μ and electron temperature T. Notice that in the calculation of the density in order to obtain Eq. (7.16), it turned out that the integral was only finite if $\beta < 1$, i.e. $v < v_{\mathrm{F}}$. This is a condition that always needs to be satisfied in order to have a non-diverging particle density. As a consequence, for the charge carriers, the Fermi velocity v_{F} has a similar role as the speed of light by putting an upper bound to the possible drift velocity in the system.

In experimental set-ups, one is interested in the carrier density n_{c} and the charge current density $\boldsymbol{J}$. The relation between the former and the three Lagrangian parameters was already obtained in Eq. (2.33). For the latter, this can be related to the drift current as:

$$\boldsymbol{J}\left(\mu, T, \beta\right) = -ev_{\mathrm{F}}(\boldsymbol{r}, t) \int \frac{d^2\boldsymbol{k}}{(2\pi)^2} \frac{\boldsymbol{k}}{k} \sum_{\lambda} n_{\lambda\boldsymbol{k}}(\boldsymbol{r}, t) \; = -ev_{\mathrm{F}} n_{\mathrm{c}}\left(\mu, T, \beta\right) \boldsymbol{\beta}. \tag{7.23}$$

Here, $\boldsymbol{\beta} = \boldsymbol{v}/v_{\mathrm{F}}$, is the dimensionless drift velocity.

In Fig. 7.1(a) the dimensionless drift velocity β is shown as a function of the current density J, for different values of the chemical potential μ. It is clear that for low current densities the relation is linear as expected from Eq. (7.23). With increasing current density the function $\beta = \beta(J)$ flattens, and $\beta \to 1$ (i.e. the induced drift velocity reaches the graphene Fermi velocity) asymptotically, as expected from Eq. (7.23). Finite-temperature effects, shown in Fig. 7.1(b), tend to suppress the induced drift velocity.

Since the system under consideration is an open system, i.e. a graphene sheet attached to leads, the usual grand-canonical procedure [268] in which the chemical potential μ is forced to readjust at each value of T to make sure that the average number of particles is conserved is not followed. In this chapter, μ is fixed by the leads (and external gating) and does not change with temperature. For the sake of definiteness, an n-doped graphene sheet is considered. Results for p-doped systems are identical since the quantities of interest are particle-hole symmetric.

7.2.3 Galilean invariance

Dropping the position and time dependencies, the Fermi-Dirac distribution function with a drift velocity can be written as

$$n_{\lambda}(\boldsymbol{k}, \boldsymbol{v}; T) = \left[\exp\left(\frac{\varepsilon_{\lambda\boldsymbol{k}} - \hbar\boldsymbol{v}\cdot\boldsymbol{k} - \mu}{k_{\mathrm{B}}T}\right) + 1\right]^{-1}. \tag{7.24}$$

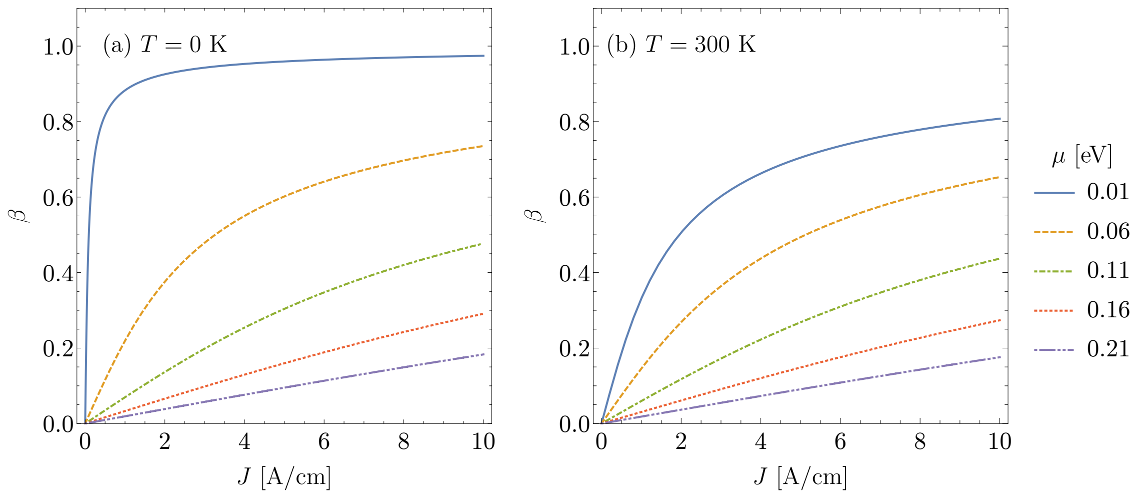

Figure 7.1: Dimensionless drift velocity β as a function of the current density J (in units of $\mathrm{A/cm}$), for different values of the chemical potential μ, as indicated in the legend. For (a) $T = 0$, and (b) $T = 300$ K.

This distribution is called the *drifted Fermi Dirac distribution*. If the energy dispersion $\varepsilon_{\lambda\boldsymbol{k}}$ is parabolic, i.e. $\varepsilon_{\lambda\boldsymbol{k}} = (\hbar k)^2 / (2m)$, this can be rewritten as

$$n_\lambda(\boldsymbol{k},\boldsymbol{v};T) = \left[\exp\left(\frac{\frac{(\hbar k)^2}{2m} - \hbar\boldsymbol{v}\cdot\boldsymbol{k} + \frac{mv^2}{2} - \frac{mv^2}{2} - \mu}{k_{\mathrm{B}}T}\right) + 1\right]^{-1}, \tag{7.25}$$

$$= \left[\exp\left(\frac{\frac{(\hbar\boldsymbol{k} - m\boldsymbol{v})^2}{2m} - \left(\mu + \frac{mv^2}{2}\right)}{k_{\mathrm{B}}T}\right) + 1\right]^{-1}. \tag{7.26}$$

Therefore, the expression for the response function can be rewritten as

$$\chi^{(0)}_{nn}(\boldsymbol{q},\omega) \sim \sum_{\boldsymbol{k}} \frac{n_\lambda(\boldsymbol{k},\boldsymbol{v};T) - n_\lambda(\boldsymbol{k}+\boldsymbol{q},\boldsymbol{v};T)}{\hbar\omega + \varepsilon_{\lambda\boldsymbol{k}} - \varepsilon_{\lambda\boldsymbol{k}+\boldsymbol{q}} + i\hbar\eta} \tag{7.27}$$

$$= \sum_{\boldsymbol{k}} \frac{n_\lambda(\boldsymbol{k},0;T) - n_\lambda(\boldsymbol{k}+\boldsymbol{q},0;T)}{\hbar\omega + \hbar\boldsymbol{q}\cdot\boldsymbol{v}/2 + \varepsilon_{\lambda\boldsymbol{k}} - \varepsilon_{\lambda\boldsymbol{k}+\boldsymbol{q}} + i\hbar\eta} \tag{7.28}$$

This corresponds to a response function with adapted Fermi level, $\mu' = \mu + mv^2/2$, where the Fermi circle is shifted in momentum space with the momentum $\boldsymbol{p}_0 = m\boldsymbol{v}$ and where the frequency is Doppler shifted as $\hbar\omega' = \hbar\omega + \hbar\boldsymbol{q}\cdot\boldsymbol{v}/2$. Apart from this, the system is invariant when transformed between two frames that move with respect to each other. This stems from the Galilean invariance of an electron gas with parabolic bands [102].

For graphene, it has been shown before that the energy dispersion is linear and, therefore, the Dirac electron gas is not Galilean invariant. Applying the same transformation as before, one finds

$$n_\lambda(\boldsymbol{k},\boldsymbol{v};T) = \left[\exp\left(\frac{\lambda v_{\rm F} k\,(1-\beta\cos\theta_{\boldsymbol{k},\boldsymbol{v}}) - \mu}{k_{\rm B}T}\right) + 1\right]^{-1} . \tag{7.29}$$

This explicitly depends on the angle $\theta_{\boldsymbol{k},\boldsymbol{v}}$ between $\boldsymbol{k}$ and $\boldsymbol{v}$, and cannot be simplified as in the parabolic case. In the following section, the density-density response function will be calculated in this case.

7.3 The density response function of a current-carrying graphene sheet

The optical properties of a current-carrying graphene sheet can be calculated by using LRT [102] with respect to the electric field of the incident light beam. The effect of an external dc current is included in a non-perturbative fashion. As seen in the previous section, the drift velocity satisfies the following inequality: $v < v_{\rm F}$. The obtained results, however, are not perturbative in the dimensionless parameter

$$\beta = \frac{v}{v_{\rm F}} . \tag{7.30}$$

To find the optical response of a current-carrying two-dimensional (2D) massless Dirac fermion (MDF) system [269], the dynamical density-density response function is calculated. This one is defined by [102]

$$\chi^{(0)}_{nn}(\boldsymbol{q},\omega;T) = N_{\rm f}\sum_{\lambda,\lambda'}\int\frac{d^2\boldsymbol{k}}{(2\pi)^2}\,|\mathcal{D}_{\lambda\lambda'}(\boldsymbol{k},\boldsymbol{k}+\boldsymbol{q})|^2\,\frac{n_{{\rm F},\lambda}(\boldsymbol{k},\boldsymbol{v};T) - n_{{\rm F},\lambda'}(\boldsymbol{k}+\boldsymbol{q},\boldsymbol{v};T)}{\hbar\omega + \varepsilon_{\boldsymbol{k},\lambda} - \varepsilon_{\boldsymbol{k}+\boldsymbol{q},\lambda'} + i\eta} . \tag{7.31}$$

Here, $N_{\rm f} = 4$ is the number of fermion flavors in graphene,

$$|\mathcal{D}_{\lambda\lambda'}(\boldsymbol{k},\boldsymbol{k}+\boldsymbol{q})|^2 = \frac{1}{2}\left[1 + \lambda\lambda'\cos(\theta_{\boldsymbol{k}} - \theta_{\boldsymbol{k}+\boldsymbol{q}})\right] \tag{7.32}$$

is the usual density vertex factor [105, 269], and $\eta = 0^+$ is a positive infinitesimal.

Replacing the frequency variable ω in the response function by $-\omega$, and replacing the integration variable $\boldsymbol{k} \to -\boldsymbol{k} - \boldsymbol{q}$, the response function becomes

$$\chi_{nn}^{(0)}(\boldsymbol{q},-\omega;T) = N_{\rm f}\sum_{\lambda,\lambda'} \int \frac{d^2\boldsymbol{k}}{(2\pi)^2}\left|\mathcal{D}_{\lambda\lambda'}(\boldsymbol{k},\boldsymbol{k}+\boldsymbol{q})\right|^2 \times \frac{n_{{\rm F},\lambda}(\boldsymbol{k},-\boldsymbol{v};T)-n_{{\rm F},\lambda'}(\boldsymbol{k}+\boldsymbol{q},-\boldsymbol{v};T)}{\hbar\omega+\varepsilon_{\lambda\boldsymbol{k}}-\varepsilon_{\lambda'\boldsymbol{k}+\boldsymbol{q}}-i\eta}\,. \tag{7.33}$$

This means that under this transformation both the sign of the velocity $\boldsymbol{v}$ as the imaginary part, η, changes. Therefore the relation becomes

$$\begin{aligned} \text{Re}\,\chi_{nn}^{(0)}(\boldsymbol{q},-\omega;T)\big|_{\boldsymbol{v}} &= \text{Re}\,\chi_{nn}^{(0)}(\boldsymbol{q},\omega;T)\big|_{-\boldsymbol{v}}\,, &(7.34)\\ \text{Im}\,\chi_{nn}^{(0)}(\boldsymbol{q},-\omega;T)\big|_{\boldsymbol{v}} &= -\text{Im}\,\chi_{nn}^{(0)}(\boldsymbol{q},\omega;T)\big|_{-\boldsymbol{v}}\,. &(7.35)\end{aligned}$$

Notice that this breaks the usual relation for the imaginary part derived in Eq. (3.70) which states that the sign of ω is opposite to that of Imχ. In this case also the direction of the velocity needs to be changed for the relation to hold. This will affect the sum rules related to the system.

7.3.1 The imaginary part of $\chi_{nn}^{(0)}$ at zero temperature

Following the method outlined in Sec. 3.1.4, at $T = 0$, the response function can be written as

$$\chi_{nn}^{(0)}(\boldsymbol{q},\omega;0) = -\chi_{\Lambda}^{-}(\boldsymbol{q},\omega)+\chi_{\mu,\boldsymbol{v}}^{-}(\boldsymbol{q},\omega)+\chi_{\mu,\boldsymbol{v}}^{+}(\boldsymbol{q},\omega)\,. \tag{7.36}$$

Notice that here the first term denotes the vacuum contribution which does not depend on the drift velocity $\boldsymbol{v}$. The other two terms can be written as

$$\chi_{\mu,\boldsymbol{v}}^{\pm}(\boldsymbol{q},\omega) = N_{\rm f}\int\frac{d^2\boldsymbol{k}}{(2\pi)^2}\sum_{\alpha=\pm1}\frac{\alpha\left|\mathcal{D}_{\pm}(\boldsymbol{k},\boldsymbol{k}+\boldsymbol{q})\right|^2\Theta\left(\mu-\varepsilon_{\boldsymbol{k}}+\alpha\hbar\boldsymbol{v}\cdot\boldsymbol{k}\right)}{\hbar\omega+\alpha\left(\varepsilon_{\boldsymbol{k}}\mp\varepsilon_{\boldsymbol{k}+\boldsymbol{q}}\right)+i\hbar\eta}. \tag{7.37}$$

This expression has a similar form as Eq. (3.32), except that the Heaviside step function now limits the radial integration to an angle-dependent wave number given by

$$k_{\rm F}^{\alpha}(\theta) = \frac{\mu}{\hbar v_{\rm F}\left(1-\alpha\beta\cos\theta_{\boldsymbol{k},\boldsymbol{v}}\right)}. \tag{7.38}$$

Notice that in Eq. (7.38) the chemical potential μ was used instead of the Fermi level $E_{\rm F}$. This is because the latter is chosen to correspond to the chemical potential at $T = 0$ and $v = 0$. In the following, the dimensionless quantities from Eq. (3.34) are redefined accordingly as

$$\overline{\boldsymbol{k}} = \frac{\hbar v_{\rm F}\boldsymbol{k}}{\mu},\ \overline{\boldsymbol{q}}\equiv\frac{\hbar v_{\rm F}\boldsymbol{q}}{\mu},\ \bar{\omega}\equiv\frac{\hbar\omega}{\mu}. \tag{7.39}$$

Because the Fermi wave vector depends on the angle between $\boldsymbol{k}$ and $\boldsymbol{v}$, the determination of the integration angle is less straightforward. Indeed, in Eq. (7.37) there are three angles that need to be considered. They appear in the factors

$$\begin{aligned} \left|\mathcal{D}_{\pm}\left(\boldsymbol{k},\boldsymbol{k}+\boldsymbol{q}\right)\right|^{2} &= \frac{1}{2}\left(1\pm\cos\left(\theta_{\boldsymbol{k},\boldsymbol{k}+\boldsymbol{q}}\right)\right), && (7.40)\\ \varepsilon_{\boldsymbol{k}+\boldsymbol{q}} &= \hbar v_{\mathrm{F}}\sqrt{k^{2}+q^{2}+2kq\cos\left(\theta_{\boldsymbol{k},\boldsymbol{q}}\right)}, && (7.41)\\ \boldsymbol{v}\cdot\boldsymbol{k} &= vk\cos\left(\theta_{\boldsymbol{k},\boldsymbol{v}}\right). && (7.42) \end{aligned}$$

In these equations, $\theta_{\boldsymbol{a},\boldsymbol{b}}$ denote the angle from vector $\boldsymbol{a}$ to vector $\boldsymbol{b}$. The first equation can be written as a function of the angle between $\boldsymbol{k}$ and $\boldsymbol{q}$ as in Eq. (3.37). For the last angle, one needs to measure it via $\boldsymbol{q}$ as

$$\theta_{\boldsymbol{k},\boldsymbol{v}}=\theta_{\boldsymbol{k},\boldsymbol{q}}+\theta_{\boldsymbol{q},\boldsymbol{v}}. \tag{7.43}$$

This introduces a new angle $\theta_{\boldsymbol{q},\boldsymbol{v}}$ that is fixed by the external conditions of the system, namely the direction of the drift velocity $\boldsymbol{v}$ and of the polarisation of the incident wave $\boldsymbol{q}$. This angle will be called $\psi\equiv\theta_{\boldsymbol{q},\boldsymbol{v}}$ and the angle $\theta\equiv\theta_{\boldsymbol{k},\boldsymbol{q}}$ will still serve as the integration variable. Notice that in that case the step function from the integrand of Eq. (7.37) becomes

$$\begin{aligned} \Theta\left(\mu-\varepsilon_{\boldsymbol{k}}+\alpha\hbar\boldsymbol{v}\cdot\boldsymbol{k}\right) &= \Theta\left(1-\bar{k}\left(1-\alpha\beta\cos\left(\theta+\psi\right)\right)\right)\\ &= \Theta\left(1-\bar{k}\left(1-\alpha\beta\left[\cos\theta\cos\psi-\sin\theta\sin\psi\right]\right)\right). && (7.44) \end{aligned}$$

Here, the dimensionless velocity β from Eq. (7.30) has been introduced.

Following the same derivation as outlined in Sec. 3.1.4, one can calculate the angular integral and obtain the expression (as before the barred notation is suppressed for clarity)

$$\begin{aligned} \mathrm{Im}\chi^{\pm}_{\mu,\boldsymbol{v}}\left(\boldsymbol{q},\omega\right) &= -\frac{D\left(\mu\right)q}{2\sqrt{q^{2}-\omega^{2}}}\sum_{\alpha=\pm1}\sum_{\gamma=\pm1}\frac{\alpha}{2}\\ &\times\int_{0}^{\infty}dk\sqrt{\left(\frac{2k+\alpha\omega}{q}\right)^{2}-1}F^{\alpha,\pm}_{\mathrm{Im}}\left(k,q,\omega\right)T^{\alpha,\gamma}_{\boldsymbol{v}}\left(k,q,\omega\right). && (7.45) \end{aligned}$$

In Eq. (7.45), the function $F^{\alpha,\pm}_{\mathrm{Im}}\left(k,q,\omega\right)$ is the same one as defined in Eq. (3.40) for the undrifted case. This function turned out to determine the PHES of the particles. However, when there is a finite drift velocity, an additional function $T^{\alpha,\gamma}_{\boldsymbol{v}}\left(k,q,\omega\right)$ appears that stems from the adapted step function. The function is defined as

$$\begin{aligned} T^{\alpha,\gamma}_{\boldsymbol{v}}\left(k,q,\omega\right)=\Theta\Bigg(&1-k+\frac{\alpha v}{2q}\Big[\cos\left(\psi\right)\left[\omega^{2}-q^{2}+2\alpha\omega k\right]\\ &-\gamma\sin\left(\psi\right)\sqrt{\left(q^{2}-\omega^{2}\right)\left[\left(2\alpha k+\omega\right)^{2}-q^{2}\right]}\Big]\Bigg). && (7.46) \end{aligned}$$

It shows that the angle ψ changes the PHES and because of the sum over $\gamma = \pm 1$, the total response function is still symmetric with respect to a sign change in ψ. Eq. (7.46) indicates that the effect of a finite drift velocity to the system is to change the radial integration domain corresponding to where the argument of Eq. (7.46) is positive. Notice that in the absence of a drift velocity the radial integration is limited as $k < k_{\mathrm{F}}$, but for a finite drift velocity this relation becomes quite complicated.

In order to evaluate the radial integral, one can introduce a new variable

$$x = \frac{2k + \alpha\omega}{q}. \tag{7.47}$$

This allows to rewrite Eq. (7.45) depending on whether $q > \omega$, corresponding to intra-band transitions or $q < \omega$, corresponding to inter-band transitions. The sign change in the argument of the square root is compensated for by the square root in front of Eq. (7.45). The remaining integral has an indefinite solution

$$\begin{aligned} \frac{1}{2} G_{\text{intra}}\left(x\right) &\equiv \int_{|x|>1} dx\sqrt{x^2-1} = \frac{1}{2}\left[x\sqrt{x^2-1} - \log\left(x + \sqrt{x^2-1}\right)\right], & (7.48) \\ \frac{1}{2} G_{\text{inter}}\left(x\right) &\equiv \int_{|x|<1} dx\sqrt{1-x^2} = \frac{1}{2}\left[x\sqrt{1-x^2} + \arcsin\left(x\right)\right]. & (7.49) \end{aligned}$$

Here, the functions $G_{\text{inter}}\left(x\right)$ and $G_{\text{intra}}\left(x\right)$ denote the solutions for the respective regions of the (q, ω) plane.

Written in this way, the effect of the step function in Eq. (7.46) is to change the integration domains of Eqs. (7.48) and (7.49). This effect depends on the value of q, ω and ψ, and can be computed by writing the function as

$$\begin{aligned} T^{\alpha,\gamma}_{\boldsymbol{v},\text{intra}}\left(x,q,\omega\right) &= \Theta\left[A_\alpha + Bx - C_\alpha\sqrt{x^2-1}\right], & (7.50) \\ T^{\alpha,\gamma}_{\boldsymbol{v},\text{inter}}\left(x,q,\omega\right) &= \Theta\left[A_\alpha + Bx - C_\alpha\sqrt{1-x^2}\right]. & (7.51) \end{aligned}$$

Here, the subscripts refer again to the relation between q and ω and the quantities A_α, B and C_α are defined as following:

$$\begin{aligned} A_\alpha &= 2 + \alpha\omega - \alpha\beta\cos(\psi)q, \\ B &= \beta\omega\cos(\psi) - q, \\ C_\alpha &= \alpha\beta\sin(\psi)\sqrt{|q^2-\omega^2|}. \end{aligned} \tag{7.52}$$

In this way, one has defined a transformation from the (q, ω, ψ)-space to the (A_α, B, C_α)-space. The latter can be used more easily to control the region where the argument of the function $T_{\boldsymbol{v}}^{\alpha,\gamma}(x,q,\omega)$ is positive. In tables 7.1 and 7.2 the expressions are summarised for different parts of the (A_α, B, C_α)-space. These expressions have been obtained by analysing the following functions:

$$\begin{aligned} g_{\text{intra}}(x) &= A_\alpha + Bx - C_\alpha\sqrt{x^2-1}\,, && (7.53)\\ g_{\text{inter}}(x) &= A_\alpha + Bx - C_\alpha\sqrt{1-x^2}\,. && (7.54)\end{aligned}$$

In Fig. 7.2 several examples of the functions $g_{\text{intra}}(x)$ and $g_{\text{inter}}(x)$ are plotted. The functions $T_{\boldsymbol{v}}^{\alpha,\gamma}(x,q,\omega)$ are only non-zero if the corresponding $g(x)$ is positive. From the definition of these functions in Eqs. (7.53) and (7.54) it clear that the function $g(x=1) = A_\alpha + B$ while $g(x=-1) = A_\alpha - B$. These points are indicated by black and red dots respectively in Fig. 7.2. Depending on whether $A_\alpha + B$ or $A_\alpha - B$ is positive or negative, the functions $g(x)$ are positive in different intervals on the x-axis. For example, by investigating Fig. 7.2(a), one sees that $g_{\text{intra}}(-1) < 0$ and, therefore, curves with $C_\alpha \leq 0$ are negative for every x. If $C_\alpha > 0$, the function is positive in a finite interval that is bordered by the intersection with the x-axis. The lower limit is given by the zero with positive derivative, while the upper limit is given by the zero with negative derivative. This analysis leads to a classification that of values of A_α, B and C_α that determine which are the boundaries to the integrals in Eq. (7.48). The result is summarized in Table 7.1.

A similar analysis can be performed for $g_{\text{inter}}(x)$. Here, however, both the signs of $A_\alpha + B$ and $A_\alpha - B$, shown as black and red dots in Fig. 7.2(c) respectively, determine upper and lower boundaries of the integrals. The result is summarised in Table 7.2.

The final result of the imaginary part of the response function can be written at $T = 0$ as:

$$\text{Im}[\chi_{nn}^{(0)}(\boldsymbol{q},\omega;0)] = f_\mu(\bar{q},\bar{\omega}) \sum_{\gamma=\pm1} U(\bar{q},\bar{\omega};\beta,\gamma\psi)\,, \tag{7.55}$$

where

$$f_\mu(x,y) = \frac{D(\mu)}{16}\frac{x^2}{\sqrt{|x^2-y^2|}}\,, \tag{7.56}$$

and

$$U(\bar{q},\bar{\omega};\beta,\psi) = -\Theta(\bar{q}-\bar{\omega})\sum_{\alpha=\pm1}\alpha H_{\text{intra}}(A_\alpha,B,C_\alpha) + \Theta(\bar{\omega}-\bar{q})[H_{\text{inter}}(A_{-1},B,C_{-1})-\pi]\,. \tag{7.57}$$

Analytical expressions for the real functions $H_{\text{intra}}(x,y,z)$ and $H_{\text{inter}}(x,y,z)$ in Eq. (7.57) are reported in Tables 7.1 and 7.2.

In Fig. 7.3 the imaginary part is shown for a polarisation along the drift velocity, i.e. $\psi = 0$ and opposite to the drift velocity, i.e. $\psi = \pi$. The results show that inter-band PHES strongly depends on the magnitude of the current and the angle ψ. If $\psi = 0$, the divergence

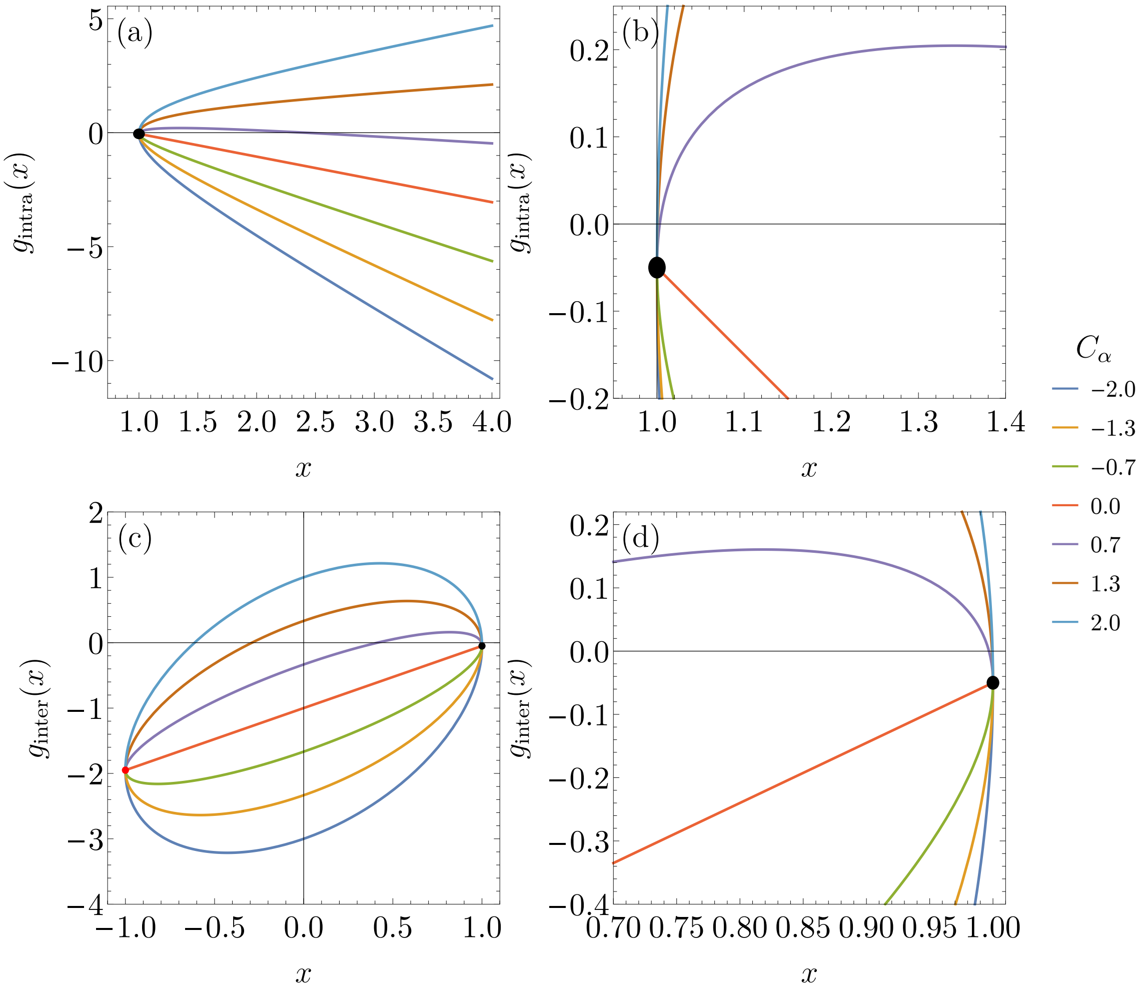

Figure 7.2: (a) Function $g_{\text{intra}}(x)$ as a function of x for different values for C_α as indicated. In this plot the values are $A_\alpha = 0.95$ and $B = -1$. (c) Function $g_{\text{inter}}(x)$ as a function of x for the values $A_\alpha = -1$ and $B = 0.95$ and different values of C_α as indicated. Figs. (b) and (d) are a zoom of (a) and (c) respectively to show that it is possible that the curve has two intersections with the x-axis. The black dots denote the position $(1, A_\alpha + B)$ and the red dot (only in (c)) denotes the position $(-1, A_\alpha - B)$. The figures show that whether the dots are above or below the x-axis determines which part of the function is positive and, therefore, contributes to the integral. This determines the categorisation presented in Tables 7.1 and 7.2.

$A_\alpha + B > 0$	$A_\alpha + B < 0$
$G_{\text{intra}}(x_-^\alpha)$	$\Theta(A_\alpha - \sqrt{B^2 - C_\alpha^2})\left[G_{\text{intra}}(x_-^\alpha) - G_{\text{intra}}(x_+^\alpha)\right]$

Table 7.1: This table summarizes the expressions that the function $H_{\text{intra}}(x, y, z)$ takes depending on the sign of the quantity $A_\alpha + B$. The left (right) column applies if $A_\alpha + B > 0$ ($A_\alpha + B < 0$). The function $G_{\text{intra}}(x) = x\sqrt{x^2 - 1} - \log(x + \sqrt{x^2 - 1})$ is evaluated at $x = x_i^\alpha$, where x_i^α is the root of the function $g_{\text{intra}}(x) = A_\alpha + Bx - C_\alpha\sqrt{x^2 - 1}$. Here, the subscript $i = \pm$ of the root x_i^α is given by the sign of the derivative $g'_{\text{intra}}(x)$ evaluated at $x = x_i^\alpha$, i.e. $g'_{\text{intra}}(x_+^\alpha) > 0$, while $g'_{\text{intra}}(x_-^\alpha) < 0$.

	$A_- + B > 0$
$A_- - B > 0$	$\Theta\left[A_- - \text{sgn}(C_-)\sqrt{B^2 + C_-^2}\right]\left[G_{\text{inter}}(y_-) - G_{\text{inter}}(y_+) + \pi\right]$ $+\Theta\left[\text{sgn}\left[C_-\right]\sqrt{B^2 + C_-^2} - A_-\right]$
$A_- - B < 0$	$\pi/2 - G_{\text{inter}}(y_+)$
	$A_- + B < 0$
$A_- - B > 0$	$G_{\text{inter}}(y_-) + \pi/2$
$A_- - B < 0$	$\Theta\left[A_- - \text{sgn}(C_-)\sqrt{B^2 + C_-^2}\right]\left[G_{\text{inter}}(y_-) - G_{\text{inter}}(y_+)\right]$

Table 7.2: Same as in Table 7.1, but for the function $H_{\text{inter}}(x, y, z)$. Here, $G_{\text{inter}}(x) = x\sqrt{1 - x^2} + \arcsin(x)$ and y_i with $i = \pm 1$ denote the roots of the function $g_{\text{inter}}(y) = A_- + By - C_-\sqrt{1 - y^2}$. As in Table 7.1, the subscript i is such that $g'_{\text{inter}}(y_+) > 0$, while $g'_{\text{inter}}(y_-) < 0$.

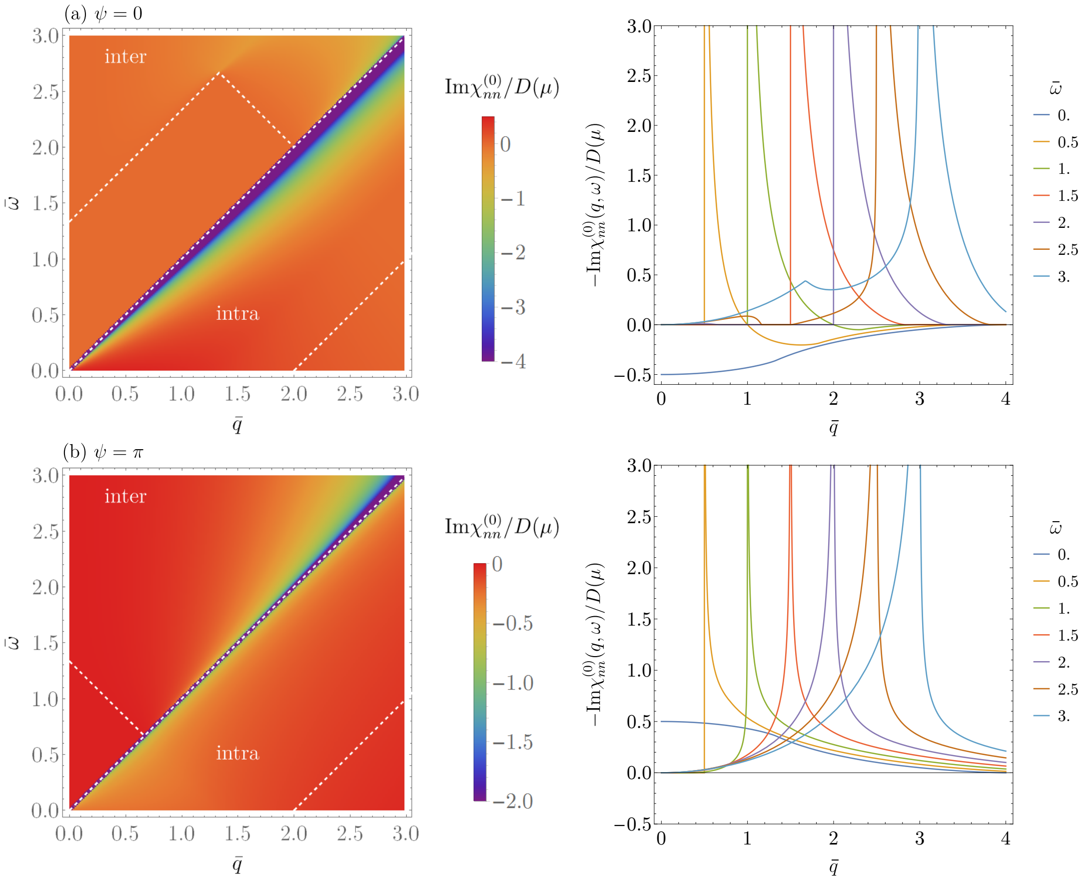

Figure 7.3: Imaginary part of the response function for a finite drift velocity $\beta = 0.5$. (a) shows the case when $\boldsymbol{q}$ is oriented along the drift velocity, (b) shows it when they are opposite.

near the light cone is made stronger over a larger range of frequencies. In the other case, the divergence is broadened. The most remarkable feature of the response function is that contrary to the case of a normal graphene flake, the imaginary part becomes positive in a region in the intra-band continuum. This is the consequence of the fact that the current in the distribution function pumps energy in the system. This energy is spontaneously released through intra-band processes. As seen in the left panels of Fig. 7.3, this also means that the imaginary part of the static response function is non-zero and opposite for opposite polarisation, as requested by Eq. (7.35).

7.3.2 The real part of $\chi_{nn}^{(0)}$ at zero temperature

The real part of $\chi_{nn}^{(0)}(\boldsymbol{q},\omega;T)$ at $T=0$ can be calculated from the following integral

$$\mathrm{Re}[\chi_{nn}^{(0)}(\boldsymbol{q},\omega;0)] = N_{\mathrm{f}} \sum_{\lambda,\lambda'} \mathcal{P} \int \frac{d^2\boldsymbol{k}}{(2\pi)^2} |\mathcal{D}_{\lambda\lambda'}(\boldsymbol{k},\boldsymbol{k}+\boldsymbol{q})|^2 \times \frac{n_{\mathrm{F},\lambda}(\boldsymbol{k},\boldsymbol{v};0) - n_{\mathrm{F},\lambda'}(\boldsymbol{k}+\boldsymbol{q},\boldsymbol{v};0)}{\hbar\omega + \varepsilon_{\lambda\boldsymbol{k}} - \varepsilon_{\lambda'\boldsymbol{k}+\boldsymbol{q}}} , \tag{7.58}$$

where $\mathcal{P}$ denotes a principal-value integration.

Without loss of generality, one can take $\boldsymbol{q} = q\boldsymbol{e}_x$ and denote by θ the polar angle of $\boldsymbol{k}$. This integral can be found by first *analytically* computing the integral over $k = |\boldsymbol{k}|$ in Eq. (7.58) and then treat the angular integration over θ numerically. The latter integration is performed over a finite domain and, therefore, can be computed numerically with relative ease. As before in the absence of a drift velocity in Sec. 3.1.4, by combining terms from the sum over λ and λ', the integral in Eq. (7.58) can be written as the sum of two contributions,

$$\mathrm{Re}[\chi_{nn}^{(0)}(\boldsymbol{q},\omega;0)] = \mathrm{Re}[\delta\chi_{nn}^{(0)}(\boldsymbol{q},\omega;0)] + \mathrm{Re}[\chi_{\mathrm{u}}(\boldsymbol{q},\omega)] , \tag{7.59}$$

where $\mathrm{Re}[\chi_{\mathrm{u}}(\boldsymbol{q},\omega)]$ is the undoped (or vacuum) contribution from Eq. (3.48), and

$$\mathrm{Re}[\delta\chi_{nn}^{(0)}(\boldsymbol{q},\omega;0)] = N_{\mathrm{f}} \sum_{\alpha,\alpha'=\pm1} \mathcal{P} \int \frac{d^2\boldsymbol{k}}{(2\pi)^2} |\mathcal{D}_{\alpha'}(\boldsymbol{k},\boldsymbol{k}+\boldsymbol{q})|^2 \frac{\alpha n_{\mathrm{F}}(\boldsymbol{k},\alpha\boldsymbol{v};0)}{\hbar\omega + \alpha(\varepsilon_{\boldsymbol{k}} - \alpha'\varepsilon_{\boldsymbol{k}+\boldsymbol{q}})}$$

is the contribution due to a finite doping.

To calculate the integral in Eq. (7.60) one can observe that, in the absence of a drift velocity ($\beta = 0$), the upper limit of the integral over k is the Fermi wave number $k_{\mathrm{F}} = \mu/(\hbar v_{\mathrm{F}})$. Indeed, for $\beta = 0$ the Fermi-Dirac distribution function in Eq. (7.60) has the form:

$$n_{\mathrm{F}}(\boldsymbol{k},0;0) = \Theta(\mu - \hbar v_{\mathrm{F}} k) = \Theta(k_{\mathrm{F}} - k) . \tag{7.60}$$

For $\beta > 0$ the distribution function changes into

$$n_{\mathrm{F}}(\boldsymbol{k},\alpha\boldsymbol{v};0) = \Theta(k_{\mathrm{F}}^{\alpha}(\theta) - k) , \tag{7.61}$$

where, the Fermi wave number from Eq. (7.38) was reintroduced. This allows to rewrite the real part of the response function as

$$\mathrm{Re}[\delta\chi_{nn}^{(0)}(\boldsymbol{q},\omega;0)] = D(\mu) \sum_{\alpha=\pm1} \int_0^{2\pi} \frac{d\theta}{2\pi} \frac{I(\theta)}{\alpha\bar{\omega} - \bar{q}\cos\theta} , \tag{7.62}$$

where

$$I(\theta) = \mathcal{P}\int_0^{\bar{\kappa}_{\rm F}(\theta)} dk k\frac{k+X(\theta)}{k+Y(\theta)}\ . \tag{7.63}$$

In Eq. (7.63) the following is defined:

$$\bar{\kappa}_{\rm F}(\theta) = \frac{\hbar v_{\rm F} k_{\rm F}(\theta)}{\mu}\ , \tag{7.64}$$

$$X(\theta) = \frac{\alpha\bar{\omega} + \bar{q}\cos\theta}{2} \tag{7.65}$$

and

$$Y(\theta) = \frac{\bar{\omega}^2 - \bar{q}^2}{2(\alpha\bar{\omega} - \bar{q}\cos\theta)}\ . \tag{7.66}$$

The quadrature in Eq. (7.63) can be carried out analytically. The end result is

$$I = \frac{1}{2}\bar{\kappa}_{\rm F}(2X - 2Y - \bar{\kappa}_{\rm F}) + Y(X-Y)\log\left|\frac{Y}{Y+\bar{\kappa}_{\rm F}}\right|\ . \tag{7.67}$$

Having found an expression for $I(\theta)$, the angular integration in Eq. (7.62) can be easily carried out numerically.

7.3.3 Extension to finite temperature

The temperature dependence of the response function in Eq. (7.31) is best evaluated by using the Maldague identity as discussed in Sec. 3.1.5. Indeed, also the drifted Fermi Dirac distribution Eq. (7.24) can be written as an integral similar to Eq. (3.58) as:

$$n_{{\rm F},\lambda}(\boldsymbol{k},\boldsymbol{v};T) = \int_{-\infty}^{\infty} dy \frac{[n_{{\rm F},\lambda}(\boldsymbol{k},\boldsymbol{v};0)]_{\mu\to y}}{4k_{\rm B}T\cosh^2\left[(y-\mu)/(2k_{\rm B}T)\right]}\ . \tag{7.68}$$

In Eq. (7.68) $n_{{\rm F},\lambda}(\boldsymbol{k},\boldsymbol{v};T)$ is expressed as an integral over μ of the zero-temperature Fermi step, accompanied by an appropriate weighting function. Then observe that the difference between the distribution functions in the numerator of Eq. (7.31) can be rewritten as:

$$\int_{-\infty}^{\infty} dy \frac{[n_{{\rm F},\lambda}(\boldsymbol{k},\boldsymbol{v};0)]_{\mu\to y} - [n_{{\rm F},\lambda'}(\boldsymbol{k}+\boldsymbol{q},\boldsymbol{v};0)]_{\mu\to y}}{4k_{\rm B}T\cosh^2[(y-\mu)/(2k_{\rm B}T)]}\ . \tag{7.69}$$

Since μ appears only in the numerator of Eq. (7.31), one can integrate first over $\boldsymbol{k}$ and then over y obtaining:

$$\chi^{(0)}_{nn}(\boldsymbol{q},\omega;T) = \int_{-\infty}^{\infty} dy \frac{\left[\chi^{(0)}_{nn}(\boldsymbol{q},\omega;0)\right]_{\mu\to y}}{4k_{\rm B}T\cosh^2[(y-\mu)/(2k_{\rm B}T)]}\ . \tag{7.70}$$

This formula expresses the finite temperature response function $\chi^{(0)}_{nn}(\boldsymbol{q},\omega;T)$ in terms of a weighted average of response functions $\chi^{(0)}_{nn}(\boldsymbol{q},\omega;0)|_{\mu\to y}$ at zero temperature and different chemical potentials.

7.4 Birefringent absorption

In this section the results for the density-density response function reported in Sect. 7.3 are used to calculate how the optical absorption spectrum of graphene is changed by a dc current.

Because the drift velocity $\boldsymbol{v}=(v_x,v_y)$ defines a preferential direction in the graphene sheet, the longitudinal conductivity $\sigma_{ij}(\omega)$ stemming from the density-density response function $\chi^{(0)}_{nn}(\boldsymbol{q},\omega;T)$ in Eq. (7.70) as defined in Eq. (3.97) transforms like a rank-2 tensor with respect to the Cartesian indices $i,j=x,y$. Notice that this conductivity is longitudinal with respect to the wave vector $\boldsymbol{q}$, but, because of the preferential direction, it is still a tensor. Following common practice—see section 3.4 in Ref. [102]—in the case of similar rank-2 tensors (like the current-current response function of a homogeneous and isotropic electron system), this tensor can be decomposed according to

$$\sigma_{ij}(\omega)=\sigma_{\rm L}(\omega)\frac{v_iv_j}{v^2}+\sigma_{\rm T}(\omega)\left(\delta_{ij}-\frac{v_iv_j}{v^2}\right)\,, \tag{7.71}$$

where the longitudinal $\sigma_{\rm L}(\omega)$ and transverse $\sigma_{\rm T}(\omega)$ components are defined by:

$$\sigma_{\rm L}(\omega)\equiv ie^2\omega\lim_{q\to 0}\left.\frac{\chi^{(0)}_{nn}(\boldsymbol{q},\omega;T)}{q^2}\right|_{\psi=0} \tag{7.72}$$

and

$$\sigma_{\rm T}(\omega)\equiv ie^2\omega\lim_{q\to 0}\left.\frac{\chi^{(0)}_{nn}(\boldsymbol{q},\omega;T)}{q^2}\right|_{\psi=\pi/2}\,. \tag{7.73}$$

Notice that here the longitudinality and transversality is defined with respect to the direction of the drift velocity $\boldsymbol{v}$. Of course, $\sigma_{\rm L}(\omega)$ and $\sigma_{\rm T}(\omega)$ depend on v.

The optical absorption $A_{ij}(\omega)$ is defined as in Eq. (3.102) by

$$A_{ij}(\omega)\equiv\frac{4\pi}{c}{\rm Re}[\sigma_{ij}(\omega)]\,. \tag{7.74}$$

Using Eq. (7.71)-(7.74) the following compact expression for the optical absorption can be found:

$$A_{ij}(\omega)=A_{\rm L}(\omega)\frac{v_iv_j}{v^2}+A_{\rm T}(\omega)\left(\delta_{ij}-\frac{v_iv_j}{v^2}\right)\,. \tag{7.75}$$

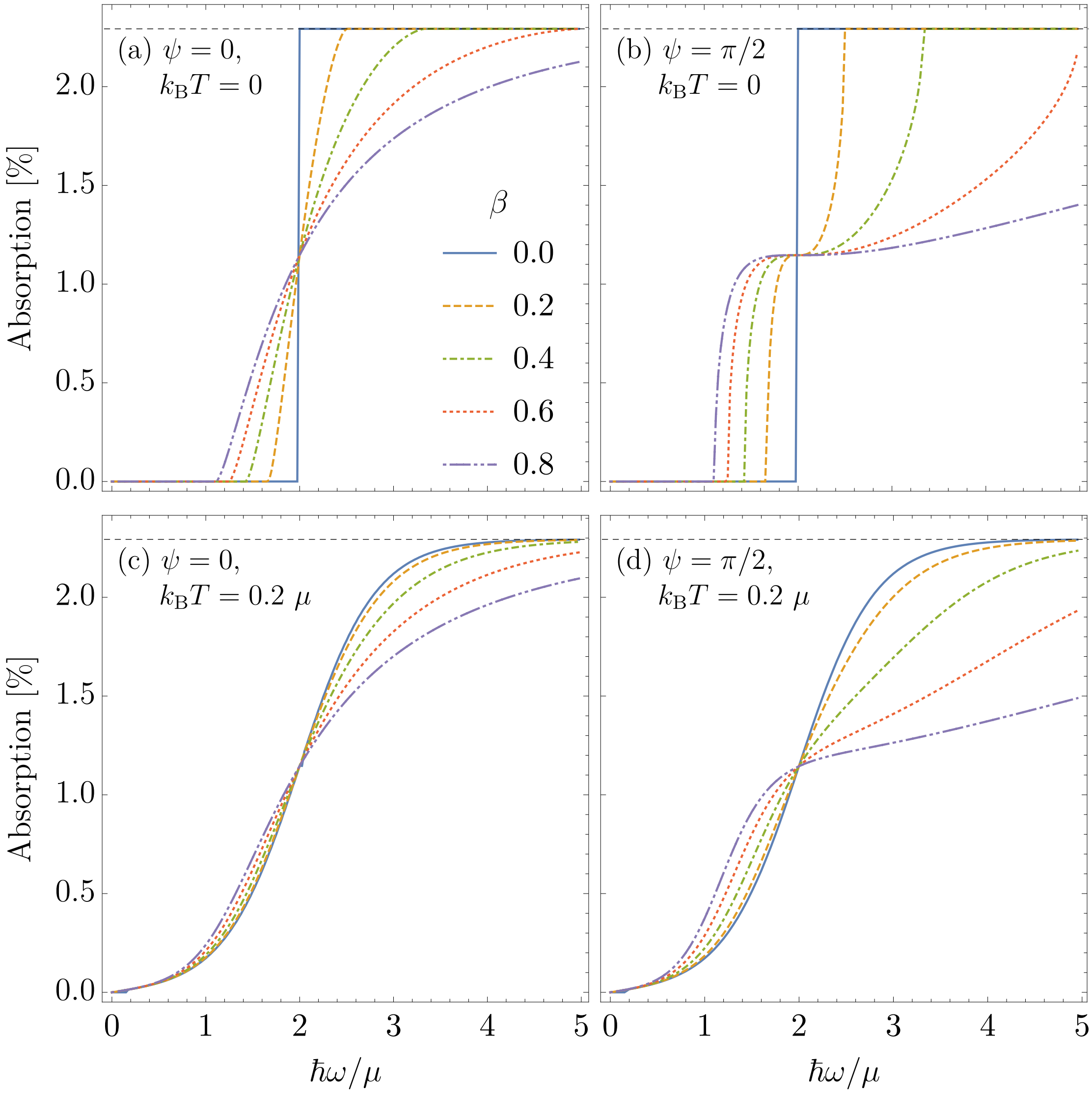

Figure 7.4: Absorption as a function of the incident photon frequency (in units of $\mu/\hbar$), for different values of the dimensionless drift velocity $\beta = v/v_{\mathrm{F}}$. Panels (a) and (b) show zero-temperature results for polarisation of light along ($\psi = 0$) and perpendicular ($\psi = \pi/2$) to the velocity direction, respectively. Panels (c) and (d) show the same quantities but for a finite temperature $k_{\mathrm{B}}T = 0.2\,\mu$. The dashed horizontal curve in each panel indicates graphene's maximal absorption, $\pi\alpha_{\mathrm{QED}} \simeq 2.3\%$.

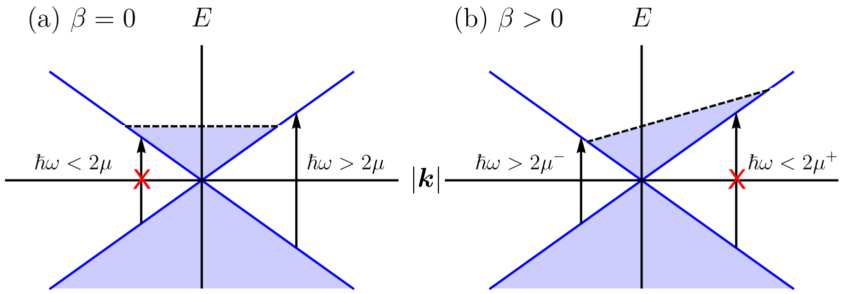

Figure 7.5: Illustration of the effect of a finite drift velocity on the Pauli blocking mechanism. Vertical arrows indicate electron-hole pair creation, while the red cross indicates transitions that are forbidden due to Pauli blocking. Panel (a) shows the Pauli blocking mechanism in the case $\beta = 0$, while panel (b) pictures the effect of a tilted Fermi level due to a finite value of β. The quantities μ^- ($< \mu$) and μ^+ ($> \mu$) have been defined in Eq. (7.78). The sharp absorption step $\pi\alpha_{\rm QED}\Theta(\hbar\omega - 2\mu)$ at $\beta = 0$ is smoothened by a finite value of β because Pauli blocking: i) is suppressed in the window $2\mu^- < \hbar\omega < 2\mu$ and ii) extends its action *above* 2μ in the window $2\mu < \hbar\omega < 2\mu^+$.

Equivalently, Eq. (7.75) can be written more explicitly in terms of the angle ψ between the polarisation of the incident light and the direction of the current:

$$A_{ij}(\omega) = A_{\rm L}(\omega)\cos^2(\psi) + A_{\rm T}(\omega)\sin^2(\psi)\ . \tag{7.76}$$

In the $T = 0$ limit this becomes

$$\begin{aligned} A_{\rm L(T)}(\omega) \quad &= \quad \pi\alpha_{\rm QED}\Theta(\hbar\omega - 2\mu) + \alpha_{\rm QED}\Theta\left(\hbar\omega - \frac{2\mu}{1+\beta}\right)\Theta\left(\frac{2\mu}{1-\beta} - \hbar\omega\right) \\ &\times \quad \left[\pm\frac{\hbar\omega - 2\mu}{\beta\hbar\omega}\sqrt{1 - \left(\frac{\hbar\omega - 2\mu}{\beta\hbar\omega}\right)^2} - {\rm sgn}\left(\frac{\hbar\omega - 2\mu}{\beta\hbar\omega}\right)\arccos\left|\frac{\hbar\omega - 2\mu}{\beta\hbar\omega}\right|\right]\ . \end{aligned} \tag{7.77}$$

Eqs. (7.76)-(7.77) are the most important results of this section. In writing these equations physical units have been restored for the sake of transparency. In the limit $\beta = 0$ Eq. (7.77) yields $A_{\rm L}(\omega) = A_{\rm T}(\omega) = \pi\alpha_{\rm QED}\Theta(\hbar\omega - 2\mu)$ as found in Eq. (3.106).

In Fig. 7.4 absorption is shown as a function of photon energy $\hbar\omega$ (in units of μ) for $\psi = 0$ (light polarisation parallel to drift velocity) and $\pi/2$ (light polarisation perpendicular to drift velocity) and different values of drift velocities (i.e. of the ratio $\beta = v/v_{\rm F}$), at zero and finite temperature. One can clearly see that the net effect of the finite drift velocity is to smooth the sharp absorption step $\pi\alpha_{\rm QED}\Theta(\hbar\omega - 2\mu)$ that occurs at $\beta = 0$. The latter stems from Pauli blocking, namely the lack of available empty states in the conduction band for vertical inter-band transitions assisted by photons with energy $\hbar\omega < 2\mu$. Absorption is allowed only for $\hbar\omega > 2\mu$. Now, for a finite drift velocity β, a window of photon energies opens up between the β-dependent boundaries over which the chemical potential is tilted by the applied dc current:

$$\mu^{\pm} \equiv \frac{\mu}{1 \mp \beta}\,, \tag{7.78}$$

with $\mu^{+} > \mu$ and $\mu^{-} < \mu$. As illustrated in Fig. 7.5, it is possible to excite electron-hole pairs if the photon energy surpasses the lower threshold $2\mu^{-} < 2\mu$. On the other hand, Pauli blocking extends its action *above* 2μ in the window $2\mu < \hbar\omega < 2\mu^{+}$.

Fig. 7.6 shows that the way in which the sharp $\beta = 0$ absorption step $\pi\alpha_{\rm QED}\Theta(\hbar\omega - 2\mu)$ is smoothed depends on the angle ψ between in plane light polarisation and drift velocity $\hat{\boldsymbol{v}}$ in two major directions, $\psi = 0$ and $\psi = \pi/2$. This results in a *birefringent* absorption in a current-carrying graphene sheet. Indeed, the absorption of the graphene sheet depends on the angle between the light polarisation and a preferential direction according to the conductivity tensor with two different principal components. Therefore, a light beam passing through the flake will respond as if the material has two different refractive indices for light with a polarisation along and perpendicular to the current direction.

In order to quantify the degree of absorption anisotropy and its dependence on temperature, one can calculate the quantity

$$\delta A(\omega) = \frac{A_{\rm L}(\omega) - A_{\rm T}(\omega)}{A_{\rm L}(\omega) + A_{\rm T}(\omega)}\,. \tag{7.79}$$

Figs. 7.7(a) and (b) show the temperature and photon frequency dependence of $\delta A(\omega)$. Note that a finite temperature yields a degree of optical anisotropy that is spread over a wider spectral range, compared with the zero-temperature case. For example, Fig. 7.6 shows that at $\hbar\omega = 2.7\,\mu$ the absorption is isotropic at $T = 0$, while Fig. 7.7(b) shows that the anisotropy $\delta A(\omega)$ is significant at that photon frequency and finite temperature. This gives the remarkable result that the anisotropy can be enhanced with increasing temperature at fixed photon energy.

It is emphasised that Figs. 7.4 and 7.7 contain absorption data at finite temperature T, which have been obtained by using the Maldague approach described in Sect. 7.3.3.

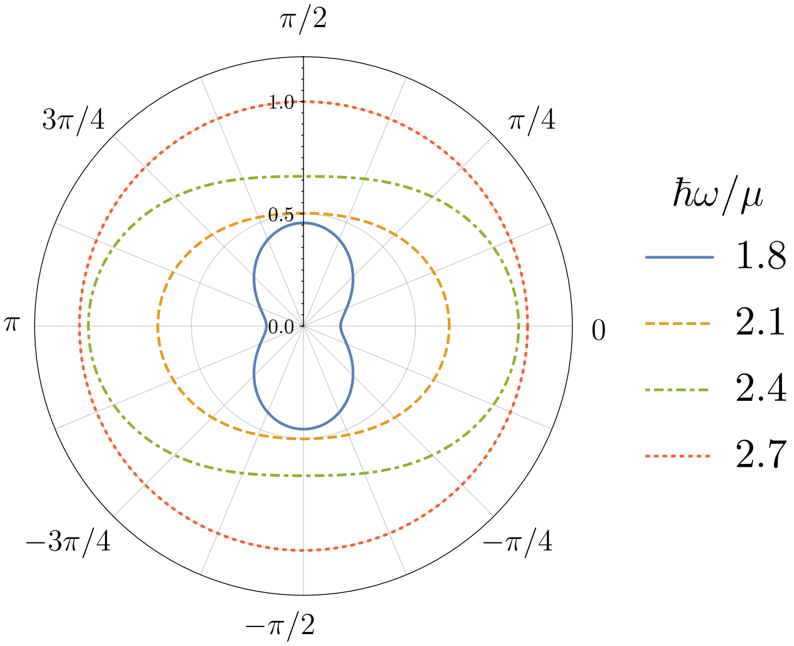

Figure 7.6: Angular dependence of the absorption $A_{ij}(\omega)$ (in units of the universal value $\pi\alpha_{\rm QED}$) as from Eq. (7.76), for different values of the incident photon energy $\hbar\omega$ (in units of μ), as indicated in the legend, and $\beta = 0.2$. In this plot the temperature is set to zero.

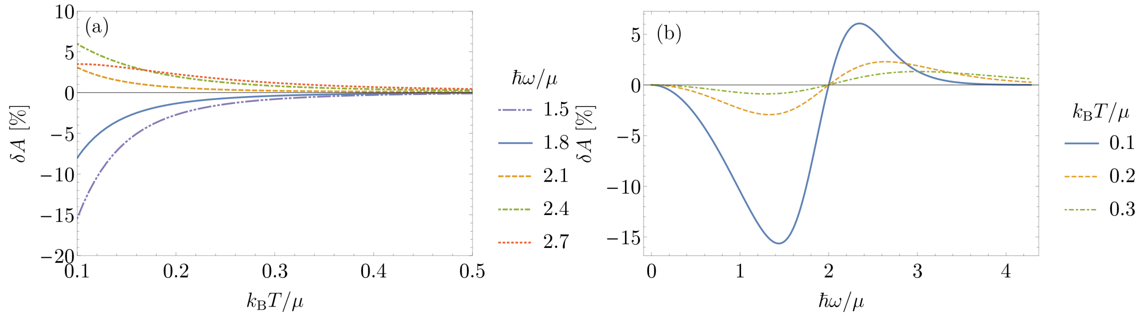

Figure 7.7: A measure of current-induced optical birefringence in a graphene sheet, as defined in Eq. (7.79). In panel (a) we show δA as a function of temperature T for different photon energies $\hbar\omega$ as indicated in the legend. In panel (b) we show δA as a function of photon energy $\hbar\omega$, for different values of temperature T.

7.5 Current-induced non-reciprocity and collimation of Dirac plasmons

Having calculated the finite-temperature response function in Eq. (7.70), one finds the dielectric screening function in the random phase approximation [102]:

$$\varepsilon(\boldsymbol{q},\omega;T) = 1 - v_{\boldsymbol{q},\omega}\chi^{(0)}_{nn}(\boldsymbol{q},\omega;T)\ . \tag{7.80}$$

Here $v_{\boldsymbol{q},\omega} = 2\pi e^2/[\epsilon(\omega)q]$ is the 2D Fourier transform of the Coulomb potential, with $\epsilon(\omega)$ an effective frequency-dependent environmental dielectric constant as for the case of graphene on hexagonal boron nitride as discussed in chapter 5. In writing these equations, for the sake of simplicity, finite-thickness effects, that could give rise to Fabry-Pérot modes as discussed before, are neglected [197, 270].

Plasmons can be found as the roots of the real part of Eq. (7.80) on the real-frequency axis, when (Landau) damping is absent or small. Alternatively, they show up as strong absorption peaks in the loss function as defined in Sec. 3.2.2:

$$L(\boldsymbol{q},\omega;T) \equiv -\mathrm{Im}\left[\frac{1}{\varepsilon(\boldsymbol{q},\omega;T)}\right]\ , \tag{7.81}$$

which is directly measured by electron-energy-loss spectroscopy [271]. The loss function displays sharp peaks at the plasmon poles and carries also precious information on interband transitions and Landau damping.

7.5.1 Non-reciprocity of plasmons

In the limit $\bar{q} < \bar{\omega} \ll \mu$, the real part of the response function in Eq. (7.58) can be expanded up to fourth order in $\bar{q}$ as

$$\begin{aligned}\frac{\mathrm{Re}[\chi^{(0)}_{nn}(\boldsymbol{q},\omega;0)]}{D(\mu)} \approx\ & \tfrac{W(\beta)}{2\beta}\tfrac{\bar{q}^2}{\bar{\omega}^2} - \frac{\bar{q}^2}{8} + \gamma\frac{W(\beta)^2}{4\beta}\frac{\bar{q}^3}{\bar{\omega}^3} \\ & + \gamma\tfrac{\beta}{32}\tfrac{\bar{q}^3}{\bar{\omega}} + \frac{\bar{q}^4}{16\bar{\omega}^2} + \frac{3}{2}\frac{W(\beta)^2}{4\beta^2}\frac{\bar{q}^4}{\bar{\omega}^4} + \dots\ ,\end{aligned} \tag{7.82}$$

where $\gamma = +1$ (-1) denotes “upstream” (“downstream”) plasmon propagation, i.e. $\boldsymbol{q}\cdot\boldsymbol{v}/(qv) = +1$ ($\boldsymbol{q}\cdot\boldsymbol{v}/(qv) = -1$), and

$$W(\beta) = 2\frac{1-\sqrt{1-\beta^2}}{\beta}\ . \tag{7.83}$$

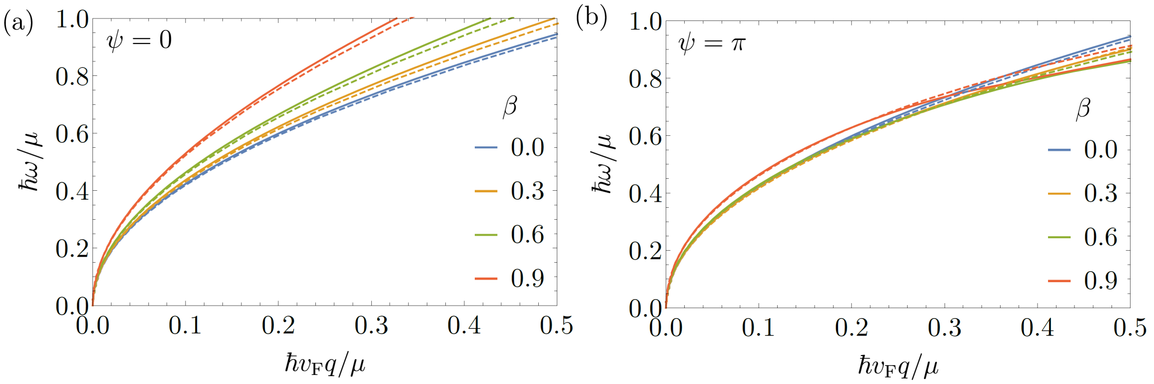

Figure 7.8: Dependence of the plasmon dispersion on the drift velocity β. Panel (a): upstream plasmons. Panel (b): downstream plasmons. Solid curves denote results obtained by numerically calculating the roots of Eq. (7.80). Dashed curves denote analytical long-wavelength results based on Eq. (7.84). Results in this figure refer to $T = 0$ and $\epsilon = 2.5$. With the scaling indicated in the horizontal and vertical axes they are "universal", in that they do not depend on the chemical potential μ.

Note that the function $W(\beta) = \beta$ for $\beta \to 0$.

Using this result, it is possible to find an approximate expression for the plasmon dispersion in the presence of current flow and in the long-wavelength $\bar{q} \ll 1$ limit. For the case of a frequency-independent dielectric constant ϵ, it becomes

$$\begin{aligned}\omega_{\rm pl}(q) = \sqrt{\frac{2\mathcal{D}_0 W(\beta)}{\epsilon\beta}} \quad & \sqrt{q} \quad \left[1 + \gamma\frac{\sqrt{2\beta W(\beta)}}{4}\sqrt{\frac{q}{k_{\rm TF}}}\right. \\ & + \left.\frac{12 - N_{\rm f}^2\alpha_{\rm ee}^2 - 3\beta W(\beta)}{16}\frac{q}{k_{\rm TF}} + \ldots\right] , \qquad (7.84)\end{aligned}$$

where $\mathcal{D}_0 = 4E_{\rm F}\sigma_{\rm uni}/\hbar$ is the Drude weight of non-interacting 2D MDFs [50], $k_{\rm TF} = N_{\rm f}\alpha_{\rm ee}k_{\rm F}$ is the $T = 0$ Thomas-Fermi screening wave vector [269], and $\alpha_{\rm ee} = e^2/(\epsilon\hbar v_{\rm F})$ is graphene's fine structure constant as introduced in chapter 3.

Eq. (7.84), which is the most important result of this section, shows that the dc current flow affects the Dirac plasmon dispersion in two ways. On the one hand, it renormalizes the Drude weight, i.e. $\mathcal{D}_0 \to \mathcal{D}_0 W(\beta)/\beta$. On the other hand, it adds a linear-in-q subleading term to the Dirac plasmon dispersion, whose sign depends on $\gamma = \pm 1$. Fig. 7.8 shows a comparison between the analytical result (7.84) (dashed lines) and the plasmon dispersion (solid lines) calculated numerically from the root of Eq. (7.80). In the limit $\beta \to 0$, Eq. (7.84) reduces to Eq. (3.144).

7.5.2 Plasmon collimation

The particle-hole excitation spectrum of a current-carrying 2D MDF differs from that in the absence of a current, i.e. for $\beta = 0$. A geometrical analysis shows that the region where single-particle excitations cannot exist, i.e. where $\mathrm{Im}[\chi^{(0)}_{nn}(\boldsymbol{q},\omega;0)] = 0$, is formed by the intersection of two cones in the $(\boldsymbol{q},\omega > 0)$ space:

$$\hbar\omega = \hbar v_{\rm F}|\boldsymbol{q}| \; , \tag{7.85}$$

and

$$\frac{2\mu}{1-\beta^2} - \hbar\omega = \left|\hbar v_{\rm F}\boldsymbol{q} - \frac{2\mu}{1-\beta^2}\boldsymbol{\beta}\right| \; , \tag{7.86}$$

where $\boldsymbol{\beta} = \beta\hat{\boldsymbol{v}}$. Eq. (7.85) defines the usual boundary between the inter- and intra-band electron-hole continua, which is a cone with its apex pointing down. Eq. (7.86) represents another cone with its apex pointing up and shifted from the origin of the $(\boldsymbol{q},\omega)$ plane by $2\mu\boldsymbol{\beta}/(1-\beta^2)$ along the $\hat{\boldsymbol{v}}$ direction and $2\mu/(1-\beta^2)$ along the ω axis.

In Fig. 7.9 the relation between the $\beta = 0$ and $\beta \neq 0$ inter- and intra-band continua is illustrated by showing a cross section of the cones along the direction of the current flow. In particular, in Figs. 7.9(a) and (b) the inter- and intra-band continua are shown in the plane $(q_{\parallel},\omega > 0)$ with $q_{\parallel} = q\cos(\psi)$, for $\psi = 0$ and $\psi = \pi$. Figs. 7.9(c) and (d) show the same quantities for a fixed value of $\omega > 0$ and arbitrary $(q_{\parallel}, q_{\perp})$, where $q_{\perp} = q\sin(\psi)$. The intersection between the two cones (7.85) and (7.86) yields the circular arcs in Fig. 7.9(d).

In Fig. 7.9 also the plasmon modes obtained from the zeroes of the real part of the dielectric function, $\mathrm{Re}[\varepsilon(\boldsymbol{q},\omega;T)] = 0$ at $T = 0$ are shown. For the sake of simplicity (to avoid the complications due to the hybridisation between plasmons and the hBN optical phonon modes) $\epsilon(\omega)$ is set to unity. One clearly sees that a finite value of β implies plasmon collimation in a window of angles $-\psi_{\rm c} \leq \psi \leq \psi_{\rm c}$ around the direction $\hat{\boldsymbol{v}}$ of current flow. This is because the lower edge of the inter-band continuum strongly depends on ψ: above a certain frequency threshold—see Fig. 7.11—only plasmon modes inside the window $-\psi_{\rm c} \leq \psi \leq \psi_{\rm c}$ cannot decay by emitting single electron-hole pairs.

In Figs. 7.10(a) and (c) the loss function $L(\boldsymbol{q},\omega;T)$ is calculated for graphene on hBN at $\hbar\omega = 140~\mathrm{meV}$, for a chemical potential $\mu = 115~\mathrm{meV}$, and in the absence of a current. The two panels report results for different values of the electron temperature T. The role of an applied current is shown in Figs. 7.10(b) and (d), where the results are presented for the same parameters but for a finite current $J = 3~\mathrm{A/cm}$. Comparing Fig. 7.10(a) with Fig. 7.10(b), one clearly sees that plasmons that are fully Landau damped at $T = 30$ K in the absence of an applied current become sharply defined modes in a relatively narrow range of angles $-\psi_{\rm c} \leq \psi \leq \psi_{\rm c}$ in the presence of a current. A similar conclusion is also reached at $T = 300$ K. This is an example of current-induced protection from damping

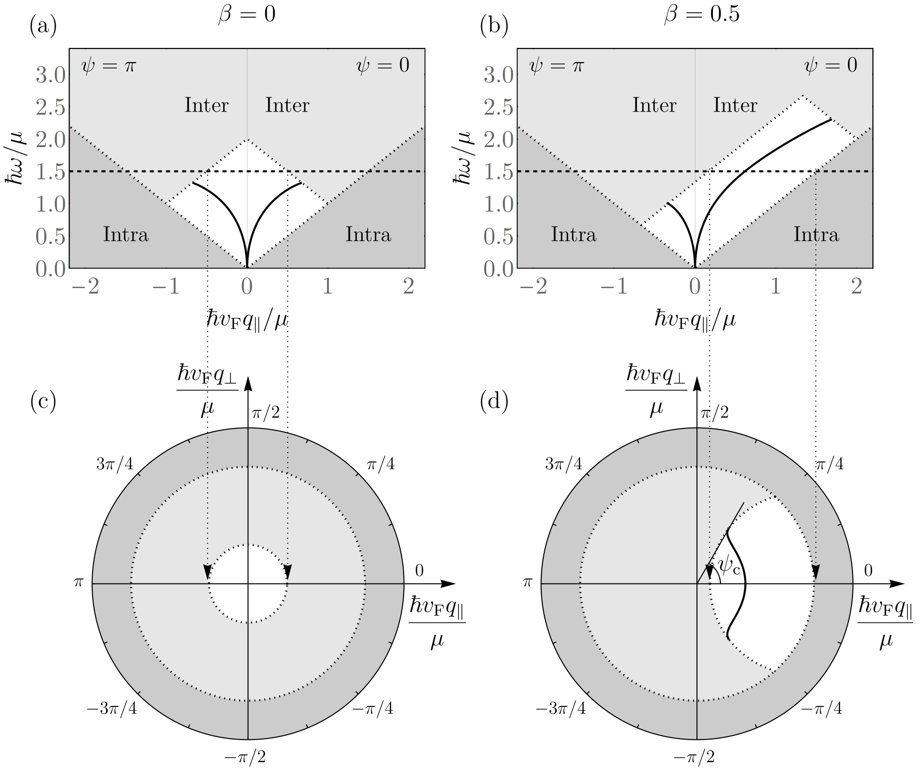

Figure 7.9: Panels (a) and (b): Inter-band (light-grey shaded areas) and intra-band (dark-grey shaded areas) electron-hole continua in the $q_{\parallel}$-ω plane for $\beta = 0$ and $\beta = 0.5$, respectively. White areas indicate regions of parameters where no particle-hole excitations are possible at $T = 0$, i.e. where $\mathrm{Im}[\chi^{(0)}_{nn}(\boldsymbol{q}, \omega)] = 0$. In these regions we have shown typical plasmon dispersions (solid lines) at $T = 0$ and for $\epsilon(\omega) = 1$. With the chosen units for $q_{\parallel}$ and ω, the plasmon dispersion depends only on $\alpha_{\rm ee} = e^2/(\epsilon \hbar v_{\rm F})$ (for a frequency-independent ϵ) and β, but not on μ. The dashed horizontal curve represents the frequency for which the plots in panels (c) and (d) have been made. In panel (a) one clearly sees that, in the absence of an applied dc current, no plasmons can propagate at a photon frequency $\omega = 1.5\ \mu/\hbar$ (since the plasmon dispersion hits the inter-band continuum at a lower value of ω). Panels (c) and (d): Inter- and intra-band continua in the $(q_{\parallel}, q_{\perp})$ plane and for a photon frequency $\omega = 1.5\ \mu/\hbar$. As explained above, in panel (c), for $\beta = 0$, no plasmon branches fall in the region (white area) where $\mathrm{Im}[\chi^{(0)}_{nn}(\boldsymbol{q}, \omega)] = 0$. On the contrary [panel (d)], an undamped collimated plasmon branch (solid line) emerges due to the application of a finite current. The quantity $\psi_{\rm c}$ denotes the collimation angle.

as mentioned in the introduction of this chapter and one of the main interests in the use of Dirac plasmons in samples with a finite drift velocity. Indeed, this result shows that although at the frequency used in Fig. 7.10, plasmons are damped due to single-particle processes, the induced current changes the PHES such that this damping is suppressed when the plasmon move inside the collimated angular range in the downstream direction.

The collimation angle $\psi_{\rm c}$, which is defined at $T = 0$ by the intersection of the solution of ${\rm Re}[\varepsilon(\boldsymbol{q}, \omega; T)] = 0$ (at a fixed energy $\hbar\omega$) with the lower threshold of the inter-band electron-hole continuum, is plotted in Fig. 7.11 as a function of $\hbar\omega/\mu$. The results shown in this figure have been obtained for the simplified case of a frequency-independent effective dielectric constant ϵ. In the case of an applied current, plasmons propagating in the range of angles $-\psi_{\rm c} \leq \psi \leq \psi_{\rm c}$ around the direction of the applied current suffer no inter-band Landau damping. Therefore it can be concluded that an applied dc current allows to collimate the propagation of Dirac plasmons.

7.5.3 General frequency and angular bounds on the collimation

As explained in the previous section, in principle, one has to perform the full calculation of the RPA plasmon and account for the frequency dependence of the dielectric environment in order to exactly determine the collimation angle at a given photon frequency ω or the bounds on the frequency where plasmon propagation is possible for a given drift velocity β. However, in order to determine bounds on the possible values for the frequency and collimation angle, it is possible to determine approximate analytical equations that can be useful for the experimental determination of the proposed physics.

As shown in Fig. 7.12, one can determine the frequency range where upstream and downstream plasmon propagation is possible as bordered by the following quantities

$$\hbar\omega_{\rm d}^{+} = \frac{2\mu}{1-\beta^2}, \; \hbar\omega_{\rm d}^{-} = \frac{\mu}{1-\beta}\,, \tag{7.87}$$

$$\hbar\omega_{\rm u}^{+} = \frac{2\mu}{1+\beta}, \; \hbar\omega_{\rm d}^{-} = \frac{\mu}{1+\beta}\,. \tag{7.88}$$

Eq. (7.87) determines the range where the downstream plasmon will enter the continuum while Eq. (7.88) corresponds to the range for the upstream plasmon. This means that all plasmons are in the continuum if the photon frequency is above $\omega_{\rm d}^{+}$ and are propagating if the frequency is below $\omega_{\rm u}^{-}$. Furthermore, in the range $\left[\omega_{\rm u}^{+}, \omega_{\rm d}^{-}\right]$, the downstream plasmons are sure to propagate while the upstream plasmons are sure to be damped by single-particle processes. In this range, one has unidirectional plasmons.

The right panel of Fig. 7.12 shows the velocity dependence of the four boundaries from Eqs. (7.87) and (7.88). The shaded region determines the range where unidirectional

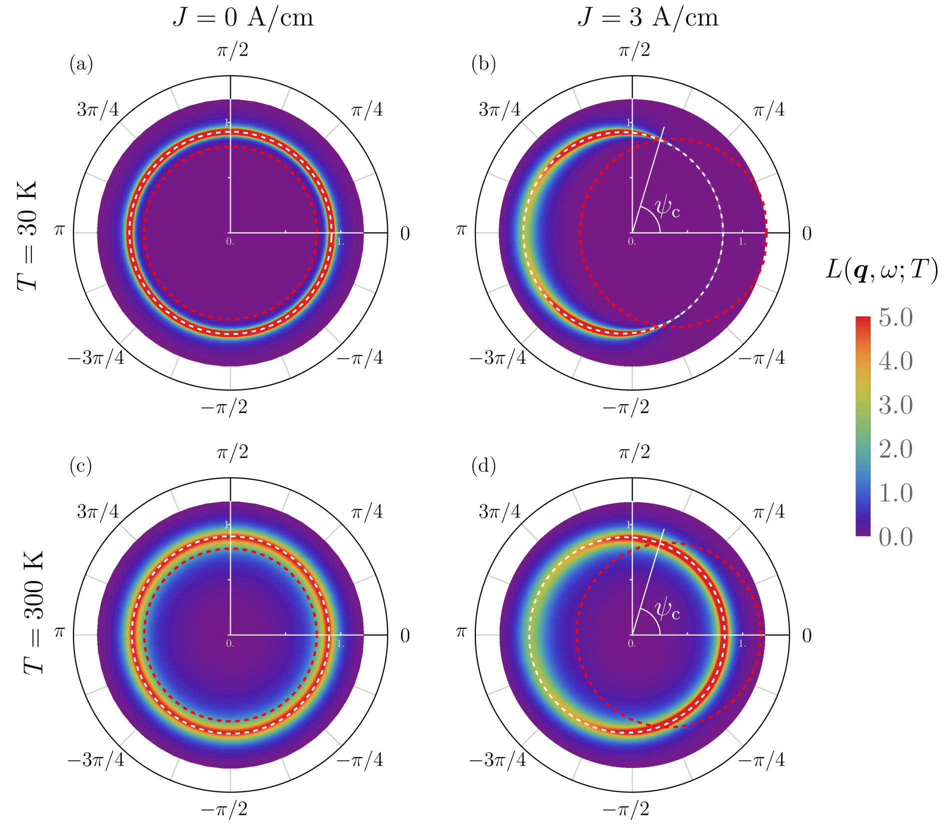

Figure 7.10: Energy loss function $L(\boldsymbol{q}, \omega; T)$ in the $(q_{\parallel}, q_{\perp})$ plane at an energy $\hbar\omega = 140$ meV and for a chemical potential $\mu = 115$ meV. These results are for a graphene sheet on hBN, i.e. for $\epsilon(\omega) = [1 + \sqrt{\epsilon_x(\omega)\epsilon_z(\omega)}]/2$. The regions inside the curves delimited by red dashed lines are regions of parameters in which there is no Landau damping at $T = 0$ (white regions in Fig. 7.9). The white dashed curves represent the solution of the equation ${\rm Re}[\varepsilon(\boldsymbol{q}, \omega; T)] = 0$. Sharp peaks in the loss function arise due to the existence of a plasmon mode. Panels (a) and (c) refer to the case of zero dc current ($\beta = 0$). Panels (b) and (d) refer to the case of an applied dc current density $J = 3$ A/cm: $\beta \simeq 0.18$ for panel (b) and $\beta \simeq 0.16$ for panel (d). The collimation angle $\psi_{\rm c}$ is also shown.

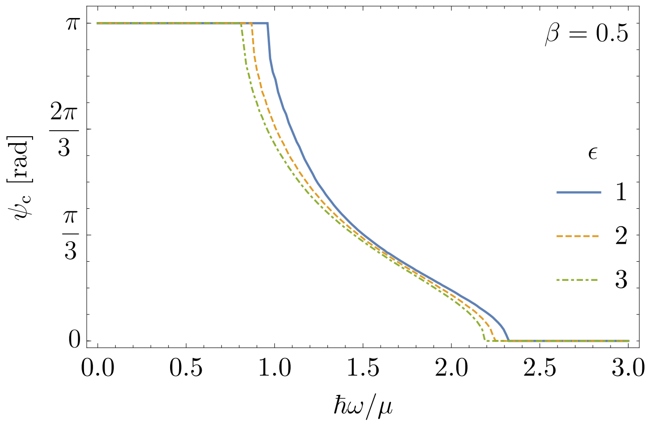

Figure 7.11: The collimation angle ψ_c, measuring the directionality of the plasmon in a current-carrying graphene sheet, is plotted as a function of ω (in units of $\mu/\hbar$), for $\beta = 0.5$. The smaller the collimation angle, the stronger the directionality of plasmon propagation. On the other hand, $\psi_c = \pi$ means non-collimated plasmons, i.e. plasmons propagating in all directions. One clearly sees that above a certain frequency threshold, undamped plasmon propagation at $T = 0$ occurs in a range of angles $-\psi_c \leq \psi \leq \psi_c$. When $\psi_c = 0$ the plasmon lies entirely inside the inter-band continuum. Different curves refer to different values of the effective dielectric constant ϵ, as indicated in the legend.

propagation can occur. In the yellow shaded region it is certain while in the blue and red regions it depends on the details of the system. Notice that if the dielectric constant is larger, the plasmon dispersion is pushes closer to the boundary of the intra-band continuum. Therefore, the plasmon will enter the continuum closer to their respective $\omega^-_{\mathrm{u(d)}}$ boundaries. As a consequence, the range for unidirectional propagation increases to the blue and red shaded regions in Fig. 7.12.

For the collimation angle, one can also find an approximate expression for the possible angles as a function of drift velocity and photon frequency. Consider for this the construction as shown in Fig. 7.13. The approximate collimation angle is the angle between the direction of the current flow and the line connecting the origin of reciprocal space with the point where the intra-band and inter-band PHES cross each other. From the expressions in Eqs. (7.85) and (7.86) these crossing points can be found as

$$\hbar v_{\mathrm{F}} q^{\mathrm{c}}_{\parallel} = \frac{\hbar\omega - \mu}{\beta}, \; \hbar v_{\mathrm{F}} q^{\mathrm{c}}_{\perp} = \pm\sqrt{(\hbar\omega)^2 - \left(\frac{\hbar\omega - \mu}{\beta}\right)^2}. \tag{7.89}$$

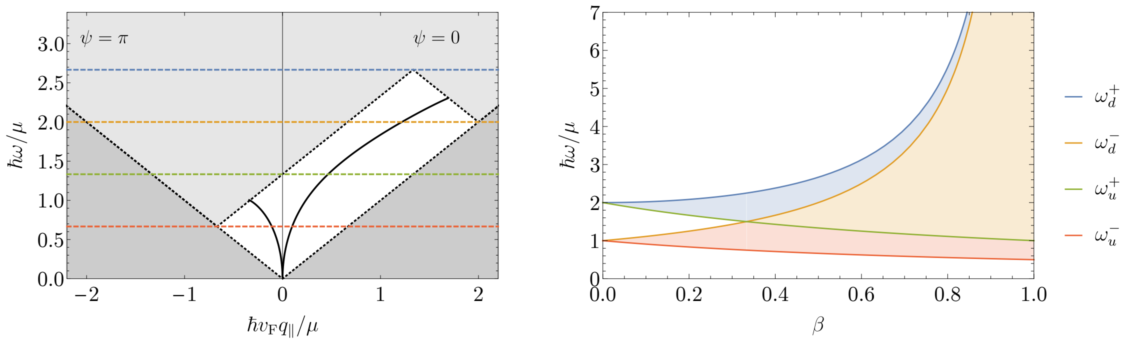

Figure 7.12: Left: Plasmon dispersion for upstream ($q < 0$) and downstream ($q > 0$) propagating plasmons. The dashed lines indicate the boundaries discussed in Eqs. (7.87) and (7.88). In this plot, $\beta = 0.5$. Right: Velocity dependence of the boundaries from Eqs. (7.87) and (7.88). The yellow shaded region is where unidirectional propagation is sure. In the blue and red shaded regions it is possible according to the details of the system.

Consequently, the approximate collimation angle ψ'_{c} can be found as

$$\psi'_{\mathrm{c}} = \arctan\left(\frac{q_{\perp}^{\mathrm{c}}}{q_{\|}^{\mathrm{c}}}\right), \tag{7.90}$$

where the branch line is taken from 0 towards $-\infty$ along the $q_{\|}$ axis. In Fig. 7.13 the approximate collimation angle is shown as a function of ω and β. The (β, ω) plane can be divided in three regions according to

$$\hbar\omega > \frac{\mu}{1-\beta}, \quad \text{Region I,} \tag{7.91}$$

$$\frac{\mu}{1+\beta} < \hbar\omega < \frac{\mu}{1-\beta}, \quad \text{Region II,} \tag{7.92}$$

$$\hbar\omega < \frac{\mu}{1+\beta}, \quad \text{Region III.} \tag{7.93}$$

In Region I the collimation angle is $\psi'_{\mathrm{c}} = 0$ because the photon energy is so strong large, there is always particle-hole damping. In Region II the collimation angle is given by Eq. (7.90). In Region III there is no particle-hole damping so $\psi'_{\mathrm{c}} = \pi$. These three regions are indicated in the right panel of Fig. 7.13 and are divided by the dashed curves.

Fig. 7.13 shows that there are two distinct paths one can take to see the effect of the collimation angle as indicated by the horizontal dotted lines in Fig. 7.13. Number (1) is at $\hbar\omega < \mu$ and therefore starts in Region III at small β. In that case the plasmon is not

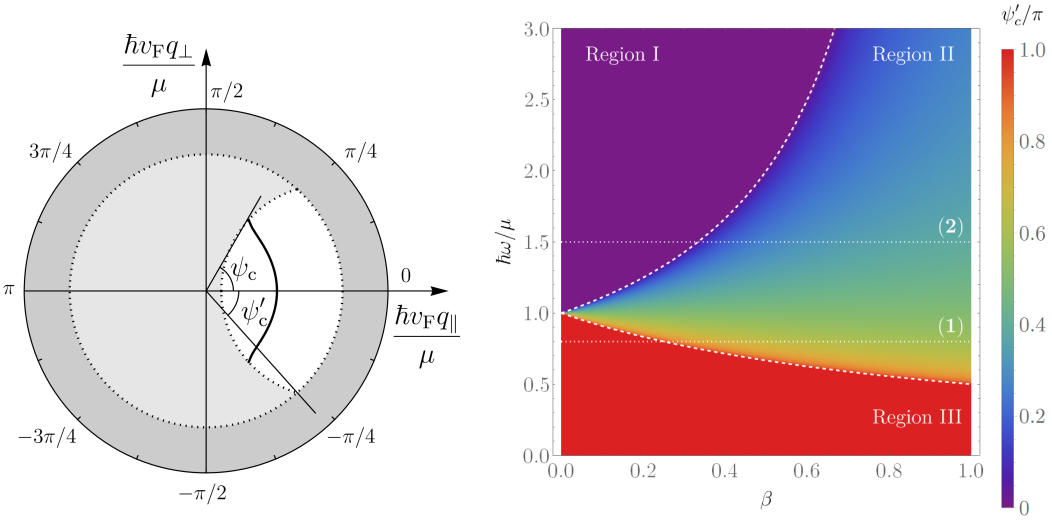

Figure 7.13: Left: Construction of the approximate collimation angle ψ'_c with respect to the real collimation angle ψ_c. Right: approximate collimation angle as a function of drift velocity β and photon energy ω. The dashed curves indicate the borders between the regions defined in Eqs. (7.91) - (7.93). The horizontal dotted lines indicate the frequency for which the real space plots are calculated.

collimated and propagates undamped. However, as β increases, the plasmon enters Region II and starts being collimated such that upstream propagating plasmons decay quickly while downstream propagating plasmons are able to propagate for much larger distances. In Fig. 7.14 the real space plasmon profile is shown. This real space profile corresponds to a plasmon wave front that propagates radially outward from a point source. This point can be the tip of a SNOM that launches plasmons in an s-SNOM experiment as explained in Sec. 3.3. The profiles show that as the drift velocity is increased, the plasmon wavelength decreases in the direction opposite to the flow and increases in the downstream direction. Furthermore, at a given drift velocity, a part of the wave fronts are damped exponentially. This damping is caused by electron-hole excitation.

Number (2) is at $\hbar\omega > \mu$ and, therefore, starts in Region I at small β where inter-band processes damp the plasmon in all directions. As β increases, it crosses the boundary into Region II where the flow is collimated and the collimation angle increases as a function of drift velocity β. This situation is also shown with real space profiles in Fig. 7.15. In this case, due to the drift velocity, plasmon propagation in the downstream direction is enhanced while it is suppressed in the upstream direction. Again, one can see a Doppler-like effect in a shortening of the upstream wavelength and increase of the downstream

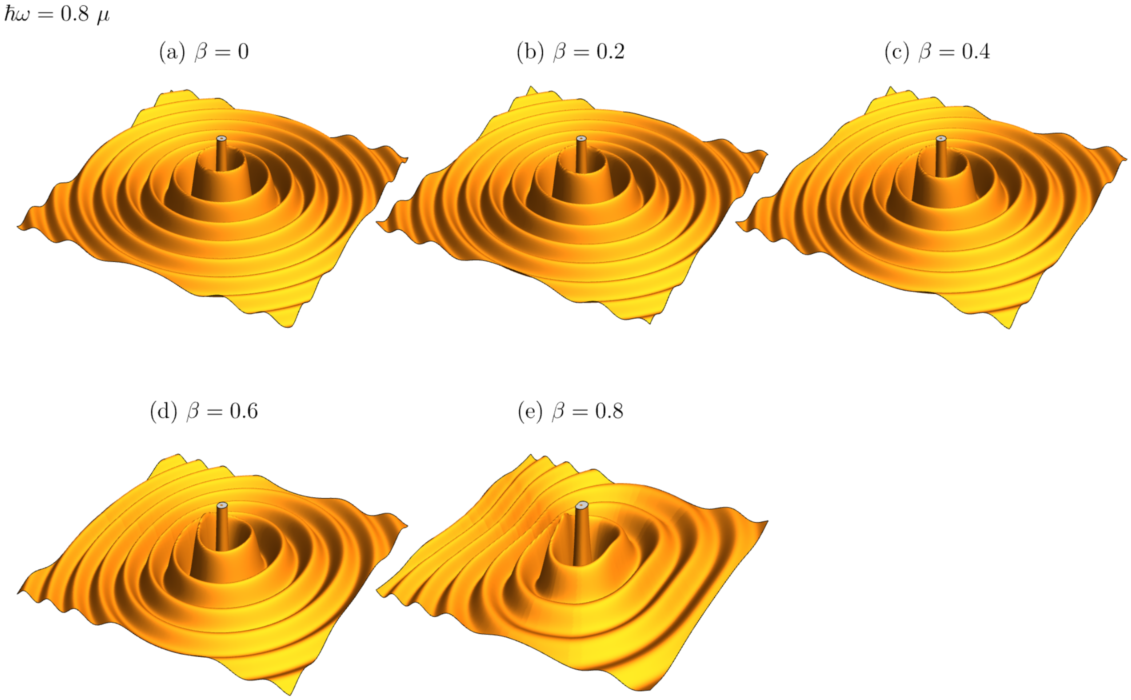

Figure 7.14: Real space plasmon profiles for a photon energy $\hbar\omega = 0.8\ \mu$ and different drift velocity as indicated. The substrate is considered to be hBN and the velocity is oriented to the right along the edge of the shown sample. These profiles correspond to the line (1) in Fig. 7.13.

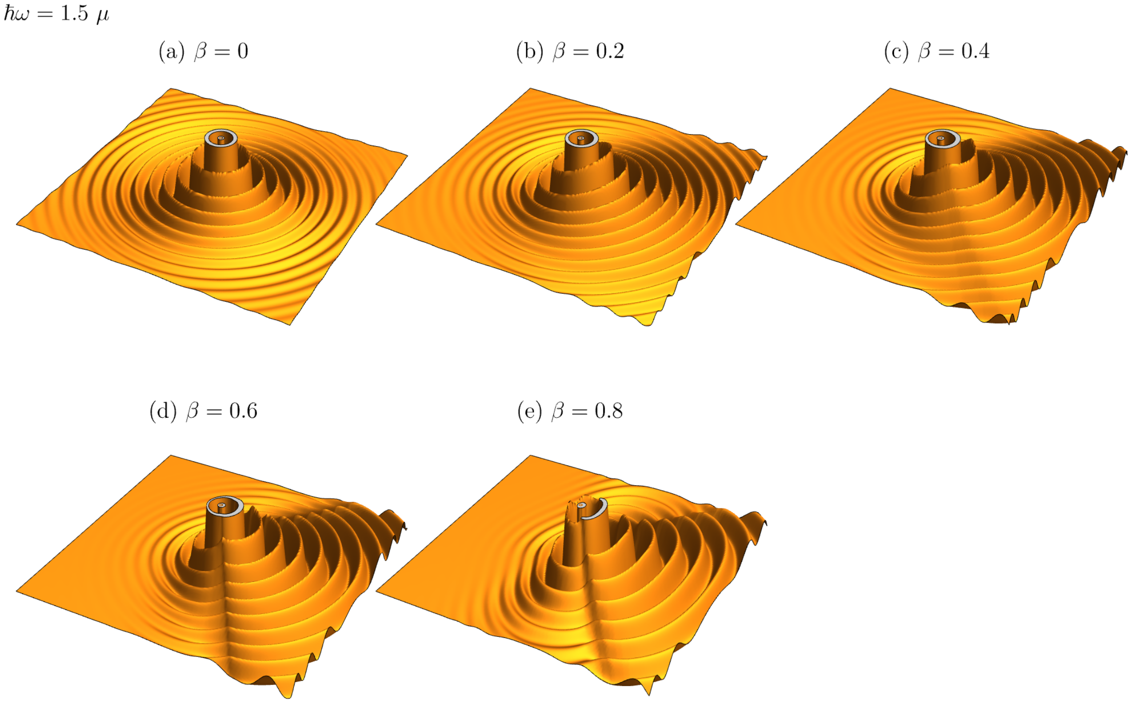

Figure 7.15: Real space plasmon profiles for a photon energy $\hbar\omega = 1.5\ \mu$ and different drift velocity as indicated. The substrate is considered to be hBN and the velocity is oriented to the right along the edge of the shown sample. These profiles correspond to the line (2) in Fig. 7.13.

wavelength. Number (2) is the same situation as considered in Fig. 7.10.

7.6 Summary and discussion

In this chapter extensive calculations of the optical and plasmonic properties of a graphene sheet carrying a dc current were presented.

In a fully analytical fashion the imaginary part of the density-density linear response function $\chi^{(0)}_{nn}(\boldsymbol{q}, \omega; T)$ of a current-carrying graphene sheet at zero temperature is calculated: the main results are reported in Sect. 7.3.1, Eqs. (7.55)-(7.57) and Tables 7.1-7.2. The corresponding real part has been calculated by performing the one-dimensional quadrature in Eq. (7.62). Results at finite temperature have been obtained by utilizing the Maldague identity in Eq. (7.70). It has to be emphasised that the latter results are not of mere academic interest, since the electron temperature can be significantly raised above the lattice temperature under the application of a large dc current.

This accurate knowledge of the density response function of a current-carrying graphene sheet has allowed to calculate the optical absorption spectrum $A_{ij}(\omega)$, which displays a birefringent character with respect to the angle ψ between the in plane light polarisation and current flow: see Eq. (7.77) and Figs. 7.4-7.6.

The non-interacting density-density response function $\chi^{(0)}_{nn}(\boldsymbol{q}, \omega; T)$ has been used to calculate the dielectric screening function in the random phase approximation, the plasmon dispersion, and the loss function of a current-carrying graphene sheet. It has been shown that graphene plasmons acquire a degree of non-reciprocity under the influence of a dc current, see Eq. (7.84), and that their propagation can be collimated in a window of angles around the current direction, see Figs. 7.9-7.11. The chapter ended with an analysis of the frequency region where unidirectional plasmon propagation is expected and how this depends on the drift velocity. Finally, an estimate of the collimation angle that can be useful for experimental purposses has been presented and the (β, ω) plane has been analysed to determine the parameter ranges where plasmon collimation is expected.

Before concluding, the possibility to test our predictions experimentally is briefly discussed. To observe the discussed effects one needs to pass a large current through a graphene flake and measure polarised optical reflection or transmission through the sample. However, the large current passing through graphene would imply large Joule losses. Hence, an efficient thermal sink is needed in order to keep the temperature of graphene in equilibrium with the thermal bath and, therefore, constant. This implies that one cannot use the same set-up that was used previously to show that graphene membranes can host large current densities. One has to immobilise the graphene flake on an inert and thermally conductive substrate that acts as the thermal sink and need to perform the measurements in an inert gas atmosphere or vacuum environment. In addition, because low temperatures are beneficial for the observation of the effect, the usage of a suitable optical cryostat is needed. Currently, experiments to detect the current induced birefringence in graphene are under way.

CHAPTER 8

Plasmon-assisted high-frequency modulation of a telecom laser

Can plasmons excited by a mid-infrared laser be used to modulate the amplitude of a telecom laser?

In this chapter, a method is proposed to achieve high-frequency modulation of a telecom laser beam at room temperature by using plasmons in graphene nanostripes. By making use of the optical properties of a graphene flake in the presence of a drift current, it is shown that one can achieve modulation speeds in the terahertz range for laser beams with frequencies that are useful for telecom applications. In contrast to gate driven modulation, the proposed method allows to achieve high-frequency modulation speeds and reduce the necessary graphene doping to modulate a telecom laser beam thanks to the velocity field induced by the plasmons.

The chapter is organised as follows: In Sec. 8.1 the usefulness and applicability of optical modulators are explained and the proposed modulation mechanism is compared to other types of graphene optical modulators. In Sec. 8.2 a semi-classical model is derived to describe excited plasmon modes in graphene nanostripes and it is shown that the results match results observed in experiments. In Sec. 8.3 the mechanism of absorption modulation is elaborated upon and the influence of doping and finite temperature on the modulation is explained. In Sec. 8.4 a concrete set-up is considered and the modulation is shown to persist up to non-zero temperature. Finally, in Sec. 8.5 the chapter is concluded with an outlook to experimental verification.

This chapter presents the theoretical part of a joint theoretical-experimental project. The content of this chapter is expected to be published as multiple joint publications.

8.1 Graphene optical modulators

One of the key components that is necessary in the use of light as a replacement of electrons in logic circuits, in order to realise *photonics*, are optical transistors [272]. Transistors are devices that can vary the fundamental characteristics of a light beam, as amplitude, phase or polarisation [64], in order to bestow the light beam with bits of information in a modulation of these characteristics. A major benefit of having optical means to transport information with respect to electronical means is that the density of information can be much higher. This is already being exploited in optical interconnects in commercially available systems [272]. A second benefit, that is not yet exploited on a commercial level, is that optics could reduce the energy required for the transfer of communication [273]. This is because the beam of light only needs to be able to charge the receiver at the end and is much less prone to energy loss during on-chip information transport.

Semiconductors were the first environment where on-chip optical modulators were introduced. Silicon-based modulators face challenges as the size of the device needs to be of the order of millimeters due to its weak electro-optical properties [274]. Furthermore, silicon-based modulators have an intrinsic narrow bandwidth and limited temperature tolerances [275]. Germanium semiconductors are, on the other hand, challenging to be integrated with other electronics and photonics platforms [276, 277]. In order to solve these problems, the scientific community recently turned to graphene.

The development of a graphene based optical modulator is a very active research domain [278]. With a first experimental demonstration, in 2011 by Liu *et al.* [279], it has been shown that it can be a very promising candidate for photonics based logic in a broad range of frequencies owing to its broad absorption spectrum as discussed in Sec. 3.1.9. In general, graphene based optical modulators are *absorption modulators* that affect the amplitude of light by changing the absorption due to inter-band or intra-band transitions [64]. For the latter, a theoretical proposal has been made that modulates the Fermi level to change the plasmonic response of graphene and, thereby, change the absorption of the graphene flake [280]. The inter-band method uses changes in the electronic distribution to change the absorption of the graphene flake by making use of the Pauli blocking mechanism that was discussed in Sec. 3.1.9 [278]. This method has been applied in several experimental set-ups [279, 281–290].

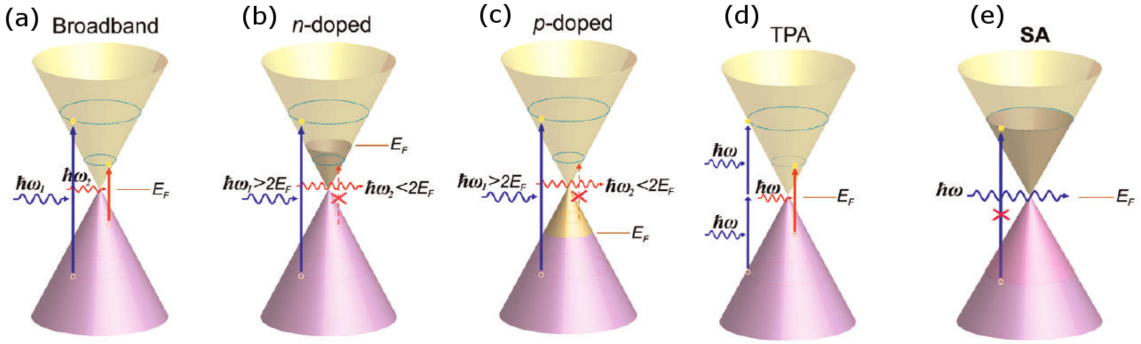

Figure 8.1: Possible modulation mechanisms using graphene. (a) Broad band absorption of the cone when the doping is zero. Electro-optical doping mechanism where the electron (b) and hole (c) concentrations are varied through the application of a gate. (d) and (e) All-optical mechanism for modulation. (d) The pump laser (red) of a lower frequency first populates the conduction band through the excitation of single particles from the valence band. (e) As a result the valence band is depleted such that transitions of up to twice the frequency of the first laser are blocked. Figure adapted from Ref. [64]

The electron redistribution is usually induced by two methods as schematically shown in Fig. 8.1. In panel (a) the general broadband mechanism of plasmon absorption is shown. There both the low and high energy photons are absorbed with the same probability. Panels (b) and (c) show the effect of an electro-optical set-up in which the electron concentration is modulated by changing the gate voltage in a periodic fashion [279, 281–285]. Modulation is achieved through Pauli blocking due to the occupation of the conduction band or the depletion of the valence band. This technique is however limited by the speed of the gate switching, which is limited to approximately 1 GHz due to the RC constant[279, 285] (Although one reference reports theoretical predictions of modulation speeds up to 500 GHz[291]). The other common way, shown in Figs. 8.1(d) and (e), is to use an all-optical setup in which a first (pump) laser thermally excites individual carriers (shown in panel (d)). This saturates the conduction band, such that the light of the second laser (probe, shown in panel (e)) cannot be absorbed by inter-band processes [286–290]. This technique allows for faster modulation, but is limited by the relaxation time due to carrier-phonon scattering necessary to form the quasi-equilibrium which limits the modulation speed at about 200 GHz.[278]

In this chapter, an alternative all-optical method is proposed to modulate the amplitude of a telecom laser by changing the optical properties of an array of graphene nanostripes with a mid-infrared (MIR) light souce. The MIR laser can excite plasmons that oscillate laterally in the stripes [53, 155]. The associated velocity and density profiles of the plasmons oscillate with the frequency of the MIR laser and affect locally the optical absorption of the electron liquid at the same rate. Therefore, the absorption of a second laser that is focussed on the array will oscillate at the same MIR frequency. In this way the second laser's amplitude is modulated at terahertz speed.

There are two main advantages of the proposed method. The first advantage is that it allows for a very high modulation frequency. Conventionally, one uses electrostatic gating to modulate the electron density of the graphene flake by changing the gate potential with a frequency ω_1. The modulation of the electron density also modulates the sample's chemical potential μ and in this way modifies the Pauli blocking [122, 292], i.e. the blocking of absorption by inter-band processes if the photon energy $\hbar\omega_2 < 2\mu$. Modulating the chemical potential, therefore, affects the absorption of photons whoes energy is near 2μ and in that way modulates the second laser's amplitude with frequency ω_1. However, as mentioned before, this modulation frequency is limited to the speed at which the gate potential can be changed which lies in the gigahertz range [278, 279]. A plasmon consists of a carrier density profile that oscillates at the frequency of the exciting laser. Therefore, one can use the changes in the density due to plasmon modes to overcome the limited speed of the gate potential.

For the conventional modulation technique that uses a gate, the photon energy $\hbar\omega_2$ needs to be comparable to 2μ. If one aims to modulate a telecom laser, typically $\hbar\omega_2 \simeq 0.8\ \mathrm{eV}$ for $\lambda_2 \simeq 1.5\ \mu\mathrm{m}$, the necessary doping will be $\bar{n} \simeq 5 \times 10^{13}\ \mathrm{cm}^{-2}$ ($\mu = \hbar v_{\mathrm{F}}\sqrt{\pi\bar{n}}$ with v_{F} the graphene Fermi velocity). This is not achievable by gate doping as previously discussed in Sec. 2.4. The second advantage of the proposed method overcomes this problem because the plasmon modes also have an associated velocity field. In the previous chapter, it was shown that if the electron liquid has a finite drift velocity $\beta = v/v_{\mathrm{F}}$, the window in which the Pauli blocking mechanism is active broadens. Instead of an abrupt absorption transition at $\hbar\omega_2 = 2\mu$, now the transition is smoothed over a range from $2\mu^-$ to $2\mu^+$, where

$$\mu^{\pm} = \frac{\mu}{1 \mp \beta} \,. \tag{8.1}$$

Therefore, by increasing the drift velocity β, one can extend the Pauli blocking above the value of 2μ. This enables to modulate a telecom laser with moderate electron density in the range $\bar{n} = 1 - 6 \times 10^{12}\ \mathrm{cm}^{-2}$. This degree of doping is achievable by electro-static gating as discussed in Sec. 2.4.

In the study at hand, first the density and current density profiles associated to graphene plasmons are derived starting from semiclassical equations. After showing that this semiclassical theory correctly describes the energy dissipation of a terahertz laser observed in graphene nanostripes due to the excitation of the plasmons, the obtained density and velocity profile to calculate the local absorption of the electron liquid in the frequency range

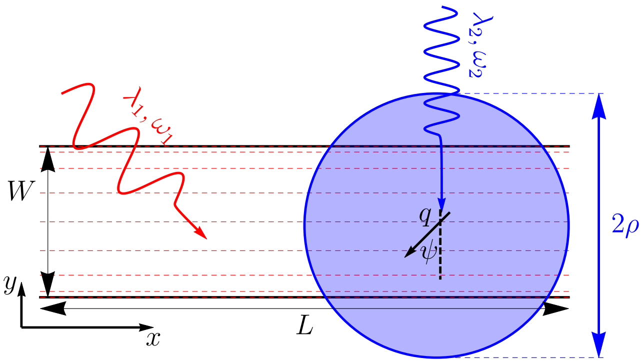

Figure 8.2: Proposed modulation setup using a nanostripe of width W. A long wavelength λ_1 laser with frequency ω_1 excites plasmons that oscillate along the y direction (dashed horizontal red lines depict the wave front). These plasmons modulate a laser shown in blue with wavelength λ_2, frequency ω_2, spot size 2ρ and polarisation along q which has an angle ψ with the y axis.

of a telecom laser are derived. Finally, by using this theory the amount of absorbed radiation from a telecom laser due to the electron liquid in an array of nanostripes at room temperature is calculated.

Note that in order to use this approach, the time scales connected to the two different phenomena needs to be substantially different: $\omega_2 \gg \omega_1$, i.e. the frequency of the second laser needs to be much larger than the oscillating frequency of the plasmons in the stripe. Then one can consider the interaction of the second laser as instantaneous with respect to the oscillation of the electron density forming the plasmon. In this case the oscillation happens at $f_1 = \omega_1/(2\pi) \simeq 28$ THz and the modulated telecom laser has a frequency $f_2 = \omega_2/(2\pi) \simeq 200$ THz, so this assumption is justified.

8.2 Plasmonic excitations in a graphene nanostripe

The nanostripes are considered to have a transverse size $W > 10$ nm and longitudinal size L (with $L \gg W$) as shown in Fig. 8.2. The x-direction is chosen to be longitudinal and the y-direction to be transverse to the nanostripe. The stripes are embedded between two dielectrics with dielectric constants ϵ_1 and ϵ_2.

The frequency of the first laser will be denoted by ω_1 and its wavelength by λ_1. Because the wavelength $\lambda_1 \gg W$, the electric field induced by the first laser is considered as homogeneous. Secondly, a laser with frequency ω_2 and wavelength λ_2 impinges on the nanostripe and will be modulated by the excited plasmons. This laser has a spot size 2ρ. The polarisation of the second laser has an angle ψ with the y-axis of the nanostripe.

In the remainder of this section, a semiclassical calculation of the plasmon modes of the nanostripe is presented. This provides the density and current density profiles of the plasmons that are necessary to calculate the amplitude modulation. Further it is shown that this semiclassical analysis reproduces qualitatively the experimental results for the absorption changes due to plasmon excitation. The semiclassical analysis is based on the discussion in Ref. [293].

8.2.1 Semiclassical calculation of plasma modes in graphene nanostructures

The equations governing the motion of the MDF liquid in the above described range of parameters are the continuity equation:

$$-i\omega n(\boldsymbol{r},\omega) + \nabla \cdot \boldsymbol{j}(\boldsymbol{r},\omega) = 0 \,, \tag{8.2}$$

and Ohm's law with a Drude conductivity:

$$-e\boldsymbol{j}(\boldsymbol{r},\omega) = \sigma_{\rm D}(\boldsymbol{r},\omega)\boldsymbol{E}_{\rm tot}(\boldsymbol{r},\omega) \,. \tag{8.3}$$

In Eq. (8.2) $n(\boldsymbol{r},\omega)$ is the carrier density perturbation, and $\boldsymbol{j}(\boldsymbol{r},\omega)$ is the associated local current density. In Eq. (8.3) the local Drude optical conductivity is introduced:

$$\sigma_{\rm D}(\boldsymbol{r},\omega) = \frac{i\mathcal{D}(\boldsymbol{r})}{\pi(\omega + i\gamma)} \,, \tag{8.4}$$

where $\mathcal{D}(\boldsymbol{r}) = e^2 v_{\rm F}\sqrt{\pi\bar{n}(\boldsymbol{r})}/\hbar$, with $\bar{n}(\boldsymbol{r})$ the background carrier density, is the Drude weight that was introduced in the context of Dirac plasmons in Sec. 3.2 [50]. Notice that the effect of having a graphene nanostripe array is only encoded in the MDF Drude weight. The remainder of the semiclassical analysis holds for any type of Fermi liquid that is confined over a certain length scale $W > 10~\rm nm$. As a consequence, this analysis neglects the discretisation of the single-particle energy levels due to lateral confinement as is well known to occur for graphene nanoribbons [79]. This assumption is, however, justified as it would only significantly affect the single-particle electron dispersion for small graphene nanoribbons $W < 10~\rm nm$. To emphasize the fact that in this section the width W is considered to be large enough to neglect the single-particle confinement, the word *nanostripe* is used in stead of nanoribbon. Notice that this also means that the results will not be affected by type of edge, e.g. zig-zag or armchair, of the nanostripe.

In this chapter non-local effects in the conductivity, as well as retardation effects are neglected, and all the damping processes are modelled with a phenomenological damping rate γ in Eq. (8.4). Neglecting retardation one can write the electric field entering Eq. (8.3) as $\boldsymbol{E}_{\rm tot}(\boldsymbol{r},\omega) = -\nabla\Phi_{\rm tot}(\boldsymbol{r},\omega) = -\nabla\Phi_{\rm ext}(\boldsymbol{r},\omega) - \nabla\Phi_{\rm ind}(\boldsymbol{r},\omega)$. Taking the divergence of Eq. (8.3) and inserting Eq. (8.2), one finds a relation between the density perturbation $n(\boldsymbol{r},\omega)$ and the potential $\Phi_{\rm tot}(\boldsymbol{r},\omega)$, valid for $\omega \neq -i\gamma$, given by:

$$\omega(\omega+i\gamma)(-e)n(\boldsymbol{r},\omega) = P[\Phi_{\rm tot}](\boldsymbol{r},\omega)\ , \tag{8.5}$$

where P is an operator defined as:

$$P[f](\boldsymbol{r},\omega) = -\nabla\left[\frac{\mathcal{D}(\boldsymbol{r})}{\pi}\nabla f(\boldsymbol{r},\omega)\right]\ . \tag{8.6}$$

Eq. (8.5) is valid in the region of the $x-y$ plane where graphene is present i.e. where $\mathcal{D}(\boldsymbol{r}) \neq 0$. On the edge of this region the electric potential must satisfy the boundary condition:

$$\hat{\boldsymbol{u}}(\boldsymbol{r})\cdot\mathcal{D}(\boldsymbol{r})\nabla\Phi_{\rm tot}(\boldsymbol{r},\omega) = 0\ , \tag{8.7}$$

where $\hat{\boldsymbol{u}}(\boldsymbol{r})$ is the outward normal to the graphene boundary. This condition implies that no charge can exit the graphene sheet. Note that the operator P is self-adjoint and semi-positive defined on the set of functions satisfying the boundary condition in Eq. (8.7).

To close the set of equations, one needs another relation between the electric potential and the density perturbation. This equation is given by:

$$\Phi_{\rm ind}(\boldsymbol{r},\omega) = -eQ[n](\boldsymbol{r},\omega)\ , \tag{8.8}$$

where the operator Q describing the electron-electron interaction reads:

$$Q[f](\boldsymbol{r},\omega) = \int \frac{d\boldsymbol{r}' f(\boldsymbol{r}',\omega)}{\bar{\epsilon}|\boldsymbol{r}-\boldsymbol{r}'|}\ . \tag{8.9}$$

Here $\bar{\epsilon} = (\epsilon_1+\epsilon_2)/2$ represents the average dielectric constant of the system. Note that the operator Q is positive defined and, therefore, can be inverted.

Using Eqs. (8.5)-(8.8) one obtains:

$$-e\omega(\omega+i\gamma)n(\boldsymbol{r},\omega) = P[\Phi_{\rm ext} - eQ[n]](\boldsymbol{r},\omega)\ . \tag{8.10}$$

Equation (8.10) describes the linear response of the system to an external electric field.

To find the collective modes of charge density oscillations one sets $\Phi_{\rm ext} \equiv 0$ and looks for non-zero solutions of Eq. (8.10). This leads to the study of the eigenvalue equation for the operator PQ:

$$P[Q[n_\alpha]] = \Omega_\alpha^2 n_\alpha\ . \tag{8.11}$$

Here $\Omega_\alpha^2 \geq 0$ denote the eigenvalues of the operator PQ, while n_α are the corresponding density eigenfunctions. The corresponding potential eigenfunctions are given by:

$$\Phi_\alpha = -eQ[n_\alpha] \, . \tag{8.12}$$

The potential eigenfunctions are eigenfunctions of the operator $QP \neq PQ$ and therefore respect the equation:

$$Q[P[\Phi_\alpha]] = \Omega_\alpha^2 \Phi_\alpha \, . \tag{8.13}$$

Note that because the operator PQ is not self-adjoint with respect to the standard scalar product its eigenfunctions are not orthogonal in the usual sense. However, it can be shown, using the simultaneous diagonalisation theorem, that the eigenfunctions follow the orthogonality condition:

$$-e\int d\boldsymbol{r}\Phi_\alpha^*(\boldsymbol{r})n_\beta(\boldsymbol{r}) = E_\alpha\delta_{\alpha\beta} \, , \tag{8.14}$$

where the E_α are the energy normalisations of the modes.

The system, therefore, supports self-sustaining oscillations of the type:

$$\begin{aligned}\Phi_{\text{tot}}(\boldsymbol{r},t) &= \frac{B_\alpha e^{-i\omega_\alpha t}}{2}\Phi_\alpha(\boldsymbol{r}) + \text{c.c.}\\ n(\boldsymbol{r},t) &= \frac{B_\alpha e^{-i\omega_\alpha t}}{2}n_\alpha(\boldsymbol{r}) + \text{c.c.}\\ \boldsymbol{j}(\boldsymbol{r},t) &= \frac{B_\alpha \omega_\alpha e^{-i\omega_\alpha t}}{2\Omega_\alpha}\boldsymbol{j}_\alpha(\boldsymbol{r}) + \text{c.c.} \, ,\end{aligned} \tag{8.15}$$

where B_α is a complex amplitude and he functions $n_\alpha(\boldsymbol{r})$ and $\Phi_\alpha(\boldsymbol{r})$ have been obtained from the eigenvalue equation Eqs. (8.11) and (8.13) respectively. The complex oscillation frequencies are given by:

$$\omega_\alpha = \begin{cases} 0 & \text{if } \Omega_\alpha = 0 \\ \Omega_\alpha\sqrt{1-\frac{\gamma^2}{4\Omega_\alpha^2}} - \frac{i\gamma}{2} & \text{if } \Omega_\alpha \neq 0 \, , \end{cases} \tag{8.16}$$

and the associated current density field is:

$$\boldsymbol{j}_\alpha(\boldsymbol{r}) = \frac{iD(\boldsymbol{r})}{\pi e\Omega_\alpha}\nabla\Phi_\alpha(\boldsymbol{r}) \, . \tag{8.17}$$

Note that Eq. (8.13) always has 0 as an eigenvalue, associated to a constant potential profile. This eigenmode corresponds to a static density perturbation proportional to the equilibrium density. The above described method can therefore be useful in calculating the electrostatic equilibrium density distribution in a generic graphene nanostructure.

8.2.2 Linear response and absorption in graphene nanostructures

Now, it is shown that the above calculated collective modes allow to express the density response to an external potential and the absorption coefficient of incident light in a simple way. Since the functions $n_\alpha(\boldsymbol{r})$ are a complete set one can use them to expand the density $n(\boldsymbol{r}, \omega)$ as:

$$n(\boldsymbol{r}, \omega) = \sum_\alpha c_\alpha(\omega) n_\alpha(\boldsymbol{r}) \ . \tag{8.18}$$

Inserting this decomposition in Eq. (8.10) one obtains:

$$P[\Phi_{\text{ext}}](\boldsymbol{r}, \omega) = -e \sum_\alpha [\omega(\omega + i\gamma) - \Omega_\alpha^2] c_\alpha(\omega) n_\alpha(\boldsymbol{r}) \ , \tag{8.19}$$

multiplying by $\Phi_\beta^*(\boldsymbol{r})$, integrating over $\boldsymbol{r}$, and making use of Eq. (8.14), an expression for the coefficients $B_\beta(\omega)$ is found:

$$\begin{aligned} B_\beta(\omega) &= \frac{\int \Phi_\beta^*(\boldsymbol{r}) P[\Phi_{\text{ext}}](\boldsymbol{r}, \omega) d\boldsymbol{r}}{E_\beta[\omega(\omega + i\gamma) - \Omega_\beta^2]} \\ &= -e\Omega_\beta^2 \frac{\int n_\beta^*(\boldsymbol{r}) \Phi_{\text{ext}}(\boldsymbol{r}, \omega) d\boldsymbol{r}}{E_\beta[\omega(\omega + i\gamma) - \Omega_\beta^2]} \ . \end{aligned} \tag{8.20}$$

In the last step the self-adjointness of the operator P was used. Inserting Eq. (8.20) back in Eq. (8.18), one finds the expression

$$n(\boldsymbol{r}, \omega) = -e \int d\boldsymbol{r}' \chi_{nn}(\boldsymbol{r}, \boldsymbol{r}', \omega) \Phi_{\text{ext}}(\boldsymbol{r}', \omega) \ , \tag{8.21}$$

where the density-density response function is given by:

$$\chi_{nn}(\boldsymbol{r}, \boldsymbol{r}', \omega) = \sum_\alpha \frac{\Omega_\alpha^2 n_\alpha(\boldsymbol{r}) n_\alpha^*(\boldsymbol{r}')}{E_\alpha[\omega(\omega + i\gamma) - \Omega_\alpha^2]} \ . \tag{8.22}$$

Using Eqs. (8.3), (8.21)-(8.22) the density and velocity response of the system under an external potential can be written as:

$$\begin{aligned} n(\boldsymbol{r}, \omega) &= \sum_\alpha B_\alpha(\omega) n_\alpha(\boldsymbol{r}) \\ \boldsymbol{j}(\boldsymbol{r}, \omega) &= \sum_\alpha B_\alpha(\omega) \frac{\omega}{\Omega_\alpha} \boldsymbol{j}_\alpha(\boldsymbol{r}) \ , \end{aligned} \tag{8.23}$$

where the mode amplitudes are defined by:

$$B_\alpha(\omega) = \frac{\Omega_\alpha^2(-e)\int d\boldsymbol{r} n_\alpha^*(\boldsymbol{r})\Phi_{\rm ext}(\boldsymbol{r},\omega)}{[\omega(\omega+i\gamma)-\Omega_\alpha^2]E_\alpha} \; . \tag{8.24}$$

In order to calculate the power dissipated in the system to excite plasmon modes, the power absorbed by the electron system needs to be calculated:

$$\begin{aligned} P_{\rm abs}(\omega) &= \int d\boldsymbol{r}\frac{1}{2}{\rm Re}[-e\boldsymbol{j}(\boldsymbol{r},\omega)\cdot\boldsymbol{E}_{\rm ext}^*(\boldsymbol{r},\omega)] \\ &= \frac{e\omega}{2}\int d\boldsymbol{r}{\rm Im}[n(\boldsymbol{r},\omega)\Phi_{\rm ext}^*(\boldsymbol{r},\omega)] \\ &= \frac{-e^2\omega}{2}\int d\boldsymbol{r}\int d\boldsymbol{r}'{\rm Im}[\chi_{nn}(\boldsymbol{r},\boldsymbol{r}',\omega)\Phi_{\rm ext}(\boldsymbol{r}',\omega)\Phi_{\rm ext}^*(\boldsymbol{r},\omega)] \\ &= \frac{e\omega}{2}\sum_\alpha \frac{\left|\int d\boldsymbol{r} n_\alpha^*(\boldsymbol{r})\Phi_{\rm ext}(\boldsymbol{r},\omega)\right|^2}{\int d\boldsymbol{r}\Phi_\alpha^*(\boldsymbol{r})n_\alpha(\boldsymbol{r})}{\rm Im}\left[\frac{\Omega_\alpha^2}{\omega(\omega+i\gamma)-\Omega_\alpha^2}\right] \; . \end{aligned} \tag{8.25}$$

To find the absorption, Eq. (8.25) needs to be divided by the total incident power

$$P_{\rm in}(\omega) = \frac{c}{8\pi}\int d\boldsymbol{r}\left|\nabla\Phi_{\rm ext}(\boldsymbol{r},\omega)\right|^2 \; , \tag{8.26}$$

such that the absorption becomes

$$A(\omega) = -\frac{4\pi\omega}{c}\sum_\alpha d_\alpha{\rm Im}\left[\frac{\Omega_\alpha^2}{\omega(\omega+i\gamma)-\Omega_\alpha^2}\right] \; , \tag{8.27}$$

where the couplings d_α are given by

$$d_\alpha = -e\frac{\left|\int d\boldsymbol{r} n_\alpha^*(\boldsymbol{r})\Phi_{\rm ext}(\boldsymbol{r},\omega)\right|^2}{[\int d\boldsymbol{r}\Phi_\alpha(\boldsymbol{r})n_\alpha^*(\boldsymbol{r})][\int d\boldsymbol{r}\left|\nabla\Phi_{\rm ext}(\boldsymbol{r},\omega)\right|^2]} \; . \tag{8.28}$$

8.2.3 Plasma modes of an infinite strip

In this section the above described method is applied to calculate the normal modes of charge density oscillation of a graphene strip of width W and length $L \gg W$. A homogeneous carrier density $\bar{n}(\boldsymbol{r}) = \bar{n}$ is assumed, neglecting the well-known accumulation of charge near the edges [294]. Accordingly also the Drude weight is assumed to be uniform throughout the strip, i.e. $\mathcal{D}(\boldsymbol{r}) = \mathcal{D}$. Since the strip is very long the boundary condition (8.7) can be substituted with a periodic boundary condition on the short edges of the strip at $x = \pm L/2$ without affecting the results. Using the translational invariance of the system in the x direction one can show that the potential, density, and current density fields of the normal modes of the strip are:

$$\begin{aligned}
\Phi_{mk}(\boldsymbol{r}) &= \bar{\Phi} e^{ikx} \varphi_{mk}\left(\frac{y}{W}\right) \\
n_{mk}(\boldsymbol{r}) &= \bar{n} e^{ikx} \rho_{mk}\left(\frac{y}{W}\right) \\
\boldsymbol{j}_{mk}(\boldsymbol{r}) &= \frac{\bar{j} e^{ikx}}{\sqrt{\xi_{mk}}} \left[kW \varphi_{mk}\left(\frac{y}{W}\right) \hat{\boldsymbol{x}} - i\varphi'_{mk}\left(\frac{y}{W}\right) \hat{\boldsymbol{y}} \right] .
\end{aligned} \tag{8.29}$$

Here the functions φ_{mk} are the solutions of the eigenvalue integro-differential equation (the convention $\tilde{y} = y/W$ and $\tilde{k} = kW$ is used):

$$\xi_{mk} \varphi_{mk}(\tilde{y}) = \int_{-\frac{1}{2}}^{\frac{1}{2}} d\tilde{y}' \frac{K_0(|\tilde{k}||\tilde{y} - \tilde{y}'|)}{\pi} (\tilde{k}^2 - \partial_{\tilde{y}}^2) \varphi_{mk}(\tilde{y}') , \tag{8.30}$$

respecting the boundary condition:

$$\varphi'_{mk}(\tilde{y} = \pm 1/2) = 0 , \tag{8.31}$$

ξ_{mk} are the corresponding eigenvalues, the functions ρ_{mk} are the solutions of the equation:

$$\varphi_{mk}(\tilde{y}) = \int_{-\frac{1}{2}}^{\frac{1}{2}} d\tilde{y}' \frac{K_0(|\tilde{k}||\tilde{y} - \tilde{y}'|)}{\pi} \rho_{mk}(\tilde{y}') , \tag{8.32}$$

and the normalisation is chosen to be:

$$\int_{-\frac{1}{2}}^{\frac{1}{2}} d\tilde{y} \rho_{mk}(\tilde{y}) \varphi^*_{pk}(\tilde{y}) = \delta_{mp} . \tag{8.33}$$

In Eqs. (8.30)-(8.32) K_0 is the modified Bessel function of the second kind that arises from performing the x-integration in Eq. (8.9) since [96]

$$K_0(z) = \int_0^\infty \frac{\cos(zt)}{\sqrt{t^2 + 1}} dt . \tag{8.34}$$

The eigenfrequencies are given by:

$$\Omega_{mk}^2 = \Omega_{\rm pl}^2 \xi_{mk} , \tag{8.35}$$

where the characteristic plasmon frequency is defined by:

$$\Omega_{\mathrm{pl}} = \sqrt{\frac{2D}{\bar{\epsilon}W}} \; . \tag{8.36}$$

The potential and current density amplitudes are:

$$\bar{\Phi} = -\frac{2\pi\bar{n}eW}{\bar{\epsilon}} \; , \tag{8.37}$$

and

$$\bar{j} = \bar{n}W\Omega_{\mathrm{pl}} \; . \tag{8.38}$$

This implies the energy normalisation:

$$-e\int d\boldsymbol{r}\Phi^{*}_{mk}(\boldsymbol{r})n_{pq}(\boldsymbol{r}) = \frac{2\pi e^2\bar{n}^2W^2L}{\bar{\epsilon}}\delta_{mp}\delta_{kq} \; . \tag{8.39}$$

In the presence of dissipation the oscillation frequencies are given by:

$$\omega_{mk} = \begin{cases} 0 & \text{if } m,k=0 \\ \Omega_{\mathrm{pl}}\sqrt{\xi_{mk} - \frac{\gamma^2}{4\Omega^2_{\mathrm{pl}}}} - \frac{i\gamma}{2} & \text{otherwise} \; . \end{cases} \tag{8.40}$$

In Fig. 8.3 the dispersion (8.40) of the modes obtained by numerically solving Eq. (8.30) is shown. The results show that one can distinguish two different types of modes. On one hand, one has a gapless mode that manifests a crossover between a 1D dispersion $\omega \sim k\sqrt{-\ln(k)}$ for $kW \ll 1$ to a 2D dispersion $\omega \sim \sqrt{k}$ for $kW \gg 1$. This mode is labelled a *Type I-mode*. On the other hand, there is a spectrum of gapped modes with gap given by $\Omega_{\mathrm{pl}}\sqrt{\xi_{m0}}$ at $\gamma = 0$. These modes arise due to the confinement of the system in the y-direction and are labelled *Type II-modes*. In Table 8.1 the numerically calculated values of ξ_{m0} for the modes with $m = 0 - 5$ are reported.

In Fig. 8.4 the numerically calculated $k = 0$ lateral profiles of the density perturbation, $\rho_{m0}(y)$, and the y-component of the current density $j^{y}_{m0}(y)$ for the Type II modes are shown. Notice that the electron density diverges near the edges of the nanostripe, which is the consequence of the used semiclassical model [295] and will be compensated for if one does assume charge accumulation at the edge of the nanostructures.

The density and current density response to an external field can be written as:

$$\begin{aligned} n(\boldsymbol{r},\omega) &= \sum_{mk} B_{mk}(\omega)n_{mk}(\boldsymbol{r}) \\ \boldsymbol{j}(\boldsymbol{r},\omega) &= \sum_{mk} B_{mk}(\omega)\frac{\omega}{\Omega_{mk}}\boldsymbol{j}_{mk}(\boldsymbol{r}) \; . \end{aligned} \tag{8.41}$$

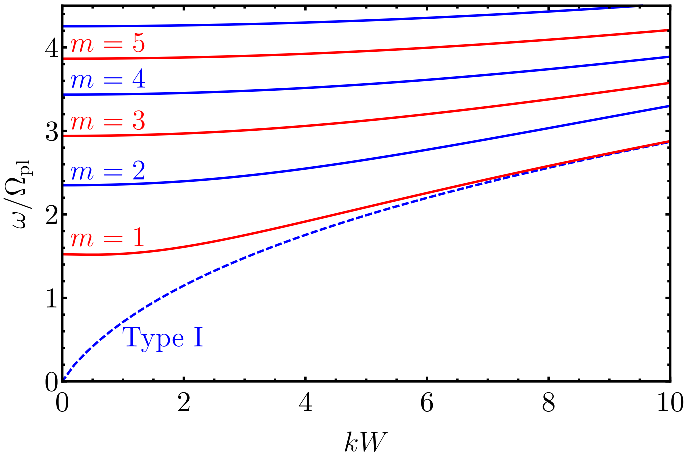

Figure 8.3: Dispersion of the different plasmon modes in a graphene nanostripe. The Type I plasmon is shown as a dashed curve, the Type II plasmons are solid curves. The blue curves are symmetric while the red ones are antisymmetric in the density perturbation. In this figure we have uses $\gamma = 0$.

m	ξ_{m0}
0	0
1	2.31
2	5.52
3	8.64
4	11.76
5	14.90

Table 8.1: Numerical values for the eigenvalues ξ_{mk} at $k = 0$ for different values of m.

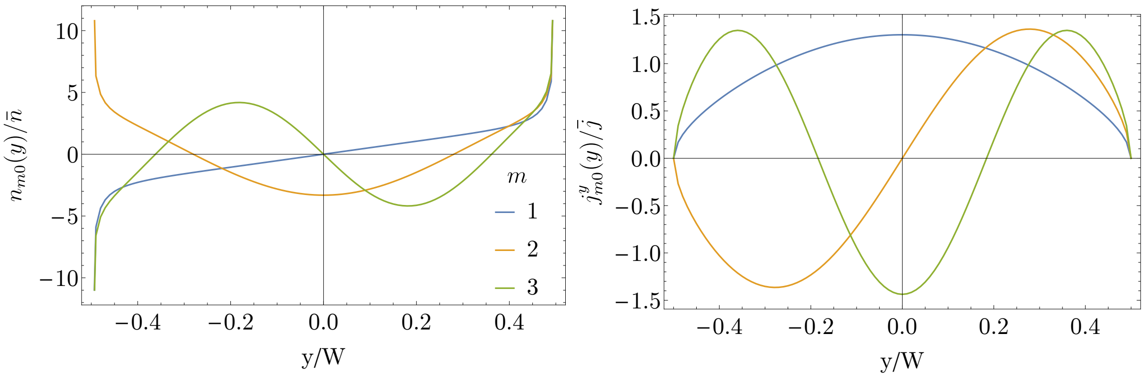

Figure 8.4: Lateral (left) density perturbation profile and (right) current density profile of the Type II plasmon modes at $k = 0$ with m indicated in the legend.

For a uniform electric field oscillating in the y-direction ($\Phi_{\text{ext}}(\boldsymbol{r},\omega) = -E(\omega)y$) one gets:

$$B_{mk}(\omega) = \delta_{k0}\frac{E(\omega)\bar{\epsilon}}{2\pi e\bar{n}}\alpha_{mk}\frac{\Omega^2_{mk}}{\omega(\omega+i\gamma)-\Omega^2_{mk}} \,, \tag{8.42}$$

while the absorption in the same situation is:

$$A_{\perp}(\omega) = \frac{4\mathcal{D}\gamma\omega^2}{c}\sum_m \frac{|\alpha_{m0}|^2\xi_{m0}}{(\omega^2-\Omega^2_{\text{pl}}\xi_{m0})^2+\gamma^2\omega^2} \,. \tag{8.43}$$

The coefficients α_{mk} are defined by:

$$\alpha_{mk} = \int_{-\frac{1}{2}}^{\frac{1}{2}} d\tilde{y}\tilde{y}\rho_{mk}(\tilde{y}) \,. \tag{8.44}$$

If on the other hand the electric field is oscillating in the x-direction ($\Phi_{\text{ext}}(\boldsymbol{r},\omega) = -E(\omega)x$), there is no density modulation or induced potential Φ_{ind}. Therefore, the current is $J(\boldsymbol{r},\omega) = \sigma_{\text{D}}(\boldsymbol{r},\omega)E_{\text{ext}}(\boldsymbol{r},\omega)$ and the absorption is the usual Drude absorption [80]:

$$A_{\parallel}(\omega) = \frac{4\mathcal{D}\gamma}{c(\omega^2+\gamma^2)} \,. \tag{8.45}$$

In Fig. 8.5 the absorption as a function of the incident photon energy for the light polarisation perpendicular and parallel to the strip is shown. The results show that the spectral weight is mainly transferred to the first mode, which corresponds to the $m = 1$-mode. Further also the $m = 3$-mode is excited at larger frequency. This absorption spectrum corresponds to the ones found earlier in experiments as discussed in Sec. 3.3 and as shown in Fig. 3.12(b) [53, 155].

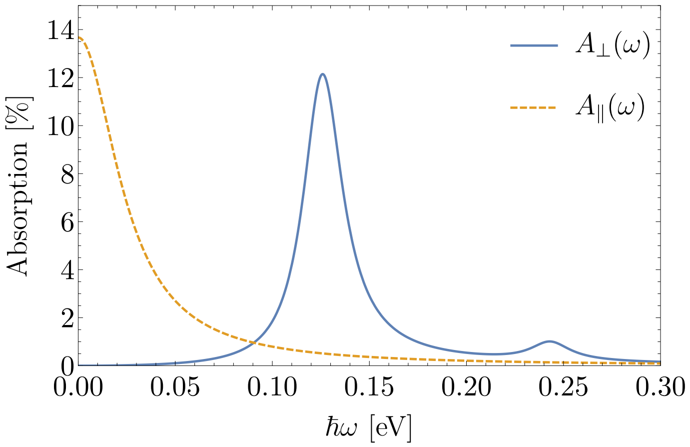

Figure 8.5: Spectral dependence of the absorption of a graphene nanostripe on hBN with width $W = 20$ nm and electron concentration $\bar{n} = 10^{12}$ cm^{-2}. The damping rate is $\gamma = 0.3\ \Omega_{\mathrm{pl}}$.

8.2.4 Time dependence of the density and velocity profiles

The time dependent density and current density profiles can be obtained by the Fourier transform over the frequency variable ω of the modes in Eq. (8.41). This Fourier integral consists of a convolution over the electric field $E(\omega)$ which can be solved easily if one assumes that the electric field of the incident laser that excites the plasmons has the form $E(\omega) = \pi(E_0\delta(\omega-\omega_1) + E_0^*\delta(\omega+\omega_1))$. The modes are given by

$$\begin{aligned} n(\boldsymbol{r},t) &= \sum_m \mathrm{Re}\left[C_m(\omega_1) n_{m0}(\boldsymbol{r}) e^{-i\omega_1 t}\right] \ , \\ \boldsymbol{j}(\boldsymbol{r},t) &= \sum_m \frac{\omega_1}{\Omega_{\mathrm{pl}}\xi_{m0}} \mathrm{Re}\left[C_m(\omega_1) \boldsymbol{j}_{m0}(\boldsymbol{r}) e^{-i\omega_1 t}\right] \ . \end{aligned} \tag{8.46}$$

In Eq. (8.46) for a uniform electric field in the y direction, the complex amplitudes $C_m(\omega)$ are given by

$$C_m(\omega) = \frac{E_0\bar{\epsilon}}{2\pi e\bar{n}} \alpha_{m0} \frac{\Omega_{\mathrm{pl}}^2 \xi_{m0}}{\omega(\omega+i\gamma) - \Omega_{\mathrm{pl}}^2 \xi_{m0}} \ . \tag{8.47}$$

Notice that because only $k = 0$ modes are excited, the velocity is oriented in the y-direction. Due to the additional imaginary i appearing in front of the y-component of the velocity in Eq. (8.29), the density and velocity profile oscillate in anti-phase.

8.3 Absorption modulation

In the preceding section, it was derived how an incident laser with frequency ω_1 excites plasmon modes that oscillate in the lateral direction of the nanostripe at the frequency of the incident laser. As shown in Eq. (8.46), these plasmon modes correspond to an oscillating electron density and current density distribution in the strip that are superpositions of the eigenmodes presented in Fig. 8.4. In this section it is calculated how the local change in electron density and current density affects local chemical potential and velocity that influence the absorption of the nanostripes at frequency ω_2.

8.3.1 Zero temperature

For a given carrier concentration n_c and current density $\boldsymbol{j}$, the chemical potential μ and drift velocity $\beta = v/v_\mathrm{F}$ at $T = 0$ can be obtained by combining Eq. (7.17) with the way the concentration depends on the chemical potential at $T = 0$, which is presented in Eq. (2.29). The chemical potential then becomes:

$$\mu(n_\mathrm{d}, \boldsymbol{v}) = \hbar v_\mathrm{F}\sqrt{\pi n_\mathrm{d}}(1-\beta^2)^{3/4} \, . \tag{8.48}$$

Here $n_\mathrm{d} = \bar{n} + n$ is the sum of the equilibrium concentration and the density perturbation and corresponds to the local doping of the system. At $T = 0$ the carrier concentration $n_\mathrm{c} = n_\mathrm{d}$ such that the drift velocity β is related to the current density as

$$j' = \frac{j}{j_\mathrm{c}} = \beta \, , \tag{8.49}$$

where $j_\mathrm{c} = en_\mathrm{d}v_\mathrm{F}$ is the critical current density corresponding to the case where all available electrons move at the speed of the Fermi velocity v_F.

In Eq. (8.48) the last factor containing the velocity β arises because a finite velocity redistributes the carriers in the Dirac cone. In order to keep the total dopant concentration n_d constant, the chemical potential needs to be lowered if the current density, and hence drift velocity, increases. This is schematically depicted in Fig. 8.6. Because the density perturbation and the current density vary in both space and time as given by Eq. (8.46), a Fermi level profile can be defined as $\mu(\boldsymbol{r}, t) \equiv \mu(n(\boldsymbol{r}, t), \boldsymbol{j}(\boldsymbol{r}, t))$. Notice that this needs to be contrasted with the case of the previous chapter where the chemical potential was fixed by the leads and the gate and therefore independent from the drift velocity. In this case the equilibrium electron concentration $\bar{n}$ is determined by electrostatic gating and the plasmons develop density profiles on top of that.

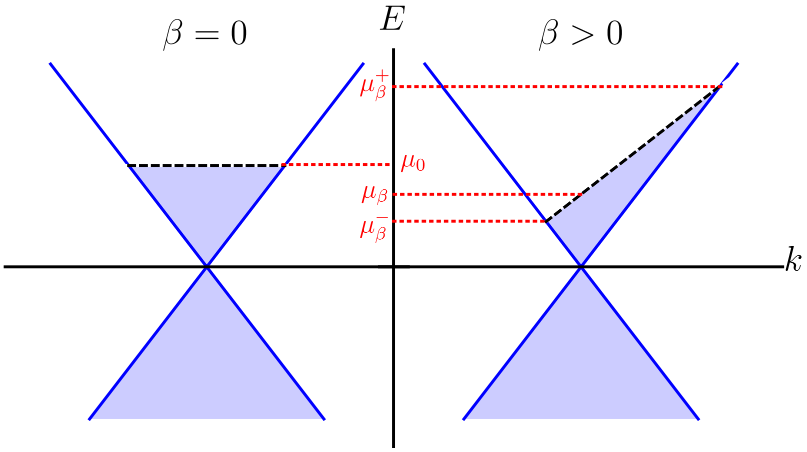

Figure 8.6: Distribution of the occupied states at $T = 0$ in graphene for a fixed doping concentration n in the conduction band. In the absence of an electron drift velocity (left) the states are occupied up to the energy determined by the chemical potential μ_0. If there is a finite drift velocity (right), the cone is partly occupied from μ_β^- to μ_β^+ as defined in Eq. (8.1). Further, in order to keep the total number of occupied states constant, the chemical potential drops to μ_β.

As shown in Eq. (7.77), the absorption of a second laser with frequency ω_2 depends on the chemical potential μ and the velocity β. For ease of reference, the formula is repeated:

$$\begin{aligned} A_{\mathrm{L(T)}}(\omega) &= \pi\alpha_{\mathrm{QED}}\Theta(\hbar\omega - 2\mu) + \alpha_{\mathrm{QED}}\Theta\left(\hbar\omega - \frac{2\mu}{1+\beta}\right)\Theta\left(\frac{2\mu}{1-\beta} - \hbar\omega\right) \\ &\times \left[\pm\frac{\hbar\omega - 2\mu}{\beta\hbar\omega}\sqrt{1 - \left(\frac{\hbar\omega - 2\mu}{\beta\hbar\omega}\right)^2} - \operatorname{sgn}\left(\frac{\hbar\omega - 2\mu}{\beta\hbar\omega}\right)\arccos\left|\frac{\hbar\omega - 2\mu}{\beta\hbar\omega}\right|\right] . \end{aligned} \tag{8.50}$$

In this set-up, those quantities vary in space and time, and therefore one can determine the local absorption $A(\omega_2, \boldsymbol{r}, t) \equiv A(\omega_2, \mu(\boldsymbol{r}, t), \beta(\boldsymbol{r}, t))$.

In order to modulate the ω_2 laser, one can use the two terms from Eq. (8.50). The first term describes the usual Fermi step and depends only on μ. This term describes Pauli blocking. Because the density and current density oscillate in time, also the chemical potential $\mu(\boldsymbol{r}, t)$ and drift velocity $\beta(\boldsymbol{r}, t)$ oscillate in time. Therefore, if the lowest value of the chemical potential of one oscillation cycle at position $\boldsymbol{r}$ is denoted by $\delta\mu_<(\boldsymbol{r})$ and the highest value by $\delta\mu_>(\boldsymbol{r})$, then the first term of Eq. (8.50) will contribute to the modulation at position $\boldsymbol{r}$ if

$$2\delta\mu_<(\boldsymbol{r}) < \hbar\omega_2 < 2\delta\mu_>(\boldsymbol{r}) . \tag{8.51}$$

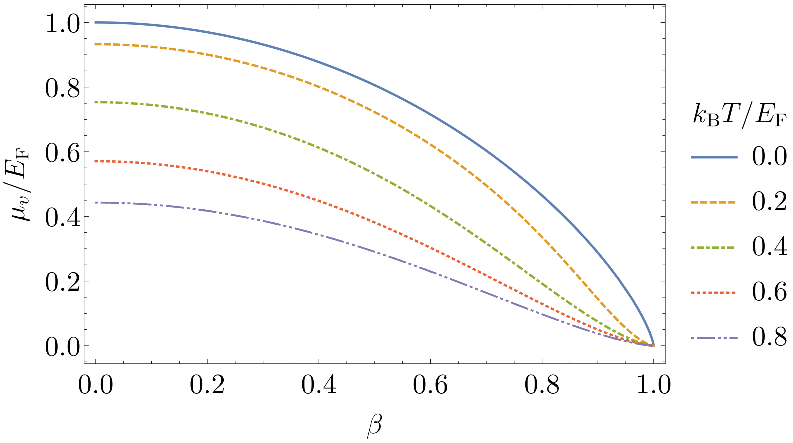

Figure 8.7: Chemical potential μ as a function of the drift velocity β. The solid curve ($T = 0$) corresponds to Eq. (8.48). The finite temperature curves are found by solving Eq. (8.53) for μ.

In this range the absorption varies between 0 and $\pi\alpha_{\mathrm{QED}}$.

The second term describes the smoothing of the Fermi step due to a drift finite velocity over the spectral window from $2\mu^-$ to $2\mu^+$ as defined in Eq. (8.1). Because, as a function of time, the drift velocity profile from Eq. (8.46) oscillates from $-\delta\beta$ to $\delta\beta$, where $\delta\beta$ is the amplitude of the velocity modulation, this window opens and closes at twice the oscillation frequency. The velocity induced opening and closing of the absorption window can be used to modulate the ω_2 laser if, at least for a part of the oscillation period, its photon energy is

$$2\mu^-(n_\mathrm{d}, \boldsymbol{v}) < \hbar\omega_2 < 2\mu^+(n_\mathrm{tot}, \boldsymbol{v}) \ . \tag{8.52}$$

Note that at $T = 0$ the upper boundary of Eq. (8.52) can become arbitrarily large if $\beta \to 1$. This means that one could modulate a large frequency ω_2 with low doping.

At each moment in time t one can integrate the local absorption $A(\omega_2, \boldsymbol{r}, t)$ over the entire strip. In this way one finds the absorption $A(\omega_2, t)$ of the ω_2 laser varying in time and hence the total amplitude modulation of this laser. Note that the two conditions in Eqs. (8.51) and (8.52) overlap. Therefore, the two modulation mechanisms described in the previous paragraphs will coexists in the overlapping region.

8.3.2 Finite temperature

The finite temperature absorption of the system was discussed in Sec. 3.1.5 following the Maldague technique [111]. Because the electrons follow a drifted Fermi distribution function [266, 267], the chemical potential appearing in the Maldague integral depends on both the temperature T and the drift velocity β. It is determined by the equation

$$\frac{n_{\mathrm{d}}(\mu, T, v)}{n_{\mathrm{d}}} = \frac{(k_{\mathrm{B}}T)^2}{E_{\mathrm{F}}^2} \frac{\mathrm{Li}_2\left[-e^{-\frac{\mu}{k_{\mathrm{B}}T}}\right] - \mathrm{Li}_2\left[-e^{\frac{\mu}{k_{\mathrm{B}}T}}\right]}{(1-\beta^2)^{3/2}} \, . \tag{8.53}$$

In Eq. (8.53) $\mathrm{Li}_2[x]$ is the dilogarithm function, $E_{\mathrm{F}} = \mu(n_{\mathrm{d}}, 0)$ is the Fermi level, i.e. the chemical potential from Eq. (8.48) at $\beta = 0$. The corresponding chemical potential as a function of the drift velocity for different temperatures is shown in Fig. 8.7. From this, one can calculate the corresponding drift velocity as

$$\beta\left(\mu, T, n_d\right) = \sqrt{1 - \left(2\left(T'\right)^2 \left[\mathrm{Li}_2\left(-\exp\left(-\frac{\mu'}{T'}\right)\right) - \mathrm{Li}_2\left(-\exp\left(\frac{\mu'}{T'}\right)\right)\right]\right)^{2/3}} \, . \tag{8.54}$$

In Eq. (8.54) the quantities $T' = k_{\mathrm{B}}T/E_{\mathrm{F}}$ and $\mu' = \mu/E_{\mathrm{F}}$ are introduced. This allows to find a relation between j' and (μ, β) as

$$j' \; = \; 2\left(T'\right)^2 \frac{-\mathrm{Li}_2\left(-\exp\left(-\frac{\mu'}{T'}\right)\right) - \mathrm{Li}_2\left(-\exp\left(\frac{\mu'}{T'}\right)\right)}{\left(1 - \beta\left(\mu', T'\right)^2\right)^{3/2}} \beta\left(\mu', T'\right) \, . \tag{8.55}$$

This equation determines the current density as a function of μ' and T'. Vice versa, this also allows to calculate the chemical potential as a function of j' and T'. The result can be finally used to calculate β from the previous equation. In Fig. 8.8 the result of this calculation is shown as the drift velocity β as a function of the reduced current density j' for different values of the temperature. The result shows that as the current density increases, the drift velocity saturates towards the $\beta = 1$ limit.

In Fig. 8.9 the room temperature absorption is shown as a function of incident photon energy for different values of the velocity. The effect of the velocity on the absorption spectrum is now twofold. On the one hand it lowers the chemical potential such that the Fermi step shifts to lower values of $\hbar\omega$, and on the other hand it widens the window defined in Eq. (8.52). Notice that for $\psi = \pi/2$ the difference between the curves is much larger for large energy.

As shown in Fig. 8.9, also the spectral boundaries for modulation presented in Eq. (8.52) are affected by temperature. Fig. 8.10 shows the boundaries $2\mu^{\pm}$ at room temperature as a function of the velocity for different dopant concentrations n_{d}. One sees that as the velocity approaches v_{F}, there is a competition between the decreasing chemical potential as shown in Fig. 8.7 pushing the boundary down, and the decreasing denominator of μ^+ pushing the boundary for μ^+ up. At finite temperature, Fig. 8.10(a) shows that the divergence of μ^+ for $\beta \to 1$ is suppressed. Notice that at finite temperature also the absorption

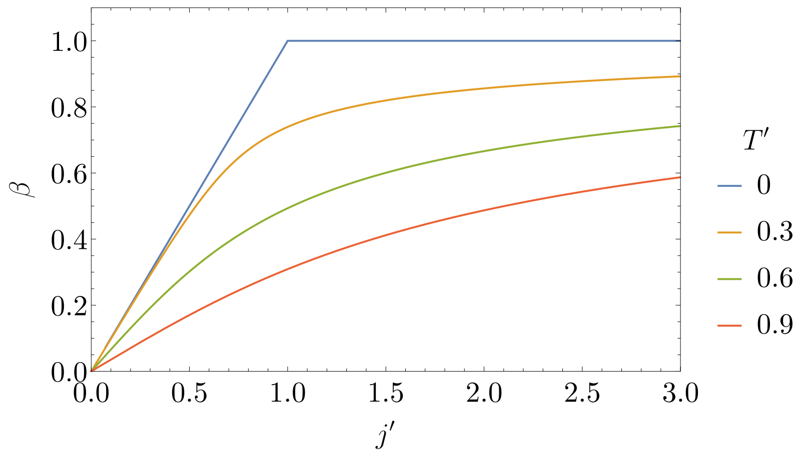

Figure 8.8: Drift velocity β as a function of the current density j' for different values of the temperature.

is smeared over a frequency range as shown in Fig. 8.9. Therefore the boundaries presented in Eq. (8.52) are not strict any more for $T \neq 0$ but can still serve as a guide to find appropriate parameters for achieving modulation.

8.4 Modulating a telecom laser at terahertz speed

The set-up under consideration uses a $\lambda_1 = 10.6\ \mu$m pump laser (i.e. $\hbar\omega_1 = 117$ meV) that excites the plasmons and that modulates a $\lambda_2 = 1.54\ \mu$m telecom probe laser ($\hbar\omega_2 = 805$ meV) for which the polarisation has an angle $\psi = 0$ with the y-axis. For different "gatable" electron concentrations the modulation is calculated and the width of the nanostripes is considered to be optimized such that the $m = 1$ plasmon-mode is in resonance with the pump laser as it has been observed that these modes are the easiest to excite [155]. This means that the width W^* is given by

$$W^* = 2\alpha_{\rm ee}\xi_{10}\frac{(\hbar v_{\rm F})^2\sqrt{\pi\bar{n}}}{\bar{\epsilon}(\hbar\omega_1)^2} = 0.44\frac{(\pi\bar{n}[10^{12}\ {\rm cm}^{-2}])^{1/2}}{\bar{\epsilon}\,(\hbar\omega_1[{\rm eV}])^2}\ {\rm nm}\ . \tag{8.56}$$

In Table 8.2 the three Fermi levels considered in these simulations are reported together with the corresponding background concentration $\bar{n}$ and optimized width W^*. Notice that in this analysis the plasmon-plasmon interaction between the graphene nanostripes is neglected because the stripes are considered to be not too close to each other [53, 155].

The system of nanostripes is considered to be deposited on a substrate of CaF$_2$ which has a dielectric constant $\epsilon_{\rm CaF_2} = 1.38^2$. Furthermore it is assumed that $\gamma = 0.3\omega_1$ [295]

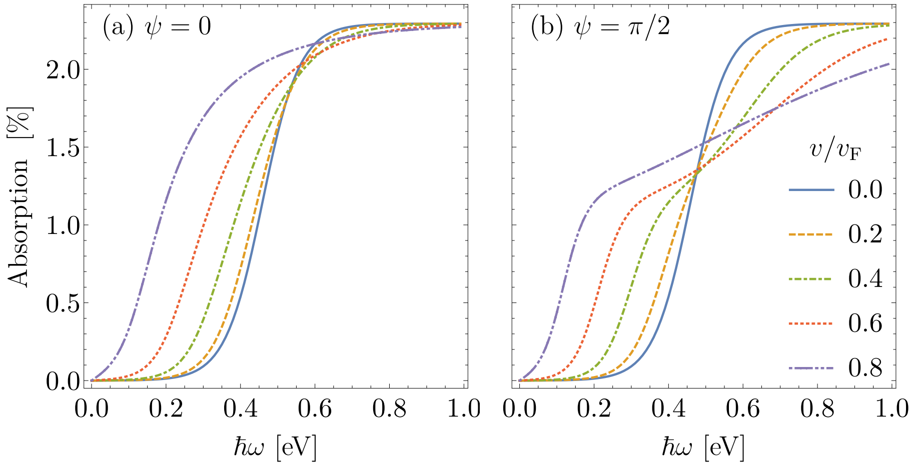

Figure 8.9: Spectral dependence of the absorption at $T = 300$ K for an electron concentration $n_\mathrm{d} = 4 \times 10^{12}$ cm^{-2} and for different velocities as indicated by the legend. The results are for a polarisation (a) parallel to the velocity and (b) perpendicular to it.

and that the pump laser has a power $P_1 = 300\,\mathrm{mW}$. Assuming that the pump laser's spot size equals its wavelength, the electric field that excites the plasmons can be inferred as

$$E_1 = \sqrt{\frac{8P_1}{c\rho_1^2}} = 9.795\frac{\sqrt{P_1\,[\mathrm{mW}]}}{\lambda_1\,[\mu\mathrm{m}]}\,\mathrm{kV/cm} = 16.01\,\mathrm{kV/cm}\,. \tag{8.57}$$

Using the data quoted above, one can calculate the time dependent profiles of the chemical potential μ and the drift velocity β at finite temperature. At several points in the oscillation cycle, these profiles are shown in Fig. 8.11 for a Fermi level of $E_\mathrm{F} = 0.2$ eV . Consequently, one can use the theory of current-affected absorption at finite temperature explained in the previous section to calculate the absorption profile as shown in the bottom panel of Fig. 8.11. The mean of the absorption profiles as a function of time for the three

E_F [eV]	$\bar{n}$ [10^{12} cm^{-2}]	W^* [nm]
0.1	0.73	19.9
0.2	2.93	39.8
0.3	6.61	59.7

Table 8.2: Parameters used for the different simulations.

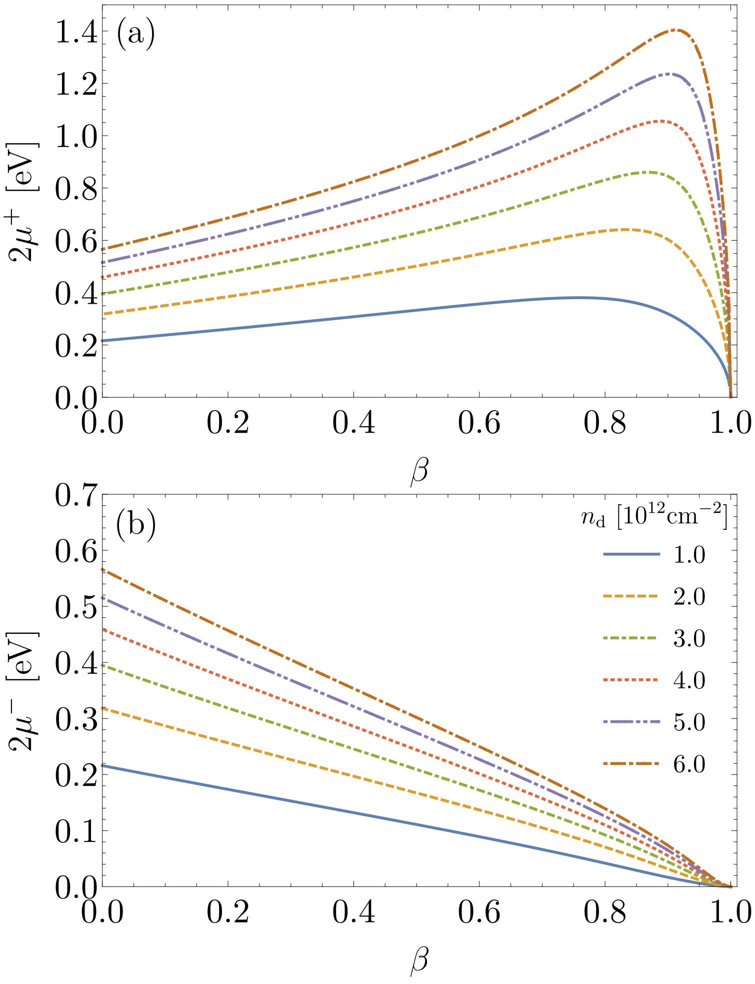

Figure 8.10: (a) Upper boundary and (b) lower boundary of the modulation window Eq. (8.52) at $T = 300$ K as a function of the drift velocity β for different concentrations as indicated by the legend.

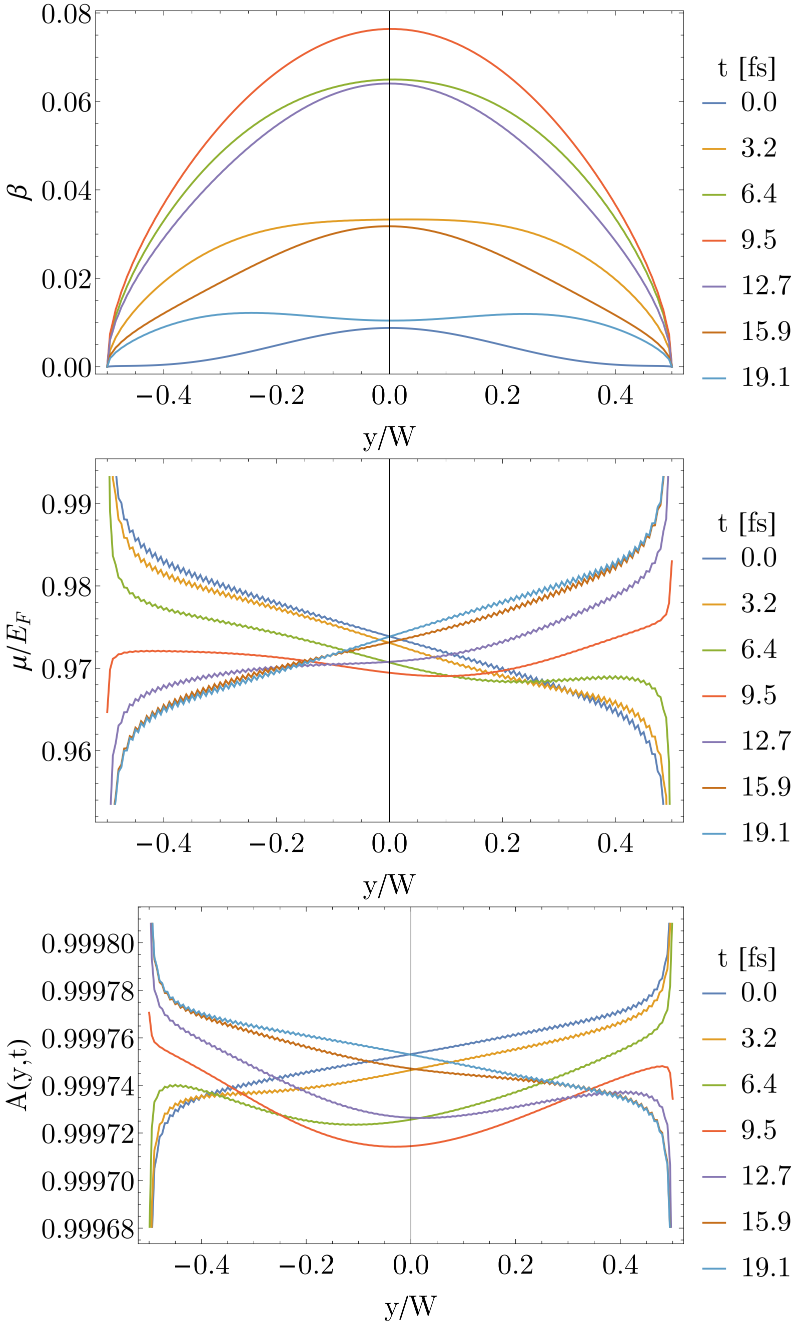

Figure 8.11: Velocity, chemical potential and absorption profile for different time instances for the case of $E_{\mathrm{F}} = 0.2$ eV and optimized width as discussed before. In all plots the temperature is $T = 300$ K.

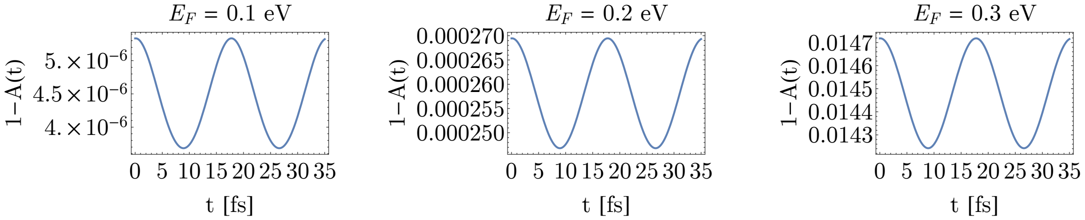

Figure 8.12: Real-time absorption profile of a nanoribbon with optimized width W^* as discussed in the text. ($A(t)$ is in units of $\pi\alpha_{\mathrm{QED}}$.)

cases considered is shown in Fig. 8.12. The modulation of the ω_2 probe laser will occur through a change in the amplitude of the electric field $\boldsymbol{E}_2$ of the probe laser as

$$\boldsymbol{E}_2(t) = \sum_{i=\mathrm{L,T}} E_{2,i} \cos(\omega_2 t) \sqrt{1 - \pi\alpha_{\mathrm{QED}} \left\langle A_i(\boldsymbol{r}, t) \right\rangle_{\boldsymbol{r}}} \boldsymbol{e}_i \,. \tag{8.58}$$

In Eq. (8.58) the time dependence of the electric field after interaction with the nanostripes is shown. The effect of a change in electric field strength will show up in experiments as a set of side-bands to the central peak that is positioned at the frequency of the probe laser ω_2. The Fourier components of this signal are shown in Fig. 8.13 at the different positions of the expected sidebands.

Fig. 8.13 shows that the odd side-bands have an amplitude that is near the machine precision and should, therefore, be neglected. It are the even side-bands that are the most prominent. This is already expected by investigation of the absorption signal as shown in Fig. 8.12 where it should be noted that the period of the plasmon oscillation is $T_1 \sim 35$ fs. The results show that in the course of one plasmon oscillation, the absorption went through two cycles. Therefore, the effect of the absorption has a frequency twice that of the pump laser ω_1.

In order to discriminate between the contribution of the drift velocity and the chemical potential in the absorption, in Fig. 8.14 the time dependent absorption at different positions over the width of the strip are shown. The figure shows that near the side of the strip the signal oscillates at the frequency of the pump laser but in anti-phase with the opposite side. Here, the effect of the density oscillation is the strongest, but because of the anti-phase oscillation it will not suffice to modulate the probe laser. At the center of the strip, however, the amplitude of the oscillation is lower but here the signal oscillates at twice the frequency of the pump laser. The absorption oscillation at the strip center is the direct consequence of the drift velocity of the charge carriers because in the center of the stip, the density has a node. Furthermore, as the absorption does not depend on the sign of the current density, the frequency of oscillation is twice that of the pump laser. Finally, the

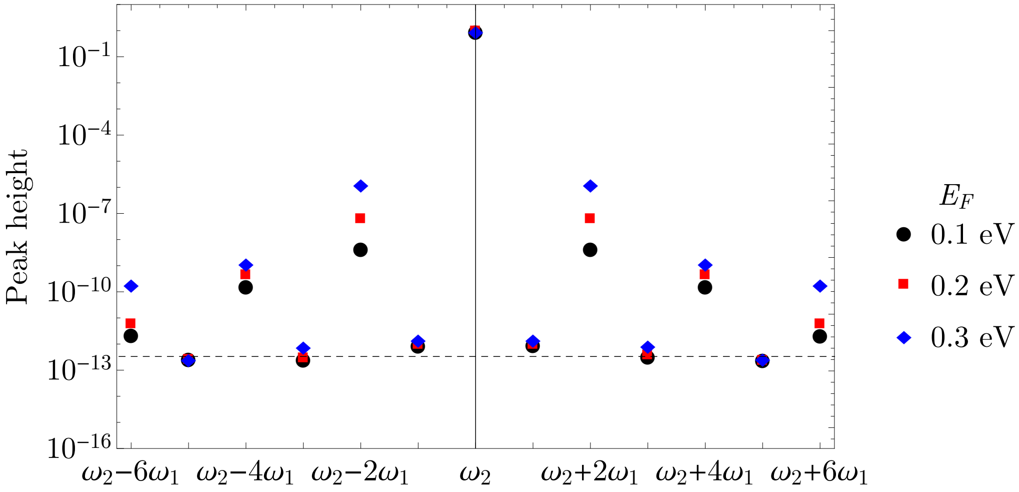

Figure 8.13: Different harmonics of the Fourier transformed signal $E_\mathrm{L}(\omega)$ based on the absorption profiles shown in Fig. 8.12. The dashed line denotes the lower boundary of the machine precision.

signal at the center of the strip cannot be compensated in the averaging. Therefore, it is clear that the notion of a current-induced absorption change is detrimental for modulation of the probe laser. Notice that if one would use the theory of graphene absorption without accounting for a finite drift velocity, the absorption would not acquire a time-dependent oscillation.

8.5 Conclusions

In this chapter it was shown that plasmons excited in a graphene nanostripe by a MIR light source can be used to modulate the amplitude of a telecom laser at twice the frequency of the pump laser. The modulation makes use of the velocity oscillations of the electron liquid associated with the plasmons in the nanostripe. If the amplitude of the drift velocity profile of the plasmons is large enough, one can use the velocity induced absorption smearing of the Pauli blocking to extend the modulation to much larger energy scales than accessibly by solely modulating the chemical potential as is usually done with graphene modulators.

In calculating the final results, care was exercised to mimic the experimental environment by e.g. calculating the results for a non-zero temperature and considering carrier concentrations that are within reach of electrostatic gating. The results show that the modulation indeed persists up to room-temperature for these concentrations. In order to boost this number, one could consider a stack of graphene stripes, such that the absorption of the

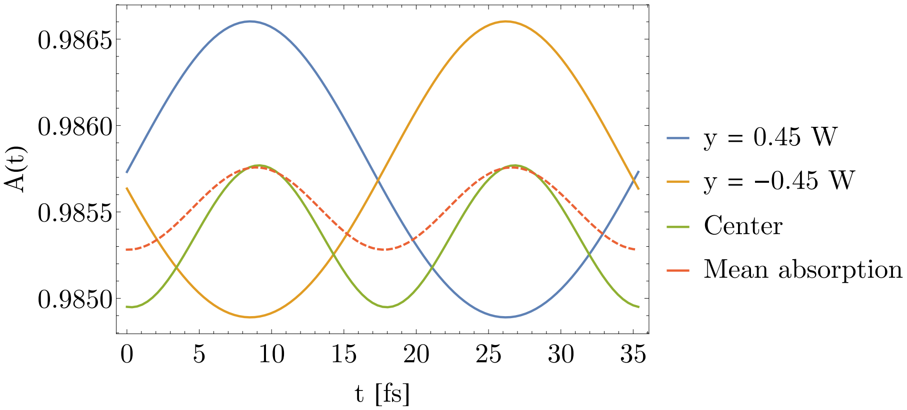

Figure 8.14: Absorption in units of $\pi\alpha_{\mathrm{QED}}$ as a function of time for the $E_{\mathrm{F}} = 0.3$ eV sample of the previous Section at different positions of the strip as indicated. The dashed line is the resulting total mean absorption of the strip.

different layers accumulates. Alternatively on can place the graphene stripes in an optical cavity where the beam that one wants to modulate passes several times through the stripes [296].

The set-up considered in this chapter was experimentally investigated by our experimental collaborator, Prof. A. N. Grigorenko and his group. Recently, they indeed measured a mixed signal where the amplitude of the telecom laser oscillates at twice the frequency of the MIR laser. This indicates that the proposed mechanism of using the velocity profile of the charge carriers to modulate a second laser beam is indeed observed.

CHAPTER 9

Conclusion and outlook

In this thesis, the plasmonic properties of graphene and related materials were theoretically investigated. Within the random phase approximation, the plasmonic modes were calculated for different configurations of the two-dimensional systems. Their quality factor, oscillator strength, energy dispersion, among others, were interpreted in the framework of linear response theory. Through the analysis, the questions that were posed in the first chapter can be answered as follows:

> **How are graphene plasmons affected by the hexagonal symmetry of the lattice?**

In chapter 4 it is shown that the hexagonal symmetry of the graphene honeycomb lattice affects the single-particle energy dispersion. As a consequence, the density-density response function changes in magnitude as well and affects the dispersion of plasmons in graphene systems with large electron or hole doping. However, the trigonal warping of the Dirac cone that is induced by the hexagonal symmetry does not to affect the isotropy of the plasmon dispersion. It has to be noted that the robustness of the plasmon dispersion to a trigonal distortion of the single-particle energy dispersion is remarkable, in particular in view of earlier calculations that showed that uniaxial distortions break the isotropy.

> **How can one excite charge neutral plasmons by valley polarising a graphene flake?**

In chapter 5 it is shown that when graphene is deposited on an hBN crystal, the electronic spectrum is gapped. If one creates a valley imbalance in the gapped system, the plasmons in both valleys start behaving differently. It is shown that as a function of the polarisation, there is a critical plasmon frequency for which the relative phase of the oscillation between both valleys transforms from being in-phase to being in anti-phase. Plasmons that oscillate in anti-phase with the same amplitude in both valleys are charge neutral. Furthermore, it is shown that a new plasmon mode appearing in a gap in the particle hole excitation spectrum is very sensitive to the valley polarisation and can become almost completely charge neutral. Finally, a novel partly damped plasmon mode for low electron doping was identified. This mode is shown to be completely charge neutral in the long wavelength limit.

How do external fields influence the lifetime of plasmons in silicene?

In chapter 6 it is shown that silicene also supports plasmons. Because external electric or exchange fields affect the single-particle energy spectrum in a spin- and valley-dependent way, the particle hole excitation spectrum acquires a spin and valley texture. Consequently, one can tune the lifetime of silicene plasmons by external electric and exchange fields that can turn the excitations of single particles of a specific spin and valley type on or off.

How does an electric current influence the optical properties of graphene and can it be used to enhance the lifetime of plasmons in graphene?

In chapter 7 it is shown that due to an electric current, the graphene sheet absorbs external radiation in a birefringent way. Furthermore, the plasmon dispersion becomes non-reciprocal, yielding a different dispersion for oppositely propagating plasmons. Finally, it is shown that the plasmons are collimated in the downstream direction and that the collimation can be tuned by changing the current density of the drift current. This mechanism can be used to enhance the plasmon lifetime. It is shown that it is possible that, for a given photon frequency, in the absence of a drift current the plasmon is damped by inter-band transitions. However, applying a current allows the plasmon to propagate in the downstream direction without being damped by single-particle processes and, hence, its lifetime is increased.

Can plasmons excited by a mid-infrared laser be used to modulate the amplitude of a telecom laser?

In chapter 8 it is shown that the current dependent absorption of the graphene flake can be used to describe the absorption of a graphene nanostripe in which plasmons are excited by a MIR laser. The oscillating density and velocity profile of these plasmons induce an oscillating local chemical potential and drift velocity that change the absorption. It is shown that these plasmons can modulate a telecom laser at twice the frequency of the MIR laser.

As explained in the thesis, the plasmonic research of graphene and related materials still progresses at a tremendous pace. There are, however, still a lot of unanswered questions regarding the use of graphene, or other two-dimensional related materials, as platforms for plasmonic applications or for new and unexpected physics. Therefore, there is a lot of potential to extend the work presented in this thesis.

The graphene/hBN platform, or other kinds of van der Waals heterostructures, are only just being explored for their use in plasmonics. As an extension of the work that is done in chapter 5, it is interesting investigating plasmons in the quasi-equilibrium state in which one of the two valleys is optically pumped. This will create a system with three kinds of charge carriers: two electron pockets in both valleys and one hole pocket. Furthermore, because it is a quasi-equilibrium system, it is important to consider a finite temperature response. It was already shown that in such a system a new non-reciprocal plasmon mode arises at the edge of the graphene flake [208]. However, the internal plasmonic response is still unknown and should be investigated.

The evaluation of the effect of external fields on the damping of silicene plasmons presented in chapter 6 is a first step in understanding plasmon dynamics in silicene. As silicene is being promoted as an ideal platform for the merger of silicon-based semiconductor physics and 2D materials, it would be useful to gain more insights in processes limiting the plasmon lifetime other than single-particle excitation. For example, it is unknown how plasmons in silicene interact with phonons in the material or the underlying substrate. For graphene plasmons it is shown that the plasmons strongly hybridise with phonons in a SiC substrate [125], therefore, a similar analysis should be done to quantify the effect. Furthermore, as silicene is tipped as an ideal platform for spintronics, it is important to understand the effect of exchange interaction on the silicene plasmons. This is not incorporated at the level of the RPA presented in this thesis, but can be included by means of local field factors [102].

In the quest to extend the plasmon lifetime in graphene systems, the proposal presented in chapter 7 is a first example of how changes to the system can decrease the plasmon decay rate. In general, one should investigate how the breaking of (local) time reversal symmetry can generate non-reciprocal plasmons in the absence of magnetic fields. The non-reciprocal edge mode mentioned above and the current-induced non-reciprocal plasmons are two examples of plasmons where due to the breaking of time-reversal symmetry (by circularly polarised light or a finite drift current respectively) reciprocity is broken. It is expected that because these modes only propagate unidirectionally, the phase space in which damping processes can occur is strongly reduced. As a consequence, these plasmons could have longer lifetimes. Therefore, it is necessary to investigate the damping processes of these kinds of plasmons more extensively.

APPENDIX A

Retarded 2D plasmon dispersion

In the thesis the Coulomb interaction is always considered to be instantaneous. As a consequence, the plasmon dispersion is found to depend on the wave vector q as $\omega_{\mathrm{pl}} \sim \sqrt{q}$ as shown in Eq. (3.117). Although this is correct for short wavelengths, it is clear that in the long wavelength limit, i.e. $q \to 0$, this cannot be correct as then the plasmon group velocity, $v_{\mathrm{g}} = \frac{\partial \omega_{\mathrm{pl}}}{\partial q}$ diverges and exceeds the speed of light. Therefore, in order to find the correct plasmon dispersion, one needs to account for a finite speed of light c. This is the subject of this appendix. The analysis presented in this appendix is based on Ref. [297].

A.1 Maxwell's equations

In order to find the retarded mode at the interface between two dielectrics (interface perpendicular to the z direction), the electric and magnetic fields are described by Maxwell's equations:

$$\nabla \cdot \boldsymbol{E}_{(j)} = 0 \tag{A.1}$$

$$\nabla \cdot \boldsymbol{B}_{(j)} = 0 \tag{A.2}$$

$$\nabla \times \boldsymbol{E}_{(j)} = -\frac{\partial \boldsymbol{B}_{(j)}}{\partial t} \tag{A.3}$$

$$\nabla \times \boldsymbol{B}_{(j)} = \frac{n_{(j)}^2}{c^2} \frac{\partial \boldsymbol{E}_{(j)}}{\partial t} \tag{A.4}$$

Here, one assumed that there are no free charges or currents in the system and $n_{(j)}$ is the refractive index of dielectric j. The boundary conditions at the interface are given by

$$\begin{aligned} \boldsymbol{n}_{12} \times (\boldsymbol{E}_2 - \boldsymbol{E}_1) &= 0 && \text{(A.5)} \\ (\varepsilon_2 \boldsymbol{E}_2 - \varepsilon_1 \boldsymbol{E}_1) \cdot \boldsymbol{n}_{12} &= \frac{4\pi}{\omega} \boldsymbol{q} \cdot \boldsymbol{J}_{2D} && \text{(A.6)} \\ (\boldsymbol{B}_2 - \boldsymbol{B}_1) \cdot \boldsymbol{n}_{12} &= 0 && \text{(A.7)} \\ \boldsymbol{n}_{12} \times \left(\mu_2^{-1} \boldsymbol{B}_2 - \mu_1^{-1} \boldsymbol{B}_1\right) &= -\frac{4\pi}{c} \boldsymbol{J}_{2D} && \text{(A.8)} \end{aligned}$$

These equations should now be solved for a mode confined to the interface. Notice that the $2D$ current density $\boldsymbol{J}_{2D}$ is related to the electric field as

$$\boldsymbol{J}_{2D} = \sigma \boldsymbol{E}. \tag{A.9}$$

Here σ is the conductivity. Notice that the transverse part of the conductivity has been neglected.

A.2 Confined mode at the interface

Suppose that the interface is positioned at $z = 0$, then we can find the confined mode by solving the equations from the previous section for a mode with an electric field that decays exponentially inside te dielectrics as

$$\boldsymbol{E}_{(j)} \left(\boldsymbol{r}, t\right) = \boldsymbol{a}_{(j)} \exp\left(iqx \pm \beta_{(j)} z - i\omega t\right) + \text{c.c.}, \tag{A.10}$$

here the mode is assumed to propagate in the x-direction, the $\pm$ ensures to an exponential decay in the respective regions and the quantity $\beta_{(j)}$ is

$$\beta_{(j)} = \sqrt{q^2 - \frac{\omega^2 n_{(j)}^2}{c^2}}. \tag{A.11}$$

Using the condition $\boldsymbol{\nabla} \cdot \boldsymbol{E} = 0$, one finds

$$\begin{aligned} iqa_{(j),x} \pm \beta_{(j)} a_{(j),z} &= 0 && \text{(A.12)} \\ a_{(j),z} &= \mp \frac{iq}{\beta_{(j)}} a_{(j),x} && \text{(A.13)} \end{aligned}$$

which relates the z component with the x component of $\boldsymbol{a}_{(j)}$.

Now one can enter these expressions in the boundary conditions from the previous section and find

$$\begin{aligned} \varepsilon_2 E_{2,z} - \varepsilon_1 E_{1,z} &= \frac{4\pi}{\omega} q J_{2D,x} = \frac{4\pi}{\omega} q \sigma E_x \\ +\varepsilon_2 \frac{iq}{\beta_{(2)}} a_x + \varepsilon_1 \frac{iq}{\beta_{(1)}} a_x &= \frac{4\pi}{\omega} q \sigma a_x \end{aligned} \tag{A.14}$$

here the condition $a_{(1),x} = a_{(2),x} = a_x$ was used to satisfy the first boundary condition. So one finds

$$\begin{aligned} -\varepsilon_2 \beta_{(1)} - \varepsilon_1 \beta_{(2)} &= \frac{4\pi}{\omega} i \sigma \beta_{(1)} \beta_{(2)}, \\ 0 &= 1 + \frac{4\pi i \sigma \beta_{(1)} \beta_{(2)}}{\omega \left(\varepsilon_2 \beta_{(1)} + \varepsilon_1 \beta_{(2)} \right)}. \end{aligned} \tag{A.15}$$

Using this expression, one can obtain the plasmon dispersion for a Drude conductivity

$$\sigma_{\mathrm{D}} = \frac{i\mathcal{D}}{\pi\omega}$$

where $\mathcal{D}$ is the Drude weight such that

$$1 = \frac{4\mathcal{D}\sqrt{c^2q^2 - \omega^2 n_{(1)}^2}\sqrt{c^2q^2 - \omega^2 n_{(2)}^2}}{\omega^2 c \left(\varepsilon_2 \sqrt{c^2q^2 - \omega^2 n_{(1)}^2} + \varepsilon_1 \sqrt{c^2q^2 - \omega^2 n_{(2)}^2} \right)}$$

in the case of a suspended sample, $n_{(j)} = 1$, this becomes

$$\omega^2 c = 2\mathcal{D}\sqrt{c^2q^2 - \omega^2} \tag{A.16}$$

$$\omega^2 = \left(\frac{2\mathcal{D}}{c} \right)^2 \frac{-1 \pm \sqrt{1 + \frac{4c^2q^2}{\frac{2\mathcal{D}}{c}}}}{2} \tag{A.17}$$

such that the positive root becomes

$$\omega_{\text{pl}}(q) = \Omega_{\text{pp}} \sqrt{\frac{1}{2} \left(\sqrt{1 + \frac{4c^2q^2}{\Omega_{\text{pp}}^2}} - 1 \right)} \tag{A.18}$$

where the quantity $\Omega_{\text{pp}} = 2\mathcal{D}/c$, i.e. the plasmon-polariton characteristic frequency has been introduced. Equation (A.18) shows the full retarded mode with limits

$$\lim_{q \to 0} \omega_{\text{pl}}(q) = cq, \tag{A.19}$$

$$\lim_{c \to \infty} \omega_{\text{pl}}(q) = \sqrt{\Omega_{\text{pp}} cq} = \sqrt{2\mathcal{D}q}. \tag{A.20}$$

The first limit shows the plasmon-polariton hybridisation at small q, the second limit shows the same $\sqrt{q}$ dependency at large wave vector as found before. The plasmon-polariton hybridisation is shown in Fig. 3.11 in the main text.

APPENDIX B

Analytical results for the response function of different systems

In this Appendix, the analytical results for the non-interacting density-density response functions of different systems are summarised for reference.

B.1 2D electron gas

The 2D electron gas has the Hamiltonian

$$H = \frac{p^2}{2m}, \tag{B.1}$$

where m is the (band)mass of the charge carriers. As a consequence, the energy spectrum is

$$\varepsilon_{\boldsymbol{k}} = \frac{(\hbar k)^2}{2m}. \tag{B.2}$$

Following [102] one can find the non-interacting density-density response function as

$$\chi_{nn}^{(0)}(q,\omega) = \frac{g_{\mathrm{s}}}{L^2} \sum_{\boldsymbol{k}} \frac{n_{\boldsymbol{k}} - n_{\boldsymbol{k}+\boldsymbol{q}}}{\hbar\omega + \varepsilon_{\boldsymbol{k}} - \varepsilon_{\boldsymbol{k}+\boldsymbol{q}} + i\hbar\eta}. \tag{B.3}$$

Notice that the density vertex equals unity in this case and that one does not have a valley dependence. The response function can be split in a similar way as for graphene as

$$\chi_{nn}^{(0)}(q,\omega)=\frac{g_{\mathrm{s}}}{L^2}\sum_{\boldsymbol{k}}\frac{n_{\boldsymbol{k}}}{\hbar\omega+\varepsilon_{\boldsymbol{k}}-\varepsilon_{\boldsymbol{k}+\boldsymbol{q}}+i\hbar\eta}+\frac{g_{\mathrm{s}}}{L^2}\sum_{\boldsymbol{k}}\frac{n_{\boldsymbol{k}}}{-\hbar\omega+\varepsilon_{\boldsymbol{k}}-\varepsilon_{\boldsymbol{k}-\boldsymbol{q}}-i\hbar\eta}. \quad (\text{B.4})$$

This shows that the second term can be obtained from the first one by replacing $\omega+i\eta\rightarrow-\omega-i\eta$. The first term can be written as

$$\frac{g_{\mathrm{s}}}{L^2}\sum_{\boldsymbol{k}}\frac{n_{\boldsymbol{k}}}{\hbar\omega+\varepsilon_{\boldsymbol{k}}-\varepsilon_{\boldsymbol{k}+\boldsymbol{q}}+i\hbar\eta}=\frac{2mg_{\mathrm{s}}}{\hbar^2}\int_0^1\frac{d\bar{k}}{2\pi}\bar{k}\int\frac{d\theta}{2\pi}\frac{1}{\bar{\omega}-2\bar{k}\bar{q}\cos\theta-\bar{q}^2+i\eta}$$

where

$$\bar{\omega}=\frac{\hbar\omega}{E_{\mathrm{F}}}=\frac{2m\hbar\omega}{(\hbar k_{\mathrm{F}})^2},\ \bar{q}=\frac{q}{k_{\mathrm{F}}},\ \bar{k}=\frac{k}{k_{\mathrm{F}}}. \quad (\text{B.5})$$

As explained in Ref. [102] this can be written in terms of the quantity

$$\nu_\alpha=\frac{\bar{\omega}}{2\bar{q}}+\alpha\frac{\bar{q}}{2}. \quad (\text{B.6})$$

Here, $\alpha=\pm1$. The final result is

$$\mathrm{Re}\chi_{nn}^{(0)}(q,\omega)=-D\left(1+\frac{1}{\bar{q}}\left[\sum_{\alpha=\pm1}\mathrm{sgn}\left[\nu_\alpha\right]\Theta\left(\nu_\alpha^2-1\right)\sqrt{\nu_\alpha^2-1}\right]\right), \quad (\text{B.7})$$

$$\mathrm{Im}\chi_{nn}^{(0)}(q,\omega)=\frac{-D}{\bar{q}}\left[\sum_{\alpha=\pm1}\Theta\left(1-\nu_\alpha^2\right)\sqrt{1-\nu_\alpha^2}\right]. \quad (\text{B.8})$$

Here, $D=g_{\mathrm{s}}m/\left(2\pi\hbar^2\right)$ is the 2DEG density of states with $g_{\mathrm{s}}=2$ the spin degeneracy factor. In Fig. B.1 the real and imaginary part of the 2DEG density-density response function are shown. The PHES is defined as the region for which the quantity in Eq. (B.6) is between -1 and 1 for both values of $\alpha=\pm1$.

B.2 Graphene

The graphene density-density response function has been calculated in depth in Sec. 3.1.3. The presented solution is compact and useful for the explications of plasmonic effects during the course of the thesis. However, as explained in Ref. [106], the solution can also

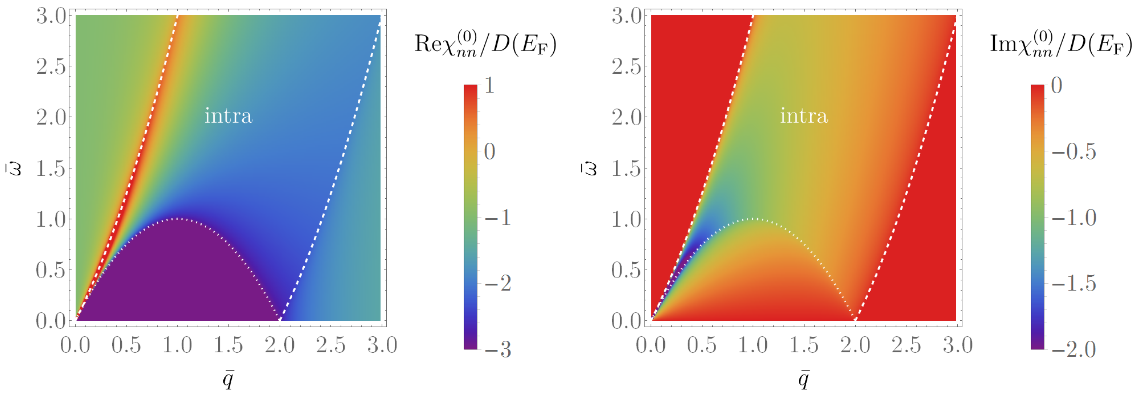

Figure B.1: Real (left) and imaginary (right) part of the non-interacting density-density response function for a 2DEG.

be written in the (q, ω) plane by dividing the plane in six regions as indicated in Fig. B.3. Introducing the following functions

$$
\begin{aligned}
f(q,\omega) &= \frac{D(E_\mathrm{F})}{8}\frac{\bar{q}^2}{\sqrt{|\bar{\omega}^2-\bar{q}^2|}}, && \text{(B.9)}\\
G_>(x) &= x\sqrt{x^2-1}-\mathrm{arcosh}(x) \text{ and } x>1 && \text{(B.10)}\\
G_<(x) &= x\sqrt{1-x^2}-\arccos(x) \text{ and } |x|<1 && \text{(B.11)}
\end{aligned}
$$

The finite doping part of the non-interacting response function $\chi_{nn}^{(0)}(q,\omega)$ labeled by $\chi_{E_\mathrm{F}}(q,\omega)$ in Eq. (3.50) is given in the language of the regions shown in Fig.B.3 by

$$
\begin{aligned}
\mathrm{Re}\chi_{E_\mathrm{F}}(q,\omega) &= -D(E_\mathrm{F})+f(q,\omega)\\
&\times\begin{cases}
\pi & 1A\\
-G_>\left(\frac{2-\bar{\omega}}{\bar{q}}\right)+G_>\left(\frac{2+\bar{\omega}}{\bar{q}}\right) & 1B\\
-G_<\left(\frac{\bar{\omega}-2}{\bar{q}}\right) & 2A\\
G_>\left(\frac{2+\bar{\omega}}{\bar{q}}\right) & 2B\\
-G_<\left(\frac{\bar{\omega}-2}{\bar{q}}\right)+G_<\left(\frac{2+\bar{\omega}}{\bar{q}}\right) & 3A\\
G_>\left(\frac{2+\bar{\omega}}{\bar{q}}\right)-G_<\left(\frac{\bar{\omega}-2}{\bar{q}}\right) & 3B
\end{cases} && \text{(B.12)}
\end{aligned}
$$

$$\mathrm{Im}\chi_{E_\mathrm{F}}(q,\omega) = f(q,\omega)\times\begin{cases} G_>\left(\frac{2-\bar{\omega}}{\bar{q}}\right)-G_>\left(\frac{2+\bar{\omega}}{\bar{q}}\right) & 1A\\ \pi & 1B\\ -G_>\left(\frac{2+\bar{\omega}}{\bar{q}}\right) & 2A\\ -G_<\left(\frac{2+\bar{\omega}}{\bar{q}}\right) & 2B\\ 0 & 3A\\ 0 & 3B \end{cases} \tag{B.13}$$

The regions are defined as

$$\begin{aligned} 1A &: \bar{q}>\bar{\omega} \text{ and } \bar{\omega}<2-\bar{q}\\ 1B &: \bar{q}<\bar{\omega} \text{ and } \bar{\omega}<2-\bar{q}\\ 2A &: \bar{q}>\bar{\omega} \text{ and } \bar{\omega}>2-\bar{q} \text{ and } \bar{\omega}>\bar{q}-2\\ 2B &: \bar{q}<\bar{\omega} \text{ and } \bar{\omega}>2-\bar{q} \text{ and } \bar{\omega}<\bar{q}+2\\ 3A &: \bar{q}>\bar{\omega} \text{ and } \bar{\omega}<\bar{q}-2\\ 3B &: \bar{q}<\bar{\omega} \text{ and } \bar{\omega}>\bar{q}+2 \end{aligned} \tag{B.14}$$

The undoped contribution is

$$\chi^u(q,\omega) = -\frac{\pi D(E_\mathrm{F})}{8}\frac{\bar{q}^2}{\sqrt{\bar{q}^2-\bar{\omega}^2}}. \tag{B.15}$$

Here, if $\bar{q}<\bar{\omega}$, the function is allowed to become imaginary.

The subdivision of the (q,ω) plane arises from the functions $F^{\alpha\beta}_{\mathrm{Im}}$ and $F^{\alpha\beta}_{\mathrm{Re}}$ from Eqs. (3.40) and (3.52) and allows to give insight in how the response function is structured. A more in-depth discussion of the function and its properties can be found in Sec. 3.1.4.

B.3 Gapped graphene

Also for the gapped graphene system, one can write the response function in the (q,ω) plane by defining different regions according to Ref. [198]. Now there are nine different regions as indicated in Fig. B.3. The function $f(q,\omega)$ from Eq. (B.9) is again defined.

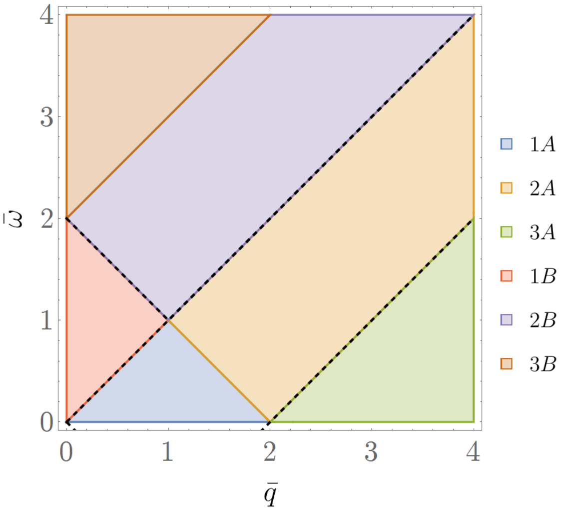

Figure B.2: Different regions in the (q, ω) plane as defined in Eq. (B.14). The black dashed curves in indicate the boundaries of the PHES.

Now, there are additional necessary functions that are defined as

$$x_0 = \sqrt{1 + \frac{4\bar{\Delta}^2}{\bar{q}^2 - \bar{\omega}^2}}, \tag{B.16}$$

$$G_<^\Delta(x) = x\sqrt{x_0^2 - x^2} - \left(2 - x_0^2\right) \operatorname{arccos}\left(x/x_0\right), \tag{B.17}$$

$$G_<^\Delta(x) = x\sqrt{x^2 - x_0^2} - \left(2 - x_0^2\right) \operatorname{arcosh}\left(x/x_0\right), \tag{B.18}$$

$$G_0^\Delta(x) = x\sqrt{x^2 - x_0^2} - \left(2 - x_0^2\right) \operatorname{arsinh}\left(x/\sqrt{-x_0^2}\right). \tag{B.19}$$

The solution then becomes

$$\begin{aligned}\mathrm{Re}\chi_{nn}\left(q,\omega\right) &= -D\left(E_{\mathrm{F}}\right)+f\left(q,\omega\right)\\ &\times\begin{cases} 0 & 1A\\ G_{<}^{\Delta}\left(\frac{2-\bar{\omega}}{\bar{q}}\right) & 2A\\ G_{<}^{\Delta}\left(\frac{2+\bar{\omega}}{\bar{q}}\right)+G_{<}^{\Delta}\left(\frac{2-\bar{\omega}}{\bar{q}}\right) & 3A\\ -G_{<}^{\Delta}\left(\frac{2+\bar{\omega}}{\bar{q}}\right)+G_{<}^{\Delta}\left(\frac{2-\bar{\omega}}{\bar{q}}\right) & 4A\\ G_{>}^{\Delta}\left(\frac{2+\bar{\omega}}{\bar{q}}\right)-G_{>}^{\Delta}\left(\frac{2-\bar{\omega}}{\bar{q}}\right) & 1B\\ G_{>}^{\Delta}\left(\frac{2+\bar{\omega}}{\bar{q}}\right) & 2B\\ G_{>}^{\Delta}\left(\frac{2+\bar{\omega}}{\bar{q}}\right)-G_{>}^{\Delta}\left(\frac{\bar{\omega}-2}{\bar{q}}\right) & 3B\\ G_{>}^{\Delta}\left(\frac{\bar{\omega}-2}{\bar{q}}\right)+G_{>}^{\Delta}\left(\frac{2+\bar{\omega}}{\bar{q}}\right) & 4B\\ G_{0}^{\Delta}\left(\frac{2+\bar{\omega}}{\bar{q}}\right)-G_{0}^{\Delta}\left(\frac{2-\bar{\omega}}{\bar{q}}\right) & 5B \end{cases},\end{aligned} \tag{B.20}$$

$$\mathrm{Im}\chi_{nn}\left(q,\omega\right) = f\left(q,\omega\right)\times\begin{cases} G_{>}^{\Delta}\left(\frac{2-\bar{\omega}}{\bar{q}}\right)-G_{>}^{\Delta}\left(\frac{2+\bar{\omega}}{\bar{q}}\right) & 1A\\ -G_{>}^{\Delta}\left(\frac{2+\bar{\omega}}{\bar{q}}\right) & 2A\\ 0 & 3A\\ 0 & 4A\\ 0 & 1B\\ -G_{<}^{\Delta}\left(\frac{2-\bar{\omega}}{\bar{q}}\right) & 2B\\ \pi\left(x_0^2-2\right) & 3B\\ \pi\left(x_0^2-2\right) & 4B\\ 0 & 5B \end{cases}. \tag{B.21}$$

On the other hand the undoped contribution is given by

$$\chi^{u}\left(q,\omega\right)=-D\left(E_{\mathrm{F}}\right)\left(\frac{\bar{\Delta}}{\bar{q}^2-\bar{\omega}^2}+\frac{\bar{k}^2-\bar{\omega}^2-4\bar{\Delta}^2}{4\left(\bar{k}^2-\bar{\omega}^2\right)^{3/2}}\left[\begin{array}{c}\Theta\left(\bar{q}-\bar{\omega}\right)\arccos\left(\frac{\bar{k}^2-\bar{\omega}^2-4\bar{\Delta}^2}{\bar{\omega}^2-\bar{k}^2-4\bar{\Delta}^2}\right)\\ -\Theta\left(\bar{q}-\bar{\omega}\right)\log\left(\frac{\left(2\bar{\Delta}+\sqrt{\bar{\omega}^2-\bar{q}^2}\right)^2}{\left|\bar{\omega}^2-\bar{k}^2-4\bar{\Delta}^2\right|}\right)\end{array}\right]\right). \tag{B.22}$$

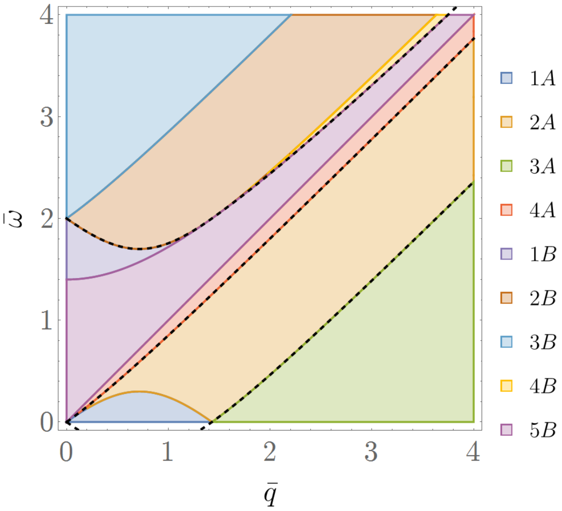

Figure B.3: Different regions in the (q, ω) plane as defined in Eq. (B.23). The used parameter for these results is $\bar{\Delta} = 0.7$. The black dashed curves in indicate the boundaries of the PHES.

The regions that are used to define the quantities are given by

$$
\begin{array}{rcl}
1A & : & \bar{\omega} < 1 - \sqrt{\left(\bar{q} - \bar{k}_{\mathrm{F}}\right)^2 + \bar{\Delta}^2} \\
2A & : & 1 - \sqrt{\left(\bar{q} - \bar{k}_{\mathrm{F}}\right)^2 + \bar{\Delta}^2} < \bar{\omega} < -1 + \sqrt{\left(\bar{q} + \bar{k}_{\mathrm{F}}\right)^2 + \bar{\Delta}^2}, \\
 & & -1 + \sqrt{\left(\bar{q} - \bar{k}_{\mathrm{F}}\right)^2 + \bar{\Delta}^2} < \bar{\omega} < -1 + \sqrt{\left(\bar{q} + \bar{k}_{\mathrm{F}}\right)^2 + \bar{\Delta}^2} \\
3A & : & \bar{\omega} < -1 + \sqrt{\left(\bar{q} - \bar{k}_{\mathrm{F}}\right)^2 + \bar{\Delta}^2} \\
4A & : & \bar{\omega} < \bar{q} \text{ and } -1 + \sqrt{\left(\bar{q} + \bar{k}_{\mathrm{F}}\right)^2 + \bar{\Delta}^2} \\
1B & : & \bar{q} < 2\bar{k}_{\mathrm{F}} \text{ and } \sqrt{\bar{q}^2 + 4\bar{\Delta}^2} < \bar{\omega} \text{ and } \bar{\omega} < 1 + \sqrt{\left(\bar{q} - \bar{k}_{\mathrm{F}}\right)^2 + \bar{\Delta}^2} \\
2B & : & 1 + \sqrt{\left(\bar{q} - \bar{k}_{\mathrm{F}}\right)^2 + \bar{\Delta}^2} < \bar{\omega} < 1 + \sqrt{\left(\bar{q} + \bar{k}_{\mathrm{F}}\right)^2 + \bar{\Delta}^2} \\
3B & : & \bar{\omega} > 1 + \sqrt{\left(\bar{q} + \bar{k}_{\mathrm{F}}\right)^2 + \bar{\Delta}^2} \\
4B & : & \bar{q} > 2\bar{k}_{\mathrm{F}} \text{ and } \sqrt{\bar{q}^2 + 4\bar{\Delta}^2} < \bar{\omega} \text{ and } \bar{\omega} < 1 + \sqrt{\left(\bar{q} - \bar{k}_{\mathrm{F}}\right)^2 + \bar{\Delta}^2} \\
5B & : & \bar{q} < \bar{\omega} \text{ and } \bar{\omega} < \sqrt{\bar{q}^2 + 4\bar{\Delta}^2}
\end{array}
\tag{B.23}
$$

In these expressions the Fermi wave vector $\bar{k}_{\mathrm{F}} = \sqrt{1 - \bar{\Delta}^2}$ was defined.

APPENDIX C

Response of the dielectric environment

In this appendix the response of an anisotropic dielectric environment on the e-e interaction in a graphene sheet is calculated. In the first section, the effect on the e-e interaction on graphene deposited on a slab with finite thickness d that is supported by a substrate is considered. In the second section, an additional slab with thickness d' is deposited on top of the graphene flake in order to create an encapsulated system. This will result in an expression for the effective hBN dielectric function as shown in Eq. (5.41) in the main text. The derivation presented in this appendix was inspired by Ref. [298].

C.1 Interaction in graphene deposited on an anisotropic dielectric medium

In order to find the interaction, one needs to solve the Poisson equation for the case of a slab of material with thickness d and a charge e on top. This system is put in between two infinite media with dielectric constant ϵ_a and ϵ_b respectively. By solving this one first obtains the interaction potential at the edge of the slab as derived in Ref. [197].

C.1.1 Maxwell equations and set-up

The main condition is that the displacement field $\boldsymbol{D}$ must satisfy the equation

$$\boldsymbol{\nabla}.\boldsymbol{D} = 0, \tag{C.1}$$

everywhere in space. Further, the boundary conditions for Maxwell's equations state that at an interface between two media one has

$$\boldsymbol{n}_{1,2} \times (\boldsymbol{E}_1 - \boldsymbol{E}_2) = 0, \tag{C.2}$$

$$\boldsymbol{n}_{1,2} . (\boldsymbol{D}_1 - \boldsymbol{D}_2) = \rho. \tag{C.3}$$

Further, note that

$$\boldsymbol{D}_i = \epsilon_i \boldsymbol{E}_i. \tag{C.4}$$

These equations imply that the electric field components along the interface need to be continuous, as is the case for the perpendicular component of $\boldsymbol{D}$ except at the top of the slab, where $\rho = -4\pi e\delta(\boldsymbol{r})$ implies there is a finite charge density.

The dielectric tensor of the slab is given by

$$\tilde{\epsilon} = \begin{bmatrix} \epsilon_x & 0 & 0 \\ 0 & \epsilon_y & 0 \\ 0 & 0 & \epsilon_z \end{bmatrix}. \tag{C.5}$$

This material is put in between two media with isotropic dielectric properties and a dielectric constant given by ϵ_a and ϵ_b respectively. This divides the space in three parts as follows:

$$\begin{cases} \epsilon_a \text{ for } z > 0 \\ \tilde{\epsilon} \text{ for } 0 > z > -d \\ \epsilon_b \text{ for } z < -d \end{cases}. \tag{C.6}$$

C.1.2 Solving for the potential

The electric potential that corresponds to the e-e interaction determines the electric field $\boldsymbol{E}$ and the displacement field $\boldsymbol{D}$. Therefore, it is this quantity that will be calculated. The relation between electric field and potential is

$$\boldsymbol{E}_i = -\boldsymbol{\nabla}\phi_i, \tag{C.7}$$

where ϕ_i is the electric potential. Because Eq. C.1 has to hold, the equation becomes

$$-\epsilon_i \nabla^2 \phi_i = 0, \tag{C.8}$$

for $i = a, b$ and

$$-\sum_{j=x,y,z} \epsilon_j \partial_j^2 \phi = 0, \tag{C.9}$$

in the slab region, which can be transformed by rescaling the coordinates as

$$x'_j = \frac{x_j}{\sqrt{\epsilon_j}}, \tag{C.10}$$

such that $\nabla'^2 \phi = 0$ holds. This gives a solution of the form

$$\begin{cases} \phi_a\left(\boldsymbol{r}, z\right) = \varphi_a e^{i\boldsymbol{k}_a.\boldsymbol{r}} e^{-k_a z} \text{ for } z > 0 \\ \phi\left(\boldsymbol{r}', z'\right) = e^{i\boldsymbol{q}.\boldsymbol{r}'}\left(Ae^{qz'} + Be^{-qz'}\right) \text{ for } 0 > z > -d \\ \phi_b\left(\boldsymbol{r}, z\right) = \varphi_b e^{i\boldsymbol{k}_b.\boldsymbol{r}} e^{k_b z} \text{ for } z < -d \end{cases}. \tag{C.11}$$

The proposed form solves the equation because

$$-\epsilon_a \nabla^2 \phi_a = -\epsilon_a \varphi_a \left(-k_a^2 + k_a^2\right) e^{i\boldsymbol{k}.\boldsymbol{r}} e^{-kz} = 0. \tag{C.12}$$

Note that Eq. (C.11) also makes sure that the potential does not diverge towards $z \to \pm\infty$. The potential in the slab can be rewritten as

$$\phi\left(\boldsymbol{r}, z\right) = e^{i\boldsymbol{k}'.\boldsymbol{r}}\left(Ae^{\frac{q}{\sqrt{\epsilon_z}}z} + Be^{-\frac{q}{\sqrt{\epsilon_z}}z}\right), \tag{C.13}$$

where $\boldsymbol{k}' = \left(\frac{q_x}{\sqrt{\epsilon_x}}, \frac{q_y}{\sqrt{\epsilon_y}}\right)$ such that

$$\epsilon_x \frac{q_x^2}{\epsilon_x} + \epsilon_y \frac{q_y^2}{\epsilon_y} - \epsilon_z \frac{q^2}{\epsilon_z} = 0. \tag{C.14}$$

Applying the boundary conditions defined in Eqs. (C.2)-(C.3), one finds the equations

$$\begin{aligned} -\varphi_a i k_{a,x} e^{i\boldsymbol{k}_a.\boldsymbol{r}} &= -i\frac{q_x}{\sqrt{\epsilon_x}} e^{i\boldsymbol{k}'.\boldsymbol{r}}\left(A + B\right), \\ -\varphi_a i k_{a,y} e^{i\boldsymbol{k}_a.\boldsymbol{r}} &= -i\frac{q_y}{\sqrt{\epsilon_y}} e^{i\boldsymbol{k}'.\boldsymbol{r}}\left(A + B\right), \\ -\epsilon_a\left(-k_a\right)\varphi_a e^{i\boldsymbol{k}_a.\boldsymbol{r}} &= -\epsilon_z e^{i\boldsymbol{k}'.\boldsymbol{r}} \frac{q}{\sqrt{\epsilon_z}}\left(A - B\right) + 4\pi e, \end{aligned} \tag{C.15}$$

which were immediately evaluated at $z = 0$. Momentum conservation yields

$$\boldsymbol{k} := \boldsymbol{k}_a = \boldsymbol{k}' = \boldsymbol{k}_b, \tag{C.16}$$

so

$$\boldsymbol{k} = \left(\frac{q_x}{\sqrt{\epsilon_x}}, \frac{q_y}{\sqrt{\epsilon_y}}\right), \tag{C.17}$$

so by defining

$$\boldsymbol{\kappa} := \frac{\boldsymbol{q}}{\sqrt{\epsilon_z}} = \left(\sqrt{\frac{\epsilon_x}{\epsilon_z}}k_x, \sqrt{\frac{\epsilon_y}{\epsilon_z}}k_y\right) \to \kappa = \sqrt{k_x^2\frac{\epsilon_x}{\epsilon_z} + \frac{\epsilon_y}{\epsilon_z}k_y^2}, \tag{C.18}$$

one gets

$$\begin{aligned} \varphi_a &= A + B, \\ \varphi_a &= A + B, \\ \epsilon_a(-k)\varphi_a &= \epsilon_z\kappa(A - B) + 4\pi e. \end{aligned} \tag{C.19}$$

Similarly, for the other side of the slab, one has that

$$\begin{aligned} -i\frac{k_x}{\sqrt{\epsilon_x}}e^{i\boldsymbol{k'}.\boldsymbol{r}}\left(Ae^{-\kappa d} + Be^{\kappa d}\right) &= -\varphi_b i k_{b,x} e^{i\boldsymbol{k}_b.\boldsymbol{r}}e^{-k_b d}, \\ -i\frac{k_y}{\sqrt{\epsilon_y}}e^{i\boldsymbol{k'}.\boldsymbol{r}}\left(Ae^{-\kappa d} + Be^{\kappa d}\right) &= -\varphi_b i k_{b,y} e^{i\boldsymbol{k}_b.\boldsymbol{r}}e^{-k_b d}, \\ -e^{i\boldsymbol{k'}.\boldsymbol{r}}\kappa\epsilon_z\left(Ae^{-\kappa d} - Be^{\kappa d}\right) &= -\epsilon_b\varphi_b k_b e^{i\boldsymbol{k}_b.\boldsymbol{r}}e^{-k_b d}. \end{aligned} \tag{C.20}$$

Introducing the same quantity as before, one finds

$$\begin{aligned} Ae^{-\kappa d} + Be^{\kappa d} &= \varphi_b e^{-kd}, \\ Ae^{-\kappa d} + Be^{\kappa d} &= \varphi_b e^{-kd}, \\ \kappa\epsilon_z\left(Ae^{-\kappa d} - Be^{\kappa d}\right) &= \epsilon_b\varphi_b k e^{-kd}. \end{aligned} \tag{C.21}$$

As a summary: one obtains four equation for the four unknown variables. These variables are namely A, B, φ_a and φ_b. The potential φ_a is the one that determines the interparticle interaction on top of the slab, so in the graphene layer that is deposited there. The relevant equations are

$$\begin{aligned} \varphi_a &= A + B, \\ \varphi_b e^{-kd} &= Ae^{-\kappa d} + Be^{\kappa d}, \\ -\epsilon_a k\varphi_a &= \epsilon_z\kappa(A - B) + 4\pi e, \\ \epsilon_b\varphi_b k e^{-kd} &= \kappa\epsilon_z\left(Ae^{-\kappa d} - Be^{\kappa d}\right). \end{aligned} \tag{C.22}$$

These need to be solved them for φ_a by finding expressions for A and B. Further one can plug in the second equation in the fourth and the first in the third to get

$$-\epsilon_a k(A + B) = \epsilon_z\kappa(A - B) + 4\pi e, \tag{C.23}$$

$$\epsilon_b k\left(Ae^{-\kappa d} + Be^{\kappa d}\right) = \kappa\epsilon_z\left(Ae^{-\kappa d} - Be^{\kappa d}\right), \tag{C.24}$$

this can be easily solved for A and B resulting in

$$A = -\frac{4\pi e\left(\epsilon_b k + \epsilon_z \kappa\right) e^{2d\kappa}}{e^{2d\kappa}\left(\epsilon_a k + \epsilon_z \kappa\right)\left(\epsilon_b k + \epsilon_z \kappa\right) - \left(\epsilon_a k - \epsilon_z \kappa\right)\left(\epsilon_b k - \epsilon_z \kappa\right)}, \tag{C.25}$$

$$B = \frac{4\pi e\left(\epsilon_b k - \epsilon_z \kappa\right)}{e^{2d\kappa}\left(\epsilon_a k + \epsilon_z \kappa\right)\left(\epsilon_b k + \epsilon_z \kappa\right) - \left(\epsilon_a k - \epsilon_z \kappa\right)\left(\epsilon_b k - \epsilon_z \kappa\right)}. \tag{C.26}$$

such that the potential φ_a is given by

$$\begin{aligned} \varphi_a &= -\frac{4\pi e}{k}\frac{\epsilon_z \kappa k \cosh\left(\kappa d\right) + \epsilon_b k^2 \sinh\left(\kappa d\right)}{\left(\epsilon_a + \epsilon_b\right)\epsilon_z k\kappa \cosh\left(\kappa d\right) + \left(\epsilon_a \epsilon_b k^2 + \epsilon_z^2 \kappa^2\right)\sinh\left(\kappa d\right)}, \\ &= -\frac{2\pi e}{k\bar{\epsilon}}\frac{\epsilon_z \kappa k + \epsilon_b k^2 \tanh\left(\kappa d\right)}{\epsilon_z k\kappa + \left(\epsilon_a \epsilon_b k^2 + \epsilon_z^2 \kappa^2\right)\tanh\left(\kappa d\right)/\bar{\epsilon}}, \end{aligned} \tag{C.27}$$

With $\bar{\epsilon} = \left(\epsilon_a + \epsilon_b\right)/2$, this is exactly Eq. (1) from the appendix of Ref. [197]. The interaction potential in graphene can then be obtained from

$$V_{\text{gr}}\left(k\right) = -e\varphi_a. \tag{C.28}$$

C.2 Interaction potential for a graphene sheet encapsulated by hBN

Similar to the case considered in the previous section, one can now consider a system with an additional layer of dielectric material but now deposited on top of the graphene sheet. The additional slab has a thickness d. Therefore, the division of the dielectric media from Eq. (C.6) becomes

$$\begin{cases} \epsilon_a \text{ for } z > d' \\ \tilde{\epsilon} \text{ for } d' > z > -d \\ \epsilon_b \text{ for } z < -d \end{cases}. \tag{C.29}$$

From this equation, one can immediately see that because the graphene flake does not affect the dielectric properties of the system and is considered to be merely a boundary condition, the physical phenomena arising from properties of the dielectric itself will respond as if it is a system with thickness $d + d'$.

Following a simimar method as described before, Eq. (C.11) now becomes

$$\begin{cases} \phi_a\left(\boldsymbol{r}, z\right) = \varphi_a e^{i\boldsymbol{k}_a \cdot \boldsymbol{r}} e^{-k_a z} \text{ for } z > d' \\ \phi_1\left(\boldsymbol{r}', z'\right) = e^{i\boldsymbol{q}\cdot\boldsymbol{r}'}\left(Ae^{qz'} + Be^{-qz'}\right) \text{ for } d' > z > 0 \\ \phi_2\left(\boldsymbol{r}', z'\right) = e^{i\boldsymbol{q}\cdot\boldsymbol{r}'}\left(Ce^{qz'} + De^{-qz'}\right) \text{ for } 0 > z > -d \\ \phi_b\left(\boldsymbol{r}, z\right) = \varphi_b e^{i\boldsymbol{k}_b \cdot \boldsymbol{r}} e^{k_b z} \text{ for } z < -d \end{cases}. \tag{C.30}$$

By applying the correct boundary conditions, this leads to the following six equations

$$\begin{aligned}
\varphi_a &= Ae^{(\kappa+k)d'} + Be^{-(\kappa-k)d'}, \\
k\epsilon_a\varphi_a &= -\epsilon_z\kappa\left(Ae^{(\kappa+k)d'} - Be^{-(\kappa-k)d'}\right), \\
\varphi_b &= Ce^{-(\kappa-k)d} + De^{(\kappa+k)d}, \\
k\epsilon_b\varphi_b &= \epsilon_z\kappa\left(Ce^{-(\kappa-k)d} - De^{(\kappa+k)d}\right), \\
A+B &= C+D, \\
\epsilon_z\kappa\left(A-B\right) &= \epsilon_z\kappa\left(C-D\right) + 4\pi e.
\end{aligned} \tag{C.31}$$

Here, the quantity κ is defined as before in Eq. (C.18). These equations can be solved algebraicly and yield

$$\begin{aligned}
V_{\text{gr}}\left(k\right) &= -e\left(A+B\right) \\
&= \frac{2\pi e^2}{k\bar{\epsilon}}\frac{k\left[\epsilon_z\kappa\cosh\left(\kappa d'\right) + k\epsilon_a\sinh\left(\kappa d'\right)\right]\left[\epsilon_z\kappa\cosh\left(\kappa d\right) + k\epsilon_b\sinh\left(\kappa d\right)\right]}{\epsilon_z\kappa\left[\epsilon_z\kappa k\cosh\left(\kappa\left(d+d'\right)\right) + \left(k^2\epsilon_a\epsilon_b + \epsilon_z^2\kappa^2\right)\sinh\left(\kappa\left(d+d'\right)\right)/\bar{\epsilon}\right]}.
\end{aligned} \tag{C.32}$$

This results in the screening potential as defined in Eq. (5.41) in the main text.

APPENDIX D

Tight-binding band structure of silicene

As explained in the main text in chapter 6, silicene consists of a buckled hexagonal lattice. Due to the buckling, the π orbitals hybridise with the σ orbitals into a mixture of sp^2 and sp^3 hybridisation. In this appendix, the construction of the Hamiltonian in Eq. (6.1) is outlined. Subsequently, the transformations that are necessary to obtain the functions ϕ_1 and ϕ_2 from Eqs. (6.2) and (6.3) explained.

D.1 Tight-binding Hamiltonian

The tight-binding Hamiltonian can be written as Eq. (6.1) as [213]

$$H_0 = \begin{bmatrix} H_\pi & H_n \\ H_n^\dagger & H_\sigma \end{bmatrix}, \tag{D.1}$$

which is written in the basis $\left\{p_z^A, p_z^B, p_y^A, p_x^A, s^A, p_y^B, p_x^B, s^B\right\}$ and where

$$H_\sigma = \begin{bmatrix} E & T \\ T^\dagger & E \end{bmatrix}. \tag{D.2}$$

In this H_σ, the diagonal matrix E describes the transitions by the σ bond in between the orbitals of the usual sp^2 hybridised system. Assuming that all the orbitals are orthogonal, only the on-site energy Δ_{sp} difference between a s and p orbital contributes such that one finds

$$E = \begin{bmatrix} 0 & 0 & 0 \\ 0 & 0 & 0 \\ 0 & 0 & \Delta_{sp} \end{bmatrix}. \tag{D.3}$$

The T matrix describes hoppings in between different sublattices and, therefore, acquires phase factors. The vectors connecting the nearest neighbours are given by

$$\begin{aligned} \boldsymbol{d}_1 &= a_0 \left(\frac{\sqrt{3}}{2}, \frac{1}{2}, \cot\theta_{\mathrm{b}} \right), && \text{(D.4)} \\ \boldsymbol{d}_2 &= a_0 \left(-\frac{\sqrt{3}}{2}, \frac{1}{2}, \cot\theta_{\mathrm{b}} \right), && \text{(D.5)} \\ \boldsymbol{d}_3 &= a_0 \left(0, -1, \cot\theta_{\mathrm{b}} \right). && \text{(D.6)} \end{aligned}$$

Here, a_0 is the in-plane projection of the inter-atomic distance and θ_{b} is the buckling angle as defined in the main text. Because the system is hexagonal, it shares the reciprocal lattice structure with graphene, but with a different lattice constant. Similarly, one can define Dirac points K and K' as well. Positioned at these Dirac points, the only effect of the hoppings is to include a notion of the buckling angle. Indeed, the hopping matrix elements are

$$t\left(k\right) = \sum_{j=1}^{3} t\left(\boldsymbol{d}_j\right) e^{i\boldsymbol{k}\cdot\boldsymbol{d}_j}. \tag{D.7}$$

Therefore, one can construct the T matrix following the quantities introduced by Slater-Koster [299] as

$$T = \begin{bmatrix} -V_1' & -iV_1' & V_2' \\ -iV_1' & V_1' & -iV_2' \\ -V_2 & iV_2' & 0 \end{bmatrix}. \tag{D.8}$$

Similarly, also the H_n matrix that connects the sp^2 hybridised atoms with the π bonds can be constructed as

$$H_n = \begin{bmatrix} 0 & 0 & 0 & V_3' & -iV_3' & 0 \\ V_3' & iV_3' & 0 & 0 & 0 & 0 \end{bmatrix}. \tag{D.9}$$

Here, the quantities V_i' are defined as

$$\begin{aligned} V_1' &\equiv \frac{3}{4}\sin^2\left(\theta_{\mathrm{b}}\right)\left(V_{pp\pi} - V_{pp\sigma}\right), \\ V_2' &\equiv \frac{3}{2}\sin\left(\theta_{\mathrm{b}}\right) V_{sp\sigma}, \\ V_3' &\equiv \frac{3}{2}\sin\left(\theta_{\mathrm{b}}\right)\cos\left(\theta_{\mathrm{b}}\right)\left(V_{pp\pi} - V_{pp\sigma}\right). \end{aligned} \tag{D.10}$$

This can be inferred by following the construction presented in Ref. [299] where the relation between the different hopping parameters $t\left(\boldsymbol{d}_j\right)$ and the energy integrals between different atomic orbitals are reported. Notice that the phase factors from Eq. (D.7) have been suppressed because the hopping has been considered to occur at a Dirac point. Therefore, Hamiltonian H_π has all zero elements.

D.2 Diagonalizing the Hamiltonian

The Hamiltonian from Eq. (D.1) can be diagonalized following the procedure discussed in Ref. [213]. This procedure first uses the C_3 symmetry of the crystal to combine the p_x and p_y orbitals for $\gamma = A, B$ as

$$\begin{aligned} \varphi_1^\gamma &= -\frac{1}{\sqrt{2}}\left(p_x^\gamma + ip_y^\gamma\right), && \text{(D.11)} \\ \varphi_2^\pm &= \frac{1}{\sqrt{2}}\left[\pm\varphi_1^{A*} - \varphi_1^{B*}\right]. && \text{(D.12)} \end{aligned}$$

This block-diagonalises the Hamiltonian in the basis $\left\{p_z^A, s^A, \varphi_1^B, p_z^B, s^B, \varphi_1^A, \varphi_2^+, \varphi_2^-\right\}$ as

$$H_0 = \begin{bmatrix} H_A & 0 & 0 \\ 0 & H_B & 0 \\ 0 & 0 & H_C \end{bmatrix}, \tag{D.13}$$

where

$$\begin{aligned} H_A &= H_B|_{V_2\to -V_2} = \begin{bmatrix} 0 & 0 & -iV_3' \\ 0 & \Delta_{sp} & iV_2' \\ iV_3' & -iV_2' & 0 \end{bmatrix}, && \text{(D.14)} \\ H_C &= \begin{bmatrix} V_1 & 0 \\ 0 & -V_1 \end{bmatrix}. && \text{(D.15)} \end{aligned}$$

The two matrices H_A and H_B have the a similar form and also share the same energy values. These energy values can be labeled ε_j with $j = 1, 2, 3$. A unitary transformation can diagonalize the Hamiltonians H_A and H_B. This transformation is shown in Ref. [213] and shall here be summarised in the matrix U_A with elements $u_{ij} = U_A|_{ij}$. The transformation that diagonalises H_B is called U_B accordingly. These two transformation matrices are identical up to a sign on the second row.

The steps shown in the previous paragraphs show that the matrix H_0 can be diagonalised by a combination of the different unitary transformations as

$$H_0' = U^\dagger H_0 U = \text{diag}\left[\varepsilon_1, \varepsilon_1, \varepsilon_2, \varepsilon_2, \varepsilon_3, \varepsilon_3, V_1, -V_1\right]. \tag{D.16}$$

This Hamiltonian is written in the basis $\left\{\phi_1, \phi_2, \phi_3, \phi_4, \phi_5, \phi_6, \varphi_2^+, \varphi_2^-\right\}$ where ϕ_j are linear combinations of $\left\{p_z^A, s^A, \varphi_1^B\right\}$ for odd j and of $\left\{p_z^B, s^B, \varphi_1^A\right\}$ for even j.

Upon calculation of the energies ε_j, it turns out that V_1 is largest energy scale, ε_2 the second largest and ε_3 the smallest. Therefore, of all eight energy levels, ε_1 corresponds to the fourth and fifth energy level. The energy levels $-V_1$ and the doubly degenerate ε_3 are occupied in an undoped silicene sheet and also the ε_1 level is partly occupied. The other energy levels remain empty. Therefore, the carrier conduction will occur using the states at the ε_1 energy level. The eigenstates corresponding to ε_1 are ϕ_1 and ϕ_2 and are given in Eqs. (6.2) and (6.3) in the main text. Note that as in the case of graphene, the energy level ε_1 is crossed by the energy spectrum in the Dirac points.

If one restores the $\boldsymbol{k}$ dependency and expands around the K-point, one finds the Hamiltonian from Eq. (6.4) with Fermi velocity

$$v_{\mathrm{F}} = -\frac{3a_0}{2}\left[\begin{array}{c} u_{11}^2\left(V_{pp\pi}\sin^2\left(\theta_{\mathrm{b}}\right) + V_{pp\sigma}\cos^2\left(\theta_{\mathrm{b}}\right)\right) - u_{21}^2 V_{ss\sigma} \\ +2u_{11}u_{21}\cos\left(\theta_{\mathrm{b}}\right)V_{sp\sigma} - \frac{1}{2}\left|u_{31}\right|^2\sin^2\left(\theta_{\mathrm{b}}\right)\left(V_{pp\sigma} - V_{pp\pi}\right) \end{array}\right]. \tag{D.17}$$

Notice that this indeed has the limit

$$v_{\mathrm{F}} = -\frac{3a_0}{2}V_{pp\pi}, \tag{D.18}$$

when the buckling disappears, corresponding to a buckling angle $\theta_{\mathrm{b}} = \pi/2$. (Notice that also the elements of the unitary transformation depend on θ_{b} such that $u_{11} \to 1$ and $u_{31} \to 0$ in this limit.)

Bibliography

[1] H. A. Atwater, “The Promise of Plasmonics”, Scientific American **296**, 56–62 (2007) (cit. on p. 3).

[2] R. Wood, “XLII. On a remarkable case of uneven distribution of light in a diffraction grating spectrum”, Philosophical Magazine Series 6 **4**, 396–402 (1902) (cit. on p. 3).

[3] L. Rayleigh, “III. Note on the remarkable case of diffraction spectra described by Prof. Wood”, Philosophical Magazine Series 6 **14**, 60–65 (1907) (cit. on p. 3).

[4] U. Fano, “The Theory of Anomalous Diffraction Gratings and of Quasi-Stationary Waves on Metallic Surfaces (Sommerfeld Waves)”, Journal of the Optical Society of America **31**, 213 (1941) (cit. on p. 3).

[5] A. Sommerfeld, “Ueber die Fortpflanzung elektrodynamischer Wellen längs eines Drahtes”, Annalen der Physik und Chemie **303**, 233–290 (1899) (cit. on p. 4).

[6] W. Crookes, “On Radiant Matter”, Nature **20**, 419–423 (1879) (cit. on p. 4).

[7] L. Tonks and I. Langmuir, “Oscillations in Ionized Gases”, Physical Review **33**, 195–210 (1929) (cit. on p. 4).

[8] I. Langmuir, “Oscillations in Ionized gases”, Proceedings of the National Academy of Sciences **14**, 627–637 (1928) (cit. on p. 4).

[9] D. Bohm and D. Pines, “A Collective Description of Electron Interactions. I. Magnetic Interactions”, Physical Review **82**, 625–634 (1951) (cit. on p. 4).

[10] D. Pines and D. Bohm, “A Collective Description of Electron Interactions: II. Collective vs Individual Particle Aspects of the Interactions”, Physical Review **85**, 338–353 (1952) (cit. on pp. 4, 57).

[11] D. Bohm and D. Pines, "A Collective Description of Electron Interactions: III. Coulomb Interactions in a Degenerate Electron Gas", Physical Review **92**, 609–625 (1953) (cit. on p. 4).

[12] R. H. Ritchie, "Plasma Losses by Fast Electrons in Thin Films", Physical Review **106**, 874–881 (1957) (cit. on p. 4).

[13] C. J. Powell and J. B. Swan, "Origin of the Characteristic Electron Energy Losses in Aluminum", Physical Review **115**, 869–875 (1959) (cit. on p. 4).

[14] E. A. Stern and R. A. Ferrell, "Surface Plasma Oscillations of a Degenerate Electron Gas", Physical Review **120**, 130–136 (1960) (cit. on p. 5).

[15] H. Raether, *Surface Plasmons on Smooth and Rough Surfaces and on Gratings* (Springer-Verlag, Berlin, 1988) (cit. on p. 5).

[16] H. T. Miyazaki and Y. Kurokawa, "Squeezing visible light waves into a 3-nm-thick and 55-nm-long plasmon cavity", Physical Review Letters **96**, 1–4 (2006) (cit. on p. 5).

[17] S. A. Maier, *Plasmonics Fundamentals and Applications* (Springer-Verlag, New York, 2007) (cit. on p. 5).

[18] H. X. Xu, E. J. Bjerneld, M. Käll, and L. Börjesson, "Spectroscopy of single hemoglobin molecules by surface enhanced Raman scattering", Phys. Rev. Lett. **83**, 4357–4360 (1999) (cit. on p. 5).

[19] H. A. Atwater and A. Polman, "Plasmonics for improved photovoltaic devices", Nature Materials **9**, 205–213 (2010) (cit. on p. 5).

[20] E. H. K. Stelzer, "Light microscopy: Beyond the diffraction limit?", Nature **417**, 806–807 (2002) (cit. on p. 5).

[21] B. Luk'yanchuk, N. I. Zheludev, S. a. Maier, N. J. Halas, P. Nordlander, H. Giessen, and C. T. Chong, "The Fano resonance in plasmonic nanostructures and metamaterials.", Nature materials **9**, 707–15 (2010) (cit. on p. 5).

[22] D. E. Chang, E. A. Demler, M. D. Lukin, and D. Quantum, "A single-photon transistor using nano-scale surface plasmons", Quantum optics **2**, 1–20 (2007) (cit. on p. 5).

[23] A. Gonzalez-Tudela, D. Martin-Cano, E. Moreno, L. Martin-Moreno, C. Tejedor, and F. J. Garcia-Vidal, "Entanglement of two qubits mediated by one-dimensional plasmonic waveguides", Physical Review Letters **106**, 1–4 (2011) (cit. on p. 5).

[24] K. Kneipp, Y. Wang, H. Kneipp, L. T. Perelman, I. Itzkan, R. R. Dasari, and M. S. Feld, "Single molecule detection using surface-enhanced Raman scattering (SERS)", Physical Review Letters **78**, 1667–1670 (1997) (cit. on p. 5).

[25] S. Nie, “Probing Single Molecules and Single Nanoparticles by Surface-Enhanced Raman Scattering”, Science **275**, 1102–1106 (1997) (cit. on p. 5).

[26] W. L. Barnes, A. Dereux, and T. W. Ebbesen, “Surface plasmon subwavelength optics”, Nature **424**, 824–30 (2003) (cit. on p. 5).

[27] H. Ditlbacher, J. R. Krenn, G. Schider, A. Leitner, and F. R. Aussenegg, “Two-dimensional optics with surface plasmon polaritons”, Applied Physics Letters **81**, 1762–1764 (2002) (cit. on p. 5).

[28] E. Kretschmann and H. Raether, “Radiative decay of non-radiative surface plasmons excited by light”, Z. Naturforsch. **23**, 2135–2136 (1968) (cit. on pp. 5, 70).

[29] A. Otto, “Excitation of nonradiative surface plasma waves in silver by the method of frustrated total reflection”, Zeitschrift fur Physik **216**, 398–410 (1968) (cit. on pp. 5, 70).

[30] B. Hecht, H. Bielefeldt, L. Novotny, Y. Inouye, and D. Pohl, “Local Excitation, Scattering, and Interference of Surface Plasmons”, Physical Review Letters **77**, 1889–1892 (1996) (cit. on p. 5).

[31] R. H. Ritchie, E. T. Arakawa, J. J. Cowan, and R. N. Hamm, “Surface-plasmon resonance effect in grating diffraction”, Physical Review Letters **21**, 1530–1533 (1968) (cit. on p. 6).

[32] K. S. Novoselov, “Electric Field Effect in Atomically Thin Carbon Films”, Science **306**, 666–669 (2004) (cit. on pp. 6, 27).

[33] K. S. Novoselov, D. Jiang, F. Schedin, T. J. Booth, V. V. Khotkevich, S. V. Morozov, and A. K. Geim, “Two-dimensional atomic crystals.”, Proceedings of the National Academy of Sciences of the United States of America **102**, 10451–3 (2005) (cit. on p. 6).

[34] A. K. Geim and K. S. Novoselov, “The rise of graphene”, Nature materials **6**, 183–91 (2007) (cit. on pp. 6–7, 20, 88).

[35] K. S. Novoselov, V. I. Fal’ko, L. Colombo, P. R. Gellert, M. G. Schwab, and K. Kim, “A roadmap for graphene”, Nature **490**, 192–200 (2012) (cit. on p. 6).

[36] S. Morozov, K. Novoselov, M. Katsnelson, F. Schedin, D. Elias, J. Jaszczak, and A. Geim, “Giant Intrinsic Carrier Mobilities in Graphene and Its Bilayer”, Physical Review Letters **100**, 016602 (2008) (cit. on pp. 6, 88).

[37] C. Lee, X. Wei, J. W. Kysar, and J. Hone, “Measurement of the Elastic Properties and Intrinsic Strength of Monolayer Graphene”, Science **321**, 385–388 (2008) (cit. on p. 6).

[38] A. A. Balandin, S. Ghosh, W. Bao, I. Calizo, D. Teweldebrhan, F. Miao, and C. N. Lau, "Superior thermal conductivity of single-layer graphene.", Nano letters **8**, 902–7 (2008) (cit. on p. 6).

[39] R. R. Nair, P. Blake, A. N. Grigorenko, K. S. Novoselov, T. J. Booth, T. Stauber, N. M. R. Peres, and A. K. Geim, "Fine Structure Constant Defines Visual Transparency of Graphene", Science **320**, 1308–1308 (2008) (cit. on pp. 6, 54).

[40] J. Moser, A. Barreiro, and A. Bachtold, "Current-induced cleaning of graphene", Applied Physics Letters **91**, 163513 (2007) (cit. on pp. 6, 141).

[41] M. Nakamura and L. Hirasawa, "Electric transport and magnetic properties in multilayer graphene", Physical Review B **77**, 045429 (2008) (cit. on p. 6).

[42] J. Ye, M. F. Craciun, M. Koshino, S. Russo, S. Inoue, H. Yuan, H. Shimotani, A. F. Morpurgo, and Y. Iwasa, "Accessing the transport properties of graphene and its multilayers at high carrier density.", Proceedings of the National Academy of Sciences of the United States of America **108**, 13002–6 (2011) (cit. on p. 6).

[43] M. Xu, T. Liang, M. Shi, and H. Chen, "Graphene-Like Two-Dimensional Materials", Chemical Reviews **113**, 3766–3798 (2013) (cit. on p. 6).

[44] B. Radisavljevic, A. Radenovic, J. Brivio, V. Giacometti, and A. Kis, "Single-layer MoS2 transistors", Nature Nanotechnology **6**, 147–150 (2011) (cit. on p. 6).

[45] C. R. Dean, a. F. Young, I. Meric, C. Lee, L. Wang, S. Sorgenfrei, K. Watanabe, T. Taniguchi, P. Kim, K. L. Shepard, and J. Hone, "Boron nitride substrates for high-quality graphene electronics", Nature Nanotechnology **5**, 722–726 (2010) (cit. on pp. 6, 88–89).

[46] A. Kara, H. Enriquez, A. P. Seitsonen, L. Lew Yan Voon, S. Vizzini, B. Aufray, and H. Oughaddou, "A review on silicene - New candidate for electronics", Surface Science Reports **67**, 1–18 (2012) (cit. on pp. 6, 120–121).

[47] A. K. Geim and I. V. Grigorieva, "Van der Waals heterostructures", Nature **499**, 419–425 (2013) (cit. on pp. 6, 89).

[48] T. Eberlein, U. Bangert, R. R. Nair, R. Jones, M. Gass, A. L. Bleloch, K. S. Novoselov, A. Geim, and P. R. Briddon, "Plasmon spectroscopy of free-standing graphene films", Physical Review B **77**, 233406 (2008) (cit. on pp. 7, 59, 69–70).

[49] Y. Liu, R. F. Willis, K. V. Emtsev, and T. Seyller, "Plasmon dispersion and damping in electrically isolated two-dimensional charge sheets", Physical Review B **78**, 201403 (2008) (cit. on pp. 7, 59, 69–70).

[50] A. N. Grigorenko, M. Polini, and K. S. Novoselov, "Graphene plasmonics", Nature Photonics **6**, 749–758 (2012) (cit. on pp. 7, 55–57, 62, 71, 121, 163, 180).

[51] A. K. Geim, “Graphene: Status and Prospects”, Science **324**, 1530–1534 (2009) (cit. on p. 7).

[52] T. Stauber, “Plasmonics in Dirac systems: from graphene to topological insulators.”, Journal of Physics: Condensed Matter **26**, 123201 (2014) (cit. on pp. 7, 69–70).

[53] L. Ju, B. Geng, J. Horng, C. Girit, M. Martin, Z. Hao, H. A. Bechtel, X. Liang, A. Zettl, Y. R. Shen, and F. Wang, “Graphene plasmonics for tunable terahertz metamaterials”, Nature Nanotechnology **6**, 630–634 (2011) (cit. on pp. 7, 71, 177, 188, 194).

[54] H. Yan, X. Li, B. Chandra, G. Tulevski, Y. Wu, M. Freitag, W. Zhu, P. Avouris, and F. Xia, “Tunable infrared plasmonic devices using graphene/insulator stacks”, Nature Nanotechnology **7**, 330–334 (2012) (cit. on pp. 7, 71).

[55] M. Jablan, H. Buljan, and M. Soljačić, “Plasmonics in graphene at infrared frequencies”, Physical Review B **80**, 245435 (2009) (cit. on p. 7).

[56] M. Freitag, T. Low, W. Zhu, H. Yan, F. Xia, and P. Avouris, “Photocurrent in graphene harnessed by tunable intrinsic plasmons”, Nature Communications **4**, 1951 (2013) (cit. on p. 7).

[57] Z. Fei, A. S. Rodin, G. O. Andreev, W. Bao, A. S. McLeod, M. Wagner, L. M. Zhang, Z. Zhao, M. Thiemens, G. Dominguez, M. M. Fogler, A. H. C. Neto, C. N. Lau, F. Keilmann, and D. N. Basov, “Gate-tuning of graphene plasmons revealed by infrared nano-imaging”, Nature **487**, 82–85 (2012) (cit. on pp. 7, 71).

[58] J. Chen, M. Badioli, P. Alonso-González, S. Thongrattanasiri, F. Huth, J. Osmond, M. Spasenović, A. Centeno, A. Pesquera, P. Godignon, A. Z. Elorza, N. Camara, F. J. García de Abajo, R. Hillenbrand, and F. H. L. Koppens, “Optical nano-imaging of gate-tunable graphene plasmons.”, Nature **487**, 77–81 (2012) (cit. on pp. 7, 71–72).

[59] A. Woessner, M. B. Lundeberg, Y. Gao, A. Principi, P. Alonso-González, M. Carrega, K. Watanabe, T. Taniguchi, G. Vignale, M. Polini, J. Hone, R. Hillenbrand, and F. H. L. Koppens, “Highly confined low-loss plasmons in graphene-boron nitride heterostructures”, Nature Materials **14**, 421–425 (2014) (cit. on pp. 7, 72, 88, 118).

[60] F. H. L. Koppens, D. E. Chang, and F. J. García De Abajo, “Graphene plasmonics: A platform for strong light-matter interactions”, Nano Letters **11**, 3370–3377 (2011) (cit. on pp. 7, 72).

[61] M. Gullans, D. E. Chang, F. H. L. Koppens, F. J. G. de Abajo, and M. D. Lukin, “Single-Photon Nonlinear Optics with Graphene Plasmons”, Physical Review Letters **111**, 247401 (2013) (cit. on p. 7).

[62] Y. V. Bludov, A. Ferreira, N. M. R. Peres, and M. I. Vasilevskiy, “A Primer on Surface Plasmon-polaritons in graphene”, International Journal of Modern Physics B **27**, 1341001 (2013) (cit. on pp. 7, 70).

[63] T. Low and P. Avouris, “Graphene plasmonics for terahertz to mid-infrared applications”, ACS Nano **8**, 1086–1101 (2014) (cit. on p. 7).

[64] Q. Bao and K. P. Loh, “Graphene photonics, plasmonics, and broadband optoelectronic devices”, ACS Nano **6**, 3677–3694 (2012) (cit. on pp. 7, 72, 176–177).

[65] F. Bonaccorso, Z. Sun, T. Hasan, and A. C. Ferrari, “Graphene Photonics and Optoelectronics”, Nature Photonics **4**, 611–622 (2010) (cit. on p. 7).

[66] X. Luo, T. Qiu, W. Lu, and Z. Ni, “Plasmons in graphene: Recent progress and applications”, Materials Science and Engineering: R: Reports **74**, 351–376 (2013) (cit. on pp. 7, 72).

[67] B. Sensale-Rodriguez, “Graphene-Based Optoelectronics”, Journal of Lightwave Technology **33**, 1100–1108 (2015) (cit. on p. 7).

[68] B. Van Duppen and F. M. Peeters, “Klein paradox for a pn junction in multilayer graphene”, EPL (Europhysics Letters) **102**, 27001 (2013) (cit. on pp. 10–11, 23–25).

[69] P. M. Krstajić, B. Van Duppen, and F. M. Peeters, “Plasmons and their interaction with electrons in trilayer graphene”, Physical Review B **88**, 195423 (2013) (cit. on pp. 10, 29, 74–75).

[70] B. Van Duppen, P. Vasilopoulos, and F. M. Peeters, “Spin and valley polarization of plasmons in silicene due to external fields”, Physical Review B **90**, 035142 (2014) (cit. on pp. 10, 119).

[71] B. Van Duppen, A. Tomadin, A. N. Grigorenko, and M. Polini, “Current-induced birefringent absorption and non-reciprocal plasmons in graphene”, 2D Materials **3**, 015011 (2016) (cit. on pp. 10, 140).

[72] M. O. Goerbig, “Electronic properties of graphene in a strong magnetic field”, Reviews of Modern Physics **83**, 1193–1243 (2011) (cit. on pp. 12, 14, 16, 18, 21, 81–82).

[73] D. Jariwala, V. K. Sangwan, L. J. Lauhon, T. J. Marks, and M. C. Hersam, “Carbon nanomaterials for electronics, optoelectronics, photovoltaics, and sensing.”, Chemical Society reviews **42**, 2824–60 (2013) (cit. on p. 12).

[74] E. F. Sheka, “The uniqueness of physical and chemical natures of graphene: their coherence and conflicts”, 22 (2013) (cit. on p. 12).

[75] M. Barbier, “Transport properties of nanostructures and superlattices on single-layer and bilayer graphene”, PhD thesis (Universiteit Antwerpen, 2012) (cit. on p. 13).

[76] A. Kekulé, “Untersuchungen über aromatische Verbindungen”, Ann. der Chem. und Pharm. **137**, 129–196 (1866) (cit. on p. 12).

[77] L. Pauling, *The Nature of Chemical Bonds* (Cornell University Press, Ithaca, 1960) (cit. on p. 14).

[78] M. I. Aroyo, U. Müller, and H. Wondratschek, “Historical introduction”, in *International tables for crystallography*, Vol. A1 (International Union of Crystallography, Chester, England, Oct. 2006), pp. 2–5 (cit. on p. 14).

[79] A. H. Castro Neto, N. M. R. Peres, K. S. Novoselov, and A. K. Geim, “The electronic properties of graphene”, Reviews of Modern Physics **81**, 109–162 (2009) (cit. on pp. 14, 26, 180).

[80] C. Kittel, *Introduction to Solid State Physics* (John Wiley & Sons Ltd., New York, 1991), p. 704 (cit. on pp. 16, 59, 90, 188).

[81] P. Wallace, “The Band Theory of Graphite”, Physical Review **71**, 622–634 (1947) (cit. on p. 16).

[82] B. Partoens and F. M. Peeters, “From graphene to graphite: Electronic structure around the K point”, Physical Review B **74**, 075404 (2006) (cit. on pp. 17–18, 75).

[83] M. Mucha-Kruczynski, O. Tsyplyatyev, A. Grishin, E. McCann, V. I. Falko, A. Bostwick, and E. Rotenberg, “Characterization of graphene through anisotropy of constant-energy maps in angle-resolved photoemission”, Physical Review B **77**, 195403 (2008) (cit. on p. 18).

[84] D. D. L. Chung, “Review: Graphite”, Journal of Materials Science **37**, 1475–1489 (2002) (cit. on p. 18).

[85] J. Tworzydlo, I. Snyman, A. R. Akhmerov, and C. W. J. Beenakker, “Valley-isospin dependence of the quantum Hall effect in a graphene p-n junction”, Physical Review B **76**, 035411 (2007) (cit. on p. 19).

[86] A. Rycerz, J. Tworzydlo, and C. W. J. Beenakker, “Valley filter and valley valve in graphene”, Nature Physics **3**, 172–175 (2007) (cit. on p. 19).

[87] P. A. M. Dirac, “The Quantum Theory of the Electron”, Proceedings of the Royal Society A: Mathematical, Physical and Engineering Sciences **117**, 610 (1928) (cit. on p. 20).

[88] M. I. Katsnelson, K. S. Novoselov, and A. K. Geim, “Chiral tunnelling and the Klein paradox in graphene”, en, Nature Physics **2**, 620–625 (2006) (cit. on pp. 20, 120).

[89] N. Stander, B. Huard, and D. Goldhaber-Gordon, “Evidence for Klein Tunneling in Graphene p-n Junctions”, Physical Review Letters **102**, 026807 (2009) (cit. on pp. 20, 22).

[90] C. L. Kane and E. J. Mele, “Quantum Spin Hall Effect in Graphene”, Physical Review Letters **95**, 226801 (2005) (cit. on p. 21).

[91] A. Bostwick, T. Ohta, T. Seyller, K. Horn, and E. Rotenberg, “Quasiparticle dynamics in graphene”, Nature Physics **3**, 36–40 (2007) (cit. on pp. 21–22).

[92] O. Klein, “Die Reflexion von Elektronen an einem Potentialsprung nach der relativistischen Dynamik von Dirac”, Zeitschrift fur Physik **53**, 157–165 (1929) (cit. on p. 22).

[93] M. Zarenia, “Confined states in mono- and bi-layer graphene nanostructures”, PhD thesis (University of Antwerp, 2013) (cit. on p. 23).

[94] T. Tudorovskiy, K. J. A. Reijnders, and M. I. Katsnelson, “Chiral tunneling in single-layer and bilayer graphene”, Physica Scripta **T146**, 014010 (2012) (cit. on pp. 23, 120).

[95] N. Gu, M. Rudner, and L. Levitov, “Chirality-Assisted Electronic Cloaking of Confined States in Bilayer Graphene”, Physical Review Letters **107**, 156603 (2011) (cit. on p. 24).

[96] M. Abramowitz and I. A. Stegun, *Handbook of Mathematical Functions with Formulas, Graphs, and Mathematical Tables* (1972), p. 1004 (cit. on pp. 26, 185).

[97] D. R. Cooper, B. D Anjou, N. Ghattamaneni, B. Harack, M. Hilke, A. Horth, N. Majlis, M. Massicotte, L. Vandsburger, E. Whiteway, and V. Yu, “Experimental Review of Graphene”, ISRN Condensed Matter Physics **2012**, 1–56 (2012) (cit. on p. 27).

[98] J. Martin, N. Akerman, G. Ulbricht, T. Lohmann, J. H. Smet, K. von Klitzing, and A. Yacoby, “Observation of electron-hole puddles in graphene using a scanning single-electron transistor”, Nature Physics **4**, 144–148 (2007) (cit. on p. 27).

[99] Y.-C. Lin, C.-Y. Lin, and P.-W. Chiu, “Controllable graphene N-doping with ammonia plasma”, Applied Physics Letters **96**, 133110 (2010) (cit. on p. 28).

[100] I. Khrapach, F. Withers, T. H. Bointon, D. K. Polyushkin, W. L. Barnes, S. Russo, and M. F. Craciun, “Novel Highly Conductive and Transparent Graphene-Based Conductors”, Advanced Materials **24**, 2844–2849 (2012) (cit. on pp. 28, 85).

[101] F. Giannazzo, V. Raineri, and E. Rimini, “Transport properties of graphene with nanoscale Lateral Resolution”, Scanning Probe Microscopy in Nanoscience and Nanotechnology **2**, 247 (2011) (cit. on p. 28).

[102] G. Giuliani and G. Vignale, *Quantum Theory of the Electron Liquid* (Cambridge University Press, 2008), p. 800 (cit. on pp. 30, 32, 39, 41–42, 46, 48, 50–52, 57–58, 64, 66–68, 73, 100, 105, 147, 157, 162, 203, 209–210).

[103] P. Nozieres and D. Pines, *Theory of Quantum Liquids* (W. A. Benjamin Inc., New York, 1966) (cit. on pp. 30, 46).

[104] J. J. Sakurai, *Modern Quantum Mechanics*, 1986 (cit. on pp. 31, 33, 46).

[105] A. Principi, G. Vignale, M. Carrega, and M. Polini, "Intrinsic lifetime of Dirac plasmons in graphene", Physical Review B **88**, 195405 (2013) (cit. on pp. 34, 68, 147).

[106] B. Wunsch, T. Stauber, F. Sols, and F. Guinea, "Dynamical polarization of graphene at finite doping", New Journal of Physics **8**, 318–318 (2006) (cit. on pp. 35, 68, 131, 210).

[107] J. Plemelj, *Problems in the sense of Riemann and Klein* (Interscience Publishers, New York, 1964) (cit. on p. 37).

[108] R. Kronig, "On the theory of dispersions of X-Rays", Journal of the Optical Society of America **12**, 547 (1926) (cit. on p. 39).

[109] H. A. Kramers, "La diffusion de la lumiere par les atomes", Transactions of Volta Centenary Congress **2**, 545 (1927) (cit. on p. 39).

[110] G. B. Arfken and H. J. Weber, *Mathematical Methods for Physicists*, 6th ed. (Elsevier Academic Press, Bulrington MA, USA, 2005) (cit. on p. 39).

[111] P. F. Maldague, "Many-body corrections to the polarizability of the two-dimensional electron gas", Surface Science **73**, 296–302 (1978) (cit. on pp. 41, 192).

[112] E. H. Hwang and S. Das Sarma, "Screening-induced temperature-dependent transport in two-dimensional graphene", Physical Review B **79**, 165404 (2009) (cit. on p. 43).

[113] R. P. Feynman, "Forces in Molecules", Physical Review **56**, 340–343 (1939) (cit. on p. 42).

[114] J. Sabio, J. Nilsson, and A. H. Castro Neto, "F-Sum Rule and Unconventional Spectral Weight Transfer in Graphene", Physical Review B **78**, 075410 (2008) (cit. on pp. 46, 50–51, 66).

[115] S. P. Goldman and G. W. F. Drake, "Relativistic sum rules and integral properties of the Dirac equation", Physical Review A **25**, 2877–2881 (1982) (cit. on p. 47).

[116] J. D. Jackson, *Classical Electrodynamics* (John Wiley & Sons Ltd., 1962) (cit. on pp. 48, 52, 59).

[117] M. I. Katsnelson, "Zitterbewegung, chirality, and minimal conductivity in graphene", European Physical Journal B **51**, 157–160 (2006) (cit. on p. 49).

[118] A. Principi, M. Polini, and G. Vignale, "Linear response of doped graphene sheets to vector potentials", Physical Review B **80**, 075418 (2009) (cit. on pp. 49, 63–64).

[119] S. H. Abedinpour, G. Vignale, a. Principi, M. Polini, W.-K. Tse, and a. H. MacDonald, "Drude weight, plasmon dispersion, and ac conductivity in doped graphene sheets", Physical Review B **84**, 045429 (2011) (cit. on p. 50).

[120] M. Peskin and D. Schroeder, *An Introduction to Quantum Field Theory* (Westview Press, 1995), p. 125 (cit. on pp. 53, 55).

[121] A. B. Kuzmenko, E. Van Heumen, F. Carbone, and D. Van Der Marel, “Universal optical conductance of graphite”, Physical Review Letters **100**, 2–5 (2008) (cit. on p. 54).

[122] F. Wang, F. Wang, Y. Zhang, C. Tian, C. Girit, and A. Zettl, “Gate-Variable Optical Transitions in Graphene”, Science **310**, 206 (2008) (cit. on pp. 54, 178).

[123] E. H. Hwang and S. Das Sarma, “Dielectric function, screening, and plasmons in two-dimensional graphene”, Physical Review B **75**, 205418 (2007) (cit. on pp. 57, 68, 131).

[124] M. Gell-Mann and F. Low, “Bound States in Quantum Field Theory”, Physical Review **84**, 350–354 (1951) (cit. on p. 57).

[125] R. J. Koch, T. Seyller, and J. A. Schaefer, “Strong phonon-plasmon coupled modes in the graphene/silicon carbide heterosystem”, Physical Review B **82**, 201413 (2010) (cit. on pp. 59, 70, 203).

[126] T. Ando, A. B. Fowler, and F. Stern, “Electronic properties of two-dimensional systems”, Reviews of Modern Physics **54**, 437–672 (1982) (cit. on p. 62).

[127] A. L. Fetter and J. D. Walecka, *Quantum Theory of Many-Particle Systems* (Dover, New York, 2003) (cit. on p. 65).

[128] R. D. Pisarski, “Chiral-symmetry breaking in three-dimensional electrodynamics”, Physical Review D **29**, 2423–2426 (1984) (cit. on p. 68).

[129] J. González, F. Guinea, and M. A. H. Vozmediano, “Electrostatic screening in fullerene molecules”, Modern Physics Letters B **7**, 1593–1599 (1993) (cit. on p. 68).

[130] T. W. Appelquist, M. Bowick, D. Karabali, and L. C. R. Wijewardhana, “Spontaneous chiral-symmetry breaking in three-dimensional QED”, Physical Review D **33**, 3704–3713 (1986) (cit. on p. 68).

[131] G. D. Mahan, *Many Particle Physics* (Plenum, New York, 1993) (cit. on p. 68).

[132] K. Shung, “Dielectric function and plasmon structure of stage-1 intercalated graphite”, Physical Review B **34**, 979–993 (1986) (cit. on p. 68).

[133] T. Ando, “Screening Effect and Impurity Scattering in Monolayer Graphene”, Journal of the Physics Society Japan **75**, 074716 (2006) (cit. on p. 68).

[134] E. Hwang and S. Das Sarma, “Plasmon modes of spatially separated double-layer graphene”, Physical Review B **80**, 205405 (2009) (cit. on pp. 68, 101).

[135] R. Roldán and L. Brey, “Dielectric screening and plasmons in AA-stacked bilayer graphene”, Physical Review B **88**, 115420 (2013) (cit. on p. 68).

[136] O. V. Gamayun, “Dynamical screening in bilayer graphene”, Physical Review B **84**, 085112 (2011) (cit. on p. 68).

[137] R. Sensarma, E. H. Hwang, and S. Das Sarma, "Dynamic screening and low-energy collective modes in bilayer graphene", Physical Review B **82**, 195428 (2010) (cit. on p. 68).

[138] A. Sabashvili, S. Östlund, and M. Granath, "Bilayer graphene spectral function in the random phase approximation and self-consistent GW approximation", Physical Review B **88**, 085439 (2013) (cit. on p. 68).

[139] X.-F. Wang and T. Chakraborty, "Coulomb screening and collective excitations in biased bilayer graphene", Physical Review B **81**, 081402 (2010) (cit. on p. 68).

[140] F. M. D. Pellegrino, G. G. N. Angilella, and R. Pucci, "Dynamical polarization of graphene under strain", Physical Review B **82**, 115434 (2010) (cit. on pp. 68, 85–86).

[141] Y. Cao, X. Li, D. Wang, X. Fan, X. Lu, Z. Zhang, C. Zeng, and Z. Zhang, "Highly anisotropic hybridization, dispersion, damping, and propagation of quantum plasmons in graphene superlattices", Physical Review B **90**, 245415 (2014) (cit. on p. 68).

[142] A. Tomadin, F. Guinea, and M. Polini, "Generation and morphing of plasmons in graphene superlattices", Physical Review B **90**, 161406 (2014) (cit. on pp. 68, 91, 97).

[143] M. Polini and F. H. L. Koppens, "Graphene: Plasmons in moiré superlattices", Nature Materials **14**, 1187–1188 (2015) (cit. on pp. 68, 89).

[144] R. Sachdeva, A. Thakur, G. Vignale, and A. Agarwal, "Plasmon modes of a massive Dirac plasma, and their superlattices", Physical Review B **91**, 205426 (2015) (cit. on p. 68).

[145] K. Shizuya, "Electromagnetic response and effective gauge theory of graphene in a magnetic field", Physical Review B **75**, 245417 (2007) (cit. on p. 68).

[146] M. Tahir and K. Sabeeh, "Inter-band magnetoplasmons in mono- and bilayer graphene", Journal of Physics: Condensed Matter **20**, 425202 (2008) (cit. on p. 68).

[147] O. Berman, G. Gumbs, and Y. Lozovik, "Magnetoplasmons in layered graphene structures", Physical Review B **78**, 085401 (2008) (cit. on p. 68).

[148] R. Roldán, J.-N. Fuchs, and M. Goerbig, "Collective modes of doped graphene and a standard two-dimensional electron gas in a strong magnetic field: Linear magnetoplasmons versus magnetoexcitons", Physical Review B **80**, 085408 (2009) (cit. on p. 68).

[149] R. Roldán, M. O. Goerbig, and J.-N. Fuchs, "The magnetic field particle-hole excitation spectrum in doped graphene and in a standard two-dimensional electron gas", Semiconductor Science and Technology **25**, 034005 (2010) (cit. on p. 68).

[150] J. M. Poumirol, W. Yu, X. Chen, C. Berger, W. A. de Heer, M. L. Smith, T. Ohta, W. Pan, M. O. Goerbig, D. Smirnov, and Z. Jiang, "Magnetoplasmons in Quasineutral Epitaxial Graphene Nanoribbons", Physical Review Letters **110**, 246803 (2013) (cit. on p. 68).

[151] N. Chamanara, D. L. Sounas, T. Szkopek, and C. Caloz, "Terahertz Magnetoplasmon Energy Concentration and Splitting in Graphene PN Junctions", 6 (2013) (cit. on p. 68).

[152] A. Principi, G. Vignale, M. Carrega, and M. Polini, "Impact of disorder on Dirac plasmon losses", Physical Review B **88**, 121405 (2013) (cit. on p. 68).

[153] A. Principi, M. Carrega, M. B. Lundeberg, A. Woessner, F. H. L. Koppens, G. Vignale, and M. Polini, "Plasmon losses due to electron-phonon scattering: The case of graphene encapsulated in hexagonal boron nitride", Physical Review B **90**, 165408 (2014) (cit. on pp. 68, 88).

[154] K.-i. Sasaki and N. Kumada, "Effects of screening on the propagation of graphene surface plasmons", Physical Review B **90**, 035449 (2014) (cit. on p. 68).

[155] H. Yan, T. Low, W. Zhu, Y. Wu, M. Freitag, X. Li, F. Guinea, P. Avouris, and F. Xia, "Damping pathways of mid-infrared plasmons in graphene nanostructures", Nature Photonics **7**, 394–399 (2013) (cit. on pp. 71, 177, 188, 194).

[156] H. Yan, F. Xia, Z. Li, and P. Avouris, "Plasmonics of coupled graphene micro-structures", New Journal of Physics **14**, 125001 (2012) (cit. on p. 71).

[157] Z. Fang, S. Thongrattanasiri, A. Schlather, Z. Liu, L. Ma, Y. Wang, P. M. Ajayan, P. Nordlander, N. J. Halas, and F. J. García de Abajo, "Gated tunability and hybridization of localized plasmons in nanostructured graphene.", ACS nano **7**, 2388–95 (2013) (cit. on p. 71).

[158] W. Zhou, J. Lee, J. Nanda, S. T. Pantelides, S. J. Pennycook, and J.-C. Idrobo, "Atomically localized plasmon enhancement in monolayer graphene", Nature Nanotechnology **7**, 161–165 (2012) (cit. on p. 72).

[159] P. Alonso-Gonzalez, A. Y. Nikitin, F. Golmar, A. Centeno, A. Pesquera, S. Velez, J. Chen, G. Navickaite, F. Koppens, A. Zurutuza, F. Casanova, L. E. Hueso, and R. Hillenbrand, "Controlling graphene plasmons with resonant metal antennas and spatial conductivity patterns", Science **344**, 1369 (2014) (cit. on pp. 72–73).

[160] J. T. Kim and S.-Y. Choi, "Graphene-based plasmonic waveguides for photonic integrated circuits", Opt. Express **19**, 24557–24562 (2011) (cit. on p. 72).

[161] A. Bostwick, F. Speck, T. Seyller, K. Horn, M. Polini, R. Asgari, A. H. MacDonald, and E. Rotenberg, "Observation of Plasmarons in Quasi-Freestanding Doped Graphene", Science **328**, 999–1002 (2010) (cit. on pp. 73–74).

[162] B. I. Lundqvist, "Single-particle spectrum of the degenerate electron gas IV. Ground state energy", Physik der Kondensierten Materie **9**, 231–235 (1969) (cit. on p. 73).

[163] A. L. Walter, A. Bostwick, K.-J. Jeon, F. Speck, M. Ostler, T. Seyller, L. Moreschini, Y. J. Chang, M. Polini, R. Asgari, A. H. MacDonald, K. Horn, and E. Rotenberg, "Effective screening and the plasmaron bands in graphene", Physical Review B **84**, 085410 (2011) (cit. on pp. 73–74).

[164] A. Overhauser, "Simplified Theory of Electron Correlations in Metals", Physical Review B **3**, 1888–1898 (1971) (cit. on p. 73).

[165] P. M. Krstajić and F. M. Peeters, "Energy-momentum dispersion relation of plasmarons in graphene", Physical Review B **85**, 205454 (2012) (cit. on p. 73).

[166] P. M. Krstajić and F. M. Peeters, "Remote electron plasmon polaron in graphene", Physical Review B **85**, 085436 (2012) (cit. on p. 74).

[167] J. D. Bernal, "The Structure of Graphite", Proceedings of the Royal Society A: Mathematical, Physical and Engineering Sciences **106**, 749–773 (1924) (cit. on p. 74).

[168] P. M. Krstajić and F. M. Peeters, "Energy-momentum dispersion relation of plasmarons in bilayer graphene", Physical Review B **88**, 165420 (2013) (cit. on p. 74).

[169] M. Aoki and H. Amawashi, "Dependence of band structures on stacking and field in layered graphene", Solid State Communications **142**, 123–127 (2007) (cit. on p. 74).

[170] S. H. Jhang, M. F. Craciun, S. Schmidmeier, S. Tokumitsu, S. Russo, M. Yamamoto, Y. Skourski, J. Wosnitza, S. Tarucha, J. Eroms, and C. Strunk, "Stacking-order dependent transport properties of trilayer graphene", Physical Review B **84**, 161408 (2011) (cit. on p. 74).

[171] C. H. Lui, Z. Li, K. F. Mak, E. Cappelluti, and T. F. Heinz, "Observation of an electrically tunable band gap in trilayer graphene", Nature Physics **7**, 944–947 (2011) (cit. on p. 74).

[172] B. Van Duppen, S. H. R. Sena, and F. M. Peeters, "Multiband tunneling in trilayer graphene", Physical Review B **87**, 195439 (2013) (cit. on p. 75).

[173] T. Stauber, "Analytical expressions for the polarizability of the honeycomb lattice", Physical Review B **82**, 201404 (2010) (cit. on p. 78).

[174] M. Ishigami, J. H. Chen, W. G. Cullen, M. S. Fuhrer, and E. D. Williams, "Atomic structure of graphene on SiO 2", Nano Letters **7**, 1643–1648 (2007) (cit. on p. 88).

[175] Y. Zhang, V. W. Brar, F. Wang, C. Girit, Y. Yayon, M. Panlasigui, A. Zettl, and M. F. Crommie, "Giant phonon-induced conductance in scanning tunnelling spectroscopy of gate-tunable graphene", Nature Physics **4**, 627–630 (2008) (cit. on p. 88).

[176] J.-h. Chen, C. Jang, S. Xiao, M. Ishigami, and M. S. Fuhrer, "Intrinsic and extrinsic performance limits of graphene devices on SiO2.", Nature nanotechnology **3**, 206–9 (2008) (cit. on p. 88).

[177] H. Wang, Y. Wu, C. Cong, J. Shang, and T. Yu, "Hysteresis of Electronic Transport in Graphene Transistors", **4**, 13 (2010) (cit. on p. 88).

[178] K. I. Bolotin, K. J. Sikes, J. Hone, H. L. Stormer, and P. Kim, "Temperature-dependent transport in suspended graphene", Physical Review Letters **101**, 1–4 (2008) (cit. on p. 88).

[179] A. S. Mayorov, R. V. Gorbachev, S. V. Morozov, L. Britnell, R. Jalil, L. a. Ponomarenko, P. Blake, K. S. Novoselov, K. Watanabe, T. Taniguchi, and a. K. Geim, "Micrometer-scale ballistic transport in encapsulated graphene at room temperature", Nano Letters **11**, 2396–2399 (2011) (cit. on p. 88).

[180] G. X. Ni, H. Wang, J. S. Wu, Z. Fei, M. D. Goldflam, F. Keilmann, B. Özyilmaz, a. H. Castro Neto, X. M. Xie, M. M. Fogler, and D. N. Basov, "Plasmons in graphene moiré superlattices.", Nature materials **14**, 1217–22 (2015) (cit. on p. 88).

[181] J. Jung, A. DaSilva, A. H. MacDonald, and S. Adam, "Origin of band gaps in graphene on hexagonal boron nitride", Nature Communications **6**, 6308 (2014) (cit. on pp. 89–90).

[182] C. R. Woods, L. Britnell, A. Eckmann, R. S. Ma, J. C. Lu, H. M. Guo, X. Lin, G. L. Yu, Y. Cao, R. V. Gorbachev, A. V. Kretinin, J. Park, L. A. Ponomarenko, M. I. Katsnelson, Y. N. Gornostyrev, K. Watanabe, T. Taniguchi, C. Casiraghi, H.-J. Gao, A. K. Geim, and K. S. Novoselov, "Commensurate - incommensurate transition in graphene on hexagonal boron nitride", Nature Physics **10**, 451–456 (2014) (cit. on pp. 89–91).

[183] M. Yankowitz, J. Xue, D. Cormode, J. D. Sanchez-Yamagishi, K. Watanabe, T. Taniguchi, P. Jarillo-Herrero, P. Jacquod, and B. J. LeRoy, "Emergence of superlattice Dirac points in graphene on hexagonal boron nitride", Nature Physics **8**, 382–386 (2012) (cit. on p. 89).

[184] L. A. Ponomarenko, R. V. Gorbachev, G. L. Yu, D. C. Elias, R. Jalil, A. A. Patel, A. Mishchenko, A. S. Mayorov, C. R. Woods, J. R. Wallbank, M. Mucha-Kruczynski, B. a. Piot, M. Potemski, I. V. Grigorieva, K. S. Novoselov, F. Guinea, V. I. Fal'ko, and A. K. Geim, "Cloning of Dirac fermions in graphene superlattices.", Nature **497**, 594–7 (2013) (cit. on p. 89).

[185] J. R. Wallbank, A. A. Patel, M. Mucha-Kruczynski, A. K. Geim, and V. I. Fal'ko, "Generic miniband structure of graphene on a hexagonal substrate", Physical Review B **87**, 245408 (2013) (cit. on pp. 89–90).

[186]R. Decker, Y. Wang, V. W. Brar, W. Regan, H.-Z. Tsai, Q. Wu, W. Gannett, A. Zettl, and M. F. Crommie, “Local Electronic Properties of Graphene on a BN Substrate via Scanning Tunneling Microscopy”, Nano Letters **11**, 2291–2295 (2011) (cit. on p. 89).

[187]R. V. Gorbachev, J. C. W. Song, G. L. Yu, A. V. Kretinin, F. Withers, Y. Cao, A. Mishchenko, I. V. Grigorieva, K. S. Novoselov, L. S. Levitov, and a. K. Geim, “Detecting topological currents in graphene superlattices”, Science **346**, 448–451 (2014) (cit. on pp. 91–92, 94–96, 113, 118).

[188]J. C. W. Song, P. Samutpraphoot, and L. S. Levitov, “Topological Bloch bands in graphene superlattices”, Proceedings of the National Academy of Sciences **112**, 10879–10883 (2015) (cit. on pp. 91, 95–96).

[189]D. J. Thouless, M. Kohmoto, M. P. Nightingale, and M. Den Nijs, “Quantized hall conductance in a two-Dimensional periodic potential”, Physical Review Letters **49**, 405–408 (1982) (cit. on p. 92).

[190]D. Xiao, M.-C. Chang, and Q. Niu, “Berry phase effects on electronic properties”, Reviews of Modern Physics **82**, 1959–2007 (2010) (cit. on p. 92).

[191]W. Yao, D. Xiao, and Q. Niu, “Valley-dependent optoelectronics from inversion symmetry breaking”, Physical Review B **77**, 235406 (2008) (cit. on pp. 95–96).

[192]H. Zeng, J. Dai, W. Yao, D. Xiao, and X. Cui, “Valley polarization in MoS2 monolayers by optical pumping”, Nature Nanotechnology **7**, 490–493 (2012) (cit. on p. 96).

[193]K. F. Mak, K. L. McGill, J. Park, and P. L. McEuen, “The valley Hall effect in MoS2 transistors”, Science **344**, 1489–1492 (2014) (cit. on p. 96).

[194]Y. Song, F. Zhai, and Y. Guo, “Generation of a fully valley-polarized current in bulk graphene”, Applied Physics Letters **103**, 183111 (2013) (cit. on pp. 96, 99).

[195]D. Gunlycke and C. T. White, “Graphene Valley Filter Using a Line Defect”, Physical Review Letters **106**, 136806 (2011) (cit. on pp. 96, 99).

[196]P. Li, M. Lewin, A. V. Kretinin, J. D. Caldwell, K. S. Novoselov, T. Taniguchi, K. Watanabe, F. Gaussmann, and T. Taubner, “Hyperbolic phonon-polaritons in boron nitride for near-field optical imaging and focusing”, Nature Communications **6**, 7507 (2015) (cit. on pp. 97, 106).

[197]A. Tomadin, A. Principi, J. C. W. Song, L. S. Levitov, and M. Polini, “Accessing Phonon Polaritons in Hyperbolic Crystals by Angle-Resolved Photoemission Spectroscopy”, Physical Review Letters **115**, 087401 (2015) (cit. on pp. 100, 108, 111, 162, 217, 221).

[198]P. K. Pyatkovskiy, “Dynamical polarization, screening, and plasmons in gapped graphene”, Journal of Physics: Condensed Matter **21**, 025506 (2009) (cit. on pp. 103, 130–132, 212).

[199] A. Poddubny, I. Iorsh, P. Belov, and Y. Kivshar, “Hyperbolic metamaterials”, Nature Photonics **7**, 948–957 (2013) (cit. on p. 106).

[200] V. G. Veselago, “The Electrodynamics of Substances with Simultaneously Negative Values of epsilon and mu”, Soviet Physics Uspekhi **10**, 509–514 (1968) (cit. on p. 106).

[201] J. D. Caldwell, A. V. Kretinin, Y. Chen, V. Giannini, M. M. Fogler, Y. Francescato, C. T. Ellis, J. G. Tischler, C. R. Woods, A. J. Giles, M. Hong, K. Watanabe, T. Taniguchi, S. a. Maier, and K. S. Novoselov, “Sub-diffractional volume-confined polaritons in the natural hyperbolic material hexagonal boron nitride”, Nature Communications **5**, 5221 (2014) (cit. on pp. 106, 108).

[202] S. Dai, Q. Ma, T. Andersen, A. S. Mcleod, Z. Fei, M. K. Liu, M. Wagner, K. Watanabe, T. Taniguchi, M. Thiemens, F. Keilmann, P. Jarillo-Herrero, M. M. Fogler, and D. N. Basov, “Subdiffractional focusing and guiding of polaritonic rays in a natural hyperbolic material”, Nature Communications **6**, 6963 (2015) (cit. on pp. 106–107).

[203] R. Geick, C. H. Perry, and G. Rupprecht, “Normal Modes in Hexagonal Boron Nitride”, Physical Review **146**, 543–547 (1966) (cit. on p. 108).

[204] A. Kumar, T. Low, K. H. Fung, P. Avouris, and N. X. Fang, “Tunable Light-Matter Interaction and the Role of Hyperbolicity in Graphene-hBN System”, Nano Letters **15**, 3172–3180 (2015) (cit. on pp. 108, 141).

[205] R. H. Lyddane, R. G. Sachs, and E. Teller, “On the polar vibrations of alkali halides”, Physical Review **59**, 673–676 (1941) (cit. on p. 108).

[206] A. Agarwal and G. Vignale, “Plasmons in spin-polarized graphene: A way to measure spin polarization”, Physical Review B **91**, 245407 (2015) (cit. on pp. 115–116).

[207] A. Agarwal, M. Polini, G. Vignale, and M. E. Flatté, “Long-lived spin plasmons in a spin-polarized two-dimensional electron gas”, Physical Review B **90**, 155409 (2014) (cit. on pp. 115–116).

[208] J. C. W. Song and M. S. Rudner, “Chiral plasmons without magnetic field”, Arxiv Preprint **03** (2015) (cit. on pp. 117, 141, 203).

[209] A. Kumar, A. Nemilentsau, K. H. Fung, G. Hanson, N. X. Fang, and T. Low, “Chiral plasmon in gapped Dirac systems”, Physical Review B **93**, 1–5 (2015) (cit. on p. 117).

[210] P. Vogt, P. De Padova, C. Quaresima, J. Avila, E. Frantzeskakis, M. C. Asensio, A. Resta, B. Ealet, and G. Le Lay, “Silicene: Compelling Experimental Evidence for Graphene-like Two-Dimensional Silicon”, Physical Review Letters **108**, 155501 (2012) (cit. on p. 120).

[211] M. E. Dávila, L. Xian, S. Cahangirov, A. Rubio, and G. Le Lay, "Germanene: a novel two-dimensional germanium allotrope akin to graphene and silicene", New Journal of Physics **16**, 095002 (2014) (cit. on p. 120).

[212] F.-f. Zhu, W.-j. Chen, Y. Xu, C.-l. Gao, D.-d. Guan, C.-h. Liu, D. Qian, S.-C. Zhang, and J.-f. Jia, "Epitaxial growth of two-dimensional stanene", Nature Materials **14**, 1020–1025 (2015) (cit. on p. 120).

[213] C.-C. Liu, H. Jiang, and Y. Yao, "Low-energy effective Hamiltonian involving spin-orbit coupling in silicene and two-dimensional germanium and tin", Physical Review B **84**, 195430 (2011) (cit. on pp. 120–125, 127, 223, 225).

[214] S. Sanvito, "Molecular spintronics", Chemical Society Reviews **40**, 3336 (2011) (cit. on pp. 120, 126).

[215] B. Huang, D. J. Monsma, and I. Appelbaum, "Coherent spin transport through a 350 micron thick silicon wafer", Physical Review Letters **99**, 1–4 (2007) (cit. on p. 120).

[216] Y. Wang, J. Zheng, Z. Ni, R. Fei, Q. Liu, R. Quhe, C. Xu, J. Zhou, Z. Gao, and J. Lu, "Half-Metallic Silicene and Germanene Nanoribbons: Towards High-Performance Spintronics Device", Nano **07**, 1250037 (2012) (cit. on p. 120).

[217] W. Han, "Perspectives for spintronics in 2D materials", APL Materials **4**, 032401 (2016) (cit. on p. 120).

[218] A. Molle, C. Grazianetti, D. Chiappe, E. Cinquanta, E. Cianci, G. Tallarida, and M. Fanciulli, "Hindering the oxidation of silicene with non-reactive encapsulation", Advanced Functional Materials **23**, 4340–4344 (2013) (cit. on p. 120).

[219] M. Houssa, A. Dimoulas, and A. Molle, "Silicene: a review of recent experimental and theoretical investigations", Journal of Physics: Condensed Matter **27**, 253002 (2015) (cit. on p. 120).

[220] B. Feng, Z. Ding, S. Meng, Y. Yao, X. He, P. Cheng, L. Chen, and K. Wu, "Evidence of silicene in honeycomb structures of silicon on Ag(111).", Nano letters **12**, 3507–11 (2012) (cit. on p. 120).

[221] D. Chiappe, C. Grazianetti, G. Tallarida, M. Fanciulli, and A. Molle, "Local Electronic Properties of Corrugated Silicene Phases", Advanced Materials **24**, 5088–5093 (2012) (cit. on p. 120).

[222] A. Fleurence, R. Friedlein, T. Ozaki, H. Kawai, Y. Wang, and Y. Yamada-Takamura, "Experimental Evidence for Epitaxial Silicene on Diboride Thin Films", Physical Review Letters **108**, 245501 (2012) (cit. on p. 120).

[223] L. Meng, Y. Wang, L. Zhang, S. Du, R. Wu, L. Li, Y. Zhang, G. Li, H. Zhou, W. A. Hofer, and H. J. Gao, "Buckled silicene formation on Ir(111)", Nano Letters **13**, 685–690 (2013) (cit. on p. 120).

[224] Y. Cai, C.-P. Chuu, C. M. Wei, and M. Y. Chou, "Stability and electronic properties of two-dimensional silicene and germanene on graphene", Physical Review B **88**, 245408 (2013) (cit. on p. 120).

[225] H. Liu, J. Gao, and J. Zhao, "Silicene on substrates: A way to preserve or tune its electronic properties", Journal of Physical Chemistry C **117**, 10353–10359 (2013) (cit. on p. 120).

[226] M. Neek-Amal, a. Sadeghi, G. R. Berdiyorov, and F. M. Peeters, "Realization of free-standing silicene using bilayer graphene", Applied Physics Letters **103**, 261904 (2013) (cit. on pp. 120, 134).

[227] L. Tao, E. Cinquanta, D. Chiappe, C. Grazianetti, M. Fanciulli, M. Dubey, A. Molle, and D. Akinwande, "Silicene field-effect transistors operating at room temperature", Nature Nanotechnology **10**, 227–231 (2015) (cit. on p. 120).

[228] N. Missault, P. Vasilopoulos, V. Vargiamidis, F. M. Peeters, and B. Van Duppen, "Spin- and valley-dependent transport through arrays of ferromagnetic silicene junctions", Physical Review B **92**, 195423 (2015) (cit. on p. 120).

[229] W.-F. Tsai, C.-Y. Huang, T.-R. Chang, H. Lin, H.-T. Jeng, and A. Bansil, "Gated silicene as a tunable source of nearly 100% spin-polarized electrons.", Nature communications **4**, 1500 (2013) (cit. on p. 120).

[230] A. Yamakage, M. Ezawa, Y. Tanaka, and N. Nagaosa, "Charge transport in pn and npn junctions of silicene", Physical Review B **88**, 085322 (2013) (cit. on p. 120).

[231] V. Vargiamidis and P. Vasilopoulos, "Electric- and exchange-field controlled transport through silicene barriers: Conductance gap and near-perfect spin polarization", Applied Physics Letters **105**, 1–6 (2014) (cit. on p. 120).

[232] V. Vargiamidis and P. Vasilopoulos, "Polarized spin and valley transport across ferromagnetic silicene junctions", Journal of Applied Physics **117**, 094305 (2015) (cit. on p. 120).

[233] C.-C. Liu, W. Feng, and Y. Yao, "Quantum Spin Hall Effect in Silicene and Two-Dimensional Germanium", Physical Review Letters **107**, 076802 (2011) (cit. on p. 121).

[234] M. Ezawa, "Hexagonally warped Dirac cones and topological phase transition in silicene superstructure", The European Physical Journal B **86**, 139 (2013) (cit. on p. 121).

[235] M. Ezawa, "Valley-Polarized Metals and Quantum Anomalous Hall Effect in Silicene", Physical Review Letters **109**, 055502 (2012) (cit. on pp. 121, 126–127).

[236] G. Guzmán-Verri and L. Lew Yan Voon, “Electronic structure of silicon-based nanostructures”, Physical Review B **76**, 075131 (2007) (cit. on p. 121).

[237] M. Tahir, A. Manchon, K. Sabeeh, and U. Schwingenschloogl, “Quantum spin/valley Hall effect and topological insulator phase transitions in silicene”, Applied Physics Letters **102**, 162412 (2013) (cit. on pp. 121, 127).

[238] K. Shakouri, P. Vasilopoulos, V. Vargiamidis, G.-Q. Hai, and F. M. Peeters, “Spin- and valley-dependent commensurability oscillations and electric-field-induced quantum Hall plateaux in periodically modulated silicene”, Applied Physics Letters **104**, 213109 (2014) (cit. on p. 121).

[239] H. Min, J. E. Hill, N. a. Sinitsyn, B. R. Sahu, L. Kleinman, and a. H. MacDonald, “Intrinsic and Rashba spin-orbit interactions in graphene sheets”, Physical Review B **74**, 165310 (2006) (cit. on pp. 125–126).

[240] G. Bihlmayer, O. Rader, and R. Winkler, “Focus on the Rashba effect”, New Journal of Physics **17**, 050202 (2015) (cit. on p. 125).

[241] Z. Qiao, S. A. Yang, W. Feng, W.-K. Tse, J. Ding, Y. Yao, J. Wang, and Q. Niu, “Quantum anomalous Hall effect in graphene from Rashba and exchange effects”, Physical Review B **82**, 161414 (2010) (cit. on p. 126).

[242] H. Haugen, D. Huertas-Hernando, and A. Brataas, “Spin transport in proximity-induced ferromagnetic graphene”, Physical Review B **77**, 115406 (2008) (cit. on p. 126).

[243] T. Yokoyama, “Spin and valley transports in junctions of Dirac fermions”, 12 (2014) (cit. on p. 126).

[244] T. Yokoyama, “Controllable valley and spin transport in ferromagnetic silicene junctions”, Physical Review B **87**, 241409 (2013) (cit. on p. 126).

[245] C. J. Tabert and E. J. Nicol, “AC/DC spin and valley Hall effects in silicene and germanene”, Physical Review B **87**, 235426 (2013) (cit. on p. 127).

[246] C. J. Tabert and E. J. Nicol, “Valley-spin polarization in the magneto-optical response of silicene and other similar 2D crystals”, Physical Review Letters **110**, 1–5 (2013) (cit. on p. 127).

[247] L. Stille, C. J. Tabert, and E. J. Nicol, “Optical signatures of the tunable band gap and valley-spin coupling in silicene”, Physical Review B **86**, 195405 (2012) (cit. on p. 129).

[248] C. J. Tabert and E. J. Nicol, “Dynamical polarization function, plasmons, and screening in silicene and other buckled honeycomb lattices”, Physical Review B **89**, 195410 (2014) (cit. on pp. 131, 135).

[249] G. R. Berdiyorov, M. Neek-Amal, F. M. Peeters, and A. C. T. van Duin, “Stabilized silicene within bilayer graphene: A proposal based on molecular dynamics and density-functional tight-binding calculations”, Physical Review B **89**, 024107 (2014) (cit. on p. 134).

[250] S. Badalyan, A. Matos-Abiague, G. Vignale, and J. Fabian, “Anisotropic plasmons in a two-dimensional electron gas with spin-orbit interaction”, Physical Review B **79**, 205305 (2009) (cit. on p. 138).

[251] D. Jalas, A. Petrov, M. Eich, W. Freude, S. Fan, Z. Yu, R. Baets, M. Popović, A. Melloni, J. D. Joannopoulos, M. Vanwolleghem, C. R. Doerr, and H. Renner, “What is - and what is not - an optical isolator”, Nature Photonics **7**, 579–582 (2013) (cit. on p. 140).

[252] P. S. Pershan, “Magneto-optical effects”, Journal of Applied Physics **38**, 1482–1490 (1967) (cit. on p. 140).

[253] J. Fujita, M. Levy, R. M. Osgood, L. Wilkens, and H. Dötsch, “Polarization-independent waveguide optical isolator based on nonreciprocal phase shift”, IEEE Photonics Technology Letters **12**, 1510–1512 (2000) (cit. on p. 140).

[254] R. J. Potton, “Reciprocity in optics”, Reports on Progress in Physics **67**, 717–754 (2004) (cit. on p. 140).

[255] D. L. Sounas, C. Caloz, and A. Alù, “Giant non-reciprocity at the subwavelength scale using angular momentum-biased metamaterials.”, Nature communications **4**, 2407 (2013) (cit. on p. 140).

[256] L. Fan, J. Wang, L. T. Varghese, H. Shen, B. Niu, Y. Xuan, a. M. Weiner, and M. Qi, “An All-Silicon Passive Optical Diode”, Science **335**, 447–450 (2012) (cit. on p. 140).

[257] S. Manipatruni, J. T. Robinson, and M. Lipson, “Optical nonreciprocity in optomechanical structures”, Physical Review Letters **102**, 100–103 (2009) (cit. on p. 140).

[258] Z. Yu and S. Fan, “Optical isolation based on nonreciprocal phase shift induced by interband photonic transitions”, Applied Physics Letters **94**, 171116 (2009) (cit. on p. 140).

[259] B. le Feber, N. Rotenberg, and L. Kuipers, “Nanophotonic control of circular dipole emission”, Nature Communications **6**, 6695 (2015) (cit. on p. 140).

[260] A. B. Khanikaev, S. H. Mousavi, W.-K. Tse, M. Kargarian, A. H. MacDonald, and G. Shvets, “Photonic topological insulators.”, Nature materials **12**, 233–9 (2013) (cit. on p. 140).

[261] Z. Wang, Y. D. Chong, J. D. Joannopoulos, and M. Soljačić, “Reflection-Free One-Way Edge Modes in a Gyromagnetic Photonic Crystal”, Physical Review Letters **100**, 013905 (2008) (cit. on p. 140).

[262]F. D. M. Haldane and S. Raghu, “Possible realization of directional optical waveguides in photonic crystals with broken time-reversal symmetry”, Physical Review Letters **100**, 1–4 (2008) (cit. on p. 140).

[263]J. F. Rodriguez-Nieva and L. S. Levitov, “Klein Scattering and Giant Non-Reciprocity in Graphene Electron Resonators”, **3**, 6 (2015) (cit. on pp. 140–141).

[264]M. V. Strikha and F. T. Vasko, “Electro-optics of graphene: Field-modulated reflection and birefringence”, Physical Review B **81**, 115413 (2010) (cit. on p. 141).

[265]M. Sabbaghi, H.-W. Lee, T. Stauber, and K. S. Kim, “Drift-induced modifications to the dynamical polarization of graphene”, Physical Review B **92**, 195429 (2015) (cit. on p. 141).

[266]R. Bistritzer and A. H. MacDonald, “Hydrodynamic theory of transport in doped graphene”, Physical Review B **80**, 085109 (2009) (cit. on pp. 141, 192).

[267]V. F. Gantmakher and Y. B. Levinson, *Carrier Scattering in Metals and Semiconductors* (Elsevier Academic Press, Amsterdam, 1987), p. 459 (cit. on pp. 141–142, 192).

[268]M. R. Ramezanali, M. M. Vazifeh, R. Asgari, M. Polini, and a. H. MacDonald, “Finite-temperature screening and the specific heat of doped graphene sheets”, Journal of Physics A: Mathematical and Theoretical **42**, 214015 (2009) (cit. on p. 145).

[269]V. N. Kotov, B. Uchoa, V. M. Pereira, F. Guinea, and a. H. Castro Neto, “Electron-Electron Interactions in Graphene: Current Status and Perspectives”, Reviews of Modern Physics **84**, 1067–1125 (2012) (cit. on pp. 147, 163).

[270]S. Dai, Z. Fei, Q. Ma, a. S. Rodin, M. Wagner, a. S. McLeod, M. K. Liu, W. Gannett, W. Regan, K. Watanabe, T. Taniguchi, M. Thiemens, G. Dominguez, A. H. Castro Neto, A. Zettl, F. Keilmann, P. Jarillo-Herrero, M. M. Fogler, and D. N. Basov, “Tunable phonon polaritons in atomically thin van der Waals crystals of boron nitride”, Science **343**, 1125–9 (2014) (cit. on p. 162).

[271]R. F. Egerton, “Electron energy-loss spectroscopy in the TEM”, Reports on Progress in Physics **72**, 16502 (2009) (cit. on p. 162).

[272]D. A. B. Miller, “Are optical transistors the logical next step?”, Nature Photonics **4**, 3–5 (2010) (cit. on p. 176).

[273]D. A. B. Miller, “Physical Reasons for Optical Interconnection”, Journal of Optoelectronics **11**, 155–168 (1997) (cit. on p. 176).

[274]A. Liu, R. Jones, L. Liao, and D. Samara-rubio, “A high-speed silicon optical modulator based on a metal -oxide - semiconductor capacitor”, Nature **427**, 615–619 (2004) (cit. on p. 176).

[275]Q. Xu, B. Schmidt, S. Pradhan, and M. Lipson, “Micrometre-scale silicon electro-optic modulator”, Nature **435**, 325–327 (2005) (cit. on p. 176).

[276]Y.-H. Kuo, Y. K. Lee, Y. Ge, S. Ren, J. E. Roth, T. I. Kamins, D. a. B. Miller, and J. S. Harris, “Strong quantum-confined Stark effect in germanium quantum-well structures on silicon”, Nature **437**, 1334–1336 (2005) (cit. on p. 176).

[277]J. Liu, M. Beals, A. Pomerene, S. Bernardis, R. Sun, J. Cheng, L. C. Kimerling, and J. Michel, “Waveguide-integrated, ultralow-energy GeSi electro-absorption modulators”, Nature Photonics **2**, 433–437 (2008) (cit. on p. 176).

[278]S. Luo, Y. Wang, X. Tong, and Z. Wang, “Graphene-based optical modulators”, Nanoscale Research Letters **10**, 199 (2015) (cit. on pp. 176–178).

[279]M. Liu, X. Yin, E. Ulin-Avila, B. Geng, T. Zentgraf, L. Ju, F. Wang, and X. Zhang, “A graphene-based broadband optical modulator.”, Nature **474**, 64–67 (2011) (cit. on pp. 176–178).

[280]D. R. Andersen, “Graphene-based long-wave infrared TM surface plasmon modulator”, Journal of the Optical Society of America B **27**, 818 (2010) (cit. on p. 176).

[281]N.-N. Feng, D. Feng, S. Liao, X. Wang, P. Dong, H. Liang, C.-C. Kung, W. Qian, J. Fong, R. Shafiiha, Y. Luo, J. Cunningham, A. V. Krishnamoorthy, and M. Asghari, “30GHz Ge electro-absorption modulator integrated with 3μm silicon-on-insulator waveguide.”, Optics express **19**, 7062–7067 (2011) (cit. on pp. 176–177).

[282]S. Yu, C. Meng, B. Chen, H. Wang, X. Wu, W. Liu, S. Zhang, Y. Liu, Y. Su, and L. Tong, “Graphene decorated microfiber for ultrafast optical modulation”, Optics Express **23**, 10764 (2015) (cit. on pp. 176–177).

[283]Y. Ding, X. Zhu, S. Xiao, H. Hu, L. H. Frandsen, N. A. Mortensen, and K. Yvind, “Effective Electro-Optical Modulation with High Extinction Ratio by a Graphene - Silicon Microring Resonator”, Nano Letters **15**, 4393–4400 (2015) (cit. on pp. 176–177).

[284]M. Mohsin, D. Schall, M. Otto, A. Noculak, D. Neumaier, and H. Kurz, “Graphene based low insertion loss electro-absorption modulator on SOI waveguide”, Optics Express **22**, 15292 (2014) (cit. on pp. 176–177).

[285]M. Liu, X. Yin, F. Wang, and X. Zhang, “Double-Layer Graphene optical modulator”, Nano letters **12**, 1482–1485 (2012) (cit. on pp. 176–177).

[286]Z. Shi, L. Gan, T. Xiao, H. Guo, and Z. Li, “All-Optical Modulation of a Graphene-Cladded Silicon Photonic Crystal Cavity”, ACS Photonics **2**, 1513–1518 (2015) (cit. on pp. 176–177).

[287] L. Yu, J. Zheng, Y. Xu, D. Dai, and S. He, “Local and Nonlocal Optically Induced Transparency Effects in Graphene - Silicon Hybrid Nanophotonic Integrated Circuits”, ACS Nano **8**, 11386–11393 (2014) (cit. on pp. 176–177).

[288] Z. Cheng and H. K. Tsang, “In-Plane Optical Absorption and Free Carrier Absorption in Graphene-on-Silicon Waveguides”, IEEE Journal of Selected Topics in Quantum Electronics **20**, 2–7 (2014) (cit. on pp. 176–177).

[289] W. Li, B. Chen, C. Meng, W. Fang, Y. Xiao, X. Li, Z. Hu, Y. Xu, L. Tong, H. Wang, W. Liu, J. Bao, and Y. R. Shen, “Ultrafast All-Optical Graphene Modulator”, Nano Letters **14**, 955–959 (2014) (cit. on pp. 176–177).

[290] R. Yu, V. Pruneri, and F. J. García de Abajo, “Resonant Visible Light Modulation with Graphene”, ACS Photonics **2**, 550–558 (2015) (cit. on pp. 176–177).

[291] J. Gosciniak and D. T. H. Tan, “Theoretical investigation of graphene-based photonic modulators”, Scientific Reports **3**, 1897 (2013) (cit. on p. 177).

[292] T. Stauber, N. M. R. Peres, and a. K. Geim, “Optical conductivity of graphene in the visible region of the spectrum”, Physical Review B **78**, 085432 (2008) (cit. on p. 178).

[293] I. Torre, “Hydrodynamic transport and viscosity in two-dimensional conductors”, PhD thesis (University of Pisa, 2014) (cit. on p. 180).

[294] S. Thongrattanasiri, I. Silveiro, and F. Javier Garcia de Abajo, “Plasmons in electrostatically doped graphene”, Applied Physics Letters **100**, 201105 (2012) (cit. on p. 184).

[295] I. Torre, A. Tomadin, R. Krahne, V. Pellegrini, and M. Polini, “Electrical plasmon detection in graphene waveguides”, Physical Review B **91**, 081402 (2015) (cit. on pp. 186, 194).

[296] R. Yu, V. Pruneri, and F. J. García de Abajo, “Resonant Visible Light Modulation with Graphene”, ACS Photonics **2**, 550–558 (2015) (cit. on p. 200).

[297] I. Torre, “2D Electrodynamics”, Private communications (2015) (cit. on p. 205).

[298] N. Forcellini, “Electrostatic Theory for Non-dispersive Media”, Private communications (2015) (cit. on p. 217).

[299] J. C. Slater and G. F. Koster, “Simplified LCAO Method for the Periodic Potential Problem”, Physical Review **94**, 1498–1524 (1954) (cit. on pp. 224–225).

Ben Van Duppen

De Boeystraat 2
2018 Antwerpen
Belgium
+32484811373
ben.vanduppen@uantwerpen.be
October 31, 1989

Education

Curriculum

2012 - present **FWO Aspirant - PhD student**
University of Antwerp
Supervisor: Prof. Dr. F. M. Peeters

2010 - 2012 **Master in physics**
Theoretical physics
Summa Cum Laude
University of Antwerp

Thesis: *Chiral Tunneling in Graphene Multilayers*
Supervisor: Prof. Dr. F. M. Peeters

Internship: *Plasmon Resonances in Au-nanoparticles on a substrate* (INSP, UPMC, Paris, FR)
Supervisor: Prof. Dr. Y. Borensztein

2007 - 2010 **Bachelor in physics**
Summa Cum Laude
University of Antwerp

Thesis (theory): *Vortex rows in Bose-Einstein Condensates*
Supervisor: Prof. Dr. J. Tempère

Thesis (experimental): *Determining the Electron Reconstruction Efficiency for the detection of the Higgs Boson at CMS, CERN*
Promotor: Prof. Dr. N. van Remortel

2001 - 2007 **Latijn-Wiskunde**
(Latin and Mathematics)
Koninklijk Atheneum, Deurne, Antwerp

Dissertation: *Aerodynamical analysis of Da Vinci's flight machine sketch proposals using finite elements techniques*

Awards

4. FWO travel grant for long stays abroad: February - June 2015
3. University of Antwerp, Faculty of Science: "Gobelijntje for Best teaching assistent, 2012 - 2013"
2. Belgian Physical Society: "Master thesis prize, 2012"
1. University of Antwerp, Department of Physics: "Best thesis presentation, 2012"

Conferences and Schools

2015 - 12	“Materials for the future”, Uppsala, SE
2015 - 07	“Interaction effects in Graphene and Related Materials”, San Sebastian, SP
2014 - 06	“Graphene Week 2014”, Graphene flagship, Chalmers University, Gothenburg, SE
2014 - 02	“Graphene study 2014, European school on graphene”, Graphene flagship, University centre Obergurgl, Obergurgl, Tirol, AU
2013 - 07	“The 2013 Lectures in Physics and Chemistry: Nanoscience and Nanotechnology”, Onassis Foundation, FORTH, Crete, GR
2013 - 06	“2013 International workshop on Bilayer Graphene”, Laboratory of Condensed Matter Physics, El Jadida, MO
2013 - 05	“General Scientific Meeting 2013”, Belgian Physical Society, Louvain-la-neuve, BE
2013 - 05	“Workshop on nanostructured graphene”, University of Antwerp, Antwerp, BE
2013 - 03	“Postgraduate AIO/OIO School 2013 Statistical Physics and Theory of Condensed Matter (SPTCM)”, Landgoed Zonheuvel, Doorn, NL
2012 - 08	“The 6th Windsor Summer School’ on Low-Dimensional Materials, Strong Correlations, and Quantum Technologies’, Cumberland Lodge, Great Park, Windsor, UK
2012 - 06	“Tweedaagse van de Theoretische en Mathematische Fysica”, Oostduinkerke, BE

Publications

International

17. Y. M. Xiao, **B. Van Duppen**, W. Xu, and F. M. Peeters: *Infrared to terahertz optical conductivity of n-type and p-type monolayer* MoS_2 *in the presence of Rashba effect*: (manuscript in preparation).

16. A. Chaves, **B. Van Duppen**, M. Z. Mayers, J. Kunstman, F. M. Peeters, and D. R. Reichman: *Theory of indirect excitons and trions in van der Waals heterostructures*, (manuscript in preparation).

15. M. Van der Donck, C. De Beule, B. Partoens, F. M. Peeters, and **B. Van Duppen**: *Piezoelectricity in asymmetrically strained bilayer graphene*, 2D Materials (2016) (submitted).

14. M. Van der Donck, F. M. Peeters, and **B. Van Duppen**: *Comment on "Creating in-plane pseudomagnetic fields in excess of 1000 T by misoriented stacking in a graphene bilayer"*, Physical Review B (2016) (submitted).

13. M. Van der Donck, F. M. Peeters, and **B. Van Duppen**: *Transport properties of bilayer graphene in a strong in-plane magnetic field.* Physical Review B **93** 115423 (2016).

12. N. Missault, P. Vasilopoulos, F.M. Peeters, and **B. Van Duppen**: *Spin- and valley-dependent miniband structure and transport in silicene superlattices.* Physical Review B **93**, 125425 (2016).

11. **B. Van Duppen**, A. Tomadin, A.N. Grigorenko, and M. Polini: *Current-induced birefringent absorption and non-reciprocal plasmons in graphene.* 2D Materials **3**, 015011 (2016) (Open access).

10. H.M. Abdullah, M. Zarenia, H. Bahlouli, F.M. Peeters, and **B. Van Duppen**: *Gate tunable layer selectivity of transport in bilayer graphene nanostructures.*, Europhysics Letters **113**, 17006 (2016).

9. N. Missault, P. Vasilopoulos, V. Vargiamidis, F.M. Peeters, and **B. Van Duppen**: *Spin- and valley-dependent transport through arrays of ferromagnetic silicene junctions.* Physical Review B **92**, 195423 (2015).

8. **B. Van Duppen**, P. Vasilopoulos, and F. M. Peeters: *Spin and valley polarization of plasmons in silicene due to external fields.* Physical Review B **90**, 035142 (2014).

7. **B. Van Duppen** and F. M. Peeters: *Thermodynamic properties of the electron gas in multilayer graphene in the presence of a perpendicular magnetic field.* Physical Review B **88**, 245429 (2013).

6. P. M. Krstajić, **B. Van Duppen**, and F. M. Peeters: *Plasmons and their interactions with electrons in trilayer graphene.* Physical Review B **88**, 195423 (2013).

5. **B. Van Duppen** and F. M. Peeters: *Four-band tunneling in bilayer graphene.* Physical Review B **87**, 205427 (2013).

4. **B. Van Duppen**, S. H. R. Sena, and F. M. Peeters: *Multiband tunneling in trilayer graphene.* Physical Review B **87**, 195439 (2013).

3. **B. Van Duppen** and F. M. Peeters: *Klein paradox for a pn junction in multilayer graphene.* Europhysics Letters **102**, 27001 (2013).

2. **B. Van Duppen** and F. M. Peeters: *Comment on Chiral tunneling in trilayer graphene [Appl. Phys. Lett. 100, 163102 (2012)].* Applied Physics Letters **101**, 226101 (2012).

1. J. Tempère, E. Vermeylen, and **B. Van Duppen**: *Skyrmion rows, vortex rows, and phase slip lines in sheared multi-component condensates.* Physica C: Superconductivity **479**, 61, (2012).

Local Journal Publications

1. **B. Van Duppen** and F. M. Peeters: *Chiral tunneling in multilayer graphene.* BΦ - Belgian Physical Society Magazine **4**, 11 (2013)

Talks

3. **B. Van Duppen**, A. Tomadin, A. N. Grigorenko, and M. Polini, *Current-induced birefringent absorption and non-reciprocal plasmons in graphene* "Materials for the Future", Uppsala Universitet, Uppsala, Sweden, December 2015 (Invited)

2. **B. Van Duppen**, *Lecture series: electronic properties of bilayer graphene*"2013 International workshop on Bilayer Graphene", El Jadida, MO, June 2013 (Invited)

1. **B. Van Duppen** and F. M. Peeters. *Chiral tunnelling in multilayer graphene. SPTCM*, Doorn, NL, March 2013

Posters

6. **B. Van Duppen** and M. Polini. *The nature of plasmons in topological graphene superlattices*, San Sebastian, SP, July 2015

5. **B. Van Duppen**, P. Vasilopoulos and F. M. Peeters, *Spin and valley polarization of plasmons in silicene due to external fields* "Graphene week", Gothenburg, SE, June 2014

4. **B. Van Duppen** and F. M. Peeters, *Chiral tunnelling in multilayer graphene*"Graphene study 2014", Obergurgl, AU, Februari 2014

3. **B. Van Duppen** and F. M. Peeters,*Chiral tunnelling in multilayer graphene* "Belgian Physical Society - General Scientific Meeting 2013', Louvain-la-neuve, BE, May 2013

2. **B. Van Duppen** and F. M. Peeters, *Chiral tunnelling in multilayer graphene* "Nanostructured graphene", Antwerp, BE, May 2013

1. **B. Van Duppen** and F. M. Peeters, *Chiral tunnelling in multilayer graphene* "The 6th Windsor Summer School", Windsor, UK, August 2012

Conference proceedings

1. Y. Borensztein, O. Merchiers, L. Delannoy, **B. Van Duppen**, C. Louis. Local oxidation of Au Nanoparticle / TiO_2 perimeter, probed by plasmon resonance spectroscopy: a key for its catalytic activity. *Réunion Plénière du GdR*, Nantes, FR, April 2013

International research visits and collaborations

International visits	2015 - present	Regular Research visit (1 - 2 weeks) to Prof. M. Polini, Scuola Normale Superiore, Pisa, Italy and IIT, Genova, Italy
	2015 - 02	Research visit (5 months) to Prof. M. Polini, Scuola Normale Superiore, Pisa, Italy
	2014 - 11	Research visit (2 weeks) to Prof. A. Chaves, Fortaleza, Brasil with the project "Multi-component and multilayered nanostructures"
International collaborations	2015 - present	Collaboration with Prof. A.N. Grigorenko (University of Manchester) on "Plasmon assisted modulation with graphene"
	2015 - present	Collaboration with Prof. M. Polini (IIT Genova) on "Plasmonics in 2D materials"
	2014 - present	Collaboration with Prof. A. Chaves (Universidade do Ceara, Brazil) on "Excitons and trions in van der Waals heterostructures"

Teaching experience

Courses	2014	"Mathematical methods for physicists" (Exercise sessions),	University of Antwerp, Bachelor in Physics
	2013 - 2015	"Introduction to graphene - Low dimensional systems" (Lectures and exercise sessions),	University of Antwerp, Master in Physics
	2012 - 2015	"Introduction to Quantum Physics" (Exercise sessions),	University of Antwerp, Bachelor in Physics

Updated: April 28, 2016